The Sensitivity to Oscillation Parameters from a Simultaneous Beam and Atmospheric Neutrino Analysis that combines the T2K and SK Experiments

Daniel Robert Clement Barrow

Magdalen College

University of Oxford

A thesis submitted for the degree of

Doctor of Philosophy

Michaelmas 2022

Abstract

Lorem ipsum dolor sit amet, consectetur adipiscing elit. Pellentesque sit amet nibh volutpat, scelerisque nibh a, vehicula neque. Integer placerat nulla massa, et vestibulum velit dignissim id. Ut eget nisi elementum, consectetur nibh in, condimentum velit. Quisque sodales dui ut tempus mattis. Duis malesuada arcu at ligula egestas egestas. Phasellus interdum odio at sapien fringilla scelerisque. Mauris sagittis eleifend sapien, sit amet laoreet felis mollis quis. Pellentesque dui ante, finibus eget blandit sit amet, tincidunt eu neque. Vivamus rutrum dapibus ligula, ut imperdiet lectus tincidunt ac. Pellentesque ac lorem sed diam egestas lobortis.

Suspendisse leo purus, efficitur mattis urna a, maximus molestie nisl. Aenean porta semper tortor a vestibulum. Suspendisse viverra facilisis lorem, non pretium erat lacinia a. Vestibulum tempus, quam vitae placerat porta, magna risus euismod purus, in viverra lorem dui at metus. Sed ac sollicitudin nunc. In maximus ipsum nunc, placerat maximus tortor gravida varius. Suspendisse pretium, lorem at porttitor rhoncus, nulla urna condimentum tortor, sed suscipit nisi metus ac risus.

Aenean sit amet enim quis lorem tristique commodo vitae ut lorem. Duis vel tincidunt lacus. Sed massa velit, lacinia sed posuere vitae, malesuada vel ante. Praesent a rhoncus leo. Etiam sed rutrum enim. Pellentesque lobortis elementum augue, at suscipit justo malesuada at. Lorem ipsum dolor sit amet, consectetur adipiscing elit. Praesent rhoncus convallis ex. Etiam commodo nunc ex, non consequat diam consectetur ut. Pellentesque vitae est nec enim interdum dapibus. Donec dapibus purus ipsum, eget tincidunt ex gravida eget. Donec luctus nisi eu fringilla mollis. Donec eget lobortis diam.

Suspendisse finibus placerat dolor. Etiam ornare elementum ex ut vehicula. Donec accumsan mattis erat. Quisque cursus fringilla diam, eget placerat neque bibendum eu. Ut faucibus dui vitae dolor porta, at elementum ipsum semper. Sed ultrices dui non arcu pellentesque placerat. Etiam posuere malesuada turpis, nec malesuada tellus malesuada.

Acknowledgements

Personal

This is where you thank your advisor, colleagues, and family and friends.

Lorem ipsum dolor sit amet, consectetur adipiscing elit. Vestibulum feugiat et est at accumsan. Praesent sed elit mattis, congue mi sed, porta ipsum. In non ullamcorper lacus. Quisque volutpat tempus ligula ac ultricies. Nam sed erat feugiat, elementum dolor sed, elementum neque. Aliquam eu iaculis est, a sollicitudin augue. Cras id lorem vel purus posuere tempor. Proin tincidunt, sapien non dictum aliquam, ex odio ornare mauris, ultrices viverra nisi magna in lacus. Fusce aliquet molestie massa, ut fringilla purus rutrum consectetur. Nam non nunc tincidunt, rutrum dui sit amet, ornare nunc. Donec cursus tortor vel odio molestie dignissim. Vivamus id mi erat. Duis porttitor diam tempor rutrum porttitor. Lorem ipsum dolor sit amet, consectetur adipiscing elit. Sed condimentum venenatis consectetur. Lorem ipsum dolor sit amet, consectetur adipiscing elit.

Aenean sit amet lectus nec tellus viverra ultrices vitae commodo nunc. Mauris at maximus arcu. Aliquam varius congue orci et ultrices. In non ipsum vel est scelerisque efficitur in at augue. Nullam rhoncus orci velit. Duis ultricies accumsan feugiat. Etiam consectetur ornare velit et eleifend.

Suspendisse sed enim lacinia, pharetra neque ac, ultricies urna. Phasellus sit amet cursus purus. Quisque non odio libero. Etiam iaculis odio a ex volutpat, eget pulvinar augue mollis. Mauris nibh lorem, mollis quis semper quis, consequat nec metus. Etiam dolor mi, cursus a ipsum aliquam, eleifend venenatis ipsum. Maecenas tempus, nibh eget scelerisque feugiat, leo nibh lobortis diam, id laoreet purus dolor eu mauris. Pellentesque habitant morbi tristique senectus et netus et malesuada fames ac turpis egestas. Nulla eget tortor eu arcu sagittis euismod fermentum id neque. In sit amet justo ligula. Donec rutrum ex a aliquet egestas.

Institutional

If you want to separate out your thanks for funding and institutional support, I don’t think there’s any rule against it. Of course, you could also just remove the subsections and do one big traditional acknowledgement section.

Lorem ipsum dolor sit amet, consectetur adipiscing elit. Ut luctus tempor ex at pretium. Sed varius, mauris at dapibus lobortis, elit purus tempor neque, facilisis sollicitudin felis nunc a urna. Morbi mattis ante non augue blandit pulvinar. Quisque nec euismod mauris. Nulla et tellus eu nibh auctor malesuada quis imperdiet quam. Sed eget tincidunt velit. Cras molestie sem ipsum, at faucibus quam mattis vel. Quisque vel placerat orci, id tempor urna. Vivamus mollis, neque in aliquam consequat, dui sem volutpat lorem, sit amet tempor ipsum felis eget ante. Integer lacinia nulla vitae felis vulputate, at tincidunt ligula maximus. Aenean venenatis dolor ante, euismod ultrices nibh mollis ac. Ut malesuada aliquam urna, ac interdum magna malesuada posuere.

Contents

1 Introduction

2 Neutrino Oscillation Physics

When first proposed, neutrinos were expected to be approximately massless fermions that only interact through weak and gravitational forces. This meant they were very difficult to detect as they can pass through significant amounts of matter without interacting. Despite this, experimental neutrino physics has developed many different detection techniques and observed neutrinos from both natural and artificial sources. In direct tension with Standard Model physics, neutrinos have been determined to oscillate between different lepton flavours, requiring them to have mass.

The observation techniques which led to the discovery of the neutrino are documented in section 2.1. The theory underpinning neutrino oscillation is described in section 2.2 and includes the approximations which can be made to simplify the understanding of neutrino oscillation in the two-flavour approximation. Past, current, and future neutrino experiments are detailed in section 2.3, including the reactor, atmospheric, and long-baseline accelerator neutrino sources that have been used to successfully constrain oscillation parameters. Finally, the current state of oscillation parameter measurements are summarised in section 2.4.

2.1 Discovery of Neutrinos

At the start of the 20^{th} century, the electrons emitted from the β-decay of the nucleus were found to have a continuous energy spectrum [1, 2]. This observation seemingly broke the energy conservation invoked within that period's nuclear models. In 1930, Pauli provided a solution to this problem in the form of a new particle, the neutrino (originally termed "neutron"). It was theorized to be an electrically neutral spin-1/2 fermion with a mass smaller than that of the electron [3]. This neutrino was emitted with the electron in β-decay to alleviate the apparent breaking of energy conservation. As a predecessor of today's weak interaction model, Fermi's theory of β-decay developed the understanding by coupling the four constituent particles: electron, proton, neutron, and neutrino, into a quantitative model [4].

Whilst Pauli was not convinced of the ability to detect neutrinos, the first observations of the particle were made in the mid-1950s when neutrinos from a reactor were observed via the inverse β-decay (IBD) process, $\bar{\nu}_e + p \rightarrow n + e^+$ [5, 6]. The detector consisted of two parts: a neutrino interaction medium and a liquid scintillator. The interaction medium was built from two water tanks, loaded with cadmium chloride to allow for increased efficiency in the detection of neutron capture. The positron emitted from IBD annihilates, $e^+ + e^- \rightarrow 2\gamma$, generating a prompt signal and the neutron is captured on the cadmium via $n +^{108} Cd \rightarrow^{109*} Cd \rightarrow^{109} Cd + \gamma$, producing a delayed signal. An increase in the coincidence rate was observed when the reactor was operating which was interpreted as interactions from neutrinos generated in the reactor.

After the discovery of the ν_e, the question of how many flavours of neutrino exist was asked. In 1962, a measurement of the ν_μ was conducted at the Brookhaven National Laboratory [7]. A proton beam was directed at a beryllium target, generating pions which then decayed via $\pi^\pm \rightarrow \mu^\pm + (\nu_\mu, \bar{\nu}_\mu)$, and the subsequent interactions of the ν_μ were observed. As the subsequent interaction of the neutrino generated muons rather than electrons, it was determined that the ν_μ was fundamentally different from ν_e. The final observation to be made was that of the ν_τ from the DONUT experiment [8]. Three neutrinos seem the obvious solution as it mirrors the known number of charged leptons (as they form weak isospin doublets) but there could be evidence of more. Several neutrino experiments have found anomalous results [9, 10] which could be attributed to "sterile" neutrinos. These hypothesised particles are not affected by gauge interactions in the Standard Model so their presence can only be inferred through the observation of non-standard oscillation modes. However, cosmological observations indicate the number of neutrino species $N_{eff} = 2.99 \pm 0.17$ [11], as measured from the cosmic microwave background power spectrum. LEP also measured the number of active neutrino flavours to be $N_\nu = 2.9840 \pm 0.0082$ [12] from measurements of the Z-decay width, but this does not strongly constrain the number of sterile neutrinos.

2.2 Theory of Neutrino Oscillation

A neutrino generated with lepton flavour α can change into a different lepton flavour β after propagating some distance. This phenomenon is called neutrino oscillation and requires that neutrinos must have a non-zero mass. This behaviour has been characterised by the Pontecorvo-Maki-Nakagawa-Sakata (PMNS) [13–15] mixing matrix which describes how the flavour and mass of neutrinos are associated. This is analogous to the Cabbibo-Kobayashi-Maskawa (CKM) [16] matrix measured in quark physics.

2.2.1 Three Flavour Oscillations

The PMNS parameterisation defines three flavour eigenstates, ν_e, ν_μ and ν_τ (indexed ν_α), which are eigenstates of the weak interaction and three mass eigenstates, ν_1, ν_2 and ν_3 (indexed ν_i). Each mass eigenstate is the superposition of all three flavour states,

$$|\nu_i\rangle = \sum_{\alpha} \mathrm{U}_{\alpha i} |\nu_\alpha\rangle . \tag{2.1}$$

Where U is the 3×3 PMNS matrix which is unitary and connects the mass and flavour eigenstates.

The weak interaction, when interacting via a $W^{\pm}$ boson, couples to flavour eigenstates so neutrinos interact with leptons of the same flavour. The propagation of a neutrino flavour eigenstate, in a vacuum, can be re-written as a plane-wave solution to the time-dependent Schrödinger equation,

$$|\nu_\alpha(t)\rangle = \sum_{i} \mathrm{U}^*_{\alpha i} |\nu_i\rangle e^{-i\phi_i}. \tag{2.2}$$

The ϕ_i term can be expressed in terms of the energy, E_i, and magnitude of the three momenta, p_i, of the neutrino, $\phi_i = E_i t - p_i x$ (t and x being time and position coordinates). The probability of observing a neutrino of flavour eigenstate β from one which originated as flavour α can be calculated as,

$$P(\nu_\alpha \rightarrow \nu_\beta) = \left|\langle \nu_\beta | \nu_\alpha(t)\rangle\right|^2 = \sum_{i,j} \mathrm{U}^*_{\alpha i}\mathrm{U}_{\beta i}\mathrm{U}_{\alpha j}\mathrm{U}^*_{\beta j} e^{-i(\phi_j - \phi_i)}. \tag{2.3}$$

The term within the exponential can be represented as,

$$\phi_j - \phi_i = E_j t - E_i t - p_j x + p_i x. \tag{2.4}$$

For a relativistic particle, $E_i \gg m_i$, a Taylor series expansion means,

$$p_i = \sqrt{E_i^2 - m_i^2} \approx E_i - \frac{m_i^2}{2E_i}. \tag{2.5}$$

Making the approximations that neutrinos are relativistic, the mass eigenstates were created with the same energy and that $x = L$, where L is the distance travelled by the neutrino, Equation 2.4 then becomes

$$\phi_j - \phi_i = \frac{\Delta m^2_{ij} L}{2E}, \tag{2.6}$$

where $\Delta m_{ij}^2 = m_i^2 - m_j^2$. This, combined with further use of unitarity relations results in Equation 2.3 becoming

$$\begin{aligned} P(\nu_\alpha \to \nu_\beta) = \delta_{\alpha\beta} - 4\sum_{i>j} \mathbb{R}\left(U_{\alpha i}^* U_{\beta i} U_{\alpha j} U_{\beta j}^*\right) \sin^2\left(\frac{\Delta m_{ij}^2 L}{4E}\right) \\ + (-)\, 2\sum_{i>j} \mathbb{I}\left(U_{\alpha i}^* U_{\beta i} U_{\alpha j} U_{\beta j}^*\right) \sin\left(\frac{\Delta m_{ij}^2 L}{2E}\right). \end{aligned} \tag{2.7}$$

Where $\delta_{\alpha\beta}$ is the Kronecker delta function and the negative sign on the last term is included for the oscillation probability of antineutrinos. As an important point to note, the observation of oscillation probability requires a non-zero value of Δm_{ij}^2, which in turn requires that neutrinos have differing masses.

Typically, the PMNS matrix is parameterised into three mixing angles, a charge parity (CP) violating phase δ_{CP}, and two Majorana phases $\alpha_{1,2}$,

$$\begin{aligned} U = \underbrace{\begin{pmatrix} 1 & 0 & 0 \\ 0 & c_{23} & s_{23} \\ 0 & -s_{23} & c_{23} \end{pmatrix}}_{\text{Atmospheric, Accelerator}} \underbrace{\begin{pmatrix} c_{13} & 0 & s_{13}e^{-i\delta_{CP}} \\ 0 & 1 & 0 \\ -s_{13}e^{-i\delta_{CP}} & 0 & c_{13} \end{pmatrix}}_{\text{Reactor, Accelerator}} \\ \times \underbrace{\begin{pmatrix} c_{12} & s_{12} & 0 \\ -s_{12} & c_{12} & 0 \\ 0 & 0 & 1 \end{pmatrix}}_{\text{Reactor, Solar}} \underbrace{\begin{pmatrix} e^{i\alpha_1/2} & 0 & 0 \\ 0 & e^{i\alpha_2/2} & 0 \\ 0 & 0 & 1 \end{pmatrix}}_{\text{Majorana}}. \end{aligned} \tag{2.8}$$

Where $s_{ij} = \sin(\theta_{ij})$ and $c_{ij} = \cos(\theta_{ij})$. The oscillation parameters are often grouped: $(1,2)$ as "solar", $(2,3)$ as "atmospheric" and $(1,3)$ as "reactor". Many neutrino experiments aim to measure the PMNS parameters from a wide array of origins, as is the purpose of this thesis.

The Majorana phase, $\alpha_{1,2}$, included within the fourth matrix in Equation 2.8 is only included for completeness. For an oscillation analysis experiment, any terms containing this phase disappear due to taking the expectation value of the PMNS matrix. Measurements of these phases can be performed by experiments searching for neutrino-less double β-decay [17].

A two-flavour approximation can be obtained when one assumes the third mass eigenstate is degenerate with another. This results in the two-flavour approximation being reasonable for understanding the features of the oscillation. In this two-flavour case, the mixing matrix becomes,

$$U_{2\,\text{Flav.}} = \begin{pmatrix} \cos(\theta) & \sin(\theta) \\ -\sin(\theta) & \cos(\theta) \end{pmatrix}. \tag{2.9}$$

This culminates in the oscillation probability,

$$\begin{aligned} P(\nu_\alpha \rightarrow \nu_\alpha) &= 1 - \sin^2(2\theta)\sin^2\left(\frac{\Delta m^2 L}{4E}\right), \\ P(\nu_\alpha \rightarrow \nu_\beta) &= \sin^2(2\theta)\sin^2\left(\frac{\Delta m^2 L}{4E}\right). \end{aligned} \tag{2.10}$$

Where $\alpha \neq \beta$. For a fixed neutrino energy, the oscillation probability is a sinusoidal function depending upon the distance over which the neutrino propagates. The frequency and amplitude of oscillation are dependent upon $\Delta m^2/4E$ and $\sin^2 2\theta$, respectively. The oscillation probabilities presented thus far assume $c = 1$, where c is the speed of light in a vacuum. In more familiar units, the maximum oscillation probability for a fixed value of θ is given at $L[km]/E[GeV] \sim 1.27/\Delta m^2$. It is this calculation that determines the best L/E value for a given experiment to be designed around for measurements of a specific value of Δm^2.

2.2.2 The MSW Effect

The theory of neutrino oscillation in a vacuum has been described in subsection 2.2.1. However, the beam neutrinos and atmospheric neutrinos originating from below the horizon propagate through the matter in the Earth. The coherent scattering of neutrinos from a material target modifies the Hamiltonian of the system which results in a change in the oscillation probability. This modification is termed the Mikheyev-Smirnov-Wolfenstein (MSW) effect [18–20]. This occurs because charged current scattering ($\nu_e + e^- \rightarrow \nu_e + e^-$, propagated by a W boson) only affects electron neutrinos whereas the neutral current scattering ($\nu_l + l^- \rightarrow$

$\nu_l + l^-$, propagated by a Z^0 boson) interacts through all neutrino flavours equally. In the two-flavour approximation, the effective mixing parameter becomes

$$\sin^2(2\theta) \rightarrow \sin^2(2\theta_m) = \frac{\sin^2(2\theta)}{(A/\Delta m^2 - \cos(2\theta))^2 + \sin^2(2\theta)}, \tag{2.11}$$

where $A = 2\sqrt{2} G_F N_e E$, N_e is the electron density of the medium and G_F is Fermi's constant. It is clear that there exists a value of $A = \Delta m^2 \cos(2\theta)$ for $\Delta m^2 > 0$, which results in a divergent mixing parameter, colloquially called the matter resonance. This resonance regenerates the electron neutrino component of the neutrino flux [18–20]. The density at which the resonance occurs is given by

$$N_e = \frac{\Delta m^2 \cos(2\theta)}{2\sqrt{2} G_F E}. \tag{2.12}$$

At densities lower than this critical value, the oscillation probability will be much closer to that of vacuum oscillation. For antineutrinos, $N_e \rightarrow -N_e$ [21]. The resonance occurring from the MSW effect depends on the sign of Δm^2. Therefore, any neutrino oscillation experiment which observes neutrinos and antineutrinos which have propagated through matter can have some sensitivity to the ordering of the neutrino mass eigenstates.

2.3 Neutrino Oscillation Measurements

As evidence of beyond Standard Model physics, the 2015 Nobel Prize in Physics was awarded to the Super-Kamiokande (SK) [22] and Sudbury Neutrino Observatory (SNO) [23] collaborations for the first definitive observation of solar and atmospheric neutrino oscillation [24]. Since then, the field has seen a wide array of oscillation measurements from a variety of neutrino sources. As seen in subsection 2.2.1, the neutrino oscillation probability is dependent on the ratio of the propagation baseline, L, to the neutrino energy, E. It is this ratio that determines the type of neutrino oscillation a particular experiment is sensitive to.

As illustrated in Figure 2.1, there are many neutrino sources that span a wide range of energies. The least energetic neutrinos are from reactor and terrestrial sources at $O(1)$MeV whereas the most energetic neutrinos originate from atmospheric and galactic neutrinos of $> O(1)$TeV.

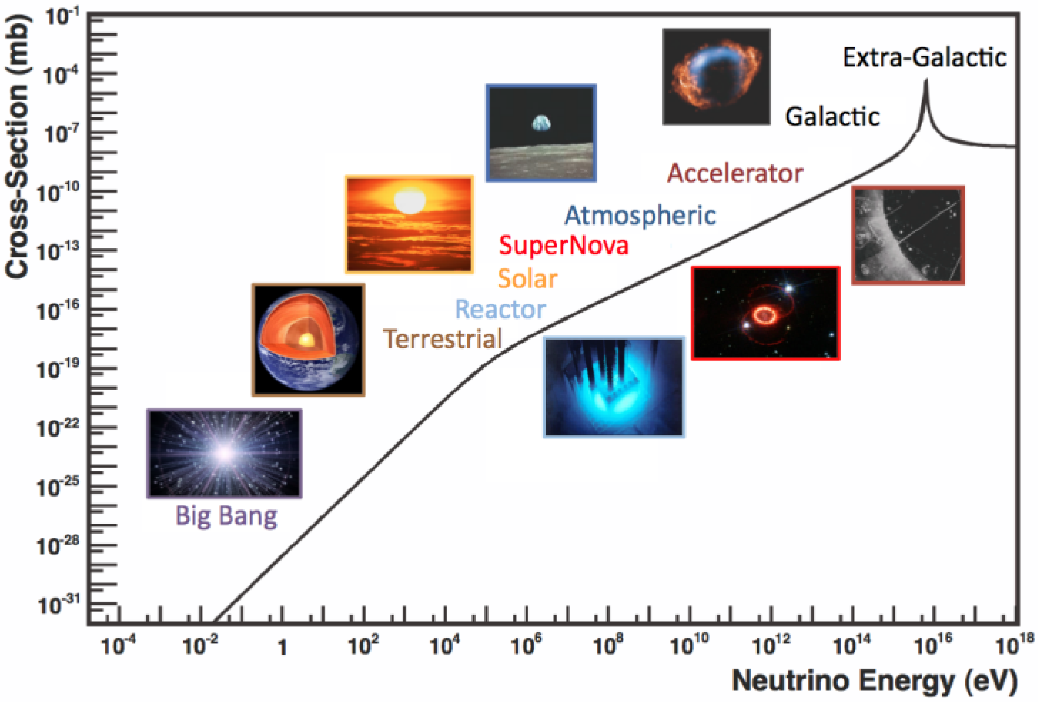

Figure 2.1: The electro-weak cross-section for $\bar{\nu}_e + e^- \rightarrow \bar{\nu}_e + e^-$ scattering on free electrons from various natural and man-made neutrino sources, as a function of neutrino energy. Taken from [25]

2.3.1 Solar Neutrinos

Solar neutrinos are emitted from fusion reaction chains at the centre of the Sun. The solar neutrino flux, given as a function of neutrino energy for different fusion and decay chains, is illustrated in Figure 2.2. Whilst proton-proton fusion generates the largest flux of neutrinos, the neutrinos are low energy and are difficult to reconstruct due to the IBD interaction threshold of 1.8MeV [26]. Consequently, most experiments focus on the neutrinos from the decay of ^8B (via $^8B \rightarrow ^8 Be^* + e^+ + \nu_e$), which are higher energy.

The first measurements of solar neutrinos observed a significant reduction in the event rate compared to predictions from the Standard Solar Model [28, 29]. A proposed solution to this "solar neutrino problem" was $\nu_e \leftrightarrow \nu_\mu$ oscillations in a

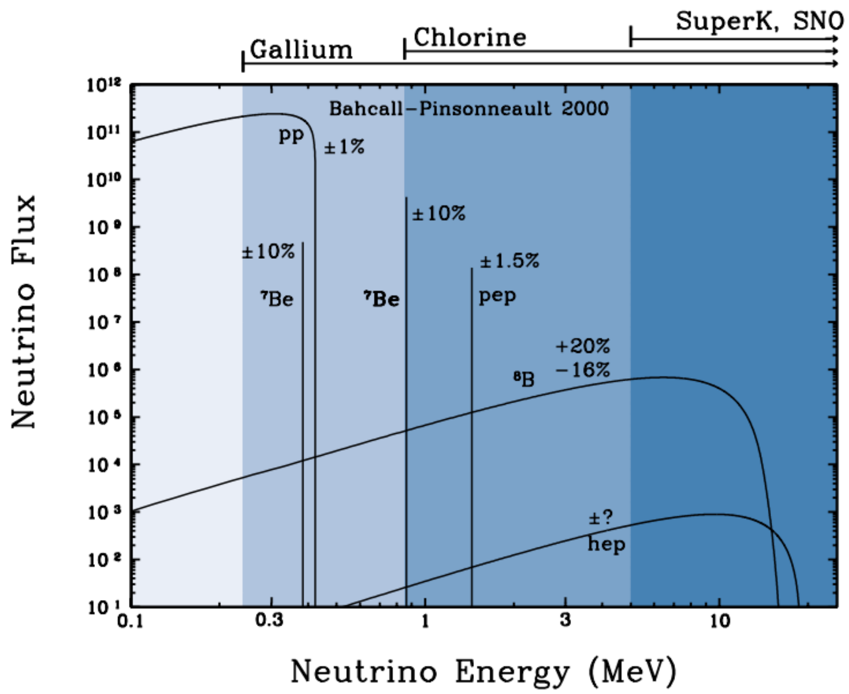

Figure 2.2: The solar neutrino flux as a function of neutrino energy for various fusion reactions and decay chains as predicted by the Standard Solar Model. Taken from [27].

precursory version of the PMNS model [30]. The Kamiokande [31], Gallex [32] and Sage [33] experiments confirmed the ~ 0.5 factor deficit of solar neutrinos.

The conclusive solution to this problem was determined by the SNO collaboration [34]. Using a deuterium water target to observe ^{8}B neutrinos, the event rate of charged current (CC), neutral current (NC), and elastic scattering (ES) interactions (Given in Equation 2.13) was simultaneously measured. CC events can only occur for electron neutrinos, whereas the NC channel is agnostic to neutrino flavour, and the ES reaction has a small excess sensitivity for the detection of electron neutrino interactions. This meant that there were direct measurements of the ν_e and ν_x neutrino flux. It was concluded that the CC and ES interaction rates were consistent with the deficit previously observed. Most importantly, the NC reaction rate was only consistent with the others under the hypothesis of flavour transformation.

$$\begin{aligned} \nu_e + d &\rightarrow p + p + e^- && (CC) \\ \nu_x + d &\rightarrow p + n + \nu_x && (NC) \\ \nu_x + e^- &\rightarrow \nu_x + e^- && (ES) \end{aligned} \tag{2.13}$$

Since the SNO measurement, many experiments have since measured the neutrino flux of different interaction chains within the sun [35–37]. The most recent measurement was that of CNO-cycle neutrinos which were recently observed with 5σ significance by the Borexino collaboration [35].

2.3.2 Accelerator Neutrinos

The concept of using an artificial "neutrino beam" was first realised in 1962 [38]. Since then, many experiments have adopted the same fundamental concepts. Typically, a proton beam is aimed at a target producing charged mesons that decay to neutrinos. The mesons can be sign-selected by the use of magnetic focusing horns to generate a neutrino or antineutrino beam. Pions are the primary mesons that decay and depending on the orientation of the magnetic field, a muon (anti-)neutrino beam is generated via $\pi^+ \rightarrow \mu^+ + \nu_\mu$ or $\pi^- \rightarrow \mu^- + \bar{\nu}_\mu$. The decay of muons and kaons results in an irreducible intrinsic electron neutrino background. In T2K, this background contamination is $O(< 1\%)$ [39]. There is also an approximately $\sim 5\%$ "wrong-sign" neutrino background of $\bar{\nu}_\mu$ generated via the same decays. As the beam is generated by proton interactions (rather than anti-proton interactions), the wrong-sign component in the antineutrino beam is larger when operating in neutrino mode.

Tuning the proton energy in the beam and using beam focusing techniques allows the neutrino energy to be set to a value that maximises the disappearance oscillation probability in the L/E term in Equation 2.10. This means that accelerator experiments are typically more sensitive to the mixing parameters as compared to a natural neutrino source. However, the disadvantage compared to atmospheric neutrino experiments is the cost of building a facility to provide high-energy neutrinos, with a high flux, which is required for longer baselines. Consequently, there is typically less sensitivity to matter effects and the ordering of the neutrino mass eigenstates.

A neutrino experiment measures

$$R(\vec{x}) = \Phi(E_\nu) \times \sigma(E_\nu) \times \epsilon(\vec{x}) \times P(\nu_\alpha \to \nu_\beta), \tag{2.14}$$

where $R(\vec{x})$ is the event rate of neutrinos at position $\vec{x}$, $\Phi(E_\nu)$ is the flux of neutrinos with energy E_ν, $\sigma(E_\nu)$ is the cross-section of the neutrino interaction and $\epsilon(\vec{x})$ is the efficiency and resolution of the detector. In order to leverage the most out of an accelerator neutrino experiment, the flux and cross-section systematics need to be constrained. This is typically done via the use of a "near detector", situated at a baseline of $O(1)$km. This detector observes the unoscillated neutrino flux and constrains the parameters used within the flux and cross-section model.

The first accelerator experiments to precisely measure oscillation parameters were MINOS [40] and K2K [41]. These experiments confirmed the ν_μ disappearance seen in atmospheric neutrino experiments by finding consistent parameter values for $\sin^2(\theta_{23})$ and Δm^2_{32}. The current generation of accelerator neutrino experiments, T2K and NOνA extended this field by observing $\bar{\nu}_\mu \to \bar{\nu}_e$ and lead the sensitivity to atmospheric mixing parameters as seen in Figure 2.6 [42]. The two experiments differ in their peak neutrino energy, baseline, and detection technique. The NOνA experiment is situated at a baseline of 810km from the NuMI beamline which delivers 2GeV neutrinos. The T2K neutrino beam is peaked around 0.6GeV and propagates 295km [43]. Additionally, the NOνA experiment uses functionally identical detectors (near and far) whereas T2K uses a plastic scintillator technique at the near detector and a water Cherenkov far detector. The future generation experiments DUNE [44] and Hyper-Kamiokande [45] will succeed these experiments as the high-precision era of neutrino oscillation parameter measurements develops.

Several anomalous results have been observed in the LSND [9] and MiniBooNE [10] detectors which were designed with purposefully short baselines.

Parts of the neutrino community attributed these results to oscillations induced by a fourth "sterile" neutrino [46] but several searches in other experiments, MicroBooNE [47] and KARMEN [48], found no hints of additional neutrino species. The solution to the anomalous results is still being determined.

2.3.3 Atmospheric Neutrinos

The interactions of primary cosmic ray protons in the Earth's upper atmosphere generate showers of energetic hadrons. These are mostly pions and kaons that decay to produce a natural source of neutrinos spanning energies of MeV to TeV [49]. The main decay is via,

$$\begin{aligned} \pi^{\pm} &\rightarrow \mu^{\pm} + (\nu_{\mu}, \bar{\nu}_{\mu}), \\ \mu^{\pm} &\rightarrow e^{\pm} + (\nu_{\mu}, \bar{\nu}_{\mu}) + (\nu_{e}, \bar{\nu}_{e}), \end{aligned} \tag{2.15}$$

such that for a single pion decay, three neutrinos can be produced. The atmospheric neutrino flux energy spectra as predicted by the Bartol [50], Honda [51–53], and FLUKA [54] models are illustrated in Figure 2.3. The flux distribution peaks at an energy of $O(10)$GeV. The uncertainties associated with these models are dominated by the hadronic production of kaon and pions as well as the primary cosmic flux.

Unlike long-baseline experiments which have a fixed baseline, the distance atmospheric neutrinos propagate is dependent upon the zenith angle at which they interact. This is illustrated in Figure 2.4. Neutrinos that are generated directly above the detector ($\cos(\theta) = 1.0$) have a baseline equivalent to the height of the atmosphere, whereas neutrinos that interact directly below the detector ($\cos(\theta) = -1.0$) have to travel a length equal to the diameter of the Earth. This means atmospheric neutrinos have a baseline that varies from $O(20)$km to $O(6 \times 10^3)$km. Any neutrino generated at or below the horizon will be subject to MSW matter resonance as they propagate through the Earth.

Figure 2.5 highlights the neutrino flux as a function of the zenith angle for different slices of neutrino energy. For medium to high-energy neutrinos (and to

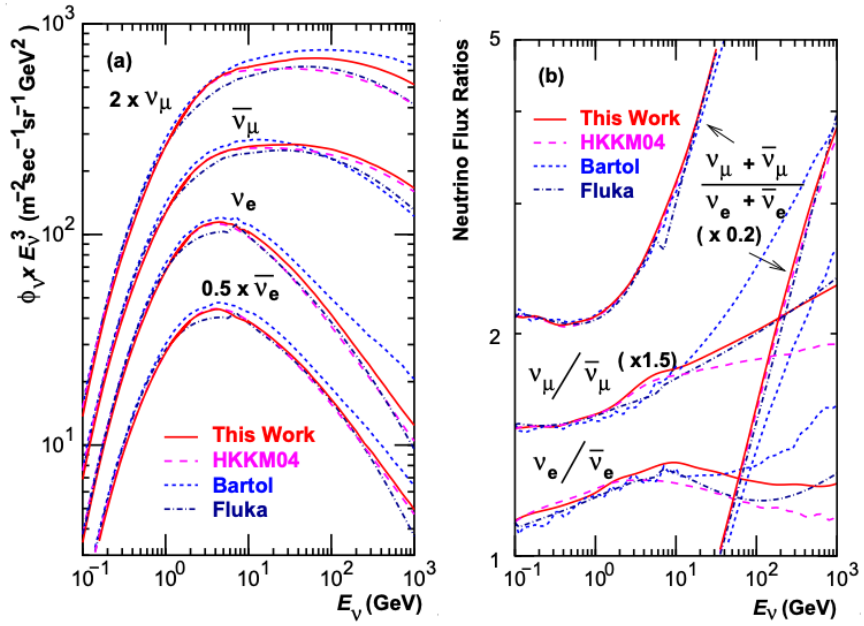

Figure 2.3: Left panel: The atmospheric neutrino flux for different neutrino flavours as a function of neutrino energy as predicted by the 2007 Honda model ("This work") [51], the 2004 Honda model ("HKKM04")[52], the Bartol model [50] and the FLUKA model [54]. Right panel: The ratio of the muon to electron neutrino flux as predicted by all the quoted models. Both figures taken from [51].

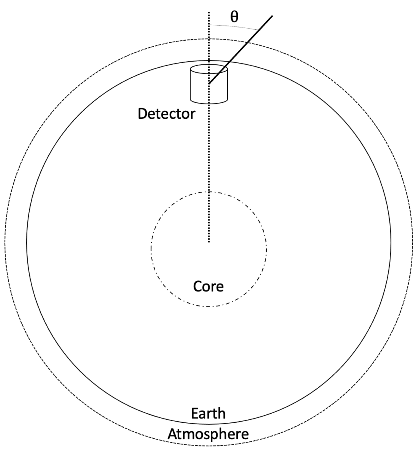

Figure 2.4: A diagram illustrating the definition of zenith angle as used in the Super Kamiokande experiment [55].

a lesser degree for low-energy neutrinos), the flux is approximately symmetric around $\cos(\theta) = 0$. To the accuracy of this approximation, the systematic uncertainties associated with atmospheric flux for comparing upward-going and down-going neutrino cancels. This allows the down-going events, which are mostly insensitive to oscillation probabilities, to act as an unoscillated prediction (similar to a near detector in an accelerator neutrino experiment).

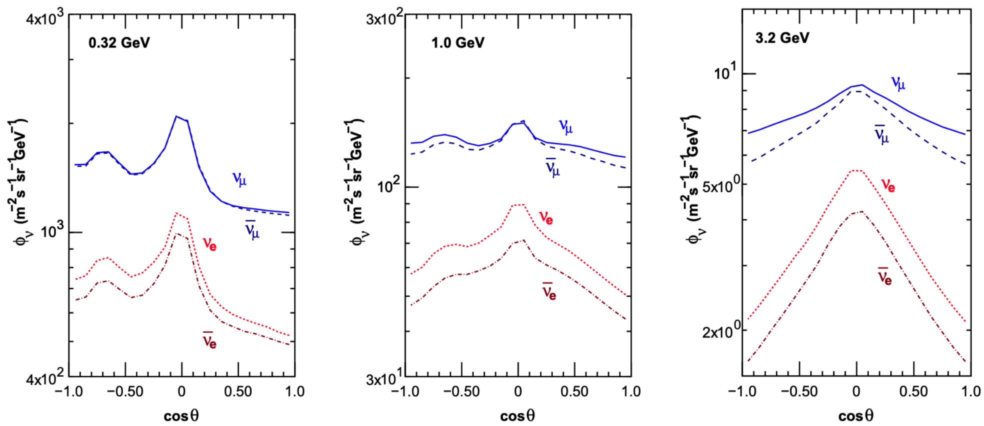

Figure 2.5: Prediction of $\nu_e, \bar{\nu}_e, \nu_\mu, \bar{\nu}_\mu$ fluxes as a function of zenith angle as calculated by the HKKM model [53]. The left, middle and right panels represent three values of neutrino energy, 0.32GeV, 1.0GeV and 3.2GeV respectively. Predictions for other models including Bartol [50], Honda [51] and FLUKA [54] are given in [55].

Precursory hints of atmospheric neutrinos were observed in the mid-1960s searching for $\overset{(-)}{\nu_\mu} + X \rightarrow X^* + \mu^\pm$ [56]. This was succeeded by the IMB-3 [57] and Kamiokande [58] experiments which measured the double ratio of muon to electron neutrinos in data to Monte Carlo, $R(\nu_\mu/\nu_e) = (\mu/e)_{Data}/(\mu/e)_{MC}$. Both experiments were found to have a consistent deficit of muon neutrinos, with $R(\nu_\mu/\nu_e) = 0.67 \pm 0.17$ and $R(\nu_\mu/\nu_e) = 0.658 \pm 0.016 \pm 0.035$, respectively. Super-Kamiokande (SK) [55] extended this analysis by fitting oscillation parameters in $P(\nu_\mu \rightarrow \nu_\tau)$ which found best fit parameters $\sin^2(2\theta) > 0.92$ and $1.5 \times 10^{-3} < \Delta m^2 < 3.4 \times 10^{-3}\text{eV}^2$.

Since then, atmospheric neutrino experiments have been making precision measurements of the $\sin^2(\theta_{23})$ and Δm^2_{32} oscillation parameters. Atmospheric neutrino oscillation is dominated by $P(\nu_\mu \rightarrow \nu_\tau)$, where SK observed a 4.6σ discovery of ν_τ appearance [59]. Figure 2.6 illustrates the current estimates on the atmospheric mixing parameters, from a wide range of atmospheric and accelerator neutrino observatories.

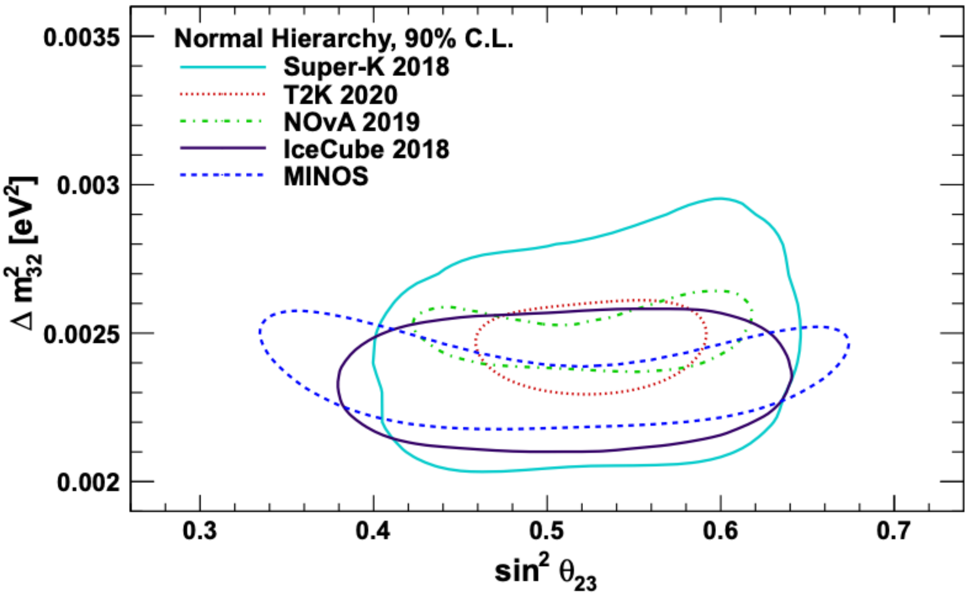

Figure 2.6: Constraints on the atmospheric oscillation parameters, $\sin^2(\theta_{23})$ and Δm^2_{32}, from atmospheric and long-baseline experiments: SK [60], T2K [61], NOνA [62], IceCube [63] and MINOS [64]. Figure taken from [65].

2.3.4 Reactor Neutrinos

As illustrated in the first discovery of neutrinos (section 2.1), nuclear reactors are a very useful artificial source of electron antineutrinos. For reactors that use low-enriched uranium ^{235}U as fuel, the antineutrino flux is dominated by the β-decay fission of ^{235}U, ^{238}U, ^{239}Pu and ^{241}Pu [66] as illustrated in Figure 2.7.

Due to their low energy, reactor electron antineutrinos predominantly interact via the inverse β-decay (IBD) interaction. The typical signature contains two signals delayed by $O(200)\mu$s; firstly the prompt photons from positron annihilation, and secondly the photon emitted ($E^{\gamma}_{tot} = 2.2$MeV) from de-excitation after neutron capture on hydrogen. Searching for both signals improves the detector's ability to distinguish between background and signal events [68].

There are many short baseline experiments (L $\sim O(1)$km) that have measured the $\sin^2(\theta_{13})$ and Δm^2_{32} oscillation parameters. Daya Bay [69], RENO [70] and Double Chooz [71] have all provided precise measurements, with the first discovery of a non-zero θ_{13} made by Daya Bay and RENO (and complemented by T2K [71]). The constraints on $\sin^2(\theta_{13})$ by the reactor experiments lead the field. They

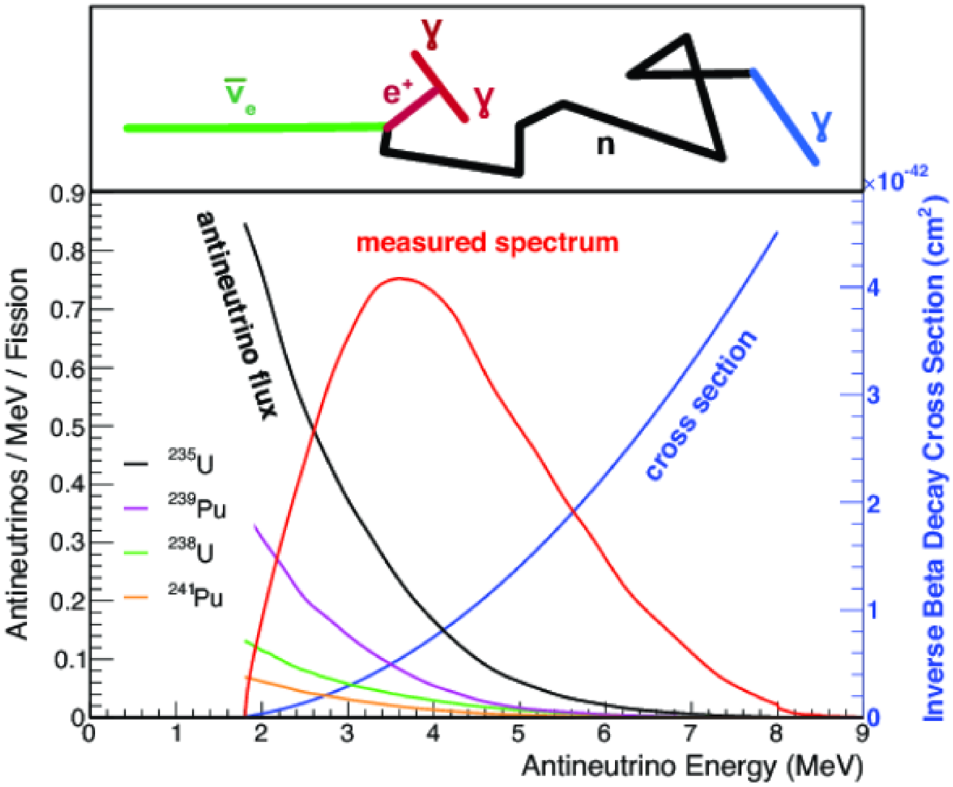

Figure 2.7: Reactor electron antineutrino fluxes for ^{235}U (Black), ^{238}U (Green), ^{239}Pu (Purple), and ^{241}Pu (Orange) isotopes. The inverse β-decay cross-section (Blue) and corresponding measurable neutrino spectrum (Red) are also given. Top panel: Schematic of Inverse β-decay interaction including the eventual capture of the emitted neutron. This capture emits a γ-ray which provides a second signal of the event. Taken from [67].

are often used as external inputs to accelerator neutrino experiments to improve their sensitivity to δ_{CP} and mass hierarchy determination. JUNO-TAO [72], a small collaboration within the larger JUNO experiment, is a next-generation reactor experiment that aims to precisely measure the isotopic antineutrino yields from the different fission chains.

Kamland [73] is the only experiment to have observed reactor neutrinos using a long baseline (flux weighted averaged baseline of $L \sim 180$km) which allows it to have sensitivity to Δm^2_{21}. Combined with the SK solar neutrino experiment, the combined analysis puts the most stringent constraint on Δm^2_{21} [74].

2.4 Summary Of Oscillation Parameter Measurements

Since the first evidence of neutrino oscillations, numerous measurements of the mixing parameters have been made. Many experiments use neutrinos as a tool for the discovery of new physics (diffuse supernova background, neutrinoless double beta decay and others) so the PMNS parameters are summarised in the Particle Data Group (PDG) review tables. The analysis presented in this thesis focuses on the 2020 T2K oscillation analysis presented in [75] which the 2020 PDG constraints [76] were used. These constraints are outlined in Table 2.1.

Parameter	2020 Constraint
$\sin^2(\theta_{12})$	0.307 ± 0.013
Δm^2_{21}	$(7.53 \pm 0.18) \times 10^{-5}\text{eV}^2$
$\sin^2(\theta_{13})$	$(2.18 \pm 0.07) \times 10^{-2}$
$\sin^2(\theta_{23})$ (I.H.)	0.547 ± 0.021
$\sin^2(\theta_{23})$ (N.H.)	0.545 ± 0.021
Δm^2_{32} (I.H.)	$(-2.546^{+0.034}_{-0.040}) \times 10^{-3}\text{eV}^2$
Δm^2_{32} (N.H.)	$(2.453 \pm 0.034) \times 10^{-3}\text{eV}^2$

Table 2.1: The 2020 Particle Data Group constraints of the oscillation parameters taken from [76]. The value of Δm^2_{32} is given for both normal hierarchy (N.H.) and inverted hierarchy (I.H.) and $\sin^2(\theta_{23})$ is broken down by whether its value is below (Q1) or above (Q2) 0.5.

The $\sin^2(\theta_{13})$ measurement stems from the electron antineutrino disappearance, $P(\bar{\nu}_e \to \bar{\nu}_e)$, and is taken as the average best-fit from the combination of Daya Bay, Reno and Double Chooz. It is often used as a prior uncertainty within other neutrino oscillation experiments, typically termed the reactor constraint. The $\sin^2(\theta_{12})$ parameter is predominantly measured through electron neutrino disappearance, $P(\nu_e \to \nu_{\mu,\tau})$, in solar neutrino experiments. The long-baseline reactor neutrino experiment Kamland also has a sensitivity to this parameter and is used in a joint fit to solar data from SNO and SK, using the reactor constraint. Measurements of $\sin^2(\theta_{23})$ are made by long-baseline and atmospheric neutrino experiments. The PDG value is a joint fit of T2K, NOνA, MINOS and IceCube DeepCore experiments. The latest T2K-only measurement, provided at Neutrino2020 and is the basis of this thesis, is given as $\sin^2(\theta_{23}) = 0.546^{+0.024}_{-0.046}$ [75].

The PDG constraint on Δm^2_{21} is provided by the KamLAND experiment using solar and geoneutrino data. This measurement utilised a $\sin^2(\theta_{13})$ constraint from accelerator (T2K, MINOS) and reactor neutrino (Daya Bay, RENO, Double Chooz) experiments. Accelerator measurements make some of the most stringent constraints on Δm^2_{32} although atmospheric experiments have more sensitivity to the mass hierarchy determination. The PDG performs a joint fit of accelerator and atmospheric data, in both normal and inverted hierarchies separately. The latest T2K-only result is $\Delta m^2_{32} = 2.49^{+0.058}_{-0.082} \times 10^{-3}\text{eV}^2$ favouring normal hierarchy [75]. The value of δ_{CP} is largely undetermined. CP-conserving values of 0 and π were rejected with $\sim 2\sigma$ intervals, as published in Nature, although more recent analyses have reduced the credible intervals to 90%. Since the 2020 PDG publication, there has been a new measurement of $\sin^2(\theta_{13}) = (2.20 \pm 0.07) \times 10^{-2}$ [77], alongside updated Δm^2_{32} and $\sin^2(\theta_{23})$ measurements.

Throughout this thesis, several sample spectra predictions and contours are presented, which require oscillation parameters to be assumed. Table 2.2 defines two sets of oscillation parameters, with "Asimov A" set being close to the preferred values from a previous T2K-only fit [78] and "Asimov B" being CP-conserving and further from maximal θ_{23} mixing.

Parameter	Asimov A	Asimov B
Δm^2_{12}	$7.53 \times 10^{-5}\text{eV}^2$	
Δm^2_{32}	$2.509 \times 10^{-3}\text{eV}^2$	
$\sin^2(\theta_{12})$	0.304	
$\sin^2(\theta_{13})$	0.0219	
$\sin^2(\theta_{23})$	0.528	0.45
δ_{CP}	-1.601	0.0

Table 2.2: Reference values of the neutrino oscillation parameters for two different oscillation parameter sets.

2.5 Overview of Oscillation Effects

The analysis presented within this thesis focuses on the determination of oscillation parameters from atmospheric and beam neutrinos. Whilst subject to the same oscillation formalism, the way in which the two samples have sensitivity to the different oscillation parameters differs significantly.

Atmospheric neutrinos have a varying baseline, or "path length" L, such that the distance each neutrino travels before interacting is dependent upon the zenith angle, θ_Z. As primary cosmic rays can interact anywhere between the Earth's surface and $\sim$ 50km above that, the height, h, in the atmosphere at which the neutrino was generated also affects the path length,

$$L = \sqrt{(R_E + h)^2 - R_E^2\left(1 - \cos^2(\theta_Z)\right)} - R_E \cos(\theta_Z). \tag{2.16}$$

DB: Ask Giles what he means about the horizontal issue and Layering in the ProdH section

Where $R_E = 6,371$km is the Earth's radius. Consequently, the oscillation probability is dependent upon two parameters, $\cos(\theta_Z)$ and E_ν.

The oscillation probability used within this analysis is based on [21]. The neutrino wavefunction in the vacuum Hamiltonian evolves in each layer of constant matter density via

$$i\frac{d\psi_j(t)}{dt} = \frac{m_j^2}{2E_\nu}\psi_j(t) - \sum_k \sqrt{2}G_F N_e U_{ej} U_{ke}^\dagger \psi_k(t), \tag{2.17}$$

where m_j^2 is the square of the j^{th} vacuum eigenstate mass, E_ν is the neutrino energy, G_F is Fermi's constant, N_e is the electron number density and U is the PMNS matrix. The transformation $N_e \rightarrow -N_e$ and $\delta_{CP} \rightarrow -\delta_{CP}$ is applied for antineutrino propagation. Thus, a model of the Earth's density is required for neutrino propagation. Following the official SK-only methodology [79], this analysis uses the Preliminary Reference Earth Model (PREM) [80] which provides piecewise cubic polynomials as a function of the Earth's radius. This density profile is illustrated in Figure 2.8. As the propagator requires layers of constant density, the SK methodology approximates the PREM model by using four layers of constant density [79], detailed in Table 2.3.

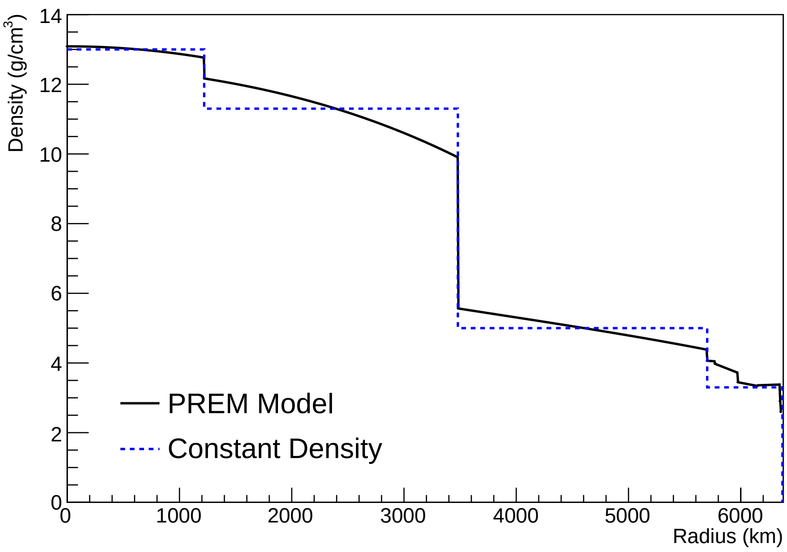

Figure 2.8: The density of the Earth given as a function of the radius, as given by the PREM model (Black), and the constant density four-layer approximation (Blue), as used in the official SK-only analysis.

Layer	Outer Radius [km]	Density [g/cm^3]	Chemical composition (Z/A)
Inner Core	1220	13	0.468 ± 0.029
Outer Core	3480	11.3	0.468 ± 0.029
Lower Mantle	5701	5.0	0.496
Transition Zone	6371	3.3	0.496

Table 2.3: Description of the four layers of the Earth invoked within the constant density approximation of the PREM model [80].

The atmospheric neutrino oscillation probabilities can be presented as two dimensional "oscillograms" as illustrated in Figure 2.9. The distinct discontinuities, as a function of $\cos(\theta_Z)$, are due to the discontinuous density in the PREM model.

Atmospheric neutrinos have sensitivity to δ_{CP} through the overall event rate. Figure 2.10 illustrates the difference in oscillation probability between CP-conserving ($\delta_{CP} = 0.$) and a CP-violating ($\delta_{CP} = -1.601$) value taken from Asimov A oscillation parameter set (Table 2.2). The result is a complicated oscillation pattern in the appearance probability for sub-GeV upgoing neutrinos. The detector does not have sufficient resolution to resolve these individual patterns so the sensitivity to δ_{CP} for atmospheric neutrinos comes via the overall normalisation of these events.

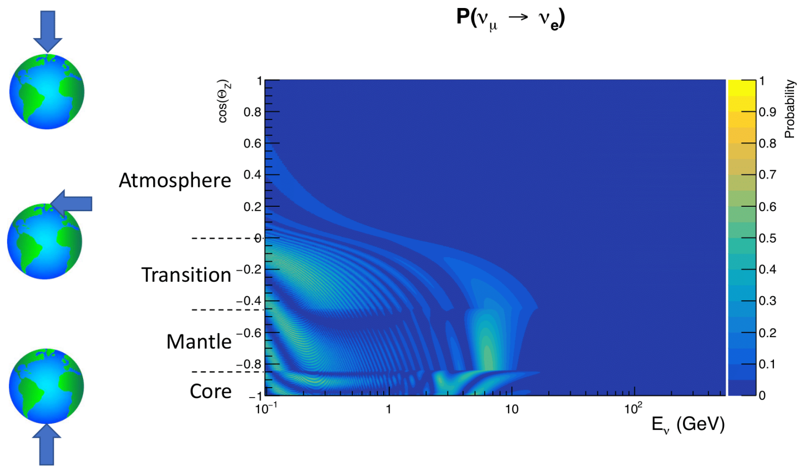

Figure 2.9: An "oscillogram" that depicts the $P(\nu_\mu \to \nu_e)$ oscillation probability as a function of neutrino energy and cosine of the zenith angle. The zenith angle is defined such that $\cos(\theta_Z) = 1.0$ represents neutrinos that travel from directly above the detector. The four-layer constant density PREM model approximation is used and Asimov A oscillation parameters are assumed (Table 2.2).

The presence of matter means that the effect δ_{CP} has on the oscillation probability is not equal between neutrinos and antineutrinos. Furthermore, the interaction cross-section for neutrinos is larger than for antineutrinos so the two effects have to be disentangled. These effects are further convoluted by detector efficiencies as SK cannot distinguish neutrinos and antineutrinos well. All of these effects lead to a difference in the number of neutrinos detected compared to antineutrinos. This changes how the δ_{CP} normalisation term is observed, resulting in a very complex sensitivity to δ_{CP}.

The vacuum and matter oscillation probabilities for $P(\nu_e \to \nu_e)$ and $P(\bar{\nu}_e \to \bar{\nu}_e)$ are presented in Figure 2.11, where the PREM model has been assumed. The oscillation probability for both neutrinos and antineutrinos is affected in the presence of matter. However, the resonance effects around $O(5)$GeV only occur for neutrinos in the normal mass hierarchy and antineutrinos in the inverse mass hierarchy. The exact position and amplitude of the resonance depend on $\sin^2(\theta_{23})$, further increasing the atmospheric neutrinos' sensitivity to the parameter.

As the T2K beam flux is centered at the first oscillation maximum ($E_\nu =$

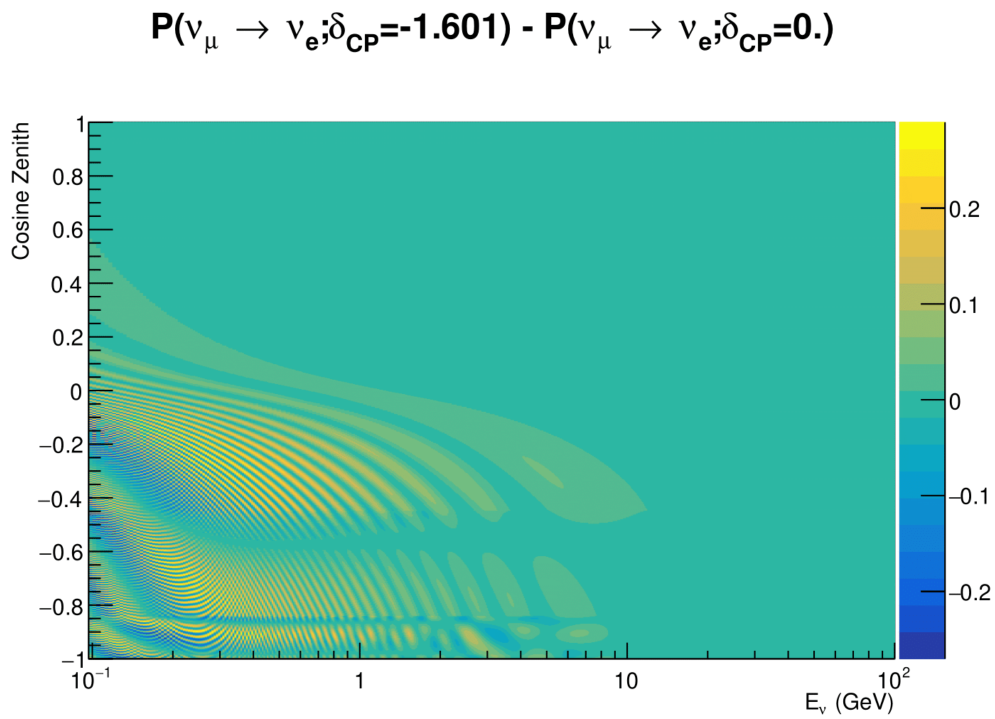

Figure 2.10: The effect of δ_{CP} for atmospheric neutrinos given in terms of the neutrino energy and zenith angle. This oscillogram compares the $P(\nu_\mu \rightarrow \nu_e)$ oscillation probability for a CP conserving ($\delta_{CP} = 0.0$) and a CP violating ($\delta_{CP} = -1.601$) value taken from the Asimov A parameter set. The other oscillation parameters assume the Asimov A oscillation parameter set given in Table 2.2.

0.6GeV) [43], the sensitivity to δ_{CP} is predominantly observed as a change in the event-rate of e-like samples in $\nu/\bar{\nu}$ modes. Figure 2.12 illustrates the $P(\nu_\mu \rightarrow \nu_e)$ oscillation probability for a range of δ_{CP} values. A circular modulation of the first oscillation peak (in both magnitude and position) is observed when varying throughout the allowable values of δ_{CP}. The CP-conserving values of $\delta_{CP} = 0, \pi$ have a lower(higher) oscillation maximum than the CP-violating values of $\delta_{CP} = -\pi/2(\delta_{CP} = \pi/2)$. A sub-dominant shift in the energy of the oscillation peak is also present, which aids in separating the two CP-conserving values of δ_{CP}.

T2K's sensitivity to $\sin^2(\theta_{23})$ and Δm^2_{32} is observed as a shape-based variation of the muon-like samples, as illustrated in Figure 2.12. The value of Δm^2_{32} laterally shifts the position of the oscillation dip (around $E_\nu \sim 0.6$GeV) in the $P(\nu_\mu \rightarrow \nu_\mu)$ oscillation probability. A variation of $\sin^2(\theta_{23})$ is predominantly observed as a vertical shift of the oscillation dip with second-order horizontal shifts being

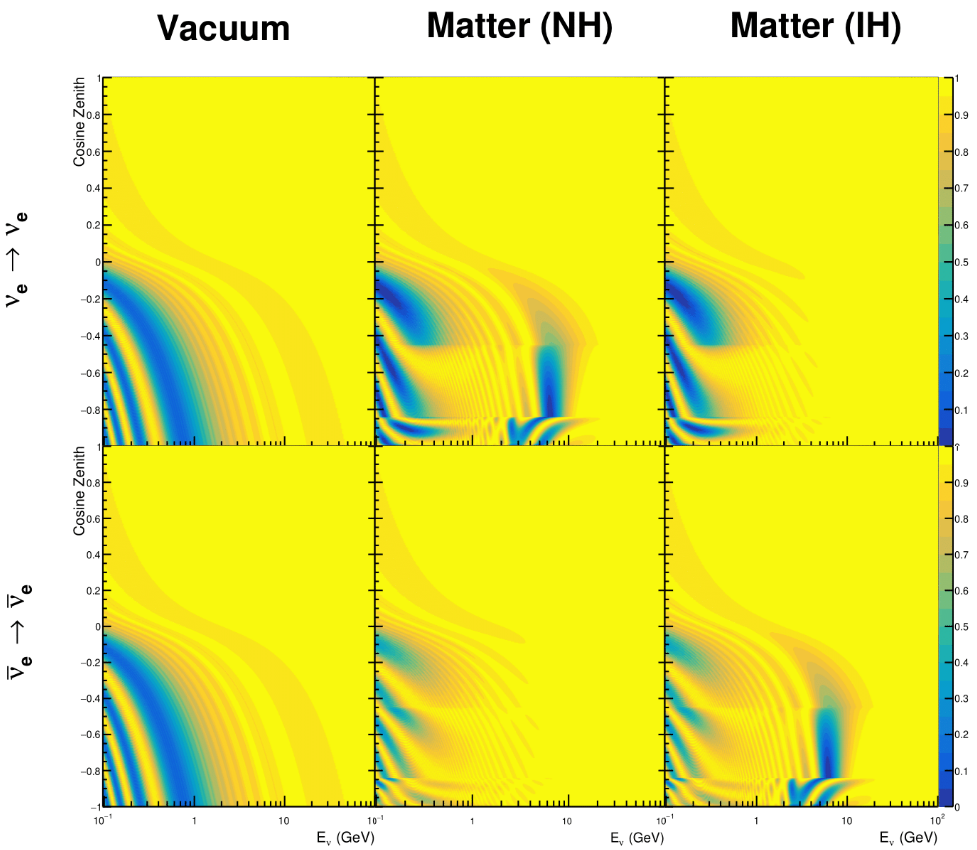

Figure 2.11: An illustration of the matter-induced effects on the oscillation probability, given as a function of neutrino energy and zenith angle. The top row of panels gives the $P(\nu_e \rightarrow \nu_e)$ oscillation probability and the bottom row illustrates the $P(\bar{\nu}_e \rightarrow \bar{\nu}_e)$ oscillation probability. The left column highlights the oscillation probability in a vacuum, whereas the middle and right column represents the oscillation probabilities when the four-layer fixed density PREM model is assumed. All oscillation probabilities assume the "Asimov A" set given in Table 2.2, but importantly, the right column sets an inverted mass hierarchy. The "matter resonance" effects at $E_\nu \sim$ 5GeV can be seen in the $P(\nu_e \rightarrow \nu_e)$ for normal mass hierarchy and $P(\bar{\nu}_e \rightarrow \bar{\nu}_e)$ for inverted hierarchy.

due to matter effects. The beam neutrinos have limited sensitivity to matter effects due to the relatively shorter baseline as well as the Earth's mantle being a relatively low-density material (as compared to the Earth's core). For some values of δ_{CP}, the degeneracy in the number of e-like events allows the mass hierarchy to be broken. This leads to a δ_{CP}-dependent mass hierarchy sensitivity which can be seen in Figure 2.13.

Whilst all oscillation channels should be included for completeness, the

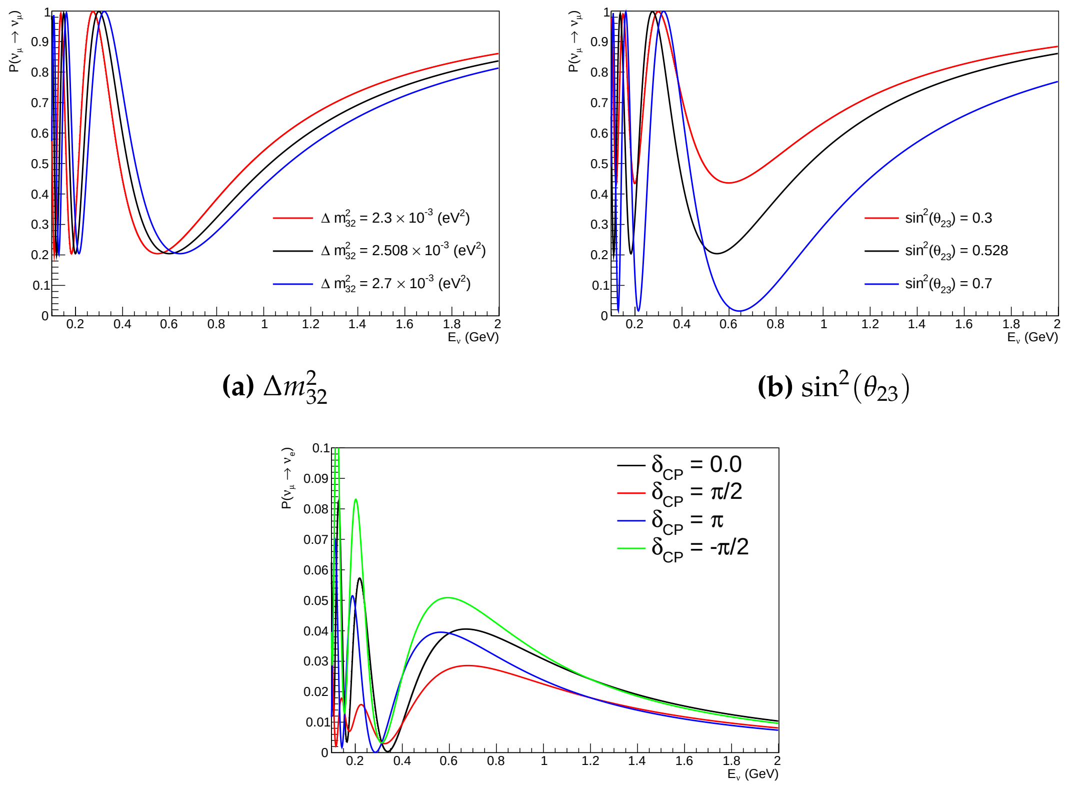

(a) Δm^2_{32}

(b) $\sin^2(\theta_{23})$

(c) δ_{CP}

Figure 2.12: The oscillation probability for beam neutrino events given as a function of neutrino energy. All oscillation parameters assume the "Asimov A" set given in Table 2.2 unless otherwise stated. Each panel represents a change in one of the oscillation parameters whilst keeping the remaining parameters fixed.

computational resources required to run a fit are limited and any reasonable approximations which reduce the number of oscillation probability calculations that need to be made should be applied. The $\nu_e \rightarrow \nu_{e,\mu,\tau}$ (and antineutrino equivalent) oscillations can be ignored for beam neutrinos as the $\nu_e/\bar{\nu}_e$ fluxes are approximately two orders of magnitude smaller than the corresponding $\nu_\mu/\bar{\nu}_\mu$ flux. Furthermore, as the peak neutrino energy of the beam is well below the threshold for charged current tau production ($E_\nu = 3.5$GeV [59]), only a small proportion of the neutrinos produced in the beam have the required energy. For the few neutrinos that have sufficient energy, the oscillation probability is very small due to their energy being well above the oscillation maximum (small value of L/E). Whilst these approximations have be made for the beam

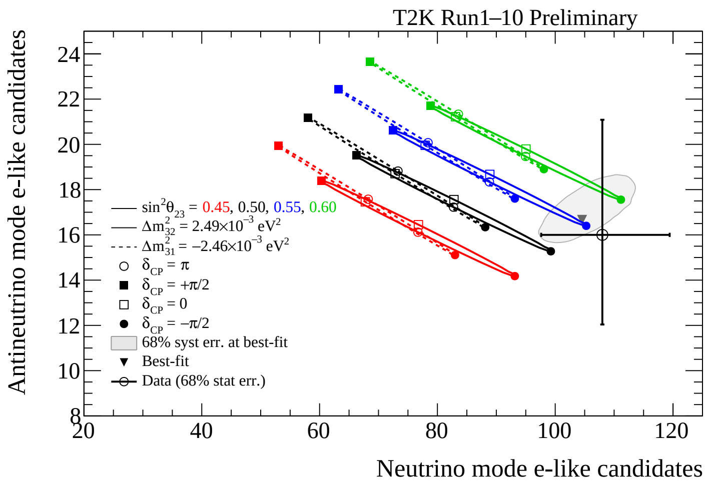

Figure 2.13: The number of electron-like events in the FHC and RHC operating mode of the beam, as a function of the oscillation probabilities. Both normal hierarchy (Solid)) and inverse hierarchy (Dashed) values of Δm^2_{32} are given.

neutrinos, the atmospheric flux of ν_e is of the same order of magnitude as the ν_μ flux and the energy distribution of atmospheric neutrinos extends well above the tau production threshold. These events can have non-negligible oscillation probabilities due to the further distance they travel.

3

T2K and SK Experiment Overview

As the successor of the Kamiokande experiment, the Super-Kamiokande (SK) collaboration has been leading atmospheric neutrino oscillation analyses for over two decades. The detector has provided some of the strongest constraints on proton decay and the first precise measurements of the Δm^2_{32} and $\sin^2(\theta_{23})$ neutrino oscillation parameters. The history, detection technique, and operation of the SK detector is described in section 3.1.

The Tokai-to-Kamioka (T2K) experiment was one of the first long-baseline experiments to use both neutrino and antineutrino beams to precisely measure charge parity violation within the neutrino sector. The T2K experiment observed the first hints of a non-zero $\sin^2(\theta_{13})$ measurement and continues to lead the field with the constraints it provides on $\sin^2(\theta_{13})$, $\sin^2(\theta_{23})$, Δm^2_{32} and δ_{CP}. In section 3.2, the techniques that T2K use to generate the neutrino beam and constrain systematic parameter through near detector constraints are described.

3.1 The Super-Kamiokande Experiment

The SK experiment began taking data in 1996 [81] and has had many modifications throughout its operation. There have been seven defined periods of data taking as noted in Table 3.1. Data taking began in SK-I which ran for five years. Between the SK-I and SK-II periods, approximately 55% of the PMTs were damaged during maintenance [82]. Those that survived were equally distributed throughout the detector in the SK-II era, which resulted in a reduced 19% photo-coverage. From SK-III onwards, repairs to the detector meant the full suite of PMTs was operational recovering the 40% photo-coverage. Before the start of SK-IV, the data acquisition and electronic systems were upgraded. Between SK-IV and SK-V, a significant effort was placed into tank open maintenance and repair/replacement of defective PMTs in preparation for the Gadolinium upgrade; a task for which the author of this thesis was required. Consequently, the detector conditions were significantly changed from this point. SK-VI marked the start of the SK-Gd era, with the detector being doped with gadolinium at a concentration of 0.01% by concentration. SK-VII, which started during the writing of this thesis, has increased the gadolinium concentration to 0.03% for continued operation [83].

The oscillation analysis presented within this thesis focuses on the SK-IV period of running and the data taken within it. This follows from the recent SK analysis presented in [84]. Therefore, the information presented within this section focuses on that period.

Period	Start Date	End Date	Live-time (days)
I	April 1996	July 2001	1489.19
II	October 2002	October 2005	798.59
III	July 2006	September 2008	518.08
IV	September 2008	May 2018	3244.4
V	January 2019	July 2020	461.02
VI	July 2020	May 2022	583.3
VII	May 2022	Ongoing	N/A

Table 3.1: The various SK periods and their respective live-time. The SK-VI live-time is calculated until 1st April 2022. SK-VII started during the writing of this thesis.

3.1.1 The SK Detector

The basic structure of the Super-Kamiokande (SK) detector is a cylindrical tank with a diameter 39.3m and height 41.1m filled with ultrapure water [82]. A diagram of the significant components of the SK detector is given in Figure 3.1.

The SK detector is situated in the Kamioka mine in Gifu, Japan. The mine is underground with roughly 1km rock overburden (2.7km water equivalent overburden) [85]. At this depth, the rate of cosmic ray muons is significantly decreased to a value of $\sim$ 2Hz (net rate) [86]. The top of the tank is covered with stainless steel which is designed as a working platform for maintenance, calibration, and location for high voltage and data acquisition electronics.

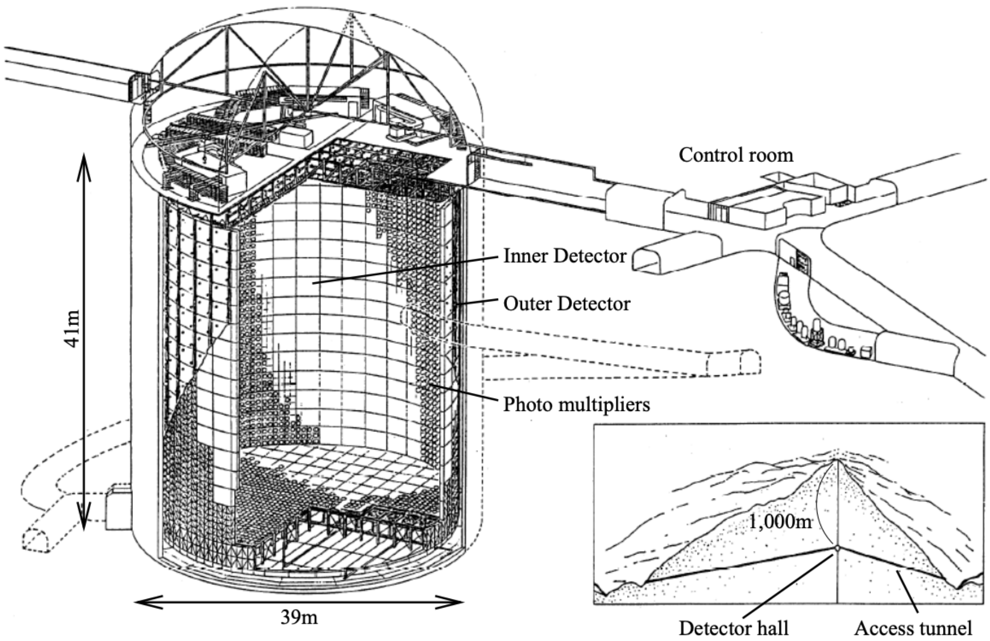

Figure 3.1: A schematic diagram of the Super-Kamiokande Detector. Taken from [87].

A smaller cylindrical structure (36.2m diameter, 33.8m height) is situated inside the tank, with an approximate 2m gap between this structure and the outer tank wall. The purpose of this structure is to support the photomultiplier tubes (PMTs). The volume inside and outside the support structure is referred to as the inner detector (ID) and outer detector (OD), respectively. In the SK-IV era, the ID and OD are instrumented by $11,129$ 50cm and $1,885$ 20cm PMTs respectively [82]. The ID contains a 32kton mass of water. Many analyses performed at SK use a "fiducial volume" defined by the volume of water inside the ID excluding some distance to the ID wall. This reduces the volume of the detector which is sensitive to neutrino events but reduces radioactive backgrounds and allows for better reconstruction performance. The nominal fiducial volume is defined as the area contained inside 2m from the ID wall for a total of 22.5kton water [88].

The two regions of the detector (ID and OD) are optically separated with opaque black plastic hung from the support structure. The purpose of this is to determine whether an event entered or exited the ID. This allows cosmic ray muons and partially contained events to be tagged and separated from neutrino events entirely contained within the ID. This black plastic is also used to cover the area between the ID PMTs to reduce photon reflection from the ID walls. Opposite to this, the OD is lined with a reflective material to allow photons to reflect around inside the OD until collected by one of the PMTs. Furthermore, each OD PMT is optically coupled with 50×50cm plates of wavelength shifting acrylic which increases the efficiency of light collection [85].

In the SK-IV data-taking period, the photocathode coverage of the detector, or the fraction of the ID wall instrumented with PMTs, is $\sim 40\%$ [85]. The PMTs have a quantum efficiency (the ratio of detected electrons to incident photons) of $\sim 21\%$ for photons with wavelengths of $360\text{nm} < \lambda < 390\text{nm}$ [89, 90]. The proportion of photoelectrons that produce a signal in the dynode of a PMT, termed the collection efficiency, is $> 70\%$ [85]. The PMTs used within SK are most sensitive to photons with wavelength $300\text{nm} \leq \lambda \leq 600\text{nm}$ [85]. One disadvantage of using PMTs as the detection media is that the Earth's geomagnetic field can modify its response. Therefore, a set of compensation coils is built around the inner surface of the detector to mitigate this effect [86].

The SK detector is filled with ultrapure water, which in a perfect world, contains no impurities. However, bacteria and organic compounds can significantly degrade the water quality. This decreases the attenuation length, which reduces the total number of photons that hit a PMT. To combat this, a sophisticated water treatment system has been developed [85, 91]. UV lights, mechanical filters, and membrane degasifiers are used to reduce the bacteria, suspended particulates, and radioactive materials from the water. The flow of water within the tank is also critical as it can remove stagnant bacterial growth or build-up of dust on the surfaces within the tank. Gravity drifts impurities in the water towards the bottom of the tank which, if left uncontrolled, can create asymmetric water conditions between the top and bottom of the tank. Typically, the water entering the tank is cooled below the ambient temperature of the tank to control convection and inhibit bacteria growth. Furthermore, the rate of dark noise hits within PMTs is sensitive to the PMT temperature [92]. Therefore controlling the temperature gradients within the tank is beneficial for stable measurements.

SK-VI is the first phase of the SK experiment to use gadolinium dopants within the ultrapure water [83]. As such, the SK water system had to be replaced to avoid removing the gadolinium concentrate from the ultrapure water [93]. For an inverse β-decay (IBD) interaction on a water target, the emitted neutron is thermally captured on hydrogen. This process releases a 2.2MeV γ ray which is difficult to detect as the resulting Compton scattered electrons are very close to the Cherenkov threshold, limiting detection capability. Thermal capture of neutrons on gadolinium generates γ rays with higher energy (8MeV [68]) meaning they are more easily detected and reconstructed. SK-VI has 0.01% Gd loading (0.02% gadolinium sulphate by mass) which causes $\approx$ 50% of neutrons emitted by IBD to be captured on gadolinium[94, 95] . Whilst predominantly useful for low energy analyses, Gd loading allows better $\nu/\bar{\nu}$ separation for atmospheric neutrino event selections [96]. Efforts are currently in place to increase the gadolinium concentrate to 0.03% for $\approx$ 75% neutron capture efficiency on gadolinium [97]. The final stage of loading targets 0.1% concentrate for $\approx$ 90% neutron capture efficiency on gadolinium.

3.1.2 Calibration

The calibration of the SK detector is documented in [82] and summarised below. The analysis presented within this thesis is dependent upon 'high energy events' (Charged particles with $O(>100)$MeV momenta). These are events that are expected to generate a larger number of photons such that each PMT will be hit with multiple photons. The reconstruction of these events depends upon the charge deposited within each PMT and the timing response of each individual PMT. Therefore, the most relevant calibration techniques to this thesis are outlined.

Before installation, 420 PMTs were calibrated to have identical charge responses and then distributed throughout the tank in a cross-shape pattern (As illustrated by Figure 3.2). These are used as a standardised measure for the rest of the PMTs installed at similar geometric positions within SK to be calibrated against. To perform this calibration, a xenon lamp is located at the center of the SK tank which flashes uniform light at 1Hz. This allows for geometrical effects, water quality variation, and timing effects to be measured in situ throughout normal data-taking periods.

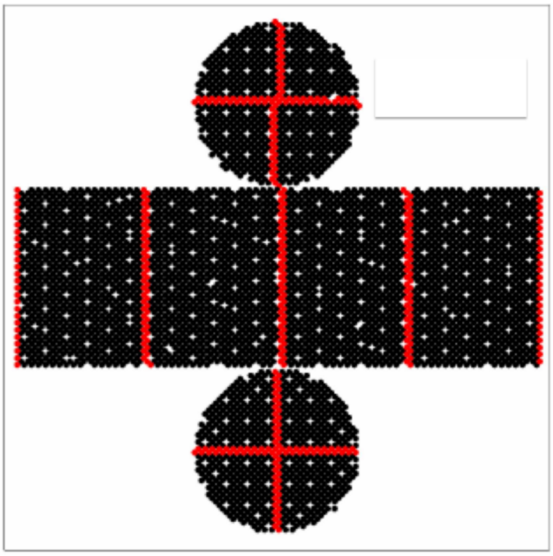

Figure 3.2: The location of "standard PMTs" (red) inside the SK detector. Taken from [82].

When specifically performing calibration of the detector (in out-of-data taking mode), the water in the tank was circulated to avoid top/bottom asymmetric water quality. Any non-uniformity within the tank significantly affects the PMT hit probability through scattering or absorption. This becomes a dominant effect for very low-intensity light sources that are designed such that only one photon is incident upon a given PMT.

The gain of a PMT is defined as the ratio of the total charge of the signal produced compared to the charge of photoelectrons emitted by the photocathodes within the PMT. To calibrate the signal of each PMT, the "relative" and "absolute" gain values are measured. The relative gain is the variation of gain among each of the PMTs whereas the absolute gain is the average gain of all PMTs.

The relative gain is calibrated as follows. A laser is used to generate two measurements: a high-intensity flash that illuminates every PMT with a sufficient number of photons, and a low-intensity flash in which only a small number of PMTs collect light. The first measurement creates an average charge, $Q_{obs}(i)$ on PMT i, whereas the second measurement ensures that each hit PMT only generates a single photoelectron. For the low-intensity measurement, the number of times each PMT records a charge larger than 1/4 photoelectrons, $N_{obs}(i)$, is counted. The values measured can be expressed as

$$\begin{aligned} Q_{obs}(i) &\propto I_H \times f(i) \times \epsilon(i) \times G(i), \\ N_{obs}(i) &\propto I_L \times f(i) \times \epsilon(i). \end{aligned} \tag{3.1}$$

Where I_H and I_L is the intensity of the high and low flashes, $f(i)$ is the acceptance efficiency of the i^{th} PMT, $\epsilon(i)$ is the product of the quantum and collection efficiency of the i^{th} PMT and $G(i)$ is the gain of the i^{th} PMT. The relative gain for each PMT can be determined by taking the ratio of these quantities.

The absolute gain calibration is performed by observing fixed energy γ-rays of $E_\gamma \sim$ 9MeV emitted isotropically from neutron capture on a NiCf source situated at the center of the detector. This generates a photon yield of about 0.004 photoelectrons/PMT/event, meaning that $>$ 99% of PMT signals are generated from single photoelectrons. A charge distribution is generated by performing this calibration over all PMTs, and the average value of this distribution is taken to be the absolute gain value.

As mentioned in subsection 3.1.1, the average quantum and collection efficiency for the SK detector PMTs is $\sim$ 21% and $>$ 70% respectively. However, these values do differ between each PMT and need to be calibrated accordingly.

Consequently, the NiCf source is also used to calibrate the "quantum $\times$ collection" efficiency (denoted "QE") value of each PMT. The NiCf low-intensity source is used as the PMT hit probability is proportional to the QE ($N_{obs}(i) \propto \epsilon(i)$ in Equation 3.1). A Monte Carlo prediction which includes photon absorption, scattering, and reflection is made to estimate the number of photons incident on each PMT and the ratio of the number of predicted to observed hits is calculated. The difference is attributed to the QE efficiency of that PMT. This technique is extended to calculate the relative QE efficiency by normalizing the average of all PMTs which removes the dependence on the light intensity.

Due to differing cable lengths and readout electronics, the timing response between a photon hitting the PMT and the signal being captured by the data acquisition can be different between each PMT. Due to threshold triggers (Described in subsection 3.1.3), the time at which a pulse reaches a threshold is dependent upon the size of the pulse. This is known as the 'time-walk' effect and also needs to be accounted for in each PMT. To calibrate the timing response, a pulse of light with width 0.2ns is emitted into the detector through a diffuser. Two-dimensional distributions of time and pulse height (or charge) are made for each PMT and are used to calibrate the timing response. This is performed in-situ during data taking with the light source pulsing at 0.03Hz.

The top/bottom water quality asymmetry is measured using the NiCf calibration data and cross-referencing these results to the "standard PMTs". The water attenuation length is continuously measured by the rate of vertically-downgoing cosmic-ray muons which enter via the top of the tank.

Dark noise is where a PMT registers a pulse that is consistent with a single photoelectron emitted from photon detection despite the PMT being in complete darkness. This is predominately caused by two processes. Firstly there is intrinsic dark noise which is where photoelectrons gain enough thermal energy to be emitted from the photocathode, and secondly, the radioactive decay of contaminants inside the structure of the PMT. Typical dark noise rate for PMTs used within SK are $O(3)$kHz [85]. This is lower than the expected number of photons generated for a 'high energy event' (As described in subsection 3.1.4) but instability in this value can cause biases in reconstruction. Dark noise is related to the gain of a PMT and is calibrated using hits inside a time window recorded before an event trigger [98].

3.1.3 Data Acquisition and Triggering

As the analysis presented in this thesis will only use the SK-IV period of the SK experiment so this subsection focuses on the relevant points of the data acquisition and triggering systems to that SK period. The earlier data acquisition and triggering systems are documented in [99, 100].

Before the SK-IV period started, the existing front-end electronics were replaced with "QTC-Based Electronics with Ethernet, QBEE" systems [101]. When the QBEE observes a signal above a 1/4 photoelectron threshold, the charge-to-time (QTC) converter generates a rectangular pulse. The start of the rectangular pulse indicates the time at which the analog photoelectron signal was received and the width of the pulse indicates the total charge integrated throughout the signal. This is then digitized by time-to-digital converters and sent to the "front-end" PCs. The digitized signal from every QBEE is then chronologically ordered and sent to the "merger" PCs. It is the merger PCs that apply the software trigger. Any triggered events are passed to the "organizer" PC. This sorts the data stream of multiple merger PCs into chronologically ordered events, which are then saved to disk. The schematic of data flow from PMTs to disk is illustrated in Figure 3.3.

The software trigger (described in [103]) operates by determining the number of PMT hits within a 200ns sliding window, N_{200}. This window coincides with the maximum time that a Cherenkov photon would take to traverse the length of the SK tank [100]. For lower energy events that generate fewer photons, this technique is useful for eliminating background processes like dark noise and radioactive decay which would be expected to be separated in time. When the value of N_{200} exceeds some pre-defined threshold, a software trigger is issued. There are several trigger thresholds used within the SK-IV period which are

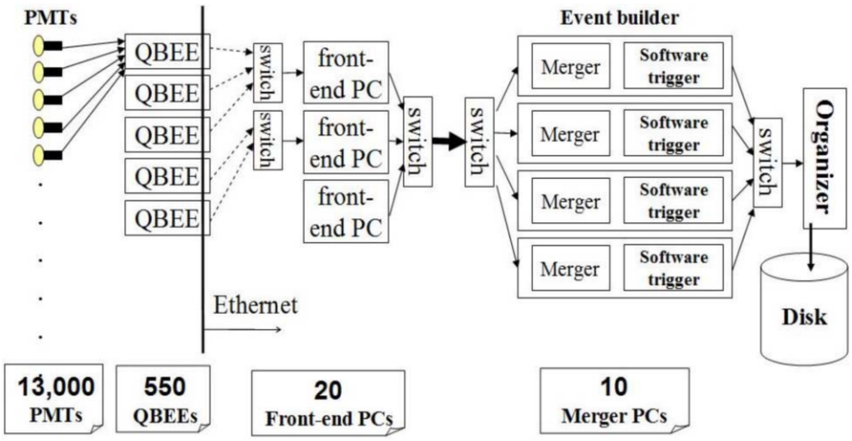

Figure 3.3: Schematic view of the data flow through the data acquisition and online system. Taken from [102].

detailed in Table 3.2. If one of these thresholds is met, the PMT hits within an extended time window are also read out and saved to disk. In the special case of an event that exceeds the SHE trigger but does not exceed the OD trigger, the AFT trigger looks for delayed coincidences of 2.2MeV gamma rays emitted from neutron capture in a 535μs window after the SHE trigger. A similar but more complex "Wideband Intelligent Trigger (WIT)" has been deployed and is described in [104].

Trigger	Acronym	Condition	Extended time window (μs)
Super Low Energy	SLE	>34/31 hits	1.3
Low Energy	LE	>47 hits	40
High Energy	HE	>50 hits	40
Super High Energy	SHE	>70/58 hits	40
Outer Detector	OD	>22 hits in OD	N/A

Table 3.2: The trigger thresholds and extended time windows saved around an event which were utilised throughout the SK-IV period. The exact thresholds can change and the values listed here represent the thresholds at the start and end of the SK-IV period.

3.1.4 Cherenkov Radiation

Cherenkov light is emitted from any highly energetic charged particle traveling with relativistic velocity, β, greater than the local speed of light in a medium [105].

Cherenkov light is formed at the surface of a cone with a characteristic pitch angle,

$$\cos(\theta) = \frac{1}{\beta n}. \tag{3.2}$$

Where n is the refractive index of the medium. Consequently, the Cherenkov momentum threshold, P_{thres}, is dependent upon the mass, m, of the charged particle moving through the medium,

$$P_{thres} = \frac{m}{\sqrt{n^2 - 1}}. \tag{3.3}$$

For water, where $n = 1.33$, the Cherenkov threshold momentum and energy for various particles are given in Table 3.3. In contrast, γ-rays are detected indirectly via the combination of photons generated by Compton scattering and pair production. The threshold for detection in the SK detector is typically higher than the threshold for photon production. This is due to the fact that the attenuation of photons in the water means that typically $\sim 75\%$ of Cherenkov photons reach the ID PMTs. Then the collection and quantum efficiencies described in subsection 3.1.1 result in the number of detected photons being lower than the number of photons which reach the PMTs.

Particle	Threshold Momentum (MeV)	Threshold Energy (MeV)
Electron	0.5828	0.7751
Muon	120.5	160.3
Pion	159.2	211.7
Proton	1070.0	1423.1

Table 3.3: The threshold momentum and total energy for a particle to generate Cherenkov light in ultrapure water, as calculated in Equation 3.2 in ultrapure water which has refractive index $n = 1.33$.

The Frank-Tamm equation [106] describes the relationship between the number of Cherenkov photons generated per unit length, dN/dx, the wavelength of the photons generated, λ, and the relativistic velocity of the charged particle,

$$\frac{d^2N}{dxd\lambda} = 2\pi\alpha \left(1 - \frac{1}{n^2\beta^2}\right) \frac{1}{\lambda^2}. \tag{3.4}$$

where α is the fine structure constant. For a 100MeV momentum electron, approximately 330 photons will be produced per centimeter in the 300nm $\leq \lambda \leq$ 700nm region which the ID PMTs are most sensitive to [85].

3.2 The Tokai to Kamioka Experiment

The Tokai to Kamioka (T2K) experiment is a long-baseline neutrino oscillation experiment located in Japan. Proposed in the early 2000s [107, 108] to replace K2K [109], T2K was designed to observe electron neutrino appearance whilst precisely measuring the oscillation parameters associated with muon neutrino disappearance [110]. The experiment consists of a neutrino beam generated at the Japan Proton Accelerator Research Complex (J-PARC), a suite of near detectors situated 280m from the beam target, and the Super Kamiokande far detector positioned at a 295km baseline. The cross-section view of the T2K experiment is drawn in Figure 3.4.

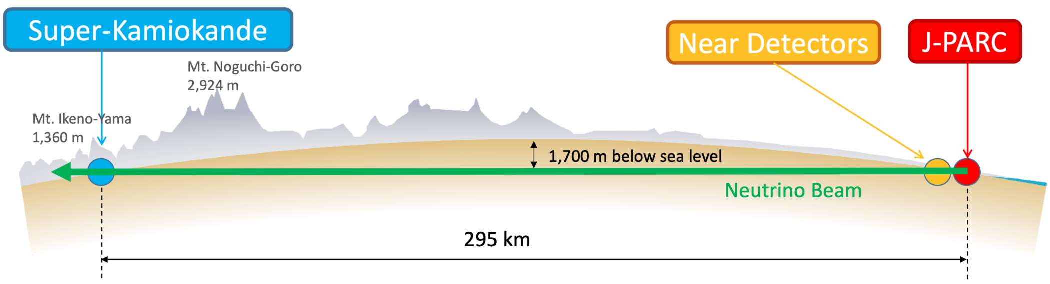

Figure 3.4: The cross-section view of the Tokai to Kamioka experiment illustrating the beam generation facility at J-PARC, the near detector situated at a baseline of 280m and the Super Kamiokande far detector situated 295km from the beam target.

The T2K collaboration makes world-leading measurements of the $\sin^2(\theta_{23})$, Δm^2_{32}, and δ_{CP} oscillation parameters. Improvements in the precision and accuracy of parameter estimates are still being made by including new data samples and developing the models which describe the neutrino interactions and detector responses [111]. Electron neutrino appearance was first observed at T2K in 2014 [112] with 7.3σ significance.

The near detectors provide constraints on the beam flux and cross-section model parameters used within the oscillation analysis by observing the unoscillated neutrino beam. There are a host of detectors situated in the near detector hall (As illustrated in Figure 3.5): ND280 (subsection 3.2.3), INGRID (subsection 3.2.4), NINJA [113], WAGASCI [114], and Baby-MIND [115]. The latter three are not currently used within the oscillation analysis presented in this thesis.

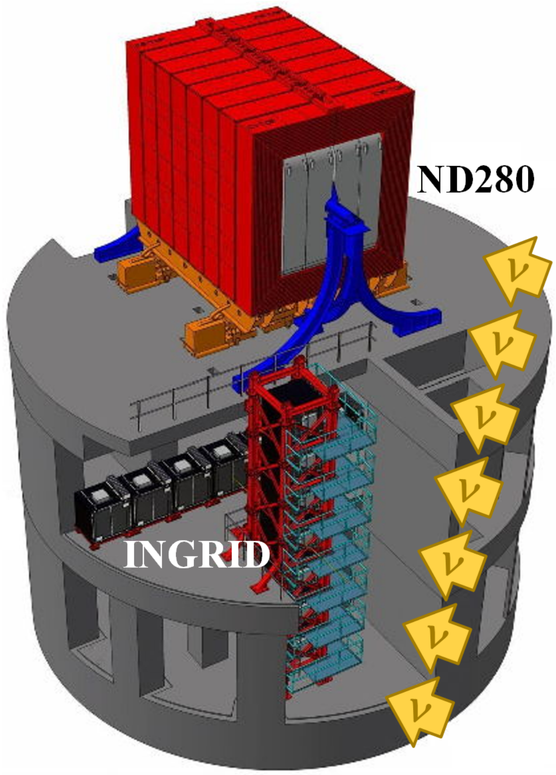

Figure 3.5: The near detector suite for the T2K experiment showing the ND280 and INGRID detectors. The distance between the detectors and the beam target is 280m.

Whilst this thesis presents the ND280 in terms of its purpose for the oscillation analysis, the detector can also make many cross-section measurements at neutrino energies of $O(1)$GeV for the different targets within the detector [116, 117]. These measurements are of equal importance as they can lead the way in determining the model parameters used in the interaction models for the future high-precision era of neutrino physics.

3.2.1 Analysis Overview

There are two independent fitters, `MaCh3` and `BANFF`, which perform the near detector fit. `MaCh3` uses a bayesian Markov Chain Monte Carlo fitting technique, whereas `BANFF` uses a frequentist gradient descent technique. The output of each fitter is compared as a method of cross-checking the behaviour of the two fitters. This is done by comparing: the Monte Carlo predictions using various tunes, the likelihood that is calculated in each fitter and the post-fit constraint associated with every parameter used in the fit. Once validated, the output converted into a covariance matrix to describe the error and correlations between all the flux and cross-section parameters. This is then propagated to the far-detector oscillation analysis group.

The far detector group has three independent fitters: `P-Theta`, `VALOR` and `MaCh3`. The first two fitters use a hybrid frequentist fitting technique where the likelihood is minimised with respect to the parameters of interest and marginalised over all other parameters. These fitters use the covariance provided by the near detector fitters as a basis for implementing the near detector constriants. The `MaCh3` fitter uses a simultaneous fit of all near and far detector samples. This removes any Gaussian assumptions when making the covariance matrix from the near detector results. The results for all three fitters are compares using a technique similar to the validation of the near detector fitters.

There are three particular tunes of the T2K flux and low energy cross section model typically considered. Firstly, the “generated” tune which is the set of dial values with which the Monte Carlo was generated. Secondly, the set of dial values which are taken from external data measurements and used as inputs. These are the “pre-fit” dial values. The reason these two sets of dial values are different is that the external data measurements are continually updated but it is very computationally intensive to regenerate a Monte Carlo prediction after each update. The final tune is the “post-fit”, “post-ND fit” or “post-BANFF” dial values. These are the values taken from the constraints provided by the near detector.

3.2.2 The Neutrino Beam

The neutrino beam used within the T2K experiment is described in [39, 43] and summarised below. The accelerator facility at J-PARC is composed of two sections; the primary and secondary beamlines. Figure 3.6 illustrates a schematic of the beamline, focusing mostly on the components of the secondary beamline. The primary beamline has three accelerators that progressively accelerate protons; a linear accelerator, a rapid-cycling synchrotron, and the main-ring (MR) synchrotron. Once fully accelerated by the MR, the protons have a kinetic energy of 30GeV. Eight bunches of these protons, separated by 500ns, are extracted per "spill" from the MR and directed towards a graphite target (a rod of length 91.4cm and diameter 2.6cm). Spills are extracted at 0.5Hz with $\sim 3 \times 10^{14}$ protons contained per spill.

The secondary beamline consists of three main components: the target station, the decay volume, and the beam dump. The target station is comprised of the target, beam monitors, and three magnetic focusing horns. The proton beam interacts with the graphite target to form a secondary beam of mostly pions and kaons. The secondary beam travels through a 96m long decay volume, generating neutrinos through the following decays [39],

$$
\begin{aligned}
\pi^+ &\to \mu^+ + \nu_\mu & \pi^- &\to \mu^- + \bar{\nu}_\mu \\
K^+ &\to \mu^+ + \nu_\mu & K^- &\to \mu^- + \bar{\nu}_\mu \\
&\to \pi^0 + e^+ + \nu_e & &\to \pi^0 + e^- + \bar{\nu}_e \\
&\to \pi^0 + \mu^+ + \nu_\mu & &\to \pi^0 + \mu^- + \bar{\nu}_\mu \\
K_L^0 &\to \pi^- + e^+ + \nu_e & K_L^0 &\to \pi^+ + e^- + \bar{\nu}_e \\
&\to \pi^- + \mu^+ + \nu_\mu & &\to \pi^+ + \mu^- + \bar{\nu}_\mu \\
\mu^+ &\to e^+ + \bar{\nu}_\mu + \nu_e & \mu^- &\to e^- + \nu_\mu + \bar{\nu}_e.
\end{aligned}
\tag{878}
$$

The electrically charged component of the secondary beam is focused towards the far detector by the three magnetic horns. These horns direct charged particles of a particular polarity towards SK whilst defocusing the oppositely charged particles. This allows a mostly neutrino or mostly antineutrino beam to be used within the experiment, denoted as "forward horn current (FHC)" or "reverse horn current (RHC)" respectively.

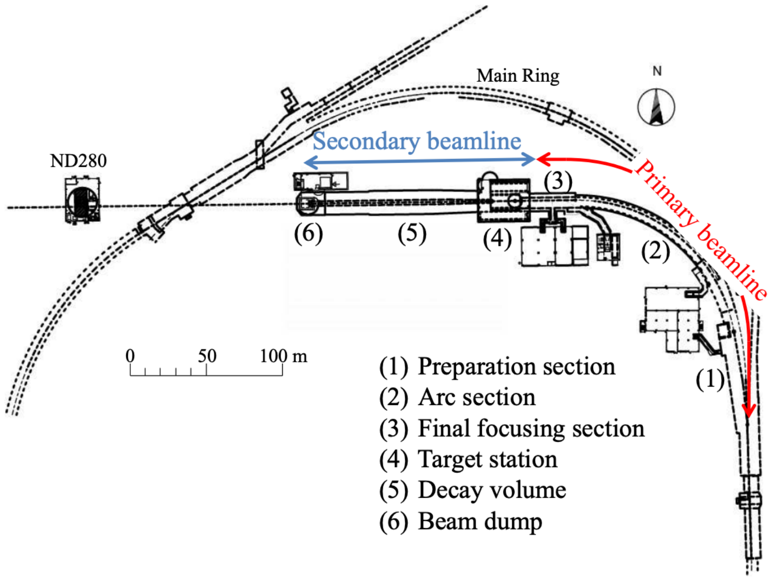

(a) Primary and secondary beamline

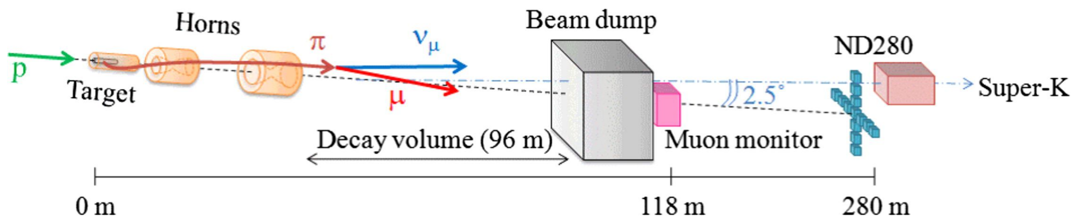

(b) Secondary beamline

Figure 3.6: Top panel: Bird's eye view of the most relevant part of primary and secondary beamline used within the T2K experiment. The primary beamline is the main-ring proton synchrotron, kicker magnet, and graphite target. The secondary beamline consists of the three focusing horns, decay volume, and beam dump. Figure taken from [43]. Bottom panel: The side-view of the secondary beamline including the focusing horns, beam dump and neutrino detectors. Figure taken from [118].

Figure 3.7 illustrates the different contributions to the FHC and RHC neutrino flux. The low energy flux is dominated by the decay of pions whereas kaon decay becomes the dominant source of neutrinos for $E_\nu > 3$GeV. The "wrong-sign" component, which is the $\bar{\nu}_\mu$ background in a ν_μ beam, and the intrinsic irreducible ν_e background, are predominantly due to muon decay for $E_\nu <$ 2GeV. As the antineutrino production cross-section is smaller than the neutrino cross-section, the wrong-sign component is more dominant in the RHC beam as compared to that in the FHC beam.

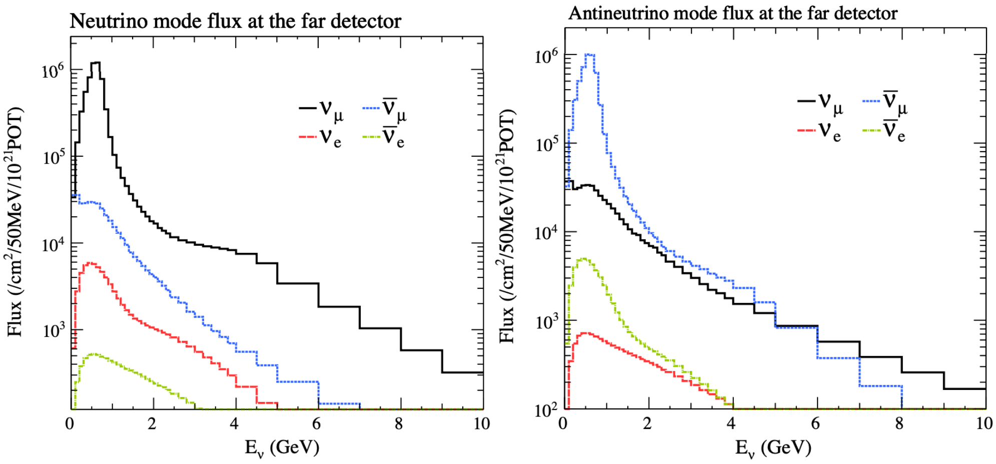

Figure 3.7: The Monte Carlo prediction of the energy spectrum for each flavour of neutrino (ν_e, $\bar{\nu}_e$, ν_μ and $\bar{\nu}_\mu$) in the neutrino dominated beam FHC mode (Left) and antineutrino dominated beam RHC mode (Right) expected at SK. Taken from [119].

The beam dump, situated at the end of the decay volume, stops all charged particles other than highly energetic muons ($p_\mu > 5$GeV). The MuMon detector monitors the penetrating muons to determine the beam direction and intensity which is used to constrain some of the beam flux systematics within the analysis [118, 120].

The T2K experiment uses an off-axis beam to narrow the neutrino energy distribution. This was the first implementation of this technique in a long-baseline neutrino oscillation experiment after its original proposal [121]. Pion decay, $\pi \rightarrow \mu + \nu_\mu$, is a two-body decay. Consequently, the neutrino energy, E_ν, can be determined based on the pion energy, E_π, and the angle at which the neutrino is emitted, θ,

$$E_\nu = \frac{m_\pi^2 - m_\mu^2}{2\left(E_\pi - p_\pi \cos(\theta)\right)}, \tag{3.5}$$

where m_π and m_μ are the mass of the pion and muon respectively. For a fixed energy pion, the neutrino energy distribution is dependent upon the angle at which the neutrinos are observed from the initial pion beam direction. For the 295km baseline at T2K, $E_\nu = 0.6$GeV maximises the electron neutrino appearance probability, $P(\nu_\mu \rightarrow \nu_e)$, whilst minimising the muon disappearance probability,

$P(\nu_\mu \to \nu_\mu)$. Figure 3.8 illustrates the neutrino energy distribution for a range of off-axis angles, as well as the oscillation probabilities most relevant to T2K.

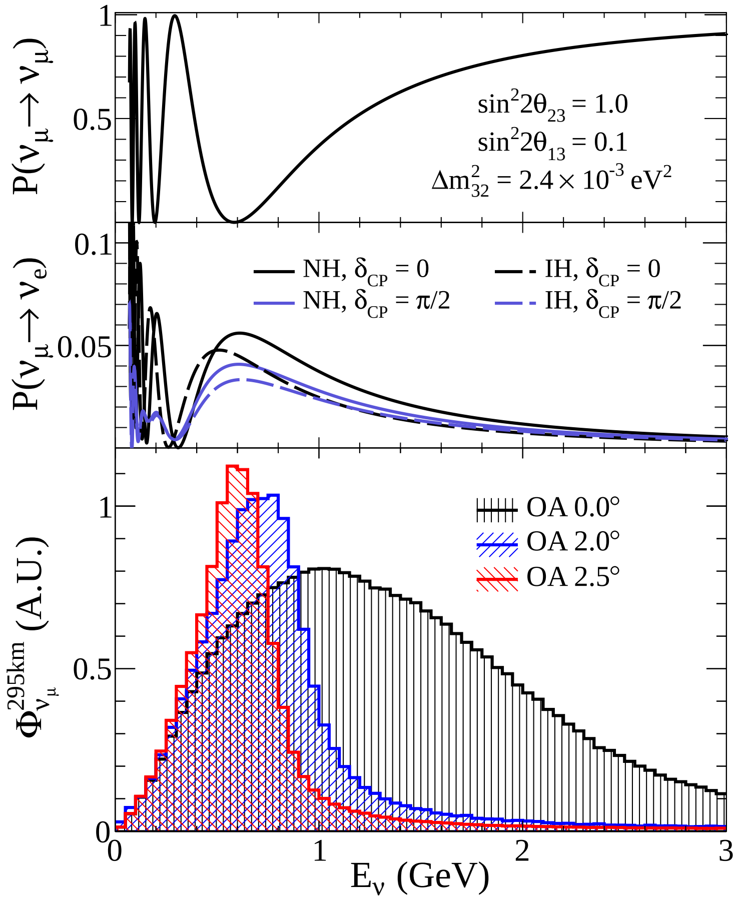

Figure 3.8: Top panel: T2K muon neutrino disappearance probability as a function of neutrino energy. Middle panel: T2K electron neutrino appearance probability as a function of neutrino energy. Bottom panel: The neutrino flux distribution for three different off-axis angles (Arbitrary units) as a function of neutrino energy.

3.2.3 The Near Detector at 280m

Whilst all the near detectors are situated in the same "pit" located at 280m from the beamline, the "ND280" detector is the off-axis detector which is situated at the same off-axis angle as the Super-Kamiokande far detector. It has two primary functions; firstly it measures the neutrino flux and secondly, it counts the event rates of different types of neutrino interactions. Both of these constrain the flux and cross-section systematics invoked within the model for a more accurate prediction of the expected event rate at the far detector.

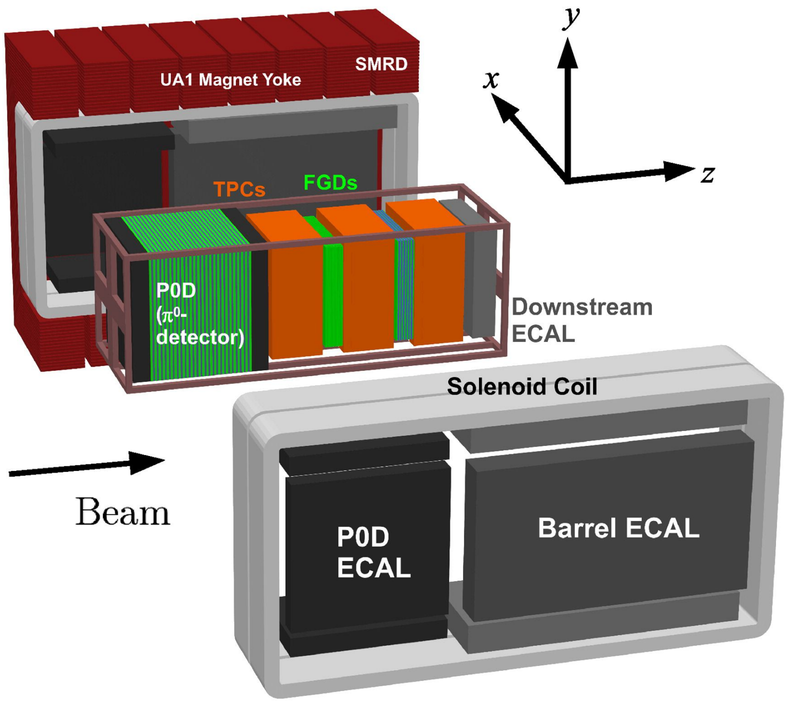

Figure 3.9: The components of the ND280 detector. The neutrino beam travels from left to right. Taken from [43].

As illustrated in Figure 3.9, the ND280 detector consists of several sub-detectors. The most important part of the detector for this analysis is the tracker region. This is comprised of two-time projection chambers (TPCs) sandwiched between three fine grain detectors (FGDs). The FGDs contain both hydrocarbon plastics and water targets for neutrino interactions and provide track reconstruction near the interaction vertex. The emitted charged particles can then propagate into the TPCs which provide particle identification and momentum reconstruction. The FGDs and TPCs are further described in subsubsection 3.2.3.1 and subsubsection 3.2.3.2 respectively. The electromagnetic calorimeter (ECAL) encapsulates the tracker region alongside the π^0 detector (P0D). The ECAL measures the deposited energy from photons emitted from interactions within the FGD. The P0D constrains the cross-section of neutral current interactions which generate neutral pions, which is one of the largest backgrounds in the electron neutrino appearance oscillation channel. The P0D and ECAL detectors are detailed in subsubsection 3.2.3.3 and subsubsection 3.2.3.4 respectively. The entire detector is located within a large yoke magnet which produces a 0.2T magnetic field. This design of the magnet also includes a scintillating detector called the side muon range detector (SMRD), which is used to track high-angle muons as well as acting as a cosmic veto. The SMRD is described in subsubsection 3.2.3.5.

3.2.3.1 Fine Grained Detectors

The T2K tracker region is comprised of two fine-grained detectors (FGD) and three Time Projection Chambers (TPC). A detailed description of the FGD design, construction, and assembly is found in [122] and summarised below. The FGDs are the primary target for neutrino interactions with a mass of 1.1 tonnes per FGD. Alongside this, the FGDs are designed to be able to track short-range particles which do not exit the FGD. Typically, short-range particles are low momentum and are observed as tracks that deposit a large amount of energy per unit length. This means the FGD needs good granularity to resolve these particles. The FGDs have the best timing resolution ($\sim$ 3ns) of any of the sub-detectors of the ND280 detector. As such, the FGDs are used for time of flight measurements to distinguish forward-going positively charged particles from backward-going negatively charged particles. Finally, any tracks which pass through multiple sub-detectors are required to be track matched to the FGD.

Both FGDs are made from square scintillator planes of side length 186cm and width 2.02cm. Each plane consists of two layers of 192 scintillator bars in an X or Y orientation. A wavelength-shifting fiber is threaded through the center of each bar and is read out by a multi-pixel photon counter (MPPC). FGD1 is the most upstream of the two FGDs and contains 15 planes of carbon plastic scintillator which is a common target in external neutrino scattering data. As the far detector is a pure water target, 7 of the 15 scintillator planes in FGD2 have been replaced with a hybrid water-scintillator target. Due to the complexity of the nucleus, nuclear effects can not be extrapolated between different nuclei. Therefore having the ability to take data on one target which is the same as external data and another target which is the same as the far detector target is beneficial for reliable model parameter estimates.

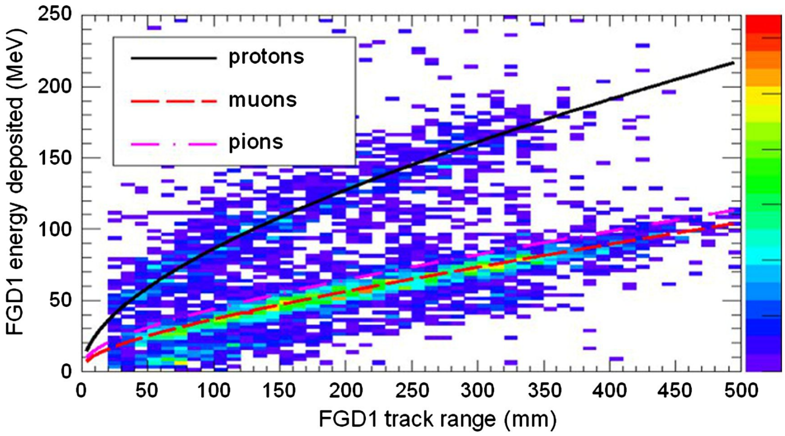

Figure 3.10: Comparison of data to Monte Carlo prediction of integrated deposited energy as a function of track length for particles that stopped in FGD1. Taken from [122].

The integrated deposited energy is used for particle identification. The FGD can distinguish protons from other charged particles by comparing the integrated deposited energy from data to Monte Carlo prediction as seen in Figure 3.10.

3.2.3.2 Time Projection Chambers

The majority of particle identification and momentum measurements within ND280 are provided by three Time Projection Chambers (TPCs) [123]. The TPCs are located on either side of the FGDs. They are located inside of the magnetic field meaning the momentum of a charged particle can be determined from the bending of the track.

Each TPC module consists of two gas-tight boxes, as shown in Figure 3.11, which are made of non-magnetic material. The outer box is filled with CO_2 which acts as an electrical insulator between the inner box and the ground. The inner box forms the field cage which produces a uniform electric drift field of $\sim$ 275V/cm and is filled with an argon gas mixture. Charged particles moving through this gas mixture ionize the gas and the ionised charge is drifted towards micromegas detectors which measure the ionization charge. The time and position information in the readout allows a three-dimensional image of the neutrino interaction.

The particle identification of tracks that pass through the TPCs is performed using dE/dx measurements. Figure 3.12 illustrates the data to Monte Carlo

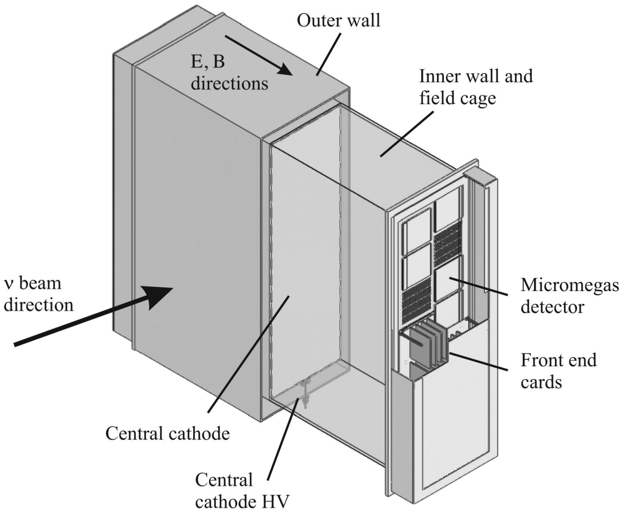

Figure 3.11: Schematic design of a Time Projection Chamber detector. Taken from [123].

distributions of the energy lost by a charged particle passing through the TPC as a function of the reconstructed particle momentum. The resolution is $7.8 \pm 0.2\%$ meaning that electrons and muons can be distinguished. This allows reliable measurements of the intrinsic ν_e component of the beam.

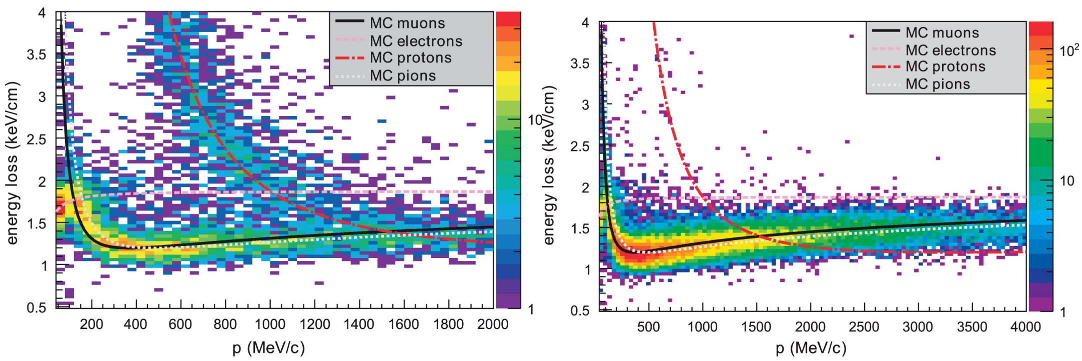

(a) Positively charged particles **(b)** Negatively charged particles

Figure 3.12: The distribution of energy loss as a function of reconstructed momentum for charged particles passing through the TPC, comparing data to Monte Carlo prediction. Taken from [123].

3.2.3.3 π^0 Detector

If one of the γ-rays from a $\pi^0 \rightarrow 2\gamma$ decay is missed at the far detector, the reconstruction will determine that event to be a charge current ν_e-like event. This is one of the main backgrounds hindering the electron neutrino appearance searches. The π^0 detector (P0D) measures the cross-section of the neutral current induced neutral pion production on a water target to constrain this background.

The P0D is a cube of approximately 2.5m length consisting of layers of scintillating bars, brass and lead sheets, and water bags as illustrated in Figure 3.13. Two electromagnetic calorimeters are positioned at the most upstream and most downstream position in the sub-detector and the water target is situated in between them. The scintillator layers are built from two triangular bars orientated in opposite directions to form a rectangular layer. Each triangular scintillator bar is threaded with optical fiber which is read out by MPPCs. The high-Z brass and lead regions produce electron showers from the photons emitted in π^0 decay.

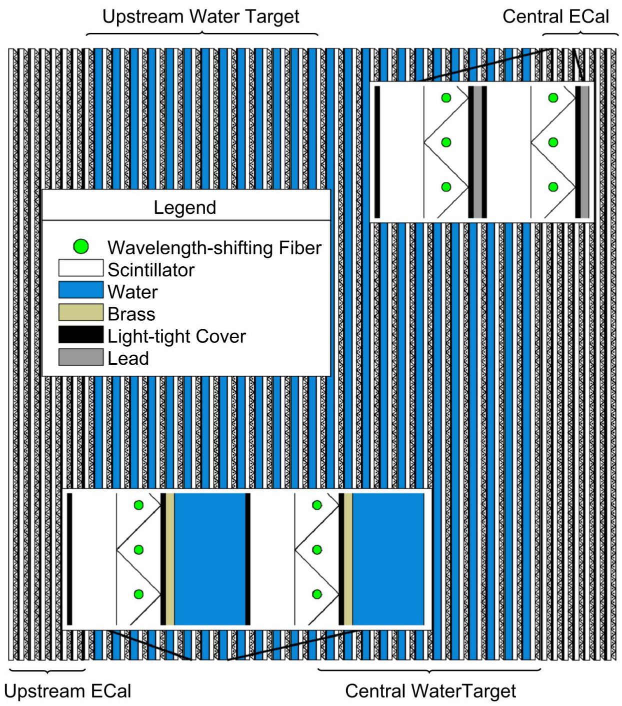

Figure 3.13: A schematic of the P0D side-view. Taken from [124].

The sub-detector can generate measurements of NC1π^0 cross-sections on a water target by measuring the event rate both with and without the water target, with the cross-section on a water target being determined as the difference. The total active mass is 16.1 tonnes when filled with water and 13.3 tonnes when empty.

3.2.3.4 Electromagnetic Calorimeter

The electromagnetic calorimeter [125] (ECal) encapsulates the P0D and tracking sub-detectors. Its primary purpose is to aid π^0 reconstruction from any interaction in the tracker. To do this, it measures the energy and direction of photon showers from $\pi^0 \rightarrow 2\gamma$ decay. It can also distinguish pion and muon tracks depending on the shape of the photon shower deposited.

The ECal is comprised of three sections; the P0D ECal which surrounds the P0D, the barrel ECal which encompasses the tracking region, and the downstream ECal which is situated downstream of the tracker region. The barrel and downstream ECals are tracking calorimeters that focus on electromagnetic showers from high-angle particles emitted from the tracking sub-detectors. Particularly in the TPC, high-angle tracks (those which travel perpendicularly to the beam-axis) can travel along a single scintillator bar resulting in very few hits. The width of the barrel and downstream ECal corresponds to ~ 11 electron radiation lengths to ensure a significant amount of the π^0 energy is contained. As the P0D has its own calorimetry which reconstructs showers, the P0D ECal determines the energy which escapes the P0D.

Each ECal is constructed of multiple layers of scintillating bars sandwiched between lead sheets. The scintillating bars are threaded with optical fiber and read out by MPPCs. Each sequential layer of the scintillator is orientated perpendicular to the previous which allows a three-dimensional event reconstruction. The target mass of the P0D ECal, barrel ECal, and downstream ECal are 1.50, 4.80, and 6.62 tonnes respectively.

3.2.3.5 Side Muon Range Detector

As illustrated in Figure 3.9, the ECal, FGDs, P0D, and TPCs are enclosed within the UA1 magnet. Reconditioned after use in the UA1 [126] and NOMAD [127] experiments, this magnet provides a uniform horizontal magnetic field of 0.2T with an uncertainty of 2×10^{-4}T.

Built into the UA1 magnet, the side muon range detector (SMRD)[128] monitors high-energy muons which leave the tracking region and permeate through the ECal. It additionally acts as a cosmic muon veto and trigger.

3.2.4 The Interactive Neutrino GRID

The Interactive Neutrino GRID (INGRID) detector is situated within the same "pit" as the other near detectors. It is aligned with the beam in the "on-axis" position and measures the beam direction, spread, and intensity. The detector was originally designed with 16 identical modules [43] (two modules have since been decommissioned) and a "proton" module. The design of the detector is 14 modules oriented in a cross with length and height 10m $\times$ 10m, as illustrated in Figure 3.14.

Each module is composed of iron sheets interlaced with eleven tracking scintillator planes for a total target mass of 7.1 tonnes per module. The scintillator design is an X-Y pattern of 24 bars in both orientations, where each bar contains wave-length shifting fibers which are connected to multi-pixel photon counters (MPPCs). Each module is encapsulated inside veto planes to aid the rejection of charged particles entering the module.

The proton module is different from the other modules in that it consists of entirely scintillator planes with no iron target. The scintillator bars are also smaller than those used in the other modules to increase the granularity of the detector and improve tracking capabilities. The module sits in the center of the beamline and is designed to give precise measurements of quasi-elastic charged current interactions to evaluate the performance of the Monte Carlo simulation of the beamline.

The INGRID detector can measure the beam direction to an uncertainty of 0.4mrad and the beam centre within a resolution of 10cm [43]. The beam direction in both the vertical and horizontal directions is discussed in [129] and it is found to be in good agreement with the MUMON monitor described in subsection 3.2.2.

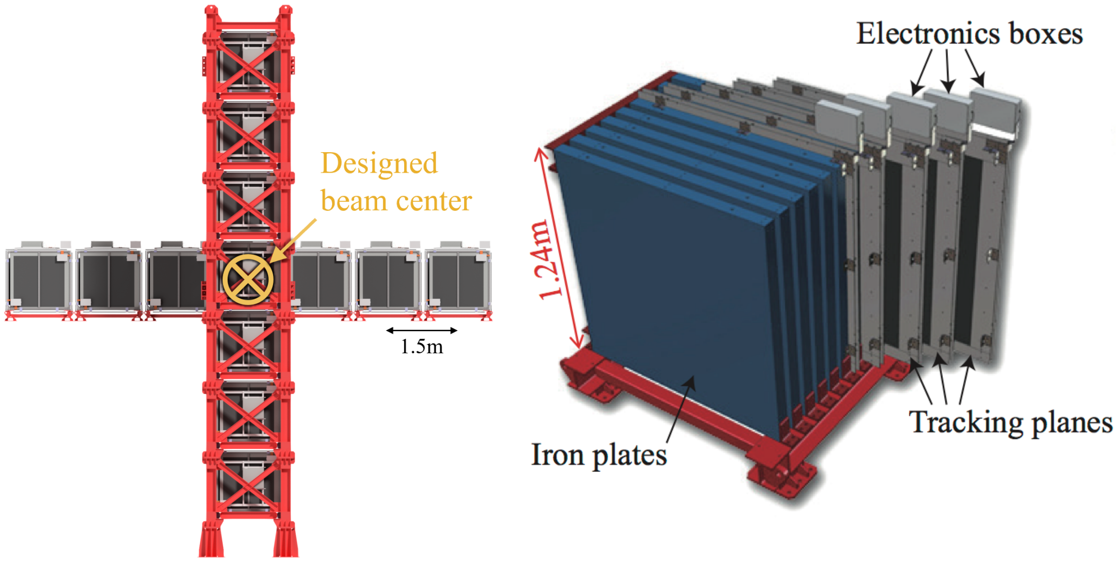

Figure 3.14: Left panel: The Interactive Neutrino GRID on-axis Detector. 14 modules are arranged in a cross-shape configuration, with the center modules being directly aligned with the on-axis beam. Right panel: The layout of a single module of the INGRID detector. Both figures are recreated from [43].

4

Bayesian Statistics and Markov Chain Monte Carlo Techniques

This thesis presents a Bayesian oscillation analysis. To extract the oscillation parameters, a Markov Chain Monte Carlo (MCMC) method is used. This chapter explains the theory of how parameter estimates can be determined using this technique and condenses the material found in the literature [130–133].

The oscillation parameter determination presented here is built upon a simultaneous fit to neutrino beam data in the near detector, beam data at SK, and atmospheric data at SK. In total, there are four oscillation parameters of interest ($\sin^2(\theta_{23})$, $\sin^2(\theta_{13})$, Δm^2_{32}, and δ_{CP}), two oscillation parameters to which this study will not be sensitive ($\sin^2(\theta_{12})$, Δm^2_{21}) and many nuisance parameters that control the systematic uncertainty models.

This analysis uses a Monte Carlo technique to generate a multi-dimensional probability distribution across all of the model parameters used in the fit. To determine an estimate for each parameter, this multi-dimensional object is integrated over all other parameters. This process is called Marginalisation and is described in subsection 4.3.1. Monte Carlo techniques approximate the probability distribution of each parameter within the limit of generating infinite samples. As ever, generating a large number of samples is time and resource-dependent. Therefore, an MCMC technique is utilised within this analysis to reduce the required number of steps to sufficiently sample the parameter space. This technique is described in further detail in subsection 4.2.1.

The Bayesian analysis techniques used within this thesis are built within the `MaCh3` framework [134]. This uses a custom MCMC library package exclusively supported and developed by the `MaCh3` collaborators (which includes the author of this thesis).

4.1 Bayesian Statistics

Bayesian inference treats observable data, D, and model parameters, $\vec{\theta}$, on equal footing such that a probability model of both data and parameters is required. This is the joint probability distribution $P(D, \vec{\theta})$ and can be described by the prior distribution for model parameters $P(\vec{\theta})$ and the likelihood of the data given the model parameters $P(D|\vec{\theta})$,

$$P(D, \vec{\theta}) = P(D|\vec{\theta})P(\vec{\theta}). \tag{4.1}$$

The prior distribution, $P(\vec{\theta})$, describes all previous knowledge about the parameters within the model. For example, if the risk of developing health problems is known to increase with age, the prior distribution would describe the increase. For the purpose of this analysis, the prior distribution is typically the best-fit values taken from external data measurements with a Gaussian uncertainty. The prior distribution can also contain correlations between model parameters. In an analysis using Monte Carlo techniques, the likelihood of measuring some data assuming some set of model parameters is calculated by comparing the Monte Carlo prediction generated at that particular set of model parameters to the data.

It is parameter estimation that is important for this analysis and as such, Bayes' theorem [135] is applied to calculate the probability for each parameter to have a certain value given the observed data, $P(\vec{\theta}|D)$, which is known as the posterior distribution (often termed the posterior). This can be expressed as

$$P(\vec{\theta}|D) = \frac{P(D|\vec{\theta})P(\vec{\theta})}{\int P(D|\vec{\theta})P(\vec{\theta})d\vec{\theta}}. \tag{4.2}$$

The denominator in Equation 4.2 is the integral of the joint probability distribution over all values of all parameters used within the fit. For brevity, the posterior distribution is

$$P(\vec{\theta}|D) \propto P(D|\vec{\theta})P(\vec{\theta}). \tag{4.3}$$

For the purposes of this analysis, it is acceptable to neglect the normalisation term and focus on this proportional relationship.

4.1.1 Application of Prior Knowledge

The posterior distribution is proportional to the prior uncertainty applied to each parameter, as illustrated by Equation 4.3. This means that it is possible to change the prior after the posterior distribution has been determined. The prior uncertainty of a particular parameter can be 'divided' out of the posterior distribution and the resulting distribution can be reweighted using the new prior uncertainty that is to be applied. The methodology and implementation of changing the prior follows that described in [136].

An example implementation that is useful for this analysis is the application of the "reactor constraint". As discussed in section 2.4, an external constraint on $\sin^2(\theta_{13})$ is determined from measurements taken from reactor experiments. However, the sensitivities from just using the T2K and SK samples is equally as important. Without this technique, two fits would have to be run, doubling the required resources. Therefore, the key benefit for this analysis is the fact that only a single 'fit' has to be performed and can be used to build the two posterior distributions of the with and without reactor constraint applied.

4.2 Monte Carlo Simulation

Monte Carlo techniques are used to numerically solve a complex problem that does not necessarily have an analytical solution. These techniques rely on building a large ensemble of samples from an unknown distribution and then using the ensemble to approximate the properties of the distribution.

An example that uses Monte Carlo techniques is to calculate the area underneath a curve. For example, take the problem of calculating the area under a straight line with gradient $M = 0.4$ and intercept $C = 1.0$. Analytically, one can calculate the area under the line is equal to 30 units for $0 \leq x \leq 10$. Using Monte Carlo techniques, one can calculate the area under this line by throwing many random values for the x and y components of each sample and then calculating whether that point falls below the line. The area can then be calculated by the ratio of points below the line to the total number of samples thrown multiplied by the total area in which samples were scattered. The study is shown in Figure 4.1 highlights this technique and finds the area under the curve to be 29.9 compared to an analytical solution of 30.0. The deviation of the numerical to analytical solution can be attributed to the number of samples used in the study. The accuracy of the approximation in which the properties of the Monte Carlo samples replicate those of the desired distribution is dependent on the number of samples used. Replicating this study with a differing number of Monte Carlo samples used in each study (As shown in Figure 4.2) highlights how the Monte Carlo techniques are only accurate within the limit of a high number of samples.

Whilst the above example has an analytical solution, these techniques are just as applicable to complex solutions. Clearly, any numerical solution is only as useful as its efficiency. As discussed, the accuracy of the Monte Carlo technique is dependent upon the number of samples generated to approximate the properties of the distribution. Furthermore, if the positions at which the samples are evaluated are not 'cleverly' picked, the efficiency of the Monte Carlo technique significantly drops. Given the example in Figure 4.1, if the region in which the samples are scattered significantly extends passed the region of interest, many calculations will be calculated but do not add to the ability of the Monte Carlo technique to achieve the correct result. For instance, any sample evaluated at a $y \geq 5$ could be removed without affecting the final result. This does bring in an aspect of the 'chicken and egg' problem in that to achieve efficient sampling, one needs to know the distribution beforehand.

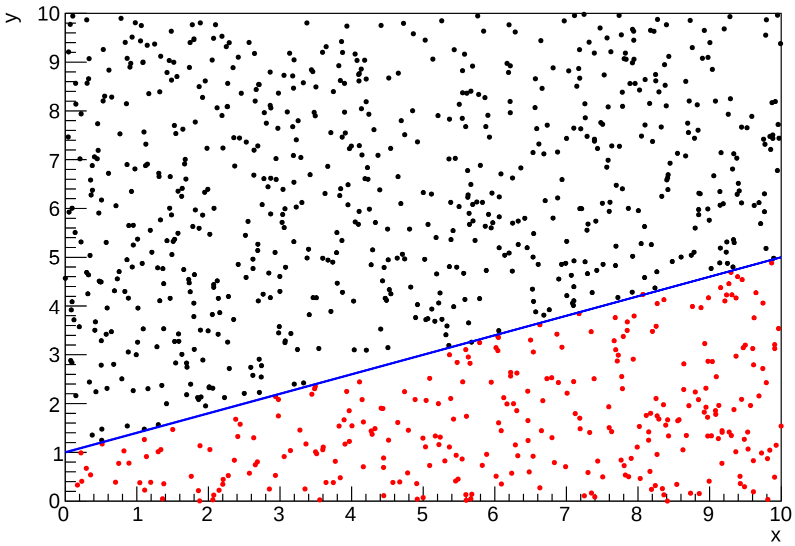

Figure 4.1: Example of using Monte Carlo techniques to find the area under the blue line. The gradient and intercept of the line are 0.4 and 1.0 respectively. The area found to be under the curve using one thousand samples is 29.9 units.

4.2.1 Markov Chain Monte Carlo

This analysis utilises a multi-dimensional probability distribution, with some dimensions being significantly more constrained than others. These constraints can be from prior knowledge of parameter distributions from external data or un-physical regions in which parameters can not exist. To maximise the efficiency of building the posterior distribution, a Markov Chain Monte Carlo (MCMC) technique is used. This employs a Markov chain to select the points at which to sample the posterior distribution. It performs a semi-random stochastic walk through the allowable parameter space. This builds a posterior distribution

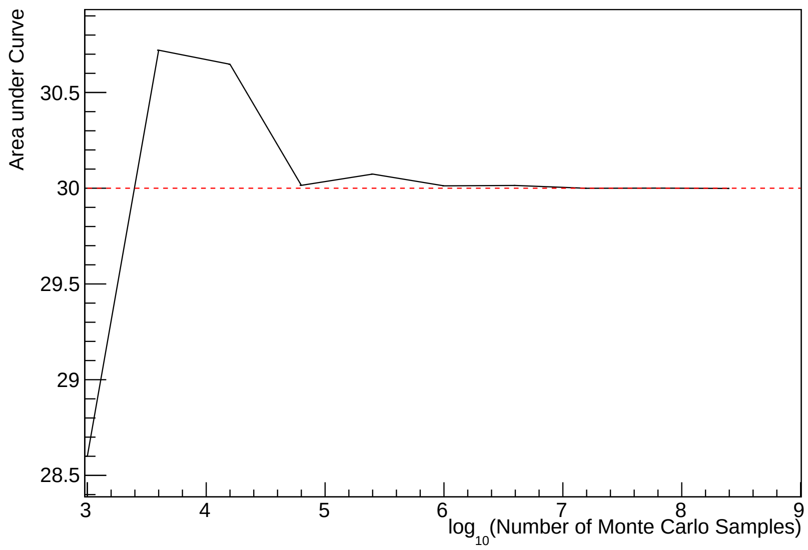

Figure 4.2: The area under a line of gradient 0.4 and intercept 1.0 for the range $0 \leq x \leq 10$ as calculated using Monte Carlo techniques as a function of the number of samples used in each repetition. The analytical solution to the area is 30 units as given by the red line.

which has the property that the density of sampled points is proportional to the probability density of that parameter. This means that the samples produced by this technique are not statistically independent but they will cover the space of the distribution.

A Markov chain functions by selecting the position of step $\vec{x}_{i+1}$ based on the position of $\vec{x}_i$. The space in which the Markov chain selects samples is dependent upon the total number of parameters utilised within the fit, where a discrete point in this space is described by the N-dimensional space $\vec{x}$. In a perfectly operating Markov chain, the position of the next step depends solely on the previous step and not on the further history of the chain ($\vec{x}_0$, $\vec{x}_1$, etc.). However, in solving the multi-dimensionality of the fit used within this analysis, each step becomes correlated with several of the steps preceding itself. Providing the MCMC chain is well optimised, it will begin to converge towards a unique stationary distribution. The period between the chain's initial starting point and the convergence to the unique stationary distribution is colloquially known as the burn-in period. Once the chain reaches the stationary distribution, all points sampled after that point will look like samples from that distribution.

Further details of the theories underpinning MCMC techniques are discussed in [131] but can be summarised by the requirement that the chain satisfies the three 'regularity conditions':

- Irreducibility: From every position in the parameter space $\vec{x}$, there must exist a non-zero probability for every other position in the parameter space to be reached.
- Recurrence: Once the chain arrives at the stationary distribution, every step following from that position must be samples from the same stationary distribution.
- Aperiodicity: The chain must not repeat the same sequence of steps at any point throughout the sampling period.

The output of the chain after burn-in (i.e. the sampled points after the chain has reached the stationary distribution) can be used to approximate the posterior distribution and model parameters $\vec{\theta}$. To achieve the requirement that the unique stationary distribution found by the chain be the posterior distribution, one can use the Metropolis-Hastings algorithm. This guides the stochastic process depending on the likelihood of the current proposed step compared to that of the previous step.

4.2.2 Metropolis-Hastings Algorithm

As a requirement for MCMCs, the Markov chain implemented in this technique must have a unique stationary distribution that is equivalent to the posterior distribution. To ensure this requirement and that the regularity conditions are met, this analysis utilises the Metropolis-Hastings (MH) algorithm [137, 138]. For the i^{th} step in the chain, the MH algorithm determines the position in the parameter space to which the chain moves to based on the current step, $\vec{x}_i$, and the proposed step, $\vec{y}_{i+1}$. The proposed step is randomly selected from some proposal function $f(\vec{x}_{i+1}|\vec{x}_i)$, which depends solely on the current step (ie. not the further history of the chain). The next step in the chain $\vec{x}_{i+1}$ can be either the current step or the proposed step determined by whether the proposed step is accepted or rejected. To decide if the proposed step is selected, the acceptance probability, $\alpha(\vec{x}_i, \vec{y}_i)$, is calculated as

$$\alpha(\vec{x}_i, \vec{y}_{i+1}) = \min\left(1, \frac{P(\vec{y}_{i+1}|D) f(\vec{x}_i|\vec{y}_{i+1})}{P(\vec{x}_i|D) f(\vec{y}_{i+1}|\vec{x}_i)}\right). \tag{4.4}$$

Where $P(\vec{y}_{i+1}|D)$ is the posterior distribution as introduced in section 4.1. To simplify this calculation, the proposal function is required to be symmetric such that $f(\vec{x}_i|\vec{y}_{i+1}) = f(\vec{y}_{i+1}|\vec{x}_i)$. In practice, a multi-variate Gaussian distribution centered on $\vec{x}_i$ is used to throw parameter proposals. This reduces Equation 4.4 to

$$\alpha(\vec{x}_i, \vec{y}_{i+1}) = \min\left(1, \frac{P(\vec{y}_{i+1}|D)}{P(\vec{x}_i|D)}\right). \tag{4.5}$$

DB: Figure out what Giles means

After calculating this quantity, a random number, β, is generated uniformly between 0 and 1. If $\beta \leq \alpha(\vec{x}_i, \vec{y}_{i+1})$, the proposed step is accepted. Otherwise, the chain sets the next step equal to the current step. This procedure is repeated for subsequent steps. This can be interpreted as if the posterior probability of the proposed step is greater than that of the current step, $(P(\vec{y}_{i+1}|D) \geq P(\vec{x}_i|D))$, the proposed step will always be accepted. If the opposite is true, $(P(\vec{y}_{i+1}|D) \leq P(\vec{x}_i|D))$, the proposed step will be accepted with probability $P(\vec{x}_i|D)/P(\vec{y}_{i+1}|D)$. This ensures that the Markov chain does not get trapped in any local minima in the potentially non-Gaussian posterior distribution. The outcome of this technique is that the density of steps taken in a discrete region is directly proportional to the probability density in that region.

4.2.3 MCMC Optimisation

As discussed in subsection 4.2.2, the proposal function invoked within the MH algorithm can take any form and the chain will still converge to the stationary distribution. At each set of proposed parameter values, a prediction of the same spectra has to be generated which requires significant computational resources. Therefore, the number of steps taken before the unique stationary distribution is found should be minimised as only steps after convergence add information to the oscillation analysis. Furthermore, the chain should entirely cover the allowable parameter space to ensure that all values have been considered. Tuning the distance that the proposal function jumps between steps on a parameter-by-parameter basis can both minimise the length of the burn-in period and ensure that the correlation between step $\vec{x}_i$ and $\vec{x}_j$ is sufficiently small.

The effect of changing the width of the proposal function is highlighted in Figure 4.3. Three scenarios, each with the same underlying stationary distribution (A Gaussian of width 1.0 and mean 0.), are presented. The only difference between the three scenarios is the width of the proposal function, colloquially known as the 'step size σ'. Each scenario starts at an initial parameter value of 10.0 which would be considered an extreme variation. For the case where $\sigma = 0.1$, it is clear to see that the chain takes a long time to reach the expected region of the parameter. This indicates that this chain would have a large burn-in period and does not converge to the stationary distribution until step ~ 500. Furthermore, whilst the chain does move towards the expected region, each step is significantly correlated with the previous. Considering the case where $\sigma = 5.0$, the chain approaches the expected parameter region almost instantly meaning that the burn-in period is not significant. However, there are clearly large regions of steps where the chain does not move. This is likely due to the chain proposing steps in the tails of the distribution which have a low probability of being accepted. Consequently, this chain would take a significant number of steps to fully span the allowable parameter region. For the final scenario, where $\sigma = 0.5$, you can see a relatively small burn-in period of approximately 100 steps. Once the chain reaches the stationary distribution, it moves throughout the expected region of parameter values many times, sufficiently sampling the full parameter region. This example is a single parameter varying across a continuous distribution and does not fully reflect the difficulties in the many-hundred multi-variate parameter distribution used within this analysis. However, it does give a conceptual idea of the importance of selecting the proposal function and associated step size.

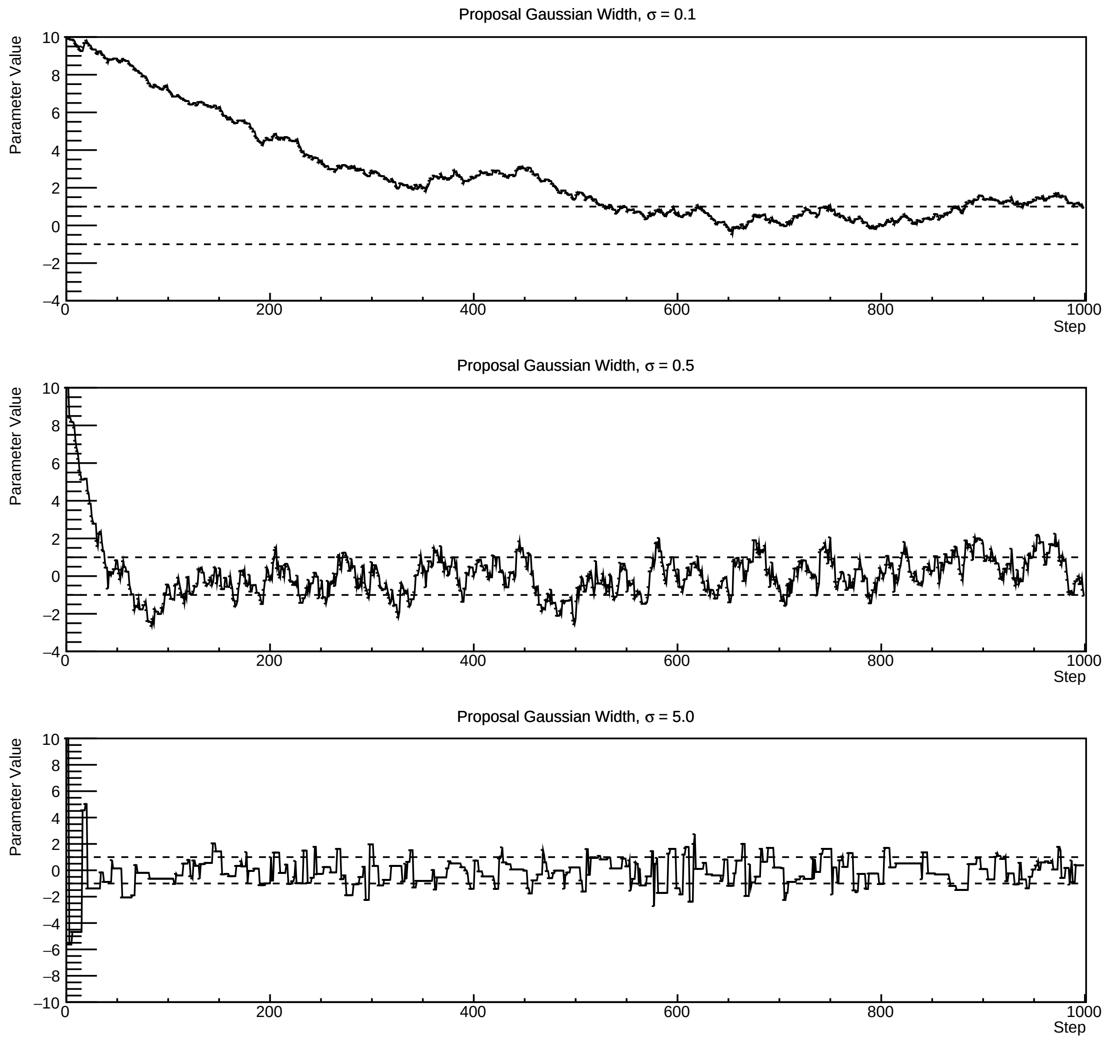

Figure 4.3: Three MCMC chains, each with a stationary distribution equal to a Gaussian centered at 0 and width 1 (As indicated by the black dotted lines). All of the chains use a Gaussian proposal function but have different widths (or 'step size σ'). The top panel has $\sigma = 0.1$, middle panel has $\sigma = 0.5$ and the bottom panel has $\sigma = 5.0$.

As discussed, step size tuning directly correlates to the average step acceptance rate. If the step size is too small, many steps will be accepted but the chain moves slowly. If the opposite is true, many steps will be rejected as the chain proposes steps in the tails of the distribution. Discussion in [139] suggests that the 'ideal' acceptance rate of a high dimension MCMC chain should be approximately $\sim$ 25%. An "ideal" step size [139] of

$$\sigma = \frac{2.4}{N_p}, \tag{4.6}$$

where N_p is the number of parameters included in the MCMC fit. However, the complex correlations between systematics mean that some parameters have to be hand-tuned and many efforts have been taken to select a set of parameter-by-parameter step sizes to approximately reach the ideal acceptance rate.

Figure 4.4 highlights the likelihood as calculated by the fit in subsection 8.2.4 as a function of the number of steps in each chain. In practice, many independent MCMC chains are run simultaneously to parallelise the task of performing the fit. This figure overlays the distribution found in each chain. As seen, the likelihood decreases from its initial value and converges towards a stationary distribution after $\sim 1 \times 10^5$ steps.

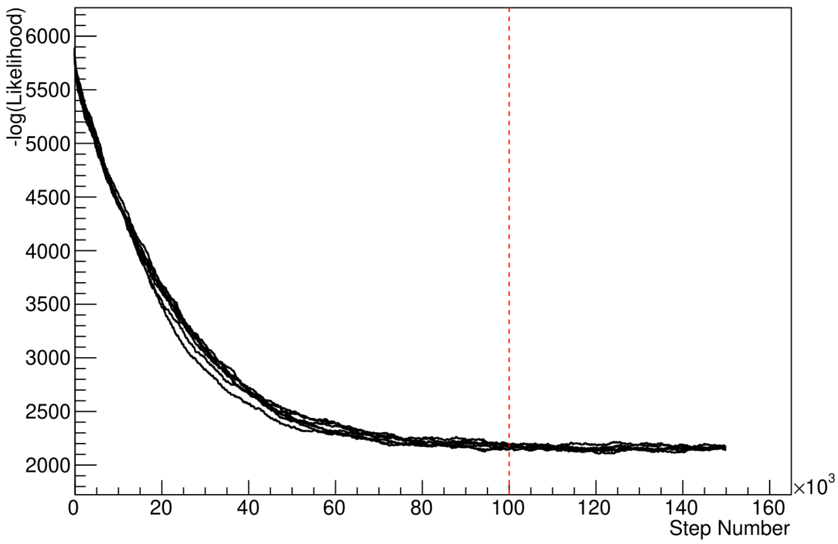

Figure 4.4: The log-likelihood from the fit detailed in subsection 8.2.4 as a function of the number of steps accumulated in each fit. Many independent MCMC chains were run in parallel and overlaid on this plot. The red line indicates the 1×10^5 step burn-in period after which the log-likelihood becomes stable.

Multiple configurations of this analysis have been performed throughout this thesis where different samples or systematics have been used. For all of these configurations, it was found that a burnin period of 1×10^5 was sufficient in all cases.

4.3 Understanding the MCMC Results

The previous sections have described how to generate the posterior probability distribution using Bayesian MCMC techniques. However, this analysis focuses on oscillation parameter determination. The posterior distribution output from the chain is a high-dimension object, with as many dimensions as there are parameters included in the oscillation analysis. However, this multi-dimensional object is difficult to conceptualize so parameter estimations are often presented in one or two-dimensional projections of this probability distribution. To do this, marginalisation techniques are invoked.

4.3.1 Marginalisation

The output of the MCMC chain is a highly dimensional probability distribution which is very difficult to interpret. From the standpoint of an oscillation analysis experiment, the one or two-dimensional 'projections' of the oscillation parameters of interest are most relevant. Despite this, the best fit values and uncertainties on the oscillation parameters of interest should correctly encapsulate the correlations to the other systematic uncertainties (colloquially called 'nuisance' parameters). For this joint beam and atmospheric analysis, the oscillation parameters of interest are $\sin^2(\theta_{23})$, $\sin^2(\theta_{13})$, Δm^2_{32}, andδ_{CP}. All other parameters (including the oscillation parameters this fit is insensitive to) are deemed nuisance parameters. To generate these projections, the posterior distribution is integrated over all nuisance parameters. This is called marginalisation. This technique also explains why it is acceptable to neglect the normalisation constant of the posterior distribution, which was discussed in section 4.1.

A simple example of the marginalisation technique is to imagine the scenario where two coins are flipped. To determine the probability that the first coin returned a 'head', the exact result of the second coin flip is disregarded and simply integrated over. For the parameters of interest, $\vec{\theta}_i$, the marginalised posterior is calculated by integrating over the nuisance parameters, $\vec{\theta}_n$. In this case, Equation 4.2 becomes

$$P(\vec{\theta}_i|D) = \frac{\int P(D|\vec{\theta}_i, \vec{\theta}_n) P(\vec{\theta}_i, \vec{\theta}_n) d\vec{\theta}_n}{\int P(D|\vec{\theta}) P(\vec{\theta}) d\vec{\theta}}. \tag{4.7}$$

Where $P(\vec{\theta}_i, \vec{\theta}_n)$ encodes the prior knowledge about the uncertainty and correlations between the parameters of interest and the nuisance parameters. In practice, this is simply taking the one or two-dimensional projection of the multi-dimensional probability distribution.

While in principle an easy solution to a complex problem, correlations between the interesting and nuisance parameters can bias the marginalised results. A similar effect is found when the parameters being marginalised over have non-Gaussian probability distributions. For example, Figure 4.5 highlights the marginalisation bias in the probability distribution found for a parameter when requiring a correlated parameter to have a positive parameter value. Due to the complex nature of the oscillation parameter fit presented in this thesis, there are correlations occurring between the oscillation parameters of interest and the other nuisance parameters included in the fit.

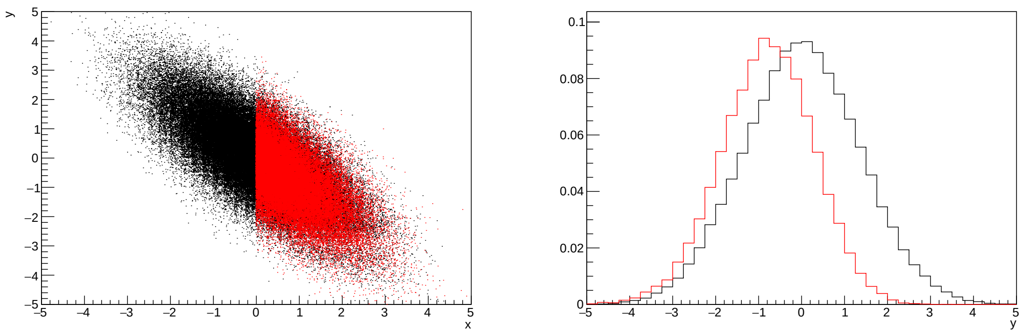

Figure 4.5: Left: The two-dimensional probability distribution for two correlated parameters x and y. The red distribution shows the two-dimensional probability distribution when $0 \leq x \leq 5$. Right: The marginalised probability distribution for the y parameter found when requiring the x to be bound between $-5 \leq x \leq 5$ and $0 \leq x \leq 5$ for the black and red distribution, respectively.

4.3.2 Parameter Estimation and Credible Intervals

The purpose of this analysis is to determine the best fit values for the oscillation parameters that the beam and atmospheric samples are sensitive to: $\sin^2(\theta_{23})$, $\sin^2(\theta_{13})$, Δm^2_{32}, and δ_{CP}. The posterior probability density, taken from the output MCMC chain, is binned in these parameters. The parameter best-fit point is then taken to be the value that has the highest posterior probability. This is performed in both one and two-dimensional projections.

However, the single best-fit point in a given parameter is not of much use on its own. The uncertainty on the best-fit point must also be presented using credible intervals. The definition of the 1σ credible interval is that there is 68% belief that the parameter is within those bounds. For a more generalised definition, the credible interval is the region, R, of the posterior distribution that contains a specific fraction of the total probability, such that

$$\int_R P(\theta|D)d\theta = \alpha. \tag{4.8}$$

Where θ is the parameter being evaluated. This technique then calculates the $\alpha \times 100\%$ credible interval.

In practice, this analysis uses the highest posterior density (HPD) credible intervals which are calculated through the following method. First, the probability distribution is area-normalised such that it has an integrated area equal to 1.0. The bins of probability are then summed from the highest to lowest until the sum exceeds the 1σ level (0.68 in this example). This process is repeated for a range of credible intervals, notably the 1σ, 2σ and 3σ along with other levels where the critical values for each level can be found in [76]. This process can be repeated for the two-dimensional probability distributions by creating two-dimensional contours of credible intervals rather than a one-dimensional result.

4.3.3 Bayesian Model Comparisons

Due to the matter resonance, this analysis has some sensitivity to the mass hierarchy of neutrino states (whether Δm^2_{32} is positive or negative) and the octant of $\sin^2(\theta_{23})$. The Bayesian approach utilised within this analysis gives an intuitive method of model comparison by determining which hypothesis is most favourable. Taking the ratio of Equation 4.3 for the two hypotheses of normal hierarchy, NH, and inverted hierarchy, IH, gives

$$\frac{P(\vec{\theta}_{NH}|D)}{P(\vec{\theta}_{IH}|D)} = \frac{P(D|\vec{\theta}_{NH})}{P(D|\vec{\theta}_{IH})} \times \frac{P(\vec{\theta}_{NH})}{P(\vec{\theta}_{IH})}. \tag{4.9}$$

The middle term defines the Bayes factor, $B(\mathrm{NH}/\mathrm{IH})$, which is a data-driven interpretation of how strong the data prefers one hierarchy to the other. For this analysis, equal priors on both mass hierarchy hypotheses are chosen ($P(\vec{\theta}_{NH}) = P(\vec{\theta}_{IH})$ = 0.5). In practice, the MCMC chain proposes a value of $|\Delta m^2_{32}|$ and then applies a 50% probability that the value is sign flipped. Consequently, the Bayes factor can be calculated from the ratio of the probability density in either hypothesis. This equates to counting the number of steps taken in the normal and inverted hierarchies and taking the ratio. The same approach can be taken to compare the upper octant (UO) compared to the lower octant (LO) hypothesis of $\sin^2(\theta_{23})$.

$\log_{10}(B_{AB})$	B_{AB}	Strength of Preference
< 0.0	< 1	No preference for hypothesis A (Supports hypothesis B)
$0.0 - 0.5$	$1.0 - 3.16$	Preference for hypothesis A is weak
$0.5 - 1.0$	$3.16 - 10.0$	Preference for hypothesis A is substantial
$1.0 - 1.5$	$10.0 - 31.6$	Preference for hypothesis A is strong
$1.5 - 2.0$	$31.6 - 100.0$	Preference for hypothesis A is very strong
> 2.0	> 100.0	Decisive preference for hypothesis A

Table 4.1: Jeffreys scale for strength of preference for two models A and B as a function of the calculated Bayes factor ($B_{AB} = B(A/B)$) between the two models [140]. The original scale is given in terms of $\log_{10}(B(A/B))$ but converted to linear scale for easy comparison throughout this thesis.

Whilst the value of the Bayes factor should always be shown, the Jeffreys scale [140] (highlighted in Table 4.1) gives an indication of the strength of preference for one model compared to the other. Other interpretations of the strength of preference of a model exist, e.g. the Kass and Raferty Scale [141].

4.3.4 Comparison of MCMC Output to Expectation

To ensure the fit is performing well, a best-fit spectrum is produced using the posterior probability distribution and compared with the data, allowing easy by-eye comparisons to be made. A simple method of doing this is to perform a comparison in the fitting parameters (For instance, the reconstructed neutrino energy and lepton direction for T2K far detector beam samples) of the spectra generated by the MCMC chain to 'data'. This 'data' could be true data or some variation of Monte Carlo prediction. This allows easy comparison of the MCMC probability distribution to the data. To perform this, N steps from the post-burnin MCMC chain are randomly selected. From these, the Monte Carlo prediction at each step is generated by reweighting the model parameters to the values specified at that step. Due to the probability density being directly correlated with the density of steps in a certain region, parameter values close to the best fit value are most likely to be selected.

In practice, for each bin of the fitting parameters has a probability distribution of event rates, with one entry per sampled MCMC step. This distribution is binned where the bin with the highest probability is selected as the mean and an error on the width of this probability distribution is calculated using the approach highlighted in subsection 4.3.2. Consequently, the best fit distribution in the fit parameter is not necessarily that which would be attained by reweighting the Monte Carlo prediction to the most probable parameter values.

A similar study can be performed to illustrate the freedom of the model parameter space prior to the fit. This can be done by throwing parameter values from the prior uncertainty of each parameter.

5

Simulation, Reconstruction, and Event Reduction

As a crucial part of the oscillation analysis, an accurate prediction of the expected neutrino spectrum at the far detector is required. This includes modeling the flux generation, neutrino interactions, and detector effects. All of the simulation packages required to do this are briefly described in section 5.1. The reconstruction of neutrino events in the far detector, including the `fiTQun` algorithm, is documented in section 5.2. This also includes data quality checks of the SK-V data which the author performed for the T2K oscillation analysis presented at the Neutrino 2020 conference [75]. Finally, section 5.3 describes the steps taken in the SK detector to trigger on events of interest whilst removing the comparatively large rate of cosmic ray muon events.

5.1 Simulation

In order to generate a Monte Carlo prediction of the expected event rate at the far detector, all the processes in the beam and atmospheric fluxes, neutrino interaction, and detector need to be modeled.

5.1.1 Neutrino Flux

The beamline simulation consists of three distinct parts: the initial hadron interaction modeled by FLUKA [142], the target station geometry and particle tracking performed by JNUBEAM, [143, 144] and any hadronic re-interactions simulated by GCALOR [145]. The primary hadronic interactions are $O(10)$GeV, where FLUKA matches external cross-section data better than GCALOR [146]. However, FLUKA is not very adaptable so a small simulation is built to model the interactions in the target and the output is then passed to JNUBEAM and GCALOR for propagation. The hadronic interactions are tuned to data from the NA61/SHINE [147–149] and HARP [150] experiments. The tuning is done by reweighting the FLUKA and GCALOR predictions to match the external data multiplicity and cross-section measurements, based on final state particle kinematics [146]. The culmination of this simulation package generates the predicted flux for neutrino and antineutrino beam modes which are illustrated in Figure 3.7.

The atmospheric neutrino flux is simulated by the HKKM model [51, 53]. The primary cosmic ray flux is tuned to AMS [151] and BESS [152] data assuming the US-standard atmosphere '76 [153] density profile and includes geomagnetic field effects. The primary cosmic rays interact to generate pions and muons. The interaction of these secondary particles to generate neutrinos is handled by DPMJET-III [154] for energies above 32GeV and JAM [53, 155] for energies below that value [49]. These hadronic interactions are tuned to BESS and L3 data [156, 157] using the same methodology as the tuning of the beamline simulation. The energy and cosine zenith predictions of $\nu_e, \bar{\nu}_e, \nu_\mu, \bar{\nu}_\mu$ flux are given in Figure 2.3 and Figure 2.5, respectively. The flux is approximately symmetrical and peaked around the horizon ($\cos(\theta_Z) = 0.0$). This is because horizontally-going pions and kaons can travel further than their vertically-going counterparts resulting in a larger probability of decaying to neutrinos. The symmetry is broken in lower-energy neutrinos due to geomagnetic effects, which modify the track of the primary cosmic rays. Updates to the HKKM model are currently ongoing [158].

5.1.2 Neutrino Interaction

Once a flux prediction has been made for all three detectors, NEUT 5.4.0 [159, 160] models the interactions of the neutrinos in the detectors. For the purposes of this analysis, quasi-elastic (QE), meson exchange (MEC), single meson production (PROD), coherent pion production (COH), and deep inelastic scattering (DIS) interactions are simulated. These interaction categories can be further broken down by whether they were propagated via a $W^{\pm}$ boson in Charged Current (CC) interactions or via a Z^0 boson in Neutral Current (NC) interactions. CC interactions have a charged lepton in the final state, which can be flavour-tagged in reconstruction to determine the flavour of the neutrino. In contrast, NC interactions have a neutrino in the final state so no flavour information can be determined from the observables left in the detector after an interaction. This is the reason why neutrinos that interact through NC modes are assumed to not oscillate within this analysis. Both CC and NC interactions are modeled for all the above interaction categories, other than MEC interactions which are only modeled for CC events.

As illustrated in Figure 5.1, CCQE interactions dominate the cross-section of neutrino interactions around $E_\nu \sim 0.5$GeV. The NEUT implementation adopts the Llewellyn Smith [161] model for neutrino-nucleus interactions, where the nuclear ground state of any bound nucleons (neutrino-oxygen interactions) is approximated by a spectral-function [162] model that simulates the effects of Fermi momentum and Pauli blocking. The cross-section of QE interactions is controlled by vector and axial-vector form factors parameterised by the BBBA05 [163] model and a dipole form factor with $M_A^{QE} = 1.21$GeV fit to external data [164], respectively. NEUT implements the Valencia [165] model to simulate MEC events, where two nucleons and two holes in the nuclear target are produced (often called 2p2h interactions).

For neutrinos of energy $O(1)$GeV, PROD interactions become dominant. These predominantly produce charged and neutral pions although γ, kaon,

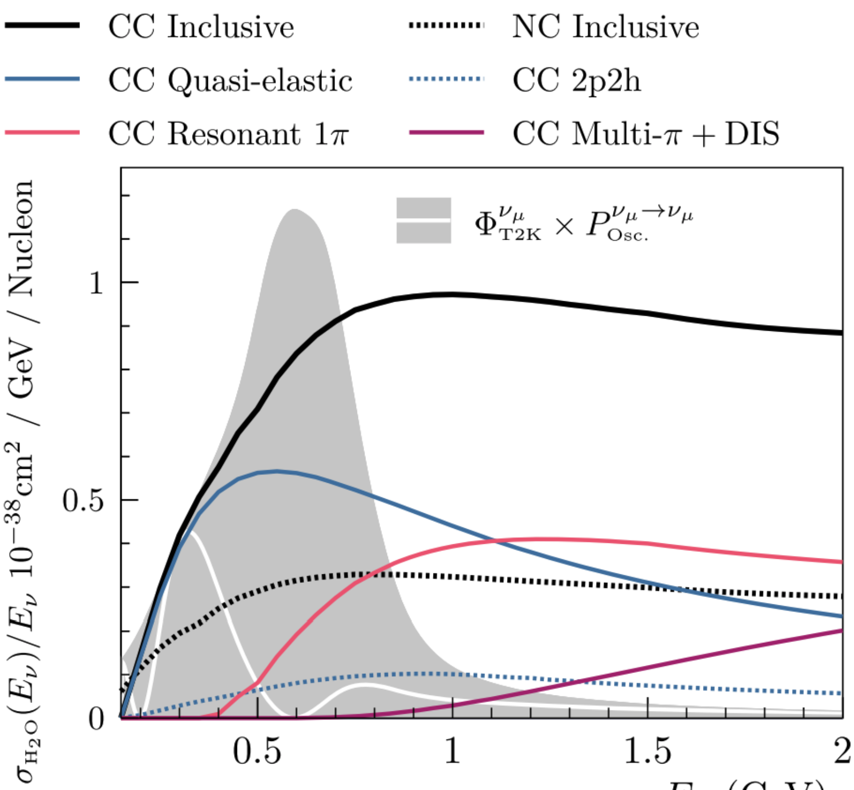

Figure 5.1: The NEUT prediction of the ν_μ-H2O cross-section overlaid on the T2K ν_μ flux. The charged current (black, solid) and neutral current (black, dashed) inclusive, charged current quasi-elastic (blue, solid), charged current 2p2h (blue, dashed), charged current single pion production (pink), and charged current multi–π and DIS (Purple) cross-sections are illustrated. Figure taken from [159].

and η production is also considered. To simulate these interactions, the Berger-Sehgal [166] model is implemented within NEUT. It simulates the excitation of a nucleon from a neutrino interaction, production of an intermediate baryon, and the subsequent decay to a single meson or γ. Pions can also be produced through COH interactions, which occur when the incoming neutrino interacts with the entire oxygen nucleus leaving a single pion outside of the nucleus. NEUT utilises the Berger-Sehgal [167] model to simulate these COH interactions.

DIS and multi-π producing interactions become the most dominant for energies $> O(5)$GeV. PYTHIA [168] is used to simulate any interaction with invariant mass $W > 2\mathrm{GeV/c^2}$, which produces at least one meson. For any interaction which produces at least two mesons but has $W < 2\mathrm{GeV/c^2}$, the

Bronner model is used [169]. Both of these models use Parton distribution functions based on the Bodek-Yang model [170–172].

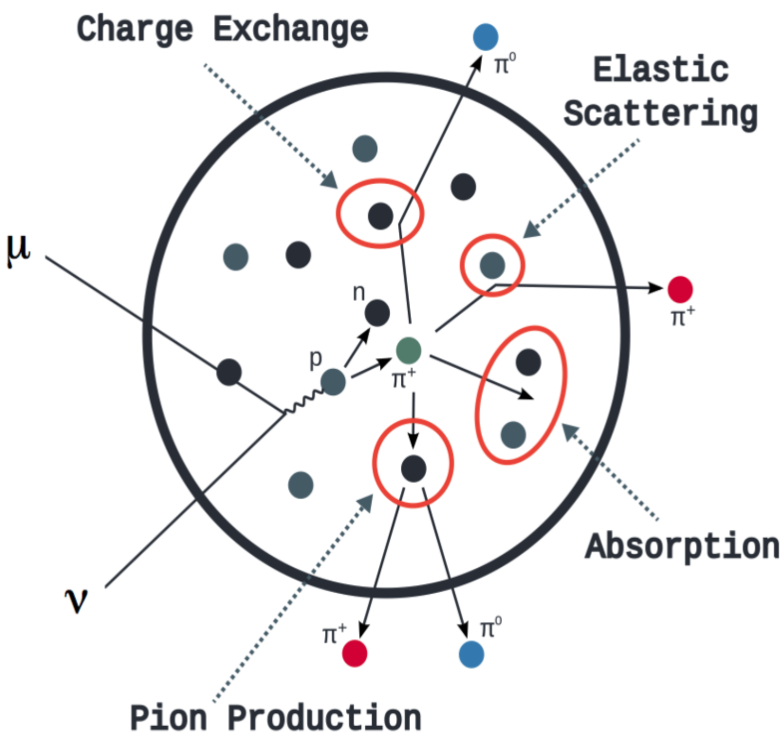

Figure 5.2: Illustration of the various processes which a pion can undergo before exiting the nucleus. Taken from [173].

Any pion that is produced within the nucleus can re-interact through final state interactions before it exits, as illustrated by the scattering, absorption, production, and exchange interactions in Figure 5.2. These re-interactions alter the observable particles within the detector. For instance, if the charged pion from a CC PROD interaction is absorbed, the observables would mimic a CC QE interaction. To simulate these effects, NEUT uses a semi-classical intranuclear cascade model [159]. This cascade functions by stepping the pion through the nucleus in fixed-length steps equivalent to $dx = R_N/100$, where R_N is the radius of the nucleus. At each step, the simulation allows the pion to interact through scattering, charged exchange, absorption, or production with an interaction-dependent probability calculated from a fit to external data [174]. This cascade continues until the pion is absorbed or exits the nucleus.

5.1.3 Detector

Once the final state particle kinematics have been determined by NEUT, they are passed into the detector simulation. The near detectors, ND280 and INGRID, are simulated using a `GEANT4` package [43, 175] to simulate the detector geometry, particle tracking, and energy deposition. The response of the detectors is simulated using the elecSim package [43].

The far detector simulation is based upon the original Kamiokande experiment software which uses the `GEANT3`-based SKDETSIM [43, 176] package. This simulates the interactions of particles in the water as well as Cherenkov light production. The water quality and PMT calibration measurements detailed in subsection 3.1.2 are also used within this simulation to make accurate predictions of the detector response.

Any event which generates optical photons that occurs in SK will be observed by the PMT array, where each PMT records the time and accumulated charge. This recorded information is shown in event displays similar to those illustrated in Figure 5.3 for simulated Monte Carlo events. To be useful for physics analyses, this series of PMT hit information needs to be reconstructed to determine the number and identity of particles and their kinematics (or track parameters): four-vertex, direction, and momentum. The reconstruction uses the fact that the charge and timing distribution of photons generated by a particular particle in an event is dependent upon its initial kinematics. Electron and muon rings are distinguished by their “fuzziness”. Muons are heavier and less affected by scattering or showering meaning they typically produce “crisp” rings. Electrons are more likely to interact via electromagnetic showering or scattering which results in larger variations of their direction from the initial direction. Consequently, electrons typically produce “fuzzier” rings compared to muons.

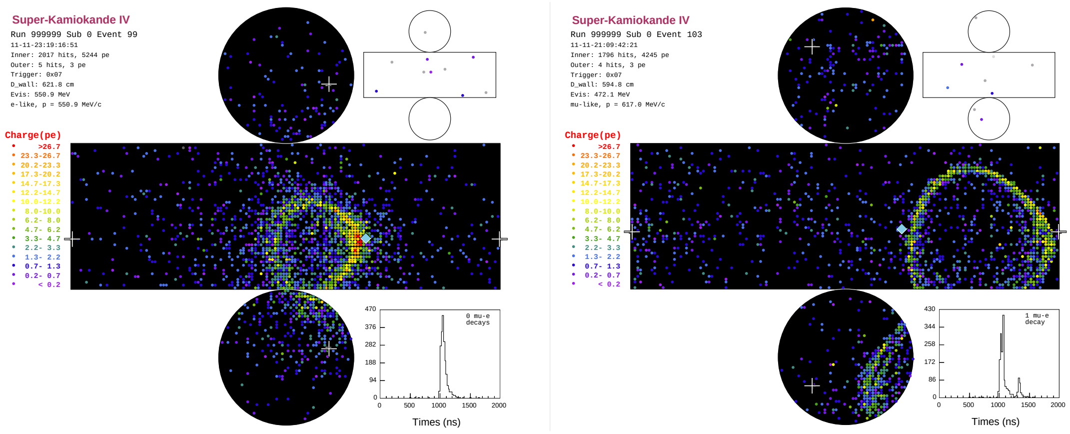

(a) ν_e **(b)** ν_μ

Figure 5.3: Event displays from Monte Carlo simulation at Super Kamiokande illustrating the "crisp" ring from a muon and the typically "fuzzier" electron ring. Each pixel represents a PMT and the color scheme denotes the accumulated charge deposited on that PMT. Figures taken from [177].

5.2 Event Reconstruction at SK

For the purposes of this analysis, the `fiTQun` reconstruction algorithm [178] is utilised. Its core function is to compare a prediction of the accumulated charged and timing distribution from each PMT, generated for a particular particle identity and track parameters, to that observed in the neutrino event. It determines the preferred values by maximising a likelihood function (or minimising a log-likelihood function) which includes information from PMTs which were hit and those that were not hit. The `fiTQun` algorithm is based on the key concepts of the MiniBooNE reconstruction algorithm [179].

The `fiTQun` algorithm improves upon the previous `APFit` algorithm [180] which has been used for many previous SK analyses. `APFit` fits the vertex from timing information and then fits the direction of the particle from PMT hits within a 43 deg Cherenkov cone (assuming an ultra-relativistic particle) using a fitting estimator. A Hough transformation is used to find the radius of a ring (related to the momentum through Equation 3.2) as well as the number of rings contained within the event. The analysis presented here uses the `fiTQun` algorithm as it improves both the accuracy of the fit parameters and the rejection of neutral current π^0 events as compared to `APFit` [181, 182].

Any event in SK can consist of prompt (or primary) and decay (or secondary) particles. For example, a charged current muon neutrino interaction can generate two particles that have the potential of generating Cherenkov photons (assuming the proton is below the Cherenkov threshold): the prompt muon, and the secondary decay-electron from the muon, approximately 2μs later. To reconstruct all particles within an event, it is divided into time clusters which are called "subevents". Subevents after the primary subevent are considered to be decay electrons.

The main steps of the `fiTQun` reconstruction algorithm are:

- **Vertex pre-fitting**: An estimate of the vertex is made using a goodness-of-fit metric based on PMT hit times
- **Peak finding**: The initial time of each subevent is determined by clustering events by time residuals
- **Single-ring fits**: Given the pre-fit vertex and estimated time of interaction, a maximum likelihood technique searches for a single particle generating light. Electron, muon, charged pion, and proton hypotheses are considered
- **Multi-ring fits**: Seeded from the single-ring fits, hypotheses with multiple light-producing particles are considered using the same maximum likelihood technique. Electron-like or charged pion-like rings are added until the likelihood stops improving

To find all the subevents in an event, a vertex goodness metric is calculated for some vertex position $\vec{x}$ and time t,

$$G(\vec{x}, t) = \sum_{i}^{\text{hit PMTs}} \exp\left(-\frac{1}{2}\left(\frac{T^i_{Res}(\vec{x}, t)}{\sigma}\right)^2\right), \tag{5.1}$$

where

$$T^i_{Res}(\vec{x},t) = t^i - t - \left| R^i_{PMT} - \vec{x} \right| / c_n, \tag{5.2}$$

is the residual hit time. It is the difference in time between the PMT hit time t^i, of the i^{th} PMT, and the expected time of the PMT hit if the photon was at the vertex. R^i_{PMT} is the position of the i^{th} PMT, c_n is the speed of light in water and $\sigma = 4$ns which is comparable to the time resolution of the PMT. When the proposed fit values of time and vertex are close to the true values, $T^i_{Res}(\vec{x},t)$ tends to zero resulting in subevents appearing as spikes in the goodness metric. The proposed fit vertex and time are grid-scanned, and the values which maximise the goodness metric are selected as the "pre-fit vertex". Whilst this predicts a vertex for use in the clustering algorithm, the final vertex is fit using the higher-precision maximum likelihood method described below.

Once the pre-fit vertex has been determined, the goodness metric is scanned as a function of t to determine the number of subevents. A peak-finding algorithm is then used on the goodness metric, requiring the goodness metric to exceed some threshold and drop below a reduced threshold before any subsequent additional peaks are considered. The thresholds are set such that the rate of false peak finding is minimised while still attaining good data to Monte Carlo agreement. To improve performance, the pre-fit vertex for each delayed subevent is re-calculated after PMT hits from the previous subevent are masked. This improves the decay-electron tagging performance. Once all subevents have been determined, the time window around each subevent is then defined by the earliest and latest time which satisfies $-180 < T^i_{Res} < 800$ns. The subevents and associated time windows are then used as seeds for further reconstruction.

For a given subevent, the `fiTQun` algorithm constructs a likelihood based on the accumulated charge q_i and time information t_i from the i^{th} PMT,

$$L(\Gamma,\vec{\theta}) = \prod_j^{\text{unhit}} P_j(\text{unhit}|\Gamma,\vec{\theta}) \prod_i^{\text{hit}} \{1 - P_i(\text{unhit}|\Gamma,\vec{\theta})\} f_q(q_i|\Gamma,\vec{\theta}) f_t(t_i|\Gamma,\vec{\theta}). \tag{5.3}$$

Where $\vec{\theta}$ defines the track parameters; vertex position, direction vector and momenta, and Γ represents the particle hypothesis. $P_i(\text{unhit}|\Gamma, \vec{\theta})$ is the probability of the i^{th} tube to not register a hit given the track parameters and particle hypothesis. The charge likelihood, $f_q(q_i|\Gamma, \vec{\theta})$, and time likelihood, $f_t(t_i|\Gamma, \vec{\theta})$, represents the probability density function of observing charge q_i and time t_i on the i^{th} PMT given the specified track parameters and particle hypothesis.

The predicted charge is calculated based on contributions from both the direct light and the scattered light. The direct light contribution is determined based on the integration of the Cherenkov photon profile along the track. PMT angular acceptance, water quality, and calibration measurements discussed in subsection 3.1.2 are included to accurately predict the charge probability density at each PMT. The scattered and reflected light is calculated in a similar way, although it includes a scattering function that depends on the vertex of the particle and the position of the PMT. The charge likelihood is calculated by comparing the prediction to the observed charge in the PMT which is tuned to the PMT simulation.

The time likelihood is approximated to depend on the vertex $\vec{x}$, direction $\vec{d}$, and time t of the track as well as the particle hypothesis. The expected time for PMT hits is calculated by assuming unscattered photons being emitted from the midpoint of the track, S_{mid},

$$t^i_{exp} = t + S_{mid}/c + |R^i_{PMT} - \vec{x} - S_{mid}\vec{d}|/c_n, \tag{5.4}$$

where c is the speed of light in a vacuum. The time likelihood is then expressed in terms of the residual difference between the PMT hit time and the expected hit time, $t^i_{Res} = t^i - t^i_{exp}$. The particle hypothesis and momentum also affect the Cherenkov photon distribution. These parameters modify the shape of the time likelihood density since in reality not all photons are emitted at the midpoint of the track. As with the charge likelihood, the contributions from both the direct and scattered light to the time likelihood density are calculated separately, which are both calculated from particle gun Monte Carlo studies.

The track parameters and particle identity which maximise $L(\Gamma, \vec{\theta})$ are defined as the best-fit parameters. In practice MINUIT [183] is used to minimise the value of $-\ln L(\Gamma, \vec{\theta})$. The `fiTQun` algorithm considers an electron-like, muon-like, and charged pion-like hypothesis for events with a single final state particle, denoted "single-ring events". The particle's identity is determined by taking the ratio of the likelihood of each of the hypotheses. For instance, electrons and muons are distinguished by considering the value of $\ln\left(L(e, \vec{\theta}_e)/L(\mu, \vec{\theta}_\mu)\right)$ in comparison to the reconstructed momentum of the electron hypothesis, as illustrated by Figure 5.4. The coefficients of the discriminator between electron-like and muon-like events are determined from Monte Carlo studies [178]. Similar distributions exist for distinguishing electron-like events from π^0-like events, and muon-like events from pion-like events. The cuts are defined as,

$$\begin{aligned} \text{Electron/Muon} &: \ln(L_e/L_\mu) > 0.2 \times p_e^{rec}[\text{MeV}], \\ \text{Electron}/\pi^0 &: \ln(L_e/L_{\pi^0}) < 175 - 0.875 \times m_{\gamma\gamma}[\text{MeV}], \\ \text{Muon/Pion} &: \ln(L_\mu/L_{\pi^\pm}) < 0.15 \times p_\mu^{rec}[\text{MeV}], \end{aligned} \tag{5.5}$$

as taken from [184], where p_e^{rec} and p_μ^{rec} are the reconstructed momentum of the single-ring electron and muon fits, respectively. $m_{\gamma\gamma}$ represents the reconstructed invariant mass of the two photons emitted from π^0 decay. Typically, the distance between a particular entry in these two-dimensional distributions and the cut-line is termed the PID parameter and is illustrated in Figure 5.5.

The `fiTQun` algorithm also considers a π^0 hypothesis. To do this, it performs a fit looking for two standard electron-hypothesis tracks which point to the same four-vertex. This assumes the electron tracks are generated from photon-conversion so the electron tracks actually appear offset from the proposed π^0 vertex. For these fits, the conversion length, direction, and momentum of each photon are also considered as track parameters which are then fit in the same methodology as the standard single-ring hypotheses.

Whilst lower energy events are predominantly single-ring events, higher energy neutrino events can generate final states with multiple particles which

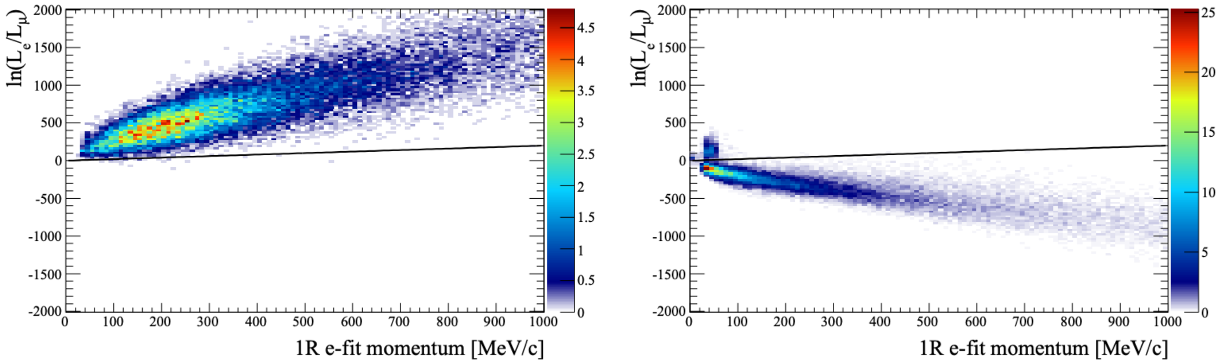

Figure 5.4: The difference of the electron-like and muon-like log-likelihood compared to the reconstructed single-ring fit momentum for atmospheric ν_e (left) and ν_μ (right) samples. The black line represents the cut used to discriminate electron-like and muon-like events, with coefficients obtained from Monte Carlo studies. Figures from [178].

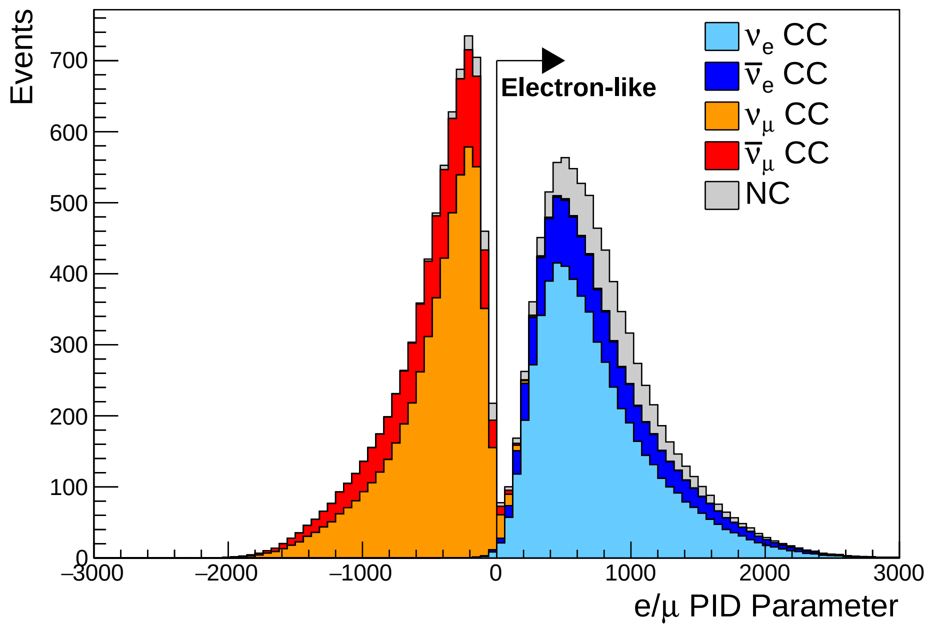

Figure 5.5: The electron/muon PID separation parameter for all sub-GeV single-ring events in SK-IV. The charged current (CC) component is broken down in four flavours of neutrino (ν_μ, $\bar{\nu}_\mu$, ν_e and $\bar{\nu}_e$). Events with positive values of the parameter are determined to be electron-like.

generate Cherenkov photons. These "multi-ring" hypotheses are also considered in the fiTQun algorithm. When calculating the charge likelihood density, the predicted charge associated with each ring is calculated separately and then summed to calculate the total accumulated charge on each PMT. Similarly, the time likelihood for the multi-ring hypothesis is calculated assuming each ring is independent. Each track is time-ordered based on the time of flight from the center of the track to the PMT and the direct light from any ring incident on the PMT is assumed to arrive before any scattered light. To reduce computational resource usage, the multi-ring fits only consider electron-like and charged pion-like rings as the pion fit can be used as a proxy for a muon fit due to their similar mass. Due to the pions ability to interact through the strong force, they are more likely to hard-scatter. That means a single charged pion can produce multiple rings in different directions. There is an additional freedom, the fraction of kinetic energy lost in a single ring segment, which is added into the `fiTQun` pion fit to cover this difference. Pion and muon rings are indistinguishable when this fraction tends to unity.

Multi-ring fits proceed by proposing another ring to the previous fit and then fitting the parameters in the method described above. Typically, multi-ring fits have the largest likelihood because of the additional degrees of freedom introduced. A likelihood value is calculated for the n-ring and $(n+1)$-ring hypotheses, where the additional ring is only included if the likelihood value is above 9.35, based on Monte Carlo studies in [185].

5.2.1 Validation of Reconstruction in SK-V

Understanding how the modelling of the detector conditions and stability effects the reconstruction is critical for ensuring accurate measurements. It is important to note that the detector systematics used in the 2020 T2K-only [75] oscillation analysis are determined using data-to-Monte Carlo comparisons of the SK-IV data [186]. Due to tank-open maintenance occurring between SK-IV and SK-V, the dark rate of each PMT was observed to increase in SK-V due to light exposure for a significant time during the repairs. This increase can be seen in Figure 5.6. Run-10 of the T2K experiment was conducted in the SK-V period, so the consistency of SK-IV and SK-V data needs to be studied to determine whether the SK-IV-defined systematics can be applied to the run-10 data. Consequently, the author of this thesis assessed the quality of `fiTQun` event reconstruction for SK-V data.

This comparison study was performed using the stopping muon data set for both the SK-IV and SK-V periods. This data sample is used due to the high rate of interactions ($O(200)$ events per hour) as well as having similar energies to muons from CCQE ν_μ interactions from beam interactions. The rate of cosmic muons does depend on the solar activity cycle [187] but has been neglected in this comparison study. This is because the shape of the distributions is most important for the purposes of being compared to the detector systematics. The SK-IV and SK-V data samples consist of 2398.42 and 626.719 hours of data which equates to 686k and 192k events respectively. These samples do not correspond to the full data sets of either period but do contain enough events to be systematics limited rather than statistics limited.

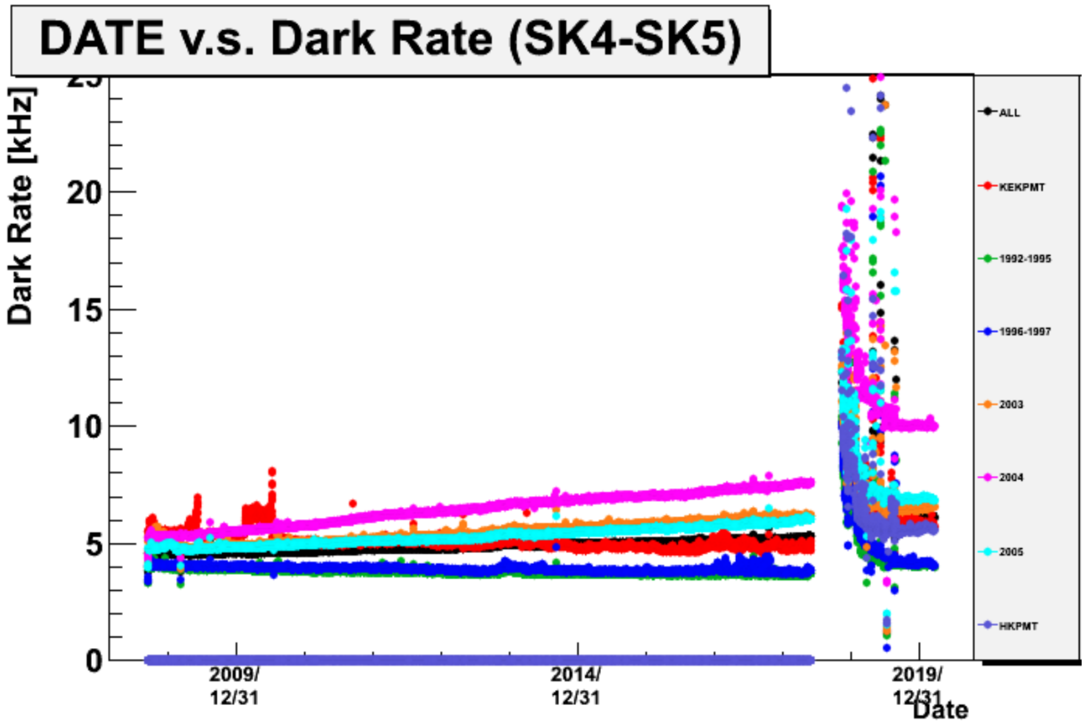

Figure 5.6: The variation of the measured dark rate as a function of date, broken down by PMT type. The SK-IV and SK-V periods span September 2008 to May 2018 and January 2019 to July 2020, respectively. The break in measurement in 2018 corresponds to the period of tank repair and refurbishment. Figure adapted from [186].

The predicted charge calculated in the `fiTQun` algorithm includes a contribution from the photoelectron emission due to dark noise. Therefore, the increase in the SK-V dark rate needs to be accounted for. In practice, the average dark rate in each SK period is calculated and used as an input in the reconstruction. This is calculated by averaging the dark rate per run for each period separately, using the calibration measurements detailed in subsection 3.1.2. The average dark rate from SK-IV and SK-V were found to be 4.57kHz and 6.30kHz, respectively. The charges associated with the muon and decay electron subevents are illustrated in Figure 5.7. The photoelectron emission from dark noise is more significant for events that have lower energy. This is because this contribution becomes more comparable to the number of photoelectrons emitted from incident photons in lower-energy events. This behaviour is observed in the data, where the charge deposited by the muon subevent is mostly unaffected by the increase in dark rate, whilst the charge associated with the decay-electron is clearly affected.

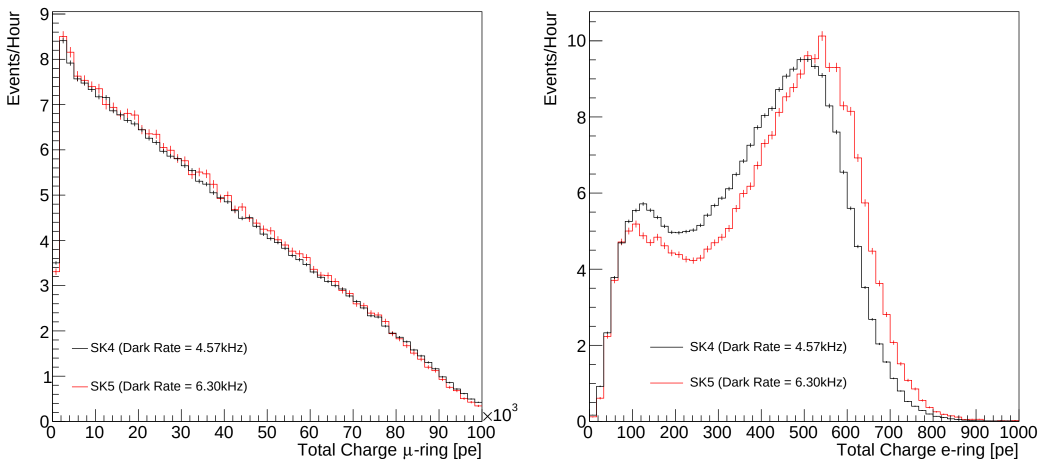

(a) Muon **(b)** Decay Electron

Figure 5.7: Comparison of the measured raw charge deposited per event from the stopping muon data samples between SK-IV (Blue) and SK-V (Red), split by the primary muon subevent (left) and the associated decay electron subevent (right).

The energy scale systematic is estimated from data-to-Monte Carlo differences in the stopping muon sample in [188] and found to be 2.1%. To determine the consistency of SK-IV and SK-V with respect to the energy scale systematic, the muon momentum distribution is compared between the two SK periods. As the total number of Cherenkov photons is integrated across the track length, the reconstructed momentum divided by track length (or range) is compared between SK-IV and SK-V as illustrated in Figure 5.8.

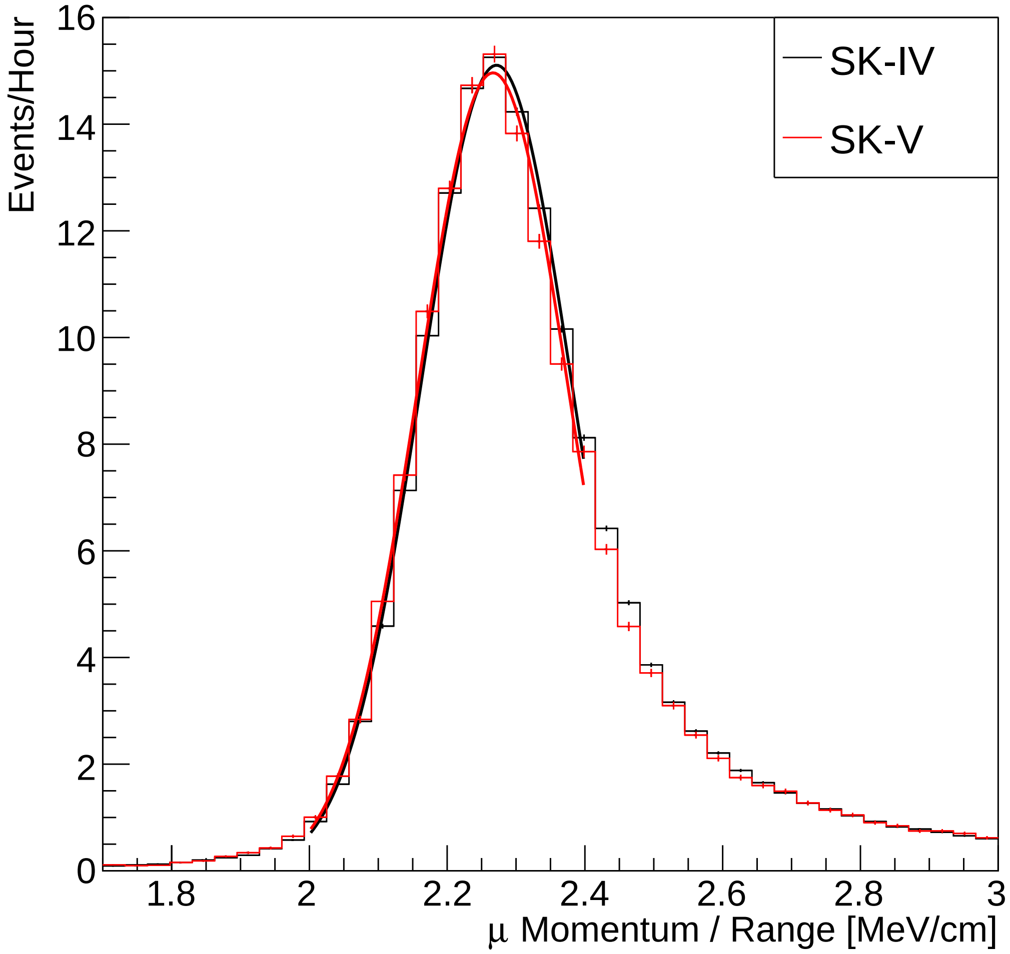

Figure 5.8: The distribution of the reconstructed momentum from the muon ring divided by the distance between the reconstructed muon and decay electron vertices as found in the stopping muon data sets of SK-IV (Black) and SK-IV (Red). Only events with one tagged decay electron are considered. A Gaussian fit is considered in the range $[2.0, 2.4]$MeV/cm and illustrated as the solid curve.

The consistency between these muon distributions has been computed in two ways. Firstly, a Gaussian is fit to the peak of each distribution separately, whose mean is found to be (2.272 ± 0.003)MeV/cm and (2.267 ± 0.006)MeV/cm for SK-IV and SK-V respectively. The ratio of these is equal to 1.002 ± 0.003. The means of the Gaussian fits are consistent with the expected stopping power of a minimum ionising muon for a target material (water) with $Z/A \sim 0.5$ [189]. The second consistency check is performed by introducing a nuisance parameter, α, which modifies the SK-V distribution. The value of α which minimises the χ^2 value between the SK-IV and SK-V is determined by scanning across a range of values. This is repeated by applying the nuisance parameter as both a multiplicative factor and an additive shift. The χ^2 distributions for different values of α is illustrated in Figure 5.9. The values which minimise the χ^2 are found to be 0.0052 and 1.0024 for the additive and multiplicative implementations, respectively. No evidence of shifts larger than the 2.1% uncertainty on the energy scale systematic has been found in the reconstructed momentum distribution of SK-IV and SK-V.

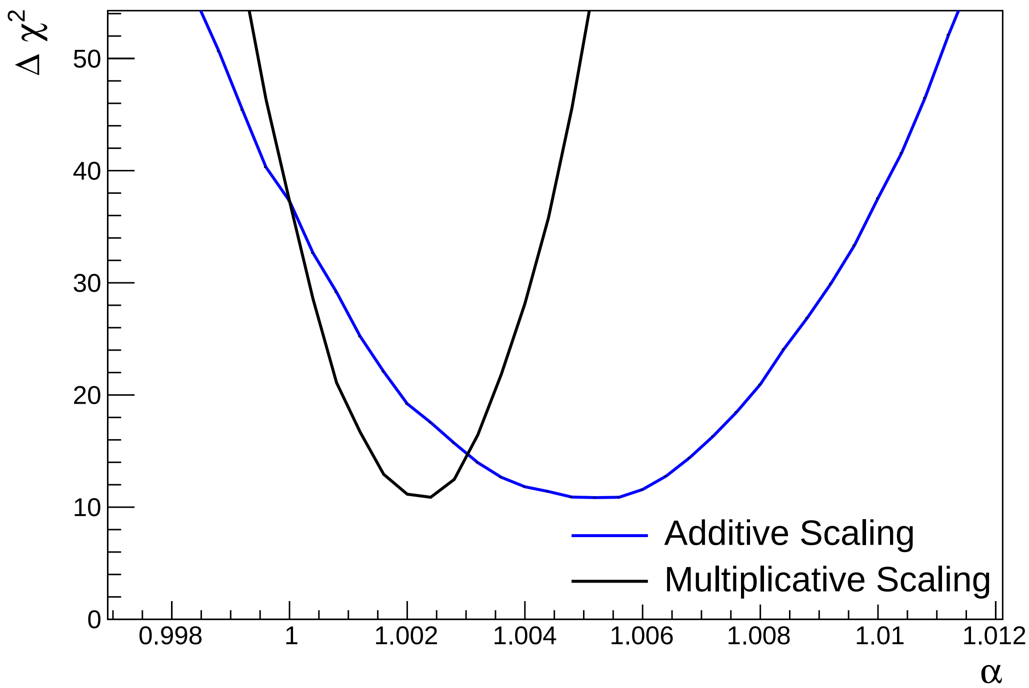

Figure 5.9: The χ^2 difference between the SK-IV and SK-V reconstructed muon momentum divided by range when the SK-V is modified by the scaling parameter α. Both additive (Blue) and multiplicative (Black) scaling factors have been considered. In practice, the additive scaling factor actually uses the value of $(\alpha - 1.0)$ but is illustrated like this so the results can be shown on the same axis range.

5.3 Event Reduction at SK

In normal data-taking operations, the SK detector observes many background events alongside the beam and atmospheric neutrino signal events of physics interest for this thesis. Cosmic ray muons and flasher events, which are the spontaneous discharge of a given PMT, contribute the largest amount of background events in the energy range relevant to this thesis. Therefore the data recorded is reduced with the aim of removing these background events. The reduction process is detailed in [55, 88] and briefly summarised below.

Atmospheric neutrino events observed in the SK detector are categorised into three different types of samples: fully contained (FC), partially contained (PC) and up-going muon (Up-μ), using PMT hit signatures in the inner and outer detector (ID and OD, respectively). To identify FC neutrino events, it is required that the neutrino interacts inside the fiducial volume of the ID and that no significant OD activity is observed. For this analysis, an event is defined to be in the fiducial volume provided the event vertex is at least 0.5m away from the ID walls. PC events have the same ID requirements but can have a larger signal present inside the OD. Typically, only high energy muons from ν_μ interactions can penetrate the ID wall. The Up-μ sample contains events where muons are created from neutrino interactions in the OD water or rock below the tank. They then propagate upwards through the detector. Downward-going muons generated from neutrino interactions above the tank are neglected because of the difficulty in separating their signature from the cosmic muon shower background. The sample categories are visually depicted in Figure 5.10.

Based on the event characteristics, as defined by the `fiTQun` event reconstruction software, the FC events are categorised by

- **Visible Energy**: equal to the sum of the reconstructed kinetic energy of particles above the Cerenkov threshold for all rings present in the event. The purpose is to separate events into sub-GeV and multi-GeV categories.

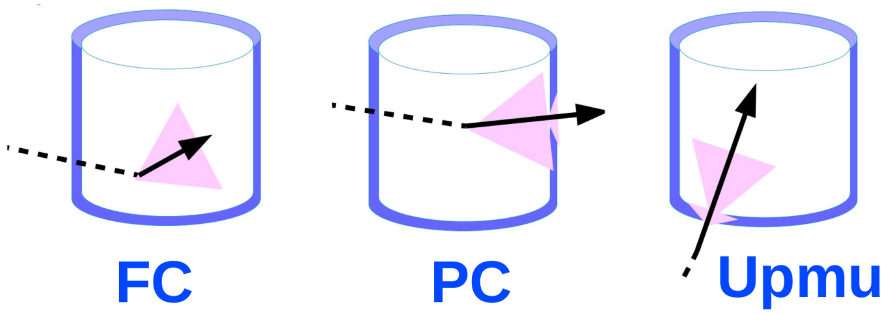

Figure 5.10: A depiction of the topology patterns for fully-contained (FC), partially-contained (PC), and up-going muon (Up-μ) samples included in this analysis.

- **Number of observed Cerenkov rings**. The purpose is to separate single-ring and multi-ring events, where single-ring events predominantly consist of quasi-elastic interactions and multi-ring events are typically resonant pion production or deep inelastic scattering events.
- **Particle identification parameter of the most energetic ring**: A value determined from the maximum likelihood value based on `fiTQun`'s electron, muon, or pion hypothesis. The purpose is to separate electron-like and muon-like events.
- **Number of decay electrons**: The purpose is to separate quasi-elastic events (which have one decay electron emitted from the muon decay) and resonant pion production events (which have two decay electrons emitted from the muon and pion).

The PC and Up-μ categories are broken down into "through-going" and "stopping" samples depending on whether the muon leaves the detector. This is because the PC stopping events deposit the entire energy of the interaction into the detector, resulting in better reconstruction. The energy of events that exit the detector has to be estimated, with a typically worse resolution, which introduces much larger systematic uncertainties. Through-going Up-μ samples are further broken down by whether any hadronic showering was observed in the event which typically indicates DIS interactions. The expected neutrino energy for the different categories is given in Figure 5.11. FC sub-GeV and multi-GeV events peak around 0.7GeV and 3GeV respectively, with slightly different peak energies for ν_e and ν_μ oscillation channels. PC and Up-μ are almost entirely comprised of ν_μ events and peak around 7GeV and 100GeV, respectively.

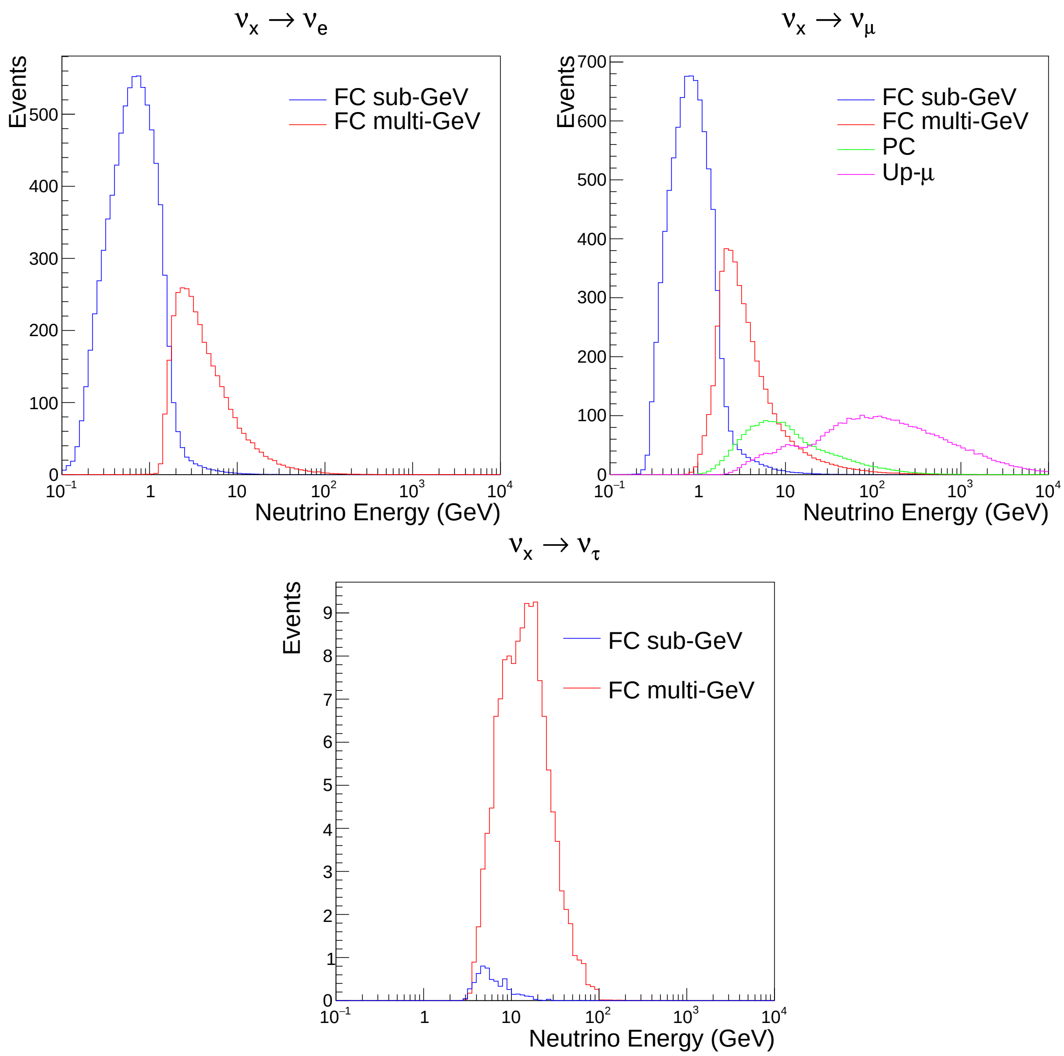

Figure 5.11: The predicted neutrino flux of the fully contained (FC) sub-GeV and multi-GeV, partially contained (PC), and upward-going muon (Up-μ) events. The prediction is broken down by the $\nu_x \to \nu_e$ prediction (top left), $\nu_x \to \nu_\mu$ prediction (top right) and $\nu_x \to \nu_\tau$ prediction (bottom). ν_x represents the flavours of neutrinos produced in the cosmic ray showers (electron and muon). Asimov A oscillation parameters are assumed (given in Table 2.2).

The first two steps in the FC reconstruction remove the majority of cosmic ray muons by requiring a significant amount of ID activity compared to that measured in the OD. Events that pass this cut are typically very high momentum muons or events that leave very little activity in the OD. Consequently, a third reduction step is then applied to select cosmic-ray muons that pass the initial reduction step. A purpose-built cosmic muon fitter is used to determine the entrance (or exit) position of the muon and a cut is applied to OD activity contained within 8m of this position. Flasher events are removed in the fourth reduction step which is based on the close proximity of PMT hits surrounding the PMT producing the flash. Events that pass all these reduction steps are reconstructed with the `APFit` algorithm. The fifth step of the reduction uses information from the more precise fitter to repeat the previous two steps with tighter cuts. Muons below the Cherenkov threshold can not generate optical photons in the ID but the associated decay electron can due to its lower mass. These are the types of events targeted in the fifth reduction step. The final cuts require the event vertex to be within the fiducial volume (0.5m from the wall although the nominal distance is 2.0m), visible energy $E_{vis} > 30$MeV and fewer than 16 hits within the higher energy OD cluster. The culmination of the fully contained reduction results in 8.09 events/day in the nominal fiducial volume [84]. The uncertainty in the reconstruction is calculated by comparing Monte Carlo prediction to data. The largest discrepancy is found to be 1.3% in the fourth reduction step.

The PC and Up-μ events are processed through their own reduction processes detailed in [55]. Both of these samples are reconstructed with the `APFit` algorithm rather than `fiTQun`. This is because the efficiency of reconstructing events that leave the detector has not been sufficiently studied for reliable systematic uncertainties with `fiTQun`. The PC and Up-μ samples acquire events at approximately 0.66 and 1.44 events/day.

Beam neutrinos events undergo the same reduction steps as FC events and are then subject to further cuts [190]. The GPS system that links the timing between the beam facility and SK needs to be operating correctly and there should be no activity within the detector in the previous 100μs before the trigger. The events then need to triggered between -2μs and 10μs of the expected spill timing.

The beam neutrino samples are not split by visible energy since their energy range is smaller than the atmospheric neutrino events. Following the T2K analysis in [75], only single-ring beam neutrino events are considered. Similar to atmospheric event selection, the number of decay electrons is used as a proxy for distinguishing CCQE and CCRES events. The expected neutrino energy, broken down by the number of decay electrons, is given in Figure 5.12.

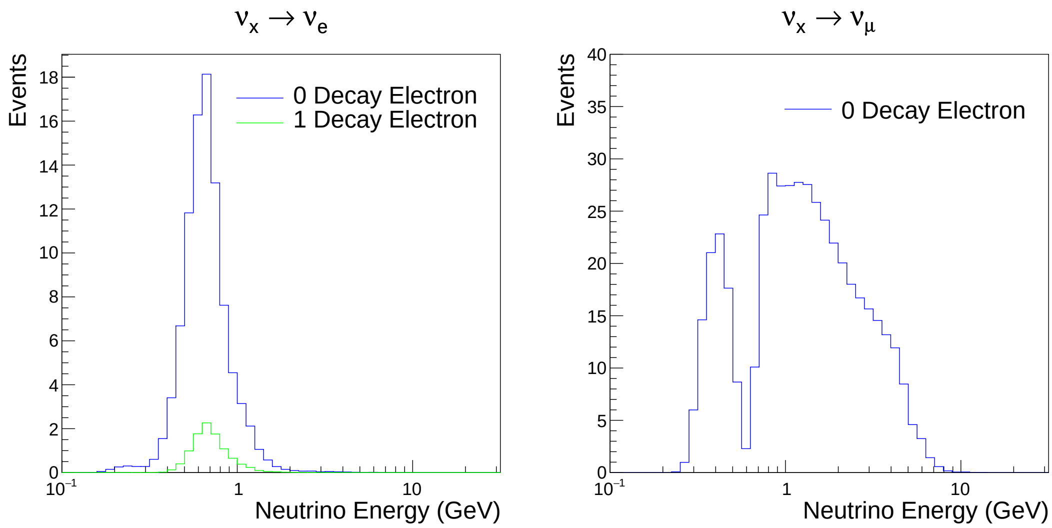

Figure 5.12: The predicted flux of beam neutrinos, as a function of neutrino energy. The predictions are broken down by the number of decay electrons associated with the particular events. Asimov A oscillation parameters are assumed (given in Table 2.2).

6

Sample Selections and Systematics

The oscillation analysis presented within this thesis is built upon a simultaneous fit to atmospheric data at SK, neutrino beam data in the near detector, and beam data measured at SK. This is the first simiultaneous oscillation analysis of beam and atmospheric samples supported by the T2K and SK collaborations. Notably, the author of this thesis has been responsible for the building and developing the `MaCh3` framework to support all sets of samples simultaneously. The definitions of the samples are documented in section 6.1, section 6.2, and section 6.3, respectively. The data collected and used within this analysis is detailed in Table 6.1. The near and far detector data corresponds to T2K runs 2-9 and runs 1-10, respectively. The accumulated POT and beam power for runs $1-10$ are illustrated in Figure 6.1.

Data Type	Total
Near Detector FHC	1.15×10^{21}POT
Near Detector RHC	8.34×10^{20}POT
Far Detector FHC	1.97×10^{21}POT
Far Detector RHC	1.63×10^{21}POT
Atmospheric SK-IV	3244.4 days

Table 6.1: The amount of data collected in each detector used within this analysis. The data collected at the near and far detector, for both neutrino beam (FHC) and antineutrino beam (RHC), is measured as the number of protons on target (POT).

The difference in POT recorded at the near and far detector is due to the difference in downtime. The SK detector is very stable with almost 100% of data recorded during beam operation. Due to various technical and operational issues, the downtime of the near detector is significantly higher due to its more complex design and operating requirements.

The systematic parameters invoked within the flux, detector, and interaction models used within this analysis are documented in section 6.4. The standard configuration of the joint beam and atmospheric data fit utilises far detector systematics provided in the official inputs from the two experiments. Additionally, a correlated detector model which fits the parameters used in sample selections to data has been developed and documented in subsection 6.4.5.

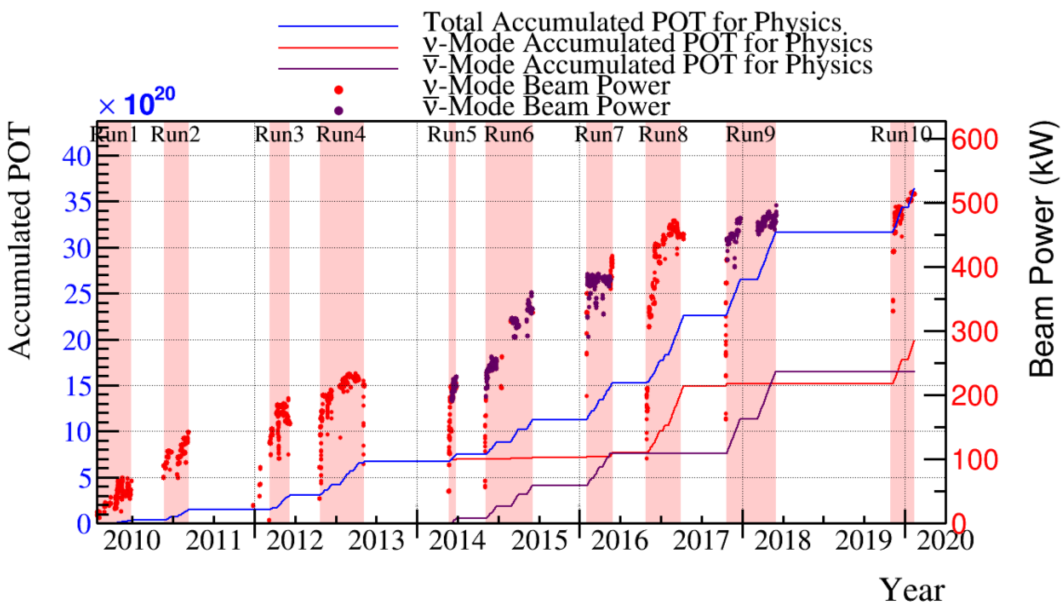

Figure 6.1: The accumulated beam data, measured as the number of protons on target (POT). The total data (blue) is given which comprises of the neutrino beam (red) and antineutrino (purple) components. The beam power for neutrino and antineutrino beams is given as the markers using the same colour scheme. The timescale runs from Run 1 which started in January 2010 until Run 10 which ended in February 2020. The ratio of accumulated data in neutrino and antineutrino beam is 54.7% : 45.3%.

6.1 Atmospheric Samples

The atmospheric event selection follows the official SK-IV analysis presented in [88] and is documented below. The Monte Carlo prediction used within this analysis corresponds to 500 years worth of neutrino events, which is scaled down to match the SK-IV livetime of 3244.4 days.

The fully contained (FC), partially contained (PC), and upward going muon events (up-μ) which pass the reduction cuts discussed in section 5.3 are further broken down into different samples based on reconstruction information. This section details the samples used within this oscillation analysis, alongside the chosen binning.

FC events are first separated by the visible energy deposited within the detector. This is calculated as the sum of the reconstructed kinetic energy above the Cherenkov threshold for all rings present in the event. Events are separated by whether they were above or below $E_{vis} = 1.33$GeV. This separates "subGeV" and "multiGeV" events. Typically, lower energy events consist of charged current quasi-elastic (CCQE) interactions which are better understood and simpler to reconstruct resulting in smaller systematic uncertainties. Events are further separated by the number of rings associated with the event due to similar reasoning. As the oscillation probability is dependant upon the flavour of neutrino, electron and muon events are separated using a similar likelihood method to that discussed in section 5.2. To reduce computational resources required for the reconstruction, only electron and pion hypotheses are considered so this separation cut depends on the ratio of the electron to pion likelihoods, $\log(L_e/L_\pi)$. Finally, the number of decay electrons is used to classify events. Charged current resonant pion production (CCRES) interactions generate a final-state pion. This can decay, mostly likely through a muon, into a decay electron. Therefore any electron-like event with one decay electron or muon-like event with two decay electrons was most likely produced by a CCRES interaction. Consequently, the number of decay electrons can be used to distinguish CCQE and CCRES interaction modes. Ultimately, FC subGeV events are separated into the samples listed in Table 6.2.

Sample Name	Description
`SubGeV-elike-0dcy`	Single ring e-like events with zero decay electrons
`SubGeV-elike-1dcy`	Single ring e-like events with one or more decay electrons
`SubGeV-mulike-0dcy`	Single ring μ-like events with zero decay electrons
`SubGeV-mulike-1dcy`	Single ring μ-like events with one decay electrons
`SubGeV-mulike-2dcy`	Single ring μ-like events with two or more decay electrons
`SubGeV-pi0like`	Two e-like ring events with zero decay electrons and reconstructed π^0 mass $85 \leq m_{\pi^0} < 215$MeV

Table 6.2: The fully contained subGeV samples, defined as events with visible energy$E_{vis} < 1.33$GeV, used within this oscillation analysis.

In addition to the cuts discussed above, multiGeV samples also have additional cuts to separate samples which target neutrino and antineutrino events. As discussed in section 2.5, the matter resonance only occurs for neutrinos in the normal hierarchy and antineutrinos in the inverted mass hierarchy. Therefore, having flavour-enriched samples aids in the determination of the mass hierarchy. For a CCRES interaction,

$$\begin{aligned}
&\bar{\nu}_e + N \rightarrow e^+ + N^{'} + \pi^-, \\
&\nu_e + N \rightarrow e^- + N^{'} + \pi^+ \\
&\qquad\qquad\qquad\quad \hookrightarrow \mu^+ + \nu_\mu \\
&\qquad\qquad\qquad\qquad\quad \hookrightarrow e^+ + \nu_e + \bar{\nu}_\mu.
\end{aligned} \tag{6.1}$$

The π^- emitted from a $\bar{\nu}_e$ interaction is more likely to be captured by an oxygen nucleus than the π^+ from ν_e interactions [191]. These pions then decay, mostly through muons, to electrons. Therefore the number of tagged decay electrons associated with an event gives an indication of whether the interaction was due to a neutrino or antineutrino: zero for $\bar{\nu}_e$ events, and one for ν_e events. The ability to separate neutrino from antineutrino events is illustrated in Table 6.4, where the `MultiGeV-elike-nue` has 78% purity of CC neutrino interactions with only 7% antineutrino background, the rest consisting of NC backgrounds.

The number of decay electrons discriminator works reasonably well for single-ring events. However, this is not the case for multi-ring events. A multiGeV multiring electron-like (MME) likelihood cut was introduced in [192, 193]. This is a two-stage likelihood selection cut. Four observables are used in the first likelihood cut to distinguish CCν_e and CC$\bar{\nu}_e$ events from background:

- The number of decay electrons
- The maximum distance between the vertex of the neutrino and the decay electrons
- The energy deposited by the highest energy ring
- The particle identification of that highest energy ring

Background events consist of CCν_μ and NC interactions. Typically, the majority of the energy in these background events is carried by the hadronic system. Additionally, muons tend to travel further than the pions from CCν_e before decaying. Thus, the parameters used within the likelihood cut target these typical background interaction kinematics.

Sample Name	Description
`MultiGeV-elike-nue`	Single ring e-like events with zero decay electrons
`MultiGeV-elike-nuebar`	Single ring e-like events with one or more decay electrons
`MultiGeV-mulike`	Single ring μ-like events
`MultiRing-elike-nue`	Two or more ring events with leading energy e-like ring and passed both MME and $\nu/\bar{\nu}$ separation cuts
`MultiRing-elike-nuebar`	Two or more ring events with leading energy e-like ring and passed MME and failed $\nu/\bar{\nu}$ separation cuts
`MultiRing-mulike`	Two or more ring events with leading energy μ-like ring and only requires $E_{vis} > 0.6$GeV
`MultiRing-Other1`	Two or more ring events with leading energy e-like ring and failed the MME likelihood cut

Table 6.3: The fully contained multiGeV samples used within this oscillation analysis. Both the sample name and description are given.

Neutrino and antineutrino events are then separated by a second likelihood method ($\nu/\bar{\nu}$ separation) detailed in [60]. This uses the number of decay electrons, the number of reconstructed rings, and the event's transverse momentum. The last two parameters are used because higher-energy samples tend to have more pions produced above the Cherenkov threshold which results in more rings compared to an antineutrino interaction. Furthermore, the angular distribution also tends to be more forward peaked in antineutrino interactions as compared to neutrino interactions [88]. These FC multiGeV sample definitions are detailed in Table 6.3.

The PC and up-μ samples are split by the amount of energy deposited within the outer detector, into "stopping" and "through-going" samples. If an event leaves the detector, the energy it takes with it has to be estimated which increases the systematic uncertainty compared to events entirely contained within the inner detector. This estimation is particularly poor at high energies, thus the up-μ through-going events are not binned in reconstructed momentum. The through-going up-μ are further separated by the presence of any electromagnetic showering in the event, as the assumption of non-showering muon does not give reliable reconstruction for these types of events [55]. In total, 13 FC, 2 PC, and 3 up-μ atmospheric samples are included within this analysis.

The atmospheric samples are binned in direct observables: reconstructed lepton momentum and direction, as given by Table A.1. The distribution of the reconstructed lepton momentum (for samples that only have one bin in reconstructed zenith angle) and reconstructed direction for each atmospheric sample used within this analysis is illustrated in Figure 6.2. The by-mode breakdown of each of the atmospheric samples is given in Appendix A.

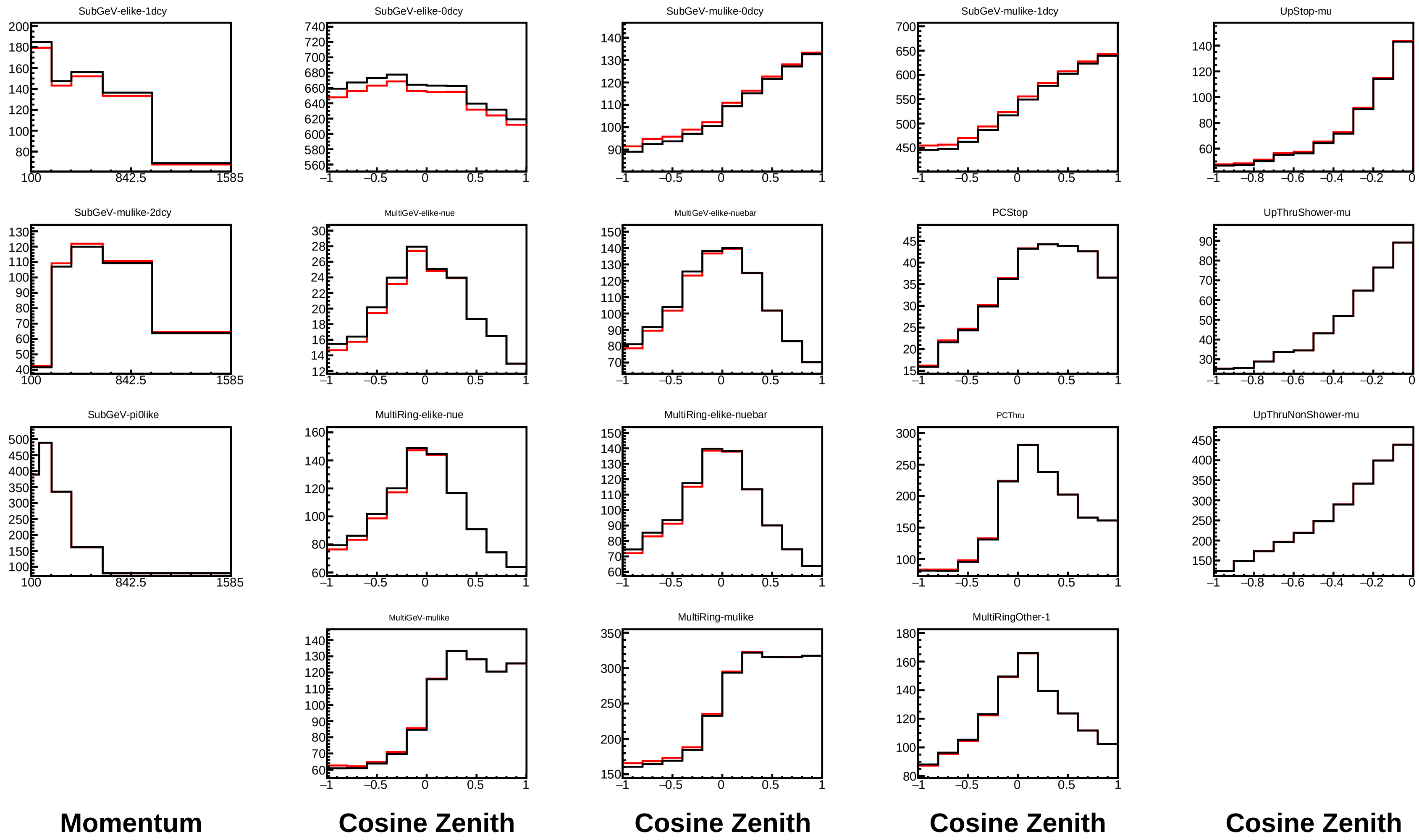

Figure 6.2: Comparison of the SK-IV atmospheric samples between predictions made with the CP-violating Asimov A (Black) and CP-conserving Asimov B (Red) oscillation parameter sets (given in Table 2.2). The subGeV samples CCRES and π^0-like samples are given in their reconstructed lepton momentum. All other samples are presented in their reconstructed zenith angle projection.

Sample	CCν_e	CC$\bar{\nu}_e$	CC($\nu_\mu + \bar{\nu}_\mu$)	CC($\nu_\tau + \bar{\nu}_\tau$)	NC
`SubGeV-elike-0dcy`	72.17	23.3	0.724	0.033	3.77
`SubGeV-elike-1dcy`	86.81	1.773	7.002	0.062	4.351
`SubGeV-mulike-0dcy`	1.003	0.380	90.07	0.036	8.511
`SubGeV-mulike-1dcy`	0.023	0.	98.46	0.029	1.484
`SubGeV-mulike-2dcy`	0.012	0.	99.25	0.030	0.711
`SubGeV-pi0like`	6.923	2.368	0.928	0.011	89.77
`MultiGeV-elike-nue`	78.18	7.041	3.439	1.886	9.451
`MultiGeV-elike-nuebar`	56.68	37.81	0.174	0.614	4.718
`MultiGeV-mulike`	0.024	0.005	99.67	0.245	0.058
`MultiRing-elike-nue`	59.32	12.39	4.906	3.385	20
`MultiRing-elike-nuebar`	52.39	31.03	1.854	1.585	13.14
`MultiRing-mulike`	0.673	0.080	97.33	0.342	1.578
`MultiRingOther-1`	27.98	2.366	34.93	4.946	29.78
`PCStop`	8.216	3.118	84.45	0.	4.214
`PCThru`	0.564	0.207	98.65	0.	0.576
`UpStop-mu`	0.829	0.370	98.51	0.	0.289
`UpThruNonShower-mu`	0.206	0.073	99.62	0.	0.103
`UpThruShower-mu`	0.128	0.054	99.69	0.	0.132

Table 6.4: The purity of each atmospheric sample used within this analysis, broken down by charged current (CC) and neutral current (NC) interactions and which neutrino flavour interacted within the detector. Each row sums to 100% by definition. Asimov A oscillation parameter sets are assumed (given in Table 2.2). Electron neutrino and antineutrino events are separated to illustrate the ability of the separation likelihood cuts used within the multiGeV and multiring sample selections.

6.2 Near Detector Beam Samples

The near detector sample selections are documented in detail within [194] and summarised below. Samples are selected based upon which of the two Fine Grained Detector (FGD) the vertex is reconstructed in as well as the operating mode of the beam: FHC or RHC. Wrong-sign neutrino background samples are considered in the RHC mode in order to add additional constraints on model parameters. Samples from the wrong-sign component of the FHC beam mode are not included as they are statistically insignificant compared to those samples already listed.

The reconstruction algorithm uses a clustering algorithm to group hits within the TPC. It then adds information from the upstream FGD to form a track that passes through both sub-detectors. In FHC(RHC), the highest momentum negative(positive) curvature track is defined as the muon candidate. Before being assigned a sample, these candidate muon events must pass CC-inclusive cuts, as defined in [195]:

- Event Timing: The DAQ must be operational and the event must occur within the expected beam time window consistent with the beam spill
- TPC Requirement: The muon-candidate track path must intercept one or more TPCs
- Fiducial volume: The event must originate from within the fiducial volume defined in [196]
- Upstream Background: Remove events that have muon tracks that originate upstream of the FGDs by requiring no high-momentum tracks within 150mm upstream of the candidate vertex. Additionally, events that occur within the downstream FGD are vetoed if a secondary track starts within the upstream FGD

- Broken track removal: All candidates where the muon candidate is broken in two are removed

- Muon PID: Measurements of dE/dx in a TPC are used to distinguish muon-like events, from electron-like or proton-like, using a likelihood cut

In addition to these cuts, RHC neutrino events also have to undergo the following cuts to aid in the separation of neutrino and antineutrino [197]:

- TPC Requirement: The track path must intercept TPC2

- Positive Track: The highest momentum track must have a positive reconstructed charge

- TPC1 Veto: Remove any events originating upstream of TPC1

Once all CC-inclusive events have been determined, they are further split by pion multiplicity: CC0π, CC1π, and CCOther. This breakdown targets the specific interaction modes CCQE, CCRES, and other CC background interactions, respectively. Pions in the TPCs and FGDs are selected by requiring a second track to be observed, which is separate from the muon track and is in the same beam spill window and sub-detector. If the pion originated within a FGD, it must also pass through the sequential downstream TPC (TPC2 for FGD1, TPC3 for FGD2).

CC0π, CC1π, and CCOther samples are defined with the following cuts:

DB: Understand pion cuts at ND

- ν_μ**CC0**π **Selection**: No electrons in TPC and no charged pions or decay electrons within the TPC or FGD

- ν_μ**CC1**π **Selection**: Exactly one charged pion in either the TPC or FGD, where the number of charged pions in the FGD is equal to the number of decay electrons

- ν_μ**CCOther Selection**: All events which are not classified into the above two selections

Counting the three selections for each FGD in FHC and RHC running, including the wrong-sign background in RHC, 18 near detector samples are used within this analysis. These samples are binned in reconstructed lepton momentum (illustrated in Figure 6.3) and direction with respect to the beam. The binning is chosen such that each event has at least 20 Monte Carlo events in each bin [196]. This is to ensure that the bins are coarse enough to ensure the reduction of statistical errors, whilst also being fine enough to sample the high-resolution peak regions. The exact binning is detailed in [196].

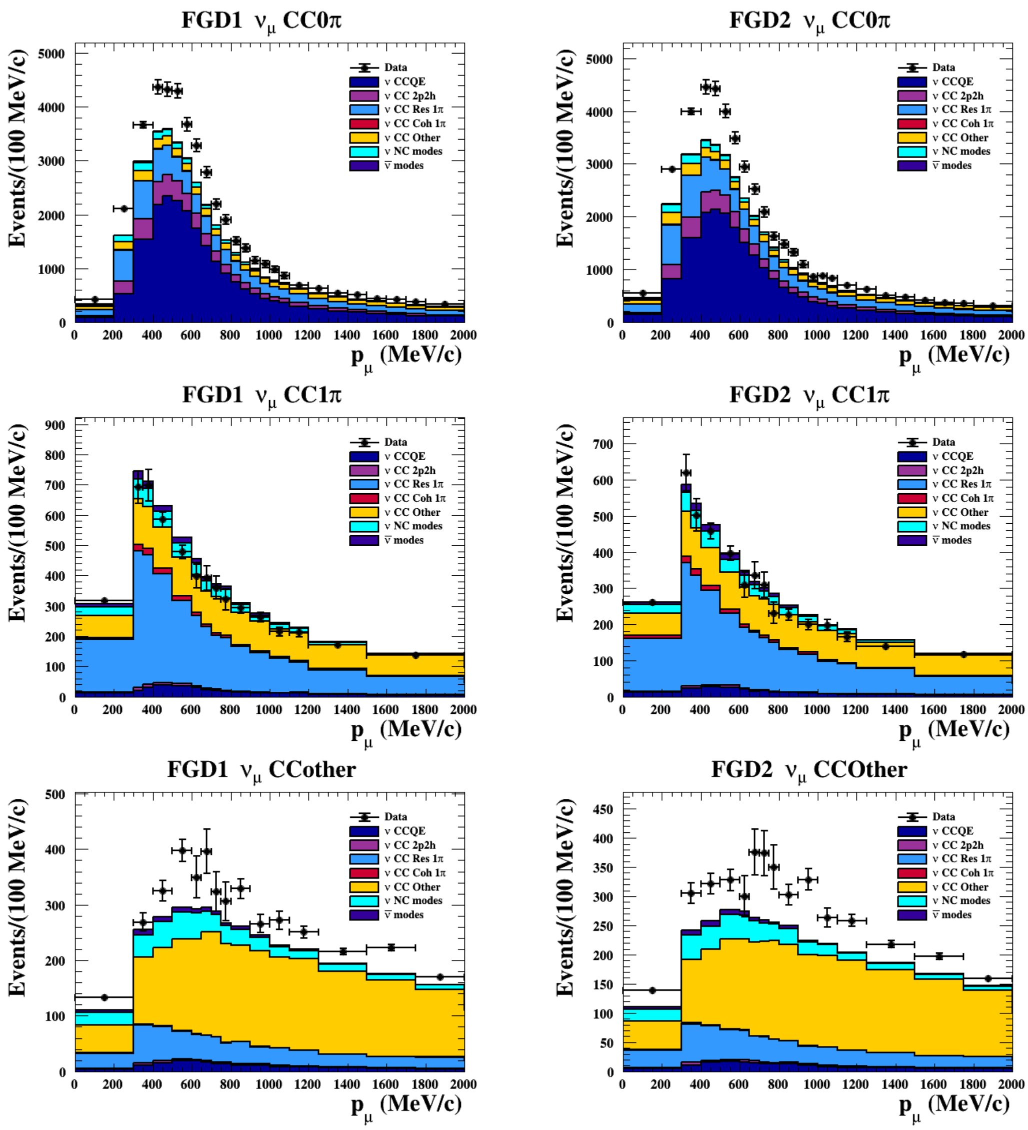

Figure 6.3: The nominal Monte Carlo predictions compared to data for the FGD1 and FGD2 samples in neutrino beam mode, broken down into the $CC\nu_\mu 0\pi$, $CC\nu_\mu 1\pi$ and $CC\nu_\mu$ Other categories. Figures taken from [194].

6.3 Far Detector Beam Samples

The beam neutrino events which occur at the SK detector, which pass the reduction cuts detailed in section 5.3, are separated based on whether the beam was operating in FHC or RHC mode. The events are then separated into three samples: electron-like (1Re), muon-like (1Rμ), and CC1π^+-like (1Re1de) which are observed as electron-like events with an associated decay electron [186]. As discussed in section 6.1, positively charged pions emitted from neutrino interactions are more likely to produce decay electrons than negatively charged pions. Consequently, the CC1π^+-like sample is only selected when the beam is operating in FHC mode. Therefore, five beam samples measured at SK are used in this analysis.

The fiducial volume definition for beam samples is slightly different from that used for the atmospheric samples. It uses both the distance to the closest wall (`dWall`) and the distance to the wall along the trajectory of the particle (`toWall`). This allows events that originate close to the wall but are facing into the tank to be included within the analysis, which would have otherwise been removed. These additional events are beneficial for a statistics-limited experiment. The exact cut values for both `dWall` and `toWall` are different for each of the three types of sample and are optimised based on T2K sensitivity to δ_{CP} [184, 198]. They are:

1Re event selection For an event to be classified as a 1Re-like, the event must satisfy:

- Fully-contained and have `dWall` $>$ 80cm and `toWall` $>$ 170cm
- Total of one ring which is reconstructed as electron-like with reconstructed momentum $P_e > 100$MeV
- Zero decay electrons are associated with the event
- Passes π^0 rejection cut discussed in section 5.2

The zero decay electron cut removes non-CCQE interactions and the π^0 rejection cut is designed to remove neutral current π^0 background events which can be easily reconstructed as 1Re-like events.

The zero decay electron cut removes non-CCQE interactions and the π^0 rejection cut is designed to remove neutral current π^0 background events which can be easily reconstructed as 1Re-like events.

CC1π^+ event selection This event selection is very similar to that of the 1Re sample. The only differences are that the `dWall` and `toWall` criteria are changed to > 50cm and > 270cm, respectively, and exactly one decay electron is required from the π^+ decay.

1Rμ event selection A 1Rμ-like event is determined by the following cuts:

- Fully-contained and have `dWall` > 50cm and `toWall` > 250cm
- Total of one ring which is reconstructed as muon-like with reconstructed momentum $P_\mu > 200$MeV
- Fewer than two decay electrons are associated with the event
- Passes π^+ rejection cut discussed in section 5.2

All of these samples are binned in reconstructed neutrino energy. This is possible under a particular interaction mode assumption, as the direction from the source is known extremely well. For the 1Re-like and 1Rμ-like samples,

$$E_\nu^{rec} = \frac{(M_N - V_{nuc})E_l - m_l^2/2 + M_N V_{nuc} - V_{nuc}^2/2 + (M_P^2 + M_N^2)/2}{M_N - V_{nuc} - E_l + P_l \cos(\theta_{beam})}. \quad (6.2)$$

Where M_N, M_P and m_l are the masses of the neutron, proton and outgoing lepton, respectively. $V_{nuc} = 27$MeV is the binding energy of the oxygen nucleus [186], θ_{beam} is the angle between the beam and the direction of the outgoing lepton, and E_l and P_l are the energy and momentum of that outgoing lepton.

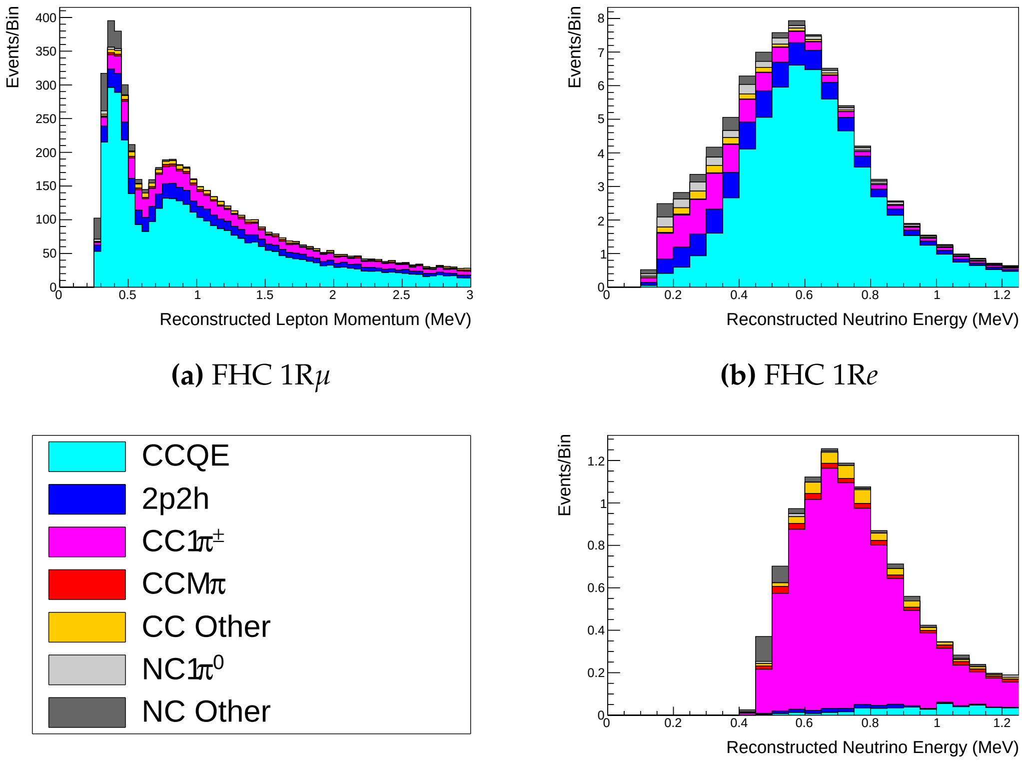

(a) FHC 1Rμ

(b) FHC 1Re

(c) FHC CC1π^+

Figure 6.4: The reconstructed neutrino energy, as defined by Equation 6.2 and Equation 6.3, for the 1Rμ-like, 1Re-like, and CC1π^+-like samples. The AsimovA oscillation parameters are assumed (given in Table 2.2). These samples are the FHC mode samples. For ease of viewing, the 1Rμ sample only shows the $0. \leq E_\nu^{rec} < 3.0$GeV but the binning extends to 30.0GeV.

The reconstructed neutrino energy of the CC1π^+-like events also accounts for the delta resonance produced within the interaction,

$$E_\nu^{rec} = \frac{2M_N E_l + M_{\Delta^{++}}^2 - M_N^2 - m_l^2}{2(M_N - E_l + P_l \cos(\theta_{beam}))}. \tag{6.3}$$

Where $M_{\Delta^{++}}$ is the mass of the delta baryon. Binding energy effects are not considered as a two-body process, with the delta baryon, is assumed. This follows the T2K oscillation analysis presented in [75], although recent developments of the interaction model in the latest T2K oscillation analysis do include effects from binding energy in this calculation [199].

The reconstructed neutrino energy for the FHC samples is illustrated in Figure 6.4. As expected, the 1Rμ-like and 1Re-like samples are heavily dominated by CCQE interactions, with smaller contributions from 2p2h meson exchange and resonant pion production interactions. The CC1π^+-like sample predominantly consists of charged current resonant pion production interactions. The 1Re-like and CC1π^+-like samples are also binned by the angle between the neutrino beam and the reconstructed lepton momentum. This is to aid in charged current and neutral current separation, as indicated in Figure 6.5. This is because the neutral current backgrounds are predominantly due to π^0-decays, which decay into two γ rays. The opening angle of which (alongside the different final state kinematics) can produce a slightly broader angular distribution compared to the final state particles originating from charged current ν_e interactions.

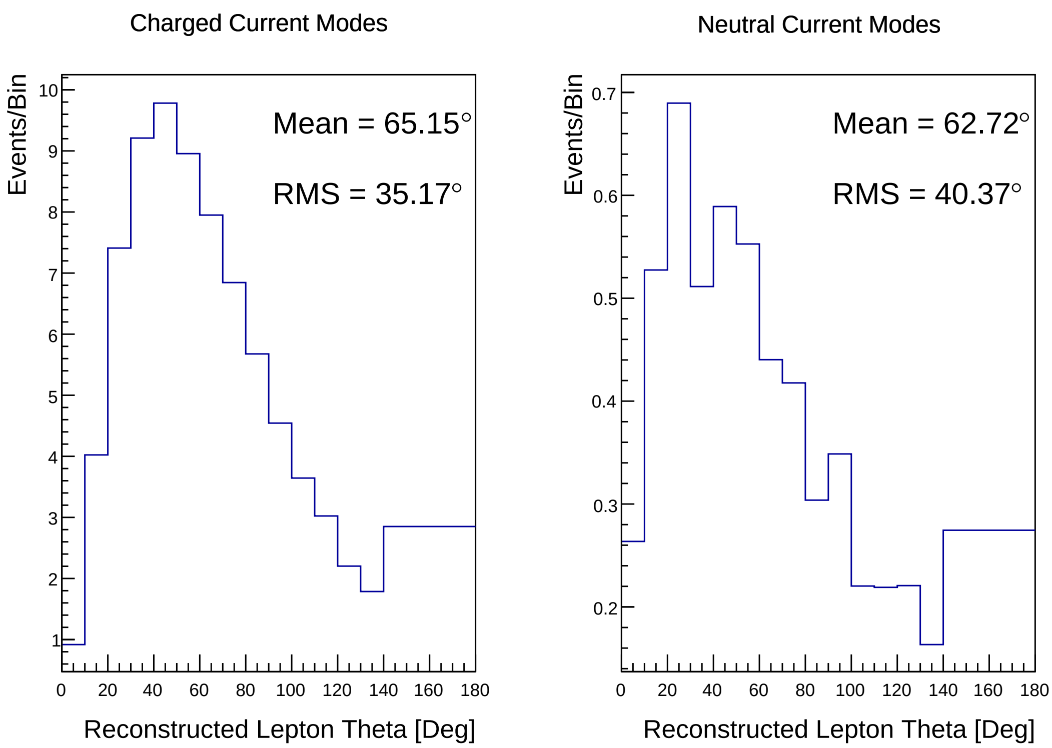

Figure 6.5: The distribution of the angle between the neutrino beam direction and the reconstructed final state lepton, for the FHC 1Re-like sample. The distribution is broken down by neutrino interaction mode into charged current (left) and neutral current (right) components. Asimov A oscillation parameter sets are assumed (given in Table 2.2). The RMS of the charged and neutral current plots are 35.17° and 40.37°, respectively.

6.4 Systematic Uncertainties

The systematic model parameters for this analysis are split into groups, or blocks, depending on their purpose. They consist of flux uncertainties, neutrino-matter interaction systematics, and detector efficiencies. There are also uncertainties on the oscillation parameters to which this analysis is not sensitive, namely Δm^2_{21} and $\sin^2(\theta_{12})$. These oscillation parameter uncertainties are taken from the 2020 PDG measurements [76]. As described in chapter 4, each model parameter used within this analysis requires a prior uncertainty. This is provided via separate covariance matrices for each block. The covariance matrices can include prior correlations between parameters within a single block, but the separate treatment means prior correlations can not be included for parameters in different groups. Some parameters in these models have no reasonably motivated uncertainties and are assigned flat priors which do not modify the likelihood penalty. In practice, these flat prior parameters are actually assigned a Gaussian with a very large width to ensure the covariance matrix is positive definite. They are then checked at run time to determine if they contribute to the likelihood. The flux, neutrino interaction, and detector modeling simulations have already been discussed in section 5.1 and section 5.2. The uncertainties invoked within each of these models are described below.

6.4.1 Beam Flux

The neutrino beam flux systematics are based upon the uncertainty in the modeling of the components of the beam simulation. This includes the model of hadron productions and reinteractions, the shape, intensity, and alignment of the beam with respect to the target, and the uniformity of the magnetic field produced by the horn, alongside other effects. The uncertainty, as a function of neutrino energy, is illustrated in Figure 6.6 which includes a depiction of the total uncertainty as well as the contribution from individual components. The uncertainty around the peak of the energy distribution ($E_\nu \sim 0.6$GeV) is dominated by uncertainties in the beam profile and alignment. Outside of this region, uncertainties on hadron production dominate the error.

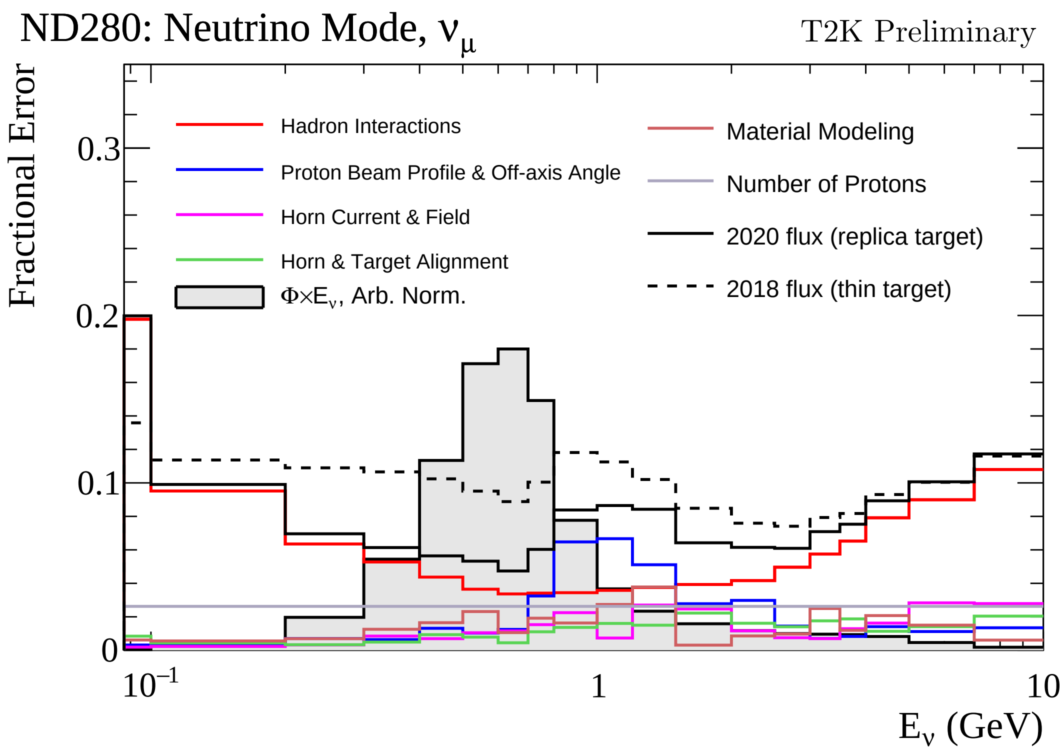

Figure 6.6: The total uncertainty evaluated on the near detector ν_μ flux prediction constrained by the replica-target data, illustrated as a function of neutrino energy. The solid(dashed) line indicates the uncertainty used within this analysis(the T2K 2018 analysis [200]). The solid histogram indicates the neutrino flux as a function of energy. Figure taken from [201].

The beam flux uncertainties are described by one hundred parameters. They are split between the ND280 and SK detectors and binned by neutrino flavour: ν_μ, $\bar{\nu}_\mu$, ν_e and $\bar{\nu}_e$. The response is then broken down as a function of neutrino energy. The bin density in the neutrino energy is the same for the ν_μ in FHC and $\bar{\nu}_\mu$ in RHC beams, and narrows for neutrino energies close to the oscillation maximum of $E_\nu = 0.6$GeV. This binning is specified in Table 6.5. All of these systematic uncertainties are applied as normalisation parameters with Gaussian priors centered at 1.0 and error specified from a covariance matrix provided by the T2K beam group [201].

Neutrino Flavour	Sign	Neutrino Energy Bin Edges (GeV)
μ	Right	$0., 0.4, 0.5, 0.6, 0.7, 1., 1.5, 2.5, 3.5, 5., 7., 30.$
μ	Wrong	$0., 0.7, 1., 1.5, 2.5, 30.$
e	Right	$0., 0.5, 0.7, 0.8, 1.5, 2.5, 4., 30.$
e	Wrong	$0., 2.5, 30.$

Table 6.5: The neutrino energy binning for the different neutrino flavours. “Right” sign indicates neutrinos in the FHC beam and antineutrinos in the RHC beam. “Wrong” sign indicates antineutrinos in the FHC beam and neutrinos in the RHC beam. The binning of the detector response is identical for the FHC and RHC modes as well as at ND280 and SK.

6.4.2 Atmospheric Flux

The atmospheric neutrino flux is modeled by the HKKM model [51]. 16 systematic uncertainties are applied to control the normalisation of each neutrino flavour, energy, and direction. They are summarised below:

- **Absolute Normalisation**: The overall normalisation of each neutrino flavour is controlled by two independent systematic uncertainties, for $E_\nu < 1$GeV and $E_\nu > 1$GeV, respectively. This is driven mostly by hadronic interaction uncertainties for the production of pions and kaons [51]. The strength of the response is dependent upon the neutrino energy. The uncertainty is parameterized following Figure 11 in [51].

- **Relative Normalisation**: Uncertainties on the ratio of $(\nu_\mu + \bar{\nu}_\mu)/(\nu_e + \bar{\nu}_e)$ are controlled by the difference between the HKKM model [51], FLUKA [54] and Bartol models [50]. Three independent parameters are applied in the energy ranges: $E_\nu < 1$GeV, 1GeV $< E_\nu <$ 10GeV, and $E_\nu >$ 10GeV.

- $\nu/\bar{\nu}$ **Normalisation**: The uncertainties in the π^+/π^- (and kaon equivalent) production uncertainties in the flux of $\nu/\bar{\nu}$. The response is applied using the same methodology as the relative normalisation parameters.

- **Up/Down and Vertical/Horizontal Ratio**: Similar to the above two systematics, the difference between the HKKM, FLUKA, and Bartol model predictions, as a function of $\cos(\theta_Z)$, is used to control the normalisation of events as a function of zenith angle.

- K/π **Ratio**: Higher energy neutrinos ($E_\nu > 10$GeV) mostly originate in kaon decay. Measurements of the ratio of K/π production [202] are used to control the systematic uncertainty of the expected ratio of pion and kaon production.

- **Solar Activity**: As the 11-year solar cycle can affect the Earth's magnetic field, the flux of primary cosmic rays varies across the same period. The uncertainty is calculated by taking a ± 1 year variation, equating to a 10% uncertainty for the SK-IV period.

- **Atmospheric Density**: The height of the interaction of the primary cosmic rays is dependent upon the atmospheric density. The HKKM assumes the US standard 1976 [153] profile. This systematic controls the uncertainty in that model.

The total uncertainty is dominated by the absolute and relative normalisation parameters. The effect of which is illustrated in Figure 6.7. Generally, the uncertainty is large at low energy, reducing to $O(10\%)$ around the peak of the flux distribution and then increasing once the neutrino energy exceeds 10GeV.

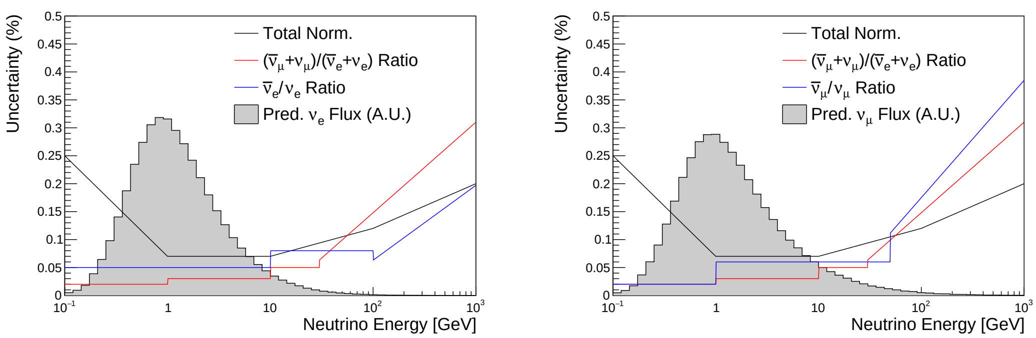

Figure 6.7: The uncertainty evaluated on the atmospheric ν_e (left) and ν_μ (right) flux predictions. The absolute normalisation and flavour ratio uncertainties are given. The solid histogram indicates the neutrino flux as a function of energy.

Updates to the HKKM and Bartol models are underway [158] to use a similar tuning technique to that used in the beam flux predictions. After those updates, it may be possible to include correlations in the hadron production uncertainty systematics for beam and atmospheric flux predictions.

6.4.3 Neutrino Interaction

Neutrino interactions in the detectors are modeled by NEUT. The two independent oscillation analyses, T2K-only [203] and the SK-only [60], have developed separate interaction models. To maximise sensitivity out of this simultaneous beam and atmospheric analysis, a correlated interaction model has been defined in [204]. Where applicable, correlations allow the systematic uncertainties applied to the atmospheric samples to be constrained by near detector neutrino beam measurements. This can lead to stronger sensitivity to oscillation parameters as compared to an uncorrelated model.

The low-energy T2K systematic model has a more sophisticated treatment of CCQE, 2p2h, and CCRES uncertainties, where extensive comparisons of this model have been performed to external data [203]. However, the model is not designed for high-energy atmospheric events, like those illustrated in Figure 5.11. Therefore the high energy systematic model from the SK-only analysis is implemented for the relevant multi-GeV, PC, and up-μ samples. The T2K CCQE model is more sophisticated so it has been implemented for all samples within this analysis, where separate low-energy and high-energy dials have been implemented. The low-energy dials are constrained by the near detector measurements and are uncorrelated to their high-energy counterparts. The author of this thesis was responsible for implementing and validating the combined cross-section model as documented in [204, 205].

The high energy systematic model includes parameters developed from comparisons of Nieves and Rein-Seghal models which affect resonant pion producing interactions, comparisons of the GRV98 and CKMT models which control DIS interactions, and hadron multiplicity measurements which modulate the normalisation of multi-pion producing events. The uncertainty on the ν_τ cross-section is particularly large and is controlled by a 25% normalisation uncertainty. These uncertainties are applied via normalisation or shape parameters. The former linearly scales the weight of all affected Monte-Carlo events, whereas the latter can increase or decrease a particular event's weight depending on its neutrino energy and mode of interaction. The response of the shape parameters is defined by third-order polynomial splines which return a weight for a particular neutrino energy. To reduce computational resources for the far detector fit, the response is binned by neutrino energy and sample binning: lepton momentum and cosine zenith binning for atmospheric splined responses and reconstructed neutrino energy and direction binning for beam samples. In total, 17 normalisation and 15 shape parameters are included in the high-energy model within this analysis.

Figure 6.8 indicates the predicted neutrino energy distribution for both beam and subGeV atmospheric samples. There is clearly significant overlap in neutrino energy between the subGeV atmospheric and beam samples, allowing similar kinematics in the final state particles. Figure 6.9 illustrates the fractional contribution of the different interaction modes per sample.

Comparing beam and atmospheric samples which target CCQE interactions (`S.G. e-like 0de`, `S.G.` μ`-like [0,1]de`, `[FHC,RHC]1R` μ`-like` and `[FHC,RHC]1R e-like` samples), there is a very similar contribution of CCQE, CC 2p2h, and CC1$\pi^\pm$ interactions. The samples which target CC1$\pi^\pm$ interactions, (`S.G. e-like 0de`, `S.G.` μ`-like 2de` and `FHC 1R+1d.e e-like`) also consist of very similar mode interactions.

As a consequence of the similarity in energy and mode contributions, correlating the systematic model between the beam and subGeV atmospheric samples ensures that this analysis attains the largest sensitivity to oscillation parameters while still ensuring neutrino interaction systematics are correctly accounted for. Due to its more sophisticated CCQE and 2p2h model, the T2K systematic model was chosen as the basis of the correlated model.

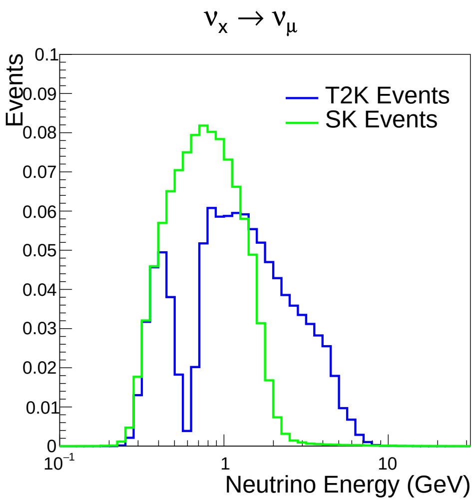

(a) μ-like

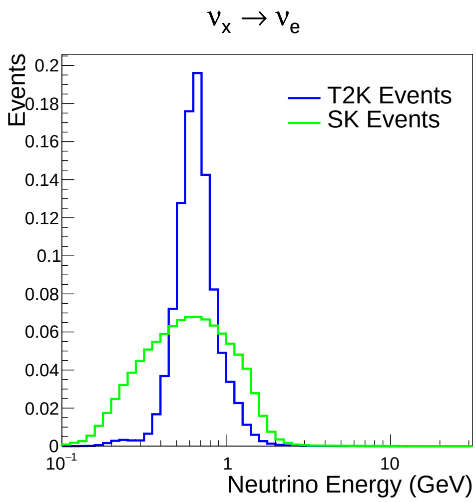

(b) e-like

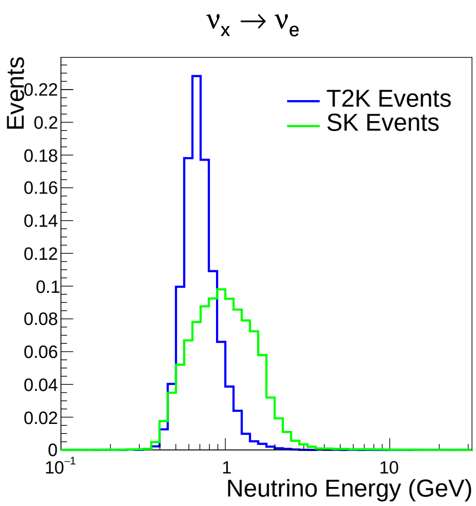

(c) e-like + 1d.e.

Figure 6.8: The predicted neutrino energy distribution for subGeV atmospheric and beam samples. FHC and RHC beam samples are summed together Asimov A oscillation parameters are assumed (given in Table 2.2). Beam and atmospheric samples with similar cuts are compared against one another.

The T2K systematic model [203] is applied in a similar methodology to the SK model parameters. It consists of 19 shape parameters and 24 normalisation parameters. Four additional parameters, which model the uncertainty in the binding energy, are applied in a way to shift the momentum of the lepton emitted from a nucleus. This controls the uncertainty specified on the 27MeV binding energy assumed within Equation 6.2. The majority of these parameters are

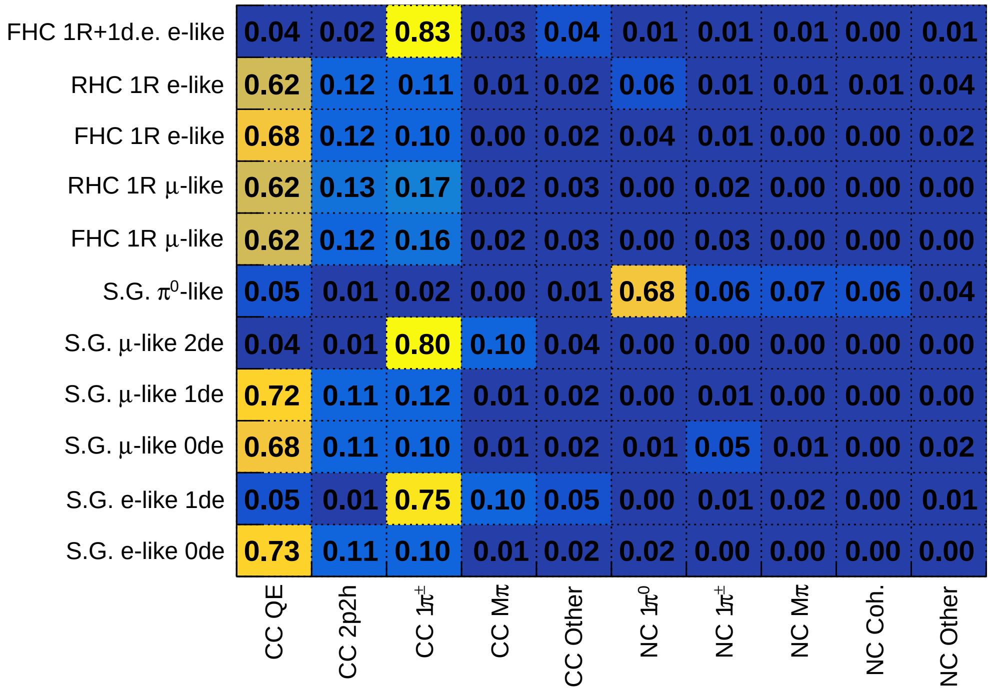

Figure 6.9: The interaction mode contribution of each sample given as a fraction of the total event rate in that sample. Asimov A oscillation parameters are assumed (given in Table 2.2). The Charged Current (CC) modes are broken into quasi-elastic (QE), 2p2h, resonant charged pion production ($1\pi^{\pm}$), multi-pion production ($M\pi$), and other interaction categories. Neutral Current (NC) interaction modes are given in interaction mode categories: π^0 production, resonant charged pion production, multi-pion production, and others.

assigned a Gaussian prior uncertainty. Those that have no reasonably motivated uncertainty, or those which have not been fit to external data, are assigned a flat prior which does not affect the penalty term.

On top of the combination of the SK and T2K interaction models, several other parameters have been specifically developed for the joint oscillation analysis. The majority of the atmospheric samples' δ_{CP} sensitivity comes from the normalisation of subGeV electron-like events. These are modeled using a spectral function to approximate the nuclear ground state. However, the near detector is not able to constrain the model so an additional systematic is introduced which models an alternative Continous Random Phase Approximation (CRPA) nuclear ground state. This dial approximates the event weights if a CRPA model had been assumed rather than a spectral function. This dial only applies to ν_e and $\bar{\nu}_e$ as the near detector does not constraint ν_e cross-section measurements. It is applied as a shape parameter.

Further additions to the model have been introduced due to the inclusion of the subGeV π^0 atmospheric sample. This particularly targets charged current and neutral current π^0 producing interactions to help constrain the systematic uncertainties. Therefore, an uncertainty that affects neutral current resonant π^0 production is incorporated into this analysis. Comparisons of NEUT's NC resonant pion production predictions have been made to MiniBooNE [206] data and a consistent 16% to 21% underprediction is observed [204]. Consequently, a conservative 30% normalisation parameter is invoked.

Down-going events are mostly insensitive to oscillation parameters and can act similar to the near detector within an accelerator experiment (Details will be discussed in chapter 7). This region of phase space can act as a sideband and allows the cross-section model and near detector constraint to be studied. The distribution of events in this region is calculated using the technique outlined in subsection 4.3.4. The results are illustrated in Figure 6.10. For CCQE-targeting samples, the application of the near detector constraint is well within the statistical fluctuation of the down-going data. This means there is no significant tension is observed between the data and the Monte Carlo prediction after the near detector constraint is applied. This is not the case for samples with target CCRES interactions. The electron-like data is consistent with the constrained prediction at high reconstructed momenta but diverges at lower momentum, whereas the muon-like sample is under-predicted throughout the range of momenta. To combat this disagreement, an additional cross-section systematic dial, specifically designed to inflate the low pion momentum systematics was developed in [204]. This is a shape parameter implemented through a splined response.

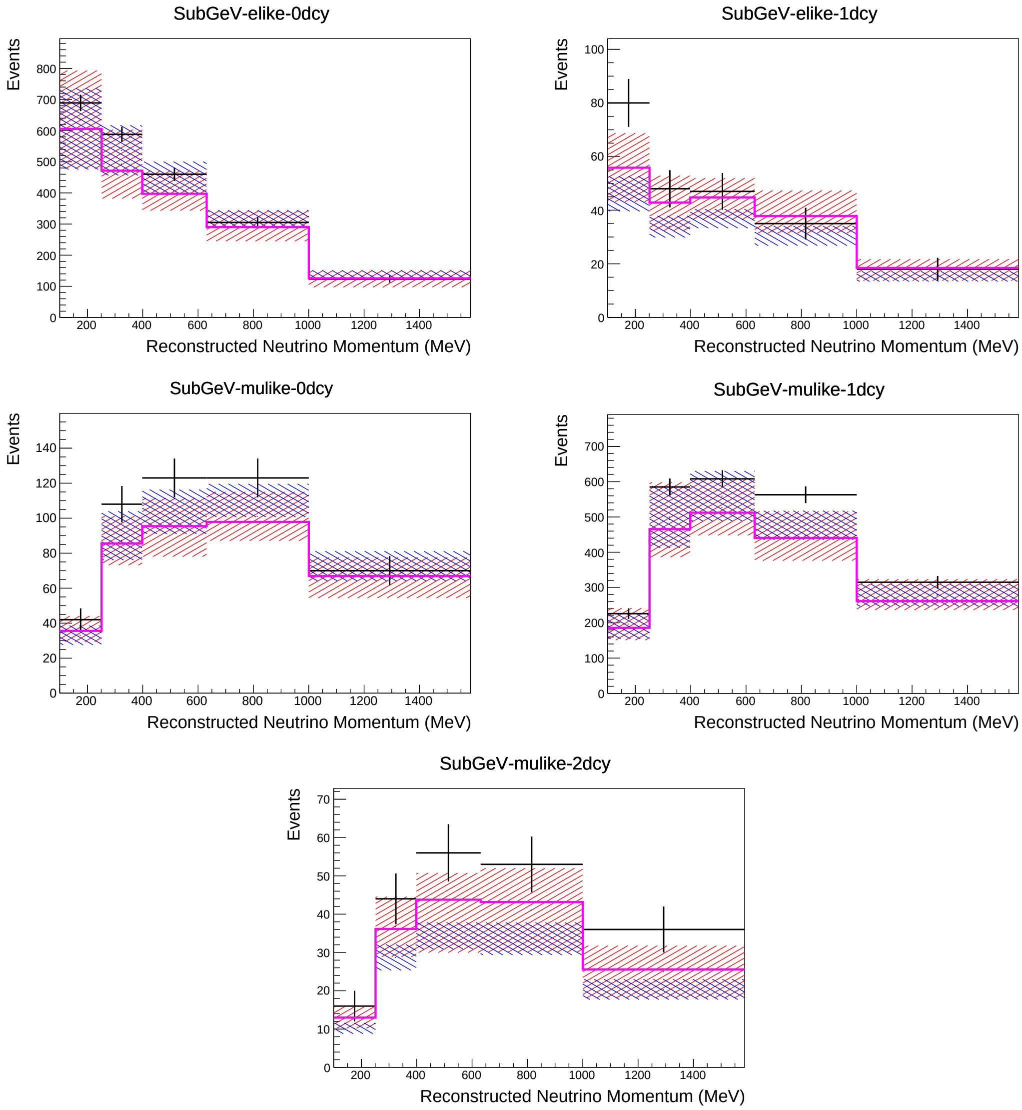

Figure 6.10: Down-going atmospheric subGeV single-ring samples comparing the mean and error of the pre-fit and post-fit Monte Carlo predictions in red and blue, respectively. The magenta histogram illustrates the Monte Carlo prediction using the generated dial values. The black points illustrate the down-going data with statistical errors given. The mean and errors of the Monte Carlo predictions are calculated by the techniques documented in subsection 4.3.4. The pre-fit spectrum is calculated by throwing the cross-section and atmospheric flux dial values from the pre-fit covariance matrix. The post-fit spectrum is calculated by sampling the cross-section dial values from an ND fit MCMC chain, whilst still throwing the atmospheric flux dials from the pre-fit covariance.

6.4.4 Near Detector

The systematics applied due to uncertainties arising from the response of the near detector is documented in [132]. The response is described by 574 normalisation parameters binned in the selected sample as well as momentum and angle,

P_μ and $\cos(\theta_\mu)$, of the final-state muon. These are applied via a covariance matrix with each parameter being assigned a Gaussian prior from that covariance matrix. These normalisation parameters are built from underlying systematics, e.g. pion secondary interaction systematics, which are randomly thrown and the variation in each $P_\mu \times \cos(\theta_\mu)$ bin is determined. Two thousand throws are evaluated and a covariance matrix response is created. This allows significant correlations between FGD1 and FGD2 samples, as well as adjacent $P_\mu \times \cos(\theta_\mu)$ bins. Statistical uncertainties are accounted for by including fluctuations of each event's weight from a Poisson distribution.

Similar to the cross-section systematics, MaCh3 and BANFF are used to constrain the uncertainty of these systematics through independent validations. Each fitter generates a post-fit covariance matrix which is compared and passed to the far-detector oscillation analysis working group. As the analysis presented within this thesis uses the `MaCh3` framework, a joint oscillation analysis fit of all three sets of samples and their respective systematics is performed.

6.4.5 Far Detector

Two configurations of the far detector systematic model implementation have been considered. Firstly, the far detector systematic uncertainties for beam and atmospheric samples are taken from their respective analysis inputs, denoted "official inputs" analysis, with no correlations assumed between the beam and atmospheric samples. The beam- and atmospheric-specific inputs are documented in subsubsection 6.4.5.1 and subsubsection 6.4.5.2. Secondly, an alternative detector model has been developed which correlates the response of the SK detector systematics between the beam and atmospheric samples. Here, the distribution of parameters used for applying event cuts (e.g. electron-muon PID separation) is modified within the fit. It follows a similar methodology to the beam far detector systematics implementation but performs a joint fit of the beam and atmospheric data. This alternative implementation is detailed in subsubsection 6.4.5.3.

6.4.5.1 Beam Samples

There are 45 systematics which describe the response of the far detector to beam events [186], split into 44 normalisation parameters and one energy scale systematic. The energy scale systematic is applied as a multiplicative scaling of the reconstructed neutrino energy. It is estimated from data-to-Monte Carlo differences in the stopping muon sample in [188] and found to be 2.1%. The normalisation parameters are assigned a Gaussian error centered at one with width taken from a covariance matrix. A detailed breakdown of the generation of the covariance matrix is found in [198]. To build the covariance matrix, a fit is performed on atmospheric data which has been selected using beam sample selection cuts. These cuts use the variables, L^i, where the index i is detailed in Table 6.6. Each L^i is a smear, α, and shift, β parameter such that,

$$L^i_j \rightarrow \bar{L}^i_j = \alpha^i_j L + \beta^i_j \tag{6.4}$$

Where L^i_j ($\bar{L}^i_j$) correspond to nominal(varied) PID cut parameters given in Table 6.6. The shift and smear parameters are nuisance parameters with no prior constraints. They are binned by final-state topology, j, where the binning is given in Table 6.7. The final-state topology binning is because the detector will respond differently to events that have one or multiple rings. For example, the detector will be able to distinguish single-ring events better than two overlapping ring events, resulting in different systematic uncertainty for one-ring events compared to two-ring events. This approach is used to allow the cut parameter distributions to be modified within the fit, allowing for better data to Monte Carlo agreement.

Cut Variable	Parameter Name
0	`fiTQun` e/μ PID
1	`fiTQun` e/π^0 PID
2	`fiTQun` μ/π PID
3	`fiTQun` Ring-Counting Parameter

Table 6.6: List of cut variables that are included within the shift/smear fit documented in [198].

Category	Description
$1e$	Only one electron above Cherenkov threshold in the final state
1μ	Only one muon above Cherenkov threshold in the final state
$1e$+other	One electron and one or more other charged particles above Cherenkov threshold in the final state
1μ+other	One muon and one or more other charged particles above Cherenkov threshold in the final state
$1\pi^0$	Only one π^0 in the final state
$1\pi^\pm$ or 1p	Only one hadron (typically charged pion or proton) in the final state
Other	Any other final state

Table 6.7: Reconstructed event topology categories on which the SK detector systematics [198] are based.

The mis-modeling of π^0 events is also considered. If one of the two rings from a π^0 event is missed, this will be reconstructed as a CCν_e-like event. This is one of the largest systematics hindering the electron neutrino appearance analyses. Consequently, additional systematics have been introduced to constrain the mis-modeling of π^0 events in SK, binned by reconstructed neutrino energy. To evaluate this systematic uncertainty, a set of "hybrid-π^0" samples is constructed. These events are built by overlaying one electron-like ring from the SK atmospheric neutrino samples or decay electron ring from a stopping cosmic ray muon with one simulated photon ring. Both rings are chosen so that momenta and opening angle follow the decay kinematics of NC π^0 events from the T2K-MC. Hybrid-π^0 Monte Carlo samples with both rings from the SK Monte Carlo are produced to compare with the hybrid-π^0 data samples and the difference in the fraction of events that pass the ν_e selection criteria is used to assign the systematic errors. In order to investigate any data to Monte Carlo differences that may originate from either the higher energy ring or lower energy ring, two samples are built; a sample in which the electron constitutes the higher energy ring from the π^0 decay (called the primary sample) and another one in which it constitutes the lower energy ring (called the secondary sample). The standard T2K ν_e fiTQun event selection criteria are used to select events.

Final contributions to the covariance matrix are determined by supplementary uncertainties obtained by comparing stopping muon data to Monte Carlo prediction, as first introduced in section 5.2. The efficiency of tagging decay electrons is estimated by the stopping muon data to Monte Carlo differences by comparing the number of one decay electron events to the number of events with one or fewer decay electrons. Similarly, the rate at which fake decay electrons are reconstructed by `fiTQun` is estimated by comparing the number of two decay electron events to the number of events with one or two reconstructed decay electrons. The two sources of systematics are added in quadrature weighted by the number of events with one true decay electron yielding a 0.2% systematic uncertainty. A fiducial volume systematic of $\pm$2.5cm which corresponds to a 0.5% shift in the normalisation of events is also applied. Additional normalisation uncertainties based on neutrino flavour and interaction mode are also defined in [186, 207, 208].

Two additional sources of uncertainty are included: secondary and photo-nuclear interactions. These are estimated by varying the underlying parameters are building a distribution of sample event rates. These contributions are then added in quadrature to the above covariance matrix. The final uncertainty on the SK detector systematics are provided in Figure 6.11.

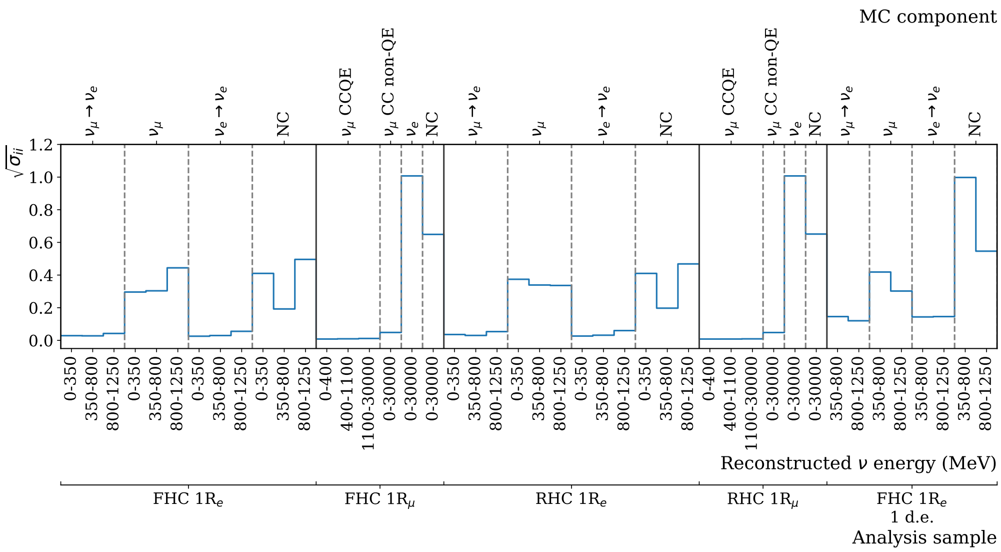

Figure 6.11: The uncertainty on each of the 44 parameters describing the SK detector systematics (The energy scale systematic is neglected). The parameters are split by sample, oscillation channel, interaction mode and reconstructed neutrino energy.

6.4.5.2 Atmospheric Samples

The detector systematics for atmospheric samples, documented in [88], are split into two sub-groups: those which are related to particle identification and ring counting systematics, and those which are related to calibration, separation, and reduction uncertainties.

The particle identification systematics consist of five parameters. The ring separation systematic enforces an anti-correlated response between the single-ring and multi-ring samples. This is implemented as a fractional increase/decrease in the overall normalisation of each sample, depending on the distance to the nearest wall from an event's vertex. The coefficients of the normalisation are estimated prior to the fit and depend on the particular atmospheric sample. Two electron-muon separation systematics are included within this model which anti-correlates the response of the electron-like and muon-like samples: one for single-ring events and another for multi-ring events.

The multi-ring electron-like separation likelihood, discussed in section 6.1, encodes the ability of the detector to separate neutrino from anti-neutrino events. Two normalisation parameters vary the relative normalisation of multi-ring ν_e and $\bar{\nu}_e$ samples whilst keeping a consistent overall event rate.

There are 22 systematics related to calibration measurements, including effects from backgrounds, reduction, and showering effects. They are documented in [88] and are briefly summarised in Table 6.8. They are applied via normalisation parameters, with the separation systematics requiring the conservation of event rate across all samples.

6.4.5.3 Correlated Detector Model

A complete uncertainty model of the SK detector would be able to determine the systematic shift on the sample spectra for a variation of the underlying parameters, e.g. PMT angular acceptance. However, this is computationally intensive, requiring Monte Carlo predictions to be made for each plausible variation. Consequently, an effective parameter model has been utilised for

Index	Description
0	Partially contained reduction
1	Fully contained reduction
2	Separation of fully contained and partially contained events
3	Separation of stopping and through-going partially contained events in top of detector
4	Separation of stopping and through-going partially contained events in barrel of detector
5	Separation of stopping and through-going partially contained events in bottom of detector
6	Background due to cosmic rays
7	Background due to flasher events
8	Vertex systematic moving events into and out of fiducial volume
9	Upward going muon event reduction
10	Separation of stopping and through-going in upward going muon events
11	Energy systematic in upward going muon events
12	Reconstruction of the path length of upward going muon events
13	Separation of showering and non-showering upward going muon events
14	Background of stopping upward going muon events
15	Background of non-showering through-going upward going muon events
16	Background of showering through-going upward going muon events
17	Efficiency of tagging two rings from π^0 decay
18	Efficiency of decay electron tagging
19	Background from downgoing cosmic muons
20	Asymmetry of energy deposition in tank
21	Energy scale deposition

Table 6.8: Sources of systematic errors specified within the grouped into the "calibration" systematics model.

a correlated detector model following from the T2K-only model implementation documented in subsubsection 6.4.5.1. It correlates the detector systematics between the far-detector beam and subGeV atmospheric samples due to their similar energies and interaction types. As there are no equivalent beam samples, the multi-GeV, multiring, PC, and Up-μ samples will be subject to the particle identification systematics implementation as described in subsubsection 6.4.5.2 rather than using this correlated detector model. The calibration systematics also described in the aforementioned chapter still apply to all atmospheric samples.

The correlated detector model utilises the same smear and shift parameters documented in subsubsection 6.4.5.1, split by final state topology. Beyond this, the shift and smear parameters are split by visible energy deposited within the detector, with binning specified in Table 6.9. This is because atmospheric events are categorised by subGeV and multi-GeV events based on visible energy, so this splitting is required when correlating the systematic model for beam and atmospheric events. Alongside the technical requirement, higher energy events will be better reconstructed due to fractionally less noise within the detector. As a result of the inclusion of visible energy binning, Equation 6.4 becomes

$$L^i_{jk} \rightarrow \bar{L}^i_{jk} = \alpha^i_{jk} L + \beta^i_{jk}, \tag{6.5}$$

where k is the visible energy bin.

Index	Range (MeV)
0	$30 \geq E_{vis} > 300$
1	$300 \geq E_{vis} > 700$
2	$700 \geq E_{vis} > 1330$
3	$E_{vis} \geq 1330$

Table 6.9: Visible energy binning for which the correlated SK detector systematics are based

The implementation of this systematic model takes the events reconstructed values of the cut parameters, modifies them by the particular shift and smear parameter for that event, and then re-applies event selection. This causes event migration, which is a new feature incorporated into the MaCh3 framework which is only achievable due to the event-by-event reweighting scheme.

Particular care has to be taken when varying the ring counting parameter. This is because the number of rings is a finite value (one-ring, two-ring, etc.) which can not be continuously varied through this shift and smear technique. Consequently a continuous ring counting parameter, RC_i, is calculated for the i^{th} event, following the definition in [185]: the preferred likelihoods from all considered one-ring (L_{1R}) and two-ring (L_{2R}) fits are determined. The difference is computed as $\Delta_{LLH} = \log(L_{1R}) - \log(L_{2R})$. The ring counting parameter is then defined as

$$RC_i = \text{sgn}\left(\Delta_{LLH}\right) \times \sqrt{|\Delta_{LLH}|}, \tag{6.6}$$

where $\text{sgn}(x) = x/|x|$. This ring counting parameter corresponds to an intermediate likelihood value used within the `fiTQun` algorithm to decide the number of rings associated with a particular event. However, fake-ring merging algorithms are applied after this likelihood value is used. Consequently, this ring counting parameter does not always exactly correspond to the number of reconstructed rings. This can be seen in Figure 6.12.

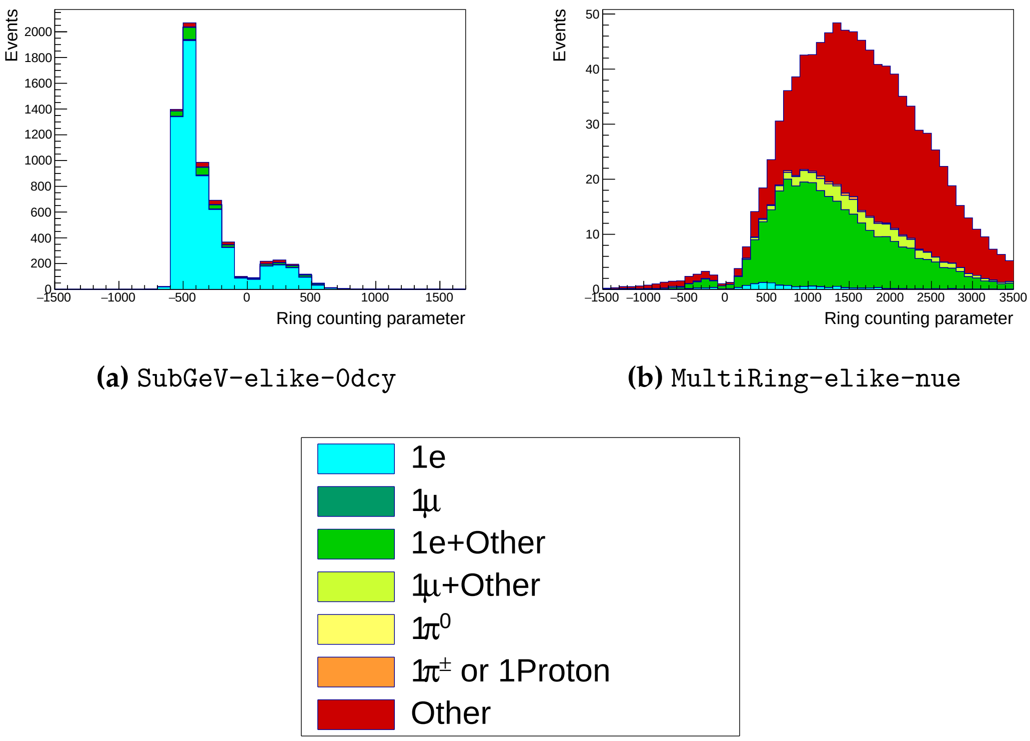

(a) `SubGeV-elike-0dcy` **(b)** `MultiRing-elike-nue`

Figure 6.12: The ring counting parameter as defined in Equation 6.6 for the `SubGeV-elike-0dcy` and `MultiRing-elike-nue` samples.

As the `fiTQun` algorithm does not provide a likelihood value after the fake-ring algorithms have been applied, the ring counting parameter distribution is correlated to the final number of reconstructed rings through "maps". These are two-dimensional distributions of the ring counting parameter and the final number of reconstructed rings. An example is illustrated in Figure 6.13. In principle, the `fiTQun` reconstruction algorithm should be re-run after the variation in the ring counting parameter. However, this is not computationally viable. Therefore the "maps" are used as a reweighting template.

The maps are split by final state topology and true neutrino flavour and all `fiTQun`-reconstructed Monte Carlo events are used to fill them. The maps are row-normalised to represent the probability of X rings for a given RC_i value. Prior to the oscillation fit, an event's nominal weight is calculated as $W^i(N^i_{Rings}, L^i_{jk})$, where N^i_{Rings} is the reconstructed number of rings for the i^{th} event and $W^i(x, y)$ is the bin content in map associated with the i^{th} event, where x number of rings and y is ring counting parameter. Then during the fit, the value of $R = W^i(N^i_{Rings}, \bar{L}^i_{jk}) / W^i(N^i_{Rings}, L^i_{jk})$ is calculated as the event weight for the i^{th} event. This is the only cut variable that uses a reweighting technique rather than event migration.

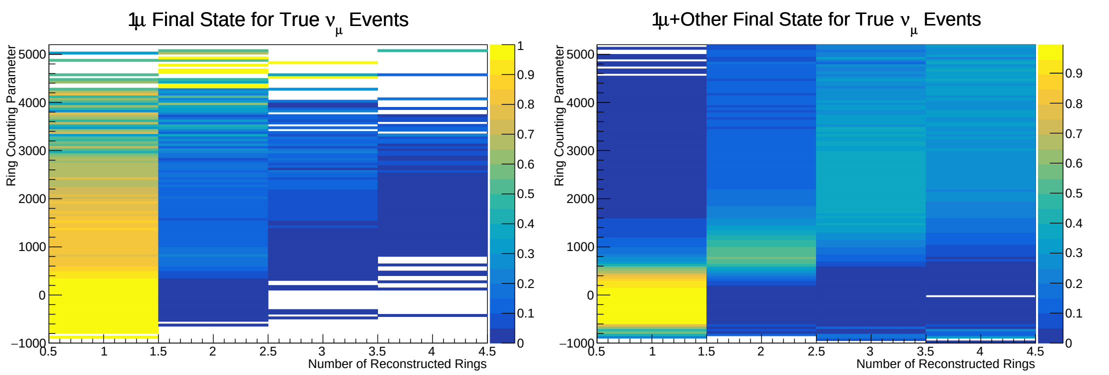

Figure 6.13: The ring counting parameter, defined in Equation 6.6, as a function of the number of reconstructed rings as found by the `fiTQun` reconstruction algorithm. Left: true ν_μ events with only one muon above the Cherenkov threshold in the final state. Right: true ν_μ events with one muon and at least one other charged particle above the Cherenkov threshold in the final state.

The π^0 systematics introduced in subsection 6.4.4 are applied via a covariance matrix. This is not possible in the alternative model as no covariance matrix is used. Thus, the implementation of the π^0 systematics has been modified. The inputs from the hybrid π^0 sample are included via the use of "χ^2 maps", which are two-dimensional histograms in α^i_{jk} and β^i_{jk} parameters over some range. Illustrative examples of the χ^2 maps are given in Figure 6.14. Due to their nature, the shift and smear parameters are typically very correlated. A map is produced for each cut parameter given in Table 6.6 and for each visible energy bin given in Table 6.9.

The maps are filled through the χ^2 comparison of the hybrid π^0 Monte Carlo and data in the particle identification parameters documented in Table 6.6. The Monte Carlo distribution is modified by the α^i_{jk} and β^i_{jk} scaling, whilst cross-section and flux nuisance parameters are thrown from their prior uncertainties. The χ^2 between the scaled Monte Carlo and data is calculated and the relevant point in the χ^2 map is filled.

The implementation within this alternative detector model is to add the bin contents of the maps, for the relevant values of the α^i_{jk} and β^i_{jk} parameters, to the likelihood penalty. Only $1\pi^0$ final state topology shift and smear parameters use this prior uncertainty.

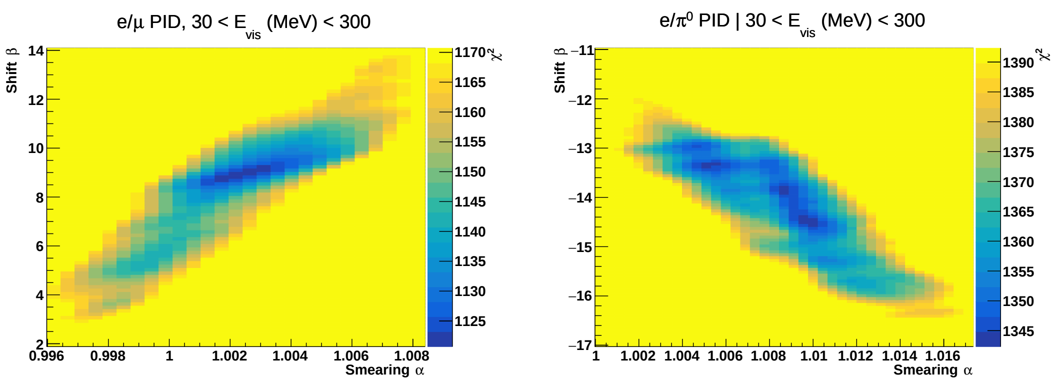

Figure 6.14: The χ^2 between the hybrid-π^0 Monte Carlo and data samples, as a function of smear (α) and shift (β) parameters, for events which have $1\pi^0$ final state topology. Left: Electron-muon separation PID parameter for events with $30 \leq E_{vis}(MeV) < 300$. Right: Electron-$\pi^0$ separation PID parameter for events with $30 \leq E_{vis}(MeV) < 300$.

Similarly, the implementation of the supplementary systematics documented in subsubsection 6.4.5.1 needs to be modified. A new framework [209] was built in tandem with the T2K-SK working group [186] so the additional parameters can be incorporated into the MaCh3 framework. These are applied as normalisation parameters, depending on the particular interaction mode, number of tagged decay electrons, and whether the primary particle generated Cherenkov light. They are assigned Gaussian uncertainties with widths described by a covariance matrix. Furthermore, the secondary interaction and photo-nuclear effects need to be accounted for in this detector model using a different implementation than that in subsubsection 6.4.5.1. This was done by including a shape parameter for of each of the secondary interactions and the photo-nuclear systematic parameters.

There are a total of 224 α^i_{jk} and β^i_{jk} parameters, of which 32 have prior constraints from the hybrid π^0 samples.

One final complexity of this correlated detector model is that the two sets of samples, beam and subGeV atmospheric, use slightly different parameters to distinguish electron and muon-like events. The T2K samples use the value of $\log(L_e/L_\mu)$ whereas the atmospheric samples use the value of $\log(L_e/L_\pi)$, where L_X is the likelihood for hypothesis X. This is because the T2K fits use single-ring `fiTQun` fitting techniques, whereas multi-ring fits are applied to the atmospheric samples where only the electron and pion hypothesis are considered. The correlation between the two likelihood ratios is illustrated in Figure 6.15. As discussed in section 5.2, the pion hypothesis is a very good approximation of the muon hypothesis due to their similar mass. Consequently, using the same shift and smear parameters correlated between the beam and subGeV atmospheric samples is deemed a good approximation.

6.5 Likelihood Calculation

This analysis performs a joint oscillation parameter fit of the ND280 beam samples, the T2K far detector beam samples, and the SK atmospheric samples introduced in this chapter.

Once the Monte Carlo predictions of each beam and atmospheric sample have been built, a likelihood needs to be constructed. This is done by comparing the binned Monte Carlo prediction to binned data. The Monte Carlo prediction is calculated at a particular point, $\vec{\theta}$, in the model parameter space such that $N_i^{MC} = N_i^{MC}(\vec{\theta})$, where N_i represents the bin content of the i^{th} bin. The data

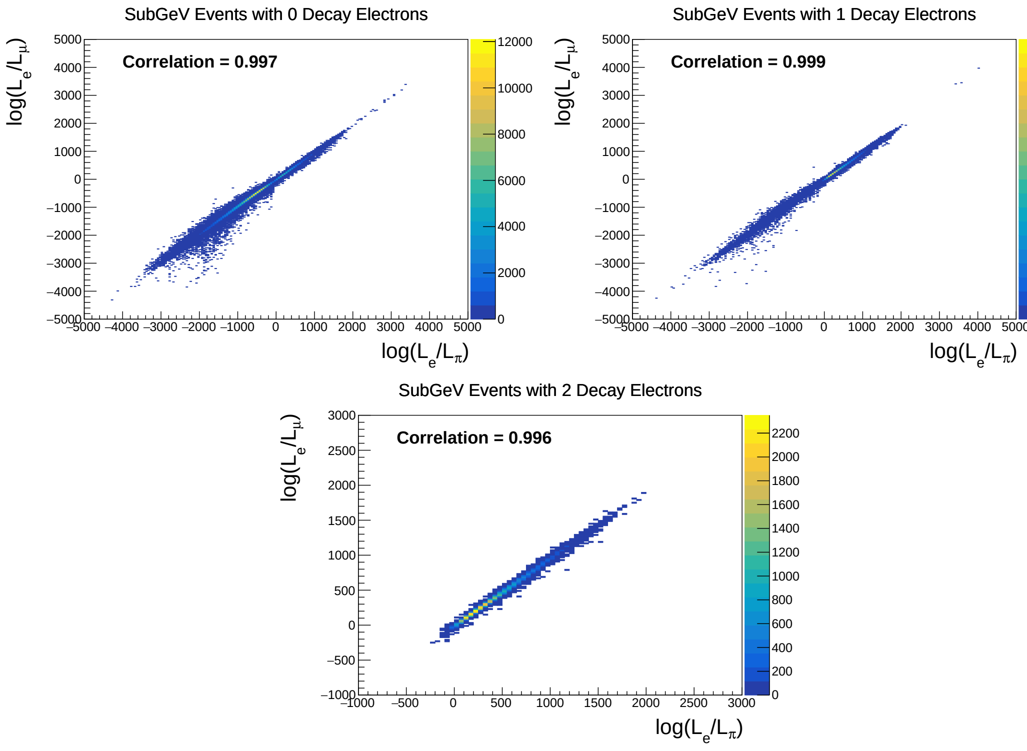

Figure 6.15: The distribution of $\log(L_e/L_\mu)$ compared to $\log(L_e/L_\pi)$ for subGeV events with zero (top left), one (top right) or two (bottom) decay electrons. The correlation in the distribution is calculated as 0.997, 0.999 and 0.996, respectively.

and Monte Carlo spectra are represented by N_i^D and N_i^{MC}, respectively. The bin contents for the beam near detector, beam far detector and atmospheric samples are denoted with ND, FD, and Atm, respectively. The binning index, i, runs over all the bins within a sample. Taking the `FHC1Rmu` far detector sample as an example, the binning index runs over all the reconstructed neutrino energy bins. The likelihood calculation between the data and the Monte Carlo prediction for a particular bin follows a Poisson distribution, where the data is treated as a fluctuation of the simulation.

The data can consist of either real data or an 'Asimov' Monte Carlo prediction, which is typically used for sensitivity studies and denoted 'Asimov data'. The process for building Asimov data is as follows. The Monte Carlo prediction is reweighted using a particular set of oscillation parameters (potentially those listed in Table 2.2) and systematic parameter tune. The resulting spectra for each sample is then defined to be the Asimov data for that sample. Whilst this results in unphysical non-integer data predictions, it eliminates statistical fluctuations from the data. Therefore, the results of a fit to Asimov data should not include any biases from statistical fluctuations. Furthermore, these results should produce posterior probability distributions consistent with the parameters which were used to make the data prediction. That is to say, the fit results should return the known parameters. Any biases seen would be attributed to correlations between each oscillation parameter and correlations between oscillation and systematic parameters. Consequently, Asimov fit results present the maximum precision at which the oscillation parameters could be measured to.

Following the T2K analysis presented in [75], the likelihood contribution for the near detector samples also includes a Monte Carlo statistical uncertainty term, derived from the Barlow and Beeston statistical treatment [210, 211]. In addition to treating the data as a Poisson fluctuation of the Monte Carlo prediction, it includes a contribution to the likelihood that which treats the generated Monte Carlo prediction as a statistical fluctuation of the actual true simulation assuming an infinite amount of statistics had been created. The technical implementation of this additional likelihood term is documented in [194] and briefly summarised as follows. The term is defined as,

$$\frac{(\beta_i - 1)^2}{2\sigma^2_{\beta_i}}, \tag{6.7}$$

where β_i represents a scaling parameter for the i^{th} bin that relates the bin content for the amount of Monte Carlo actually generated N_i^{MC} to the bin content if an infinite amount of Monte Carlo statistics had been generated $N_{i,true}^{MC}$, such that $N_{i,true}^{MC} = \beta_i \times N_i^{MC}$. In the case where a sufficient amount of Monte Carlo statistics had been generated, $\beta_i = 1$. An analytical solution for β_i is given in [194]. Additionally, $\sigma_{\beta_i} = \sqrt{\sum_i w_i^2}/N_i^{MC}$ where $\sqrt{\sum_i w_i^2}$ represents the sum of the square of the weights of the Monte Carlo events which fall into bin i.

An additional contribution to the likelihood comes from the variation of the systematic model parameters. For those parameters with well-motivated uncertainty estimates, a covariance matrix, V, describes the prior knowledge of each parameter as well as any correlations between the parameters. Due to a technical implementation, a single covariance matrix describes each "block" of model parameters, e.g. beam flux systematics. The covariance matrix associated with the k^{th} block is denoted V^k. This substitution results in $\vec{\theta} = \sum_k^{N_b} \vec{\theta}^k$ and $V = \sum_k^{N_b} V^k$ where N_b denotes the number of blocks. A single covariance matrix is provided for: the oscillation parameters, the beam flux parameters, the atmospheric flux parameters, the neutrino interaction systematics, the near detector parameters, the beam far detector systematics, and the atmospheric far detector systematics. The number of parameters in the k^{th} block is defined as $n(k)$.

The equation for the likelihood $\mathcal{L}$ includes all the terms discussed above. It is defined as,

$$
\begin{aligned}
&-\ln(\mathcal{L}) = \\
&\sum_i^{\text{NDbins}} N_i^{\text{ND},MC}(\vec{\theta}) - N_i^{\text{ND},D} + N_i^{\text{ND},D} \times \ln\left[N_i^{\text{ND},D} / N_i^{\text{ND},MC}(\vec{\theta})\right] + \frac{(\beta_i - 1)^2}{2\sigma_{\beta_i}^2} \\
&+ \sum_i^{\text{FDbins}} N_i^{\text{FD},MC}(\vec{\theta}) - N_i^{\text{FD},D} + N_i^{\text{FD},D} \times \ln\left[N_i^{\text{FD},D} / N_i^{\text{FD},MC}(\vec{\theta})\right] \\
&+ \sum_i^{\text{Atmbins}} N_i^{\text{Atm},MC}(\vec{\theta}) - N_i^{\text{Atm},D} + N_i^{\text{Atm},D} \times \ln\left[N_i^{\text{Atm},D} / N_i^{\text{Atm},MC}(\vec{\theta})\right] \\
&+ \frac{1}{2} \sum_k^{N_b} \sum_i^{n(k)} \sum_j^{n(k)} (\vec{\theta}^k)_i (V^k)_{ij}^{-1} (\vec{\theta}^k)_j.
\end{aligned}
\tag{6.8}
$$

The negative log-likelihood value is determined at each step of the MCMC to build the posterior distribution defined in chapter 4. This value is minimised when the Monte Carlo prediction tends towards the data spectrum.

7 Oscillation Probability Calculation

It is important to understand how and where the sensitivity to the oscillation parameters comes from for both atmospheric and beam samples. An overview of how these samples respond to changes in δ_{CP}, Δm^2_{32}, and $\sin^2(\theta_{23})$ is given in section 2.5. This section also explains the additional complexities involved when performing an atmospheric neutrino analysis as compared to a beam-only analysis.

Without additional techniques, atmospheric sub-GeV upward-going neutrinos ($E_\nu < 1.33\text{GeV}, \cos(\theta_Z) < 0.$) can artificially inflate the sensitivity to δ_{CP} due to the quickly varying oscillation probability in this region. Therefore, a "sub-sampling" approach has been developed to reduce these biases ensuring accurate and reliable sensitivity measurements. This technique ensures that small-scale unresolvable features of the oscillation probability have been averaged over whilst the large-scale features in the oscillation probability are unaffected. The documentation and validation of this technique are found in section 7.1. The oscillation probability calculation is computationally intensive due to the large number of matrix multiplications needed. Consequently, the `CUDAProb3` implementation choice made within the fitting framework, as detailed in section 7.2, ensures that the analysis can be done in a timely manner.

Whilst the beam neutrinos are assumed to propagate through a constant density slab of material, the density variations through the Earth result in more complex oscillation patterns for atmospheric neutrinos. Furthermore, the uncertainty in the electron density can modify the oscillation probability for the denser core layers of the Earth. The model of the Earth used within this analysis is detailed in section 7.3. This includes information about the official SK-only methodology as well as improvements that have been made to remove some of the approximations used in that analysis. Another complexity of atmospheric neutrino oscillation studies is that the height of production in the atmosphere is not known on an event-by-event basis. An analytical averaging technique that approximates the uncertainty of the oscillation probability has been followed, with the author of this thesis being responsible for the implementation and validation. This implementation of an external technique is described in section 7.4.

7.1 Treatment of Fast Oscillations

As shown in Figure 7.1, atmospheric neutrino oscillations have a significantly more complex structure for upgoing neutrinos with energy below 1GeV. This is because the L/E dependence of the oscillation probability in this region induces rapid variations for small changes in L or E. As discussed in section 2.5, this is also the region in which atmospheric neutrinos have sensitivity to δ_{CP}. In practice, the direction of the neutrino is inferred from the direction of the final state particles traveling in the detector. The correlation between these two directions can be particularly weak for low-energy neutrino interactions. This creates a distinct difference from the beam neutrinos where the position of the source is very precisely known.

As a consequence of the unresolvable structure, an event rate consistent with the averaged oscillation probability is observed in the subGeV upgoing region. This creates a computational problem: A significantly large amount of Monte Carlo statistics would be required to accurately predict the number of events if Monte Carlo averaging was the only technique used. This section describes the 'sub-sampling' approach developed for this analysis and compares it to the methodology used within the SK-only analysis.

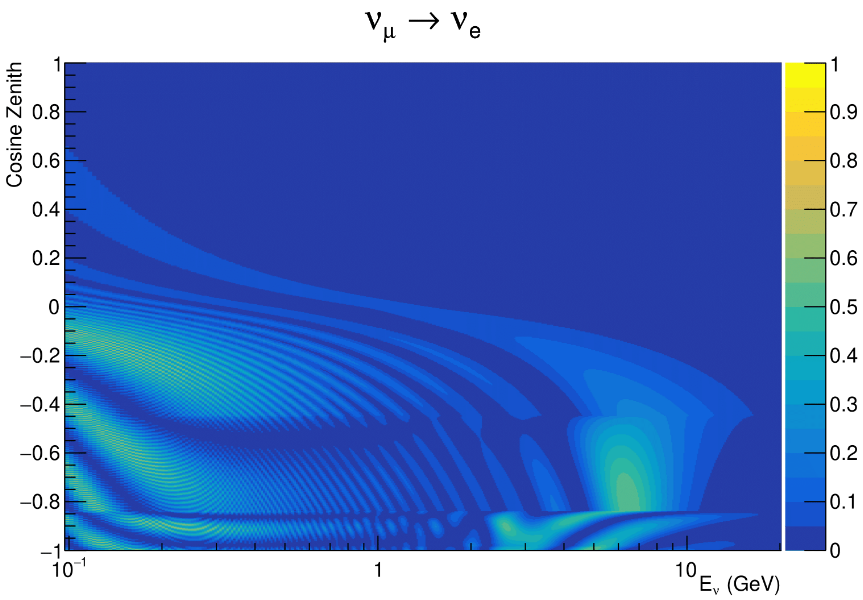

Figure 7.1: The oscillation probability $P(\nu_\mu \rightarrow \nu_e)$, given as a function of neutrino energy and zenith angle, which highlights an example of the "fast" oscillations in the sub-GeV upgoing region.

DB: Figure out what this actually means The official SK-only analysis uses the osc3++ oscillation parameter fitter [79]. To perform the fast oscillation averaging, it uses a 'nearest-neighbour' technique. For a given Monte Carlo neutrino event, the nearest twenty Monte Carlo neighbours in reconstructed lepton momentum and zenith angle are found and a distribution of their neutrino energies is built. The RMS, σ, of this distribution is then used to compute an average oscillation probability for the given neutrino Monte Carlo event.

For the i^{th} event, the oscillation weight is calculated as

$$W_i = \frac{1}{5}P(E_i, \bar{L}_i) + \frac{1}{5}\sum_{\beta=-1,-0.5,0.5,1} P(E_i + \beta\sigma_i, L_\beta), \qquad (7.1)$$

where $P(E, L)$ is the oscillation probability calculation for neutrino energy E and path length L and the two path lengths, $\bar{L}_i$ and L_β are discussed below. All of the oscillation probability calculations are performed with a fixed zenith angle such that the same density profile is used.

The uncertainty in the production height is controlled by using an "average" production height, $\bar{L}_i$, which represents the average path length computed using twenty production heights taken from the Honda flux model's prediction [53]. For a given event, the production heights are sampled in steps of 5% of their cumulative distribution function. L_β values are similarly calculated but instead use different combinations of four production heights,

$$\begin{aligned}
L_{-1.0} &= \frac{1}{4}L(45, 50, 55, 60), \\
L_{-0.5} &= \frac{1}{4}L(35, 40, 65, 70), \\
L_{+0.5} &= \frac{1}{4}L(25, 30, 75, 68), \\
L_{+1.0} &= \frac{1}{4}L(15, 20, 85, 89).
\end{aligned} \tag{7.2}$$

This averaging technique works because of the inference between the zenith angle and the reconstructed direction of final state particles in the detector. For low-energy neutrinos, where the resolution of the true neutrino direction is poor, σ_i will be large, resulting in significant averaging effects. Contrary to this, the inferred direction of high-energy neutrinos will be much closer to the true value, meaning that σ_i will be smaller, culminating in small averaging effects.

In practice, these calculations are performed prior to the fit as only oscillation parameters at fixed points are considered. The MCMC technique used in this thesis requires oscillation probabilities to be evaluated at arbitrary parameter values, not known *a priori*. Calculating the five oscillation probabilities per event required by the SK technique is computationally infeasible, so a different averaging technique is used. However, the concept of the averaging technique can be taken from it.

To perform a similar averaging as the SK analysis, a sub-sampling approach using binned oscillograms has been devised. A coarsely binned oscillogram is defined in $\cos(\theta_Z)$ and E_ν. For a given set of oscillation parameters, a single oscillation probability will be assigned to each coarse bin. This value will then apply to all Monte Carlo events which fall into that bin. To assign these oscillation probabilities, the probability is calculated at $N \times N$ points on a grid within a particular bin. This ensemble of oscillation probabilities is averaged to define the coarse bin's oscillation probability, assuming a flat prior in E_ν and $\cos(\theta_Z)$ within the bin. Figure 7.2 illustrates the $N = 2$ example where the assigned value to a coarse bin is the average of the four fine bins which fall in that coarse bin. Whilst the coarse bin edges do not have to be linear on either axis, the sub-division of the fine bins is linear within the range of a coarse bin.

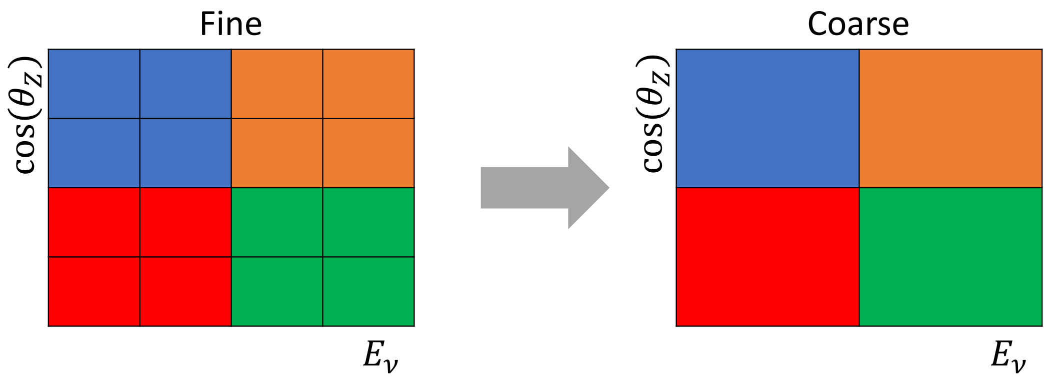

Figure 7.2: Illustration of the averaging procedure for $N = 2$. The oscillation probabilities calculated on the finer left binning are averaged to obtain the oscillation probabilities in the coarser right binning. These averaged oscillation probabilities with the coarser binning are then applied to each event during the fit.

The coarse binning is defined with 67×52 bins in true neutrino energy $\times$ cosine zenith. It is picked to be identical to that provided in [212]. In general, the binning is logarithmically spaced in neutrino energy but has some hand-picked bin edges around the matter resonance to smoothly increased the bin density. This is to avoid smearing this region which can be well sampled by the Monte Carlo. The cosine zenith binning is approximately linearly spaced across the allowable range but the values of layer transitions are hit precisely: -0.8376 (core-mantle) and -0.4464 (mantle/transition zone). Bins are spread further apart for downgoing events as this is a region unaffected by the fast oscillation wavelengths and reduces the total number of calculations required to perform the calculation.

The choice of N is justified based on two studies. Firstly, the variation of event rates of each sample is studied as a function of N. For a given set of oscillation parameters thrown from the PDG prior constraints (detailed in Table 2.1), the oscillation probabilities are calculated using a given value of N. Each sample is re-weighted and the event rate is stored. The value of N is scanned from 1, which corresponds to no averaging, to 19, which corresponds to the largest computationally viable subdivision binning. The event rate of each sample at large N is expected to converge to a stationary value due to the fine binning fully sampling the small-scale structure. Figure 7.3 illustrates this behaviour for the `SubGeV_elike_0dcy` sample for 9 different throws of the oscillation parameters.

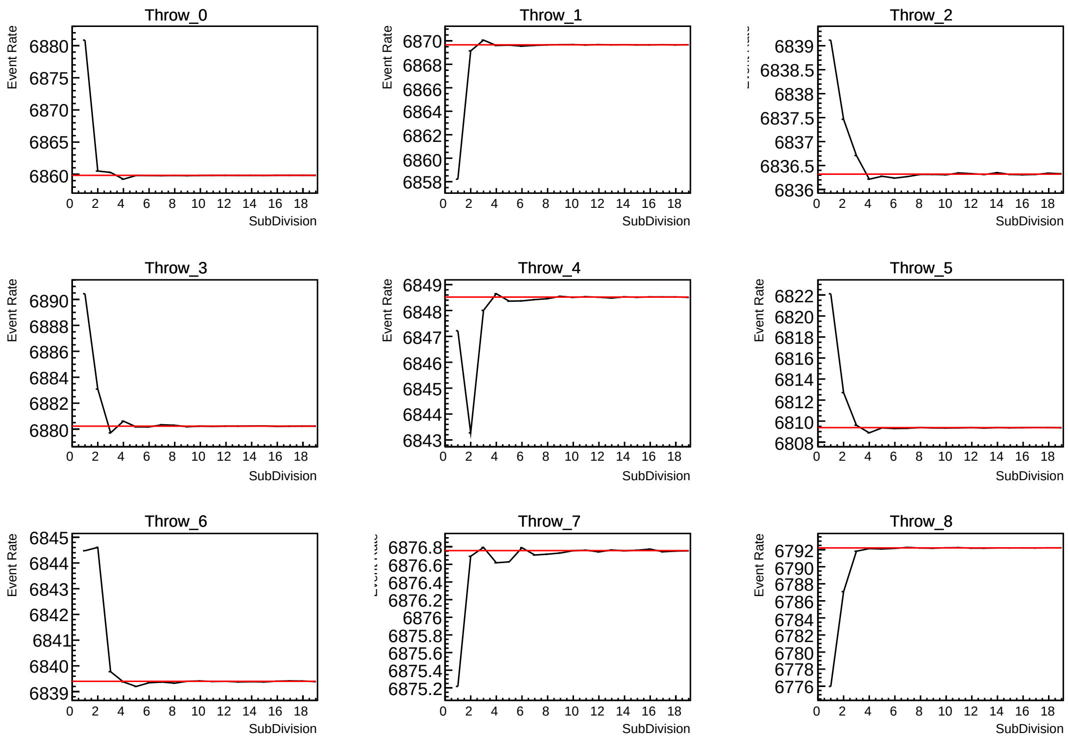

Figure 7.3: Event rate of the `SubGeV_elike_0dcy` sample as a function of the number of sub-divisions per coarse bin. Each subplot represents the event rate of the sample at a different oscillation parameter set thrown from the PDG priors detailed in Table 2.1. The red line in each subplot represents the mean of the event rate over the different values of sub-divisions for that particular oscillation parameter throw.

Denoting the event rate for one sample for a given throw t at each N by λ_t^N, the average over all considered N values ($\overline{\lambda}_t = \frac{1}{24}\sum_{N=1}^{24}\lambda_t^N$) is computed. The variance in the event rate at each N is then calculated as

$$\mathrm{Var}\left[\lambda^N\right] = \frac{1}{N_{\mathrm{throws}}} \sum_{t=1}^{N_{\mathrm{throws}}} \left(\lambda_t^N - \overline{\lambda}_t\right)^2 - \left[\frac{1}{N_{\mathrm{throws}}} \sum_{t=1}^{N_{\mathrm{throws}}} \left(\lambda_t^N - \overline{\lambda}_t\right)\right]^2 . \tag{7.3}$$

In practice, the following procedure is undertaken. For a particular throw, the difference between the event rate at a particular choice of N and the mean of the distribution is calculated. This is illustrated in Figure 7.4. This value is then calculated for all the 2000 throws, generating a distribution of $\lambda_t^N - \overline{\lambda}_t$. This is repeated for each of the values of N considered within this study. The distributions of this value, for $N = \{1, 5\}$, are given in Figure 7.5. As expected, the distribution gets narrower and tends towards zero for the higher values of N.

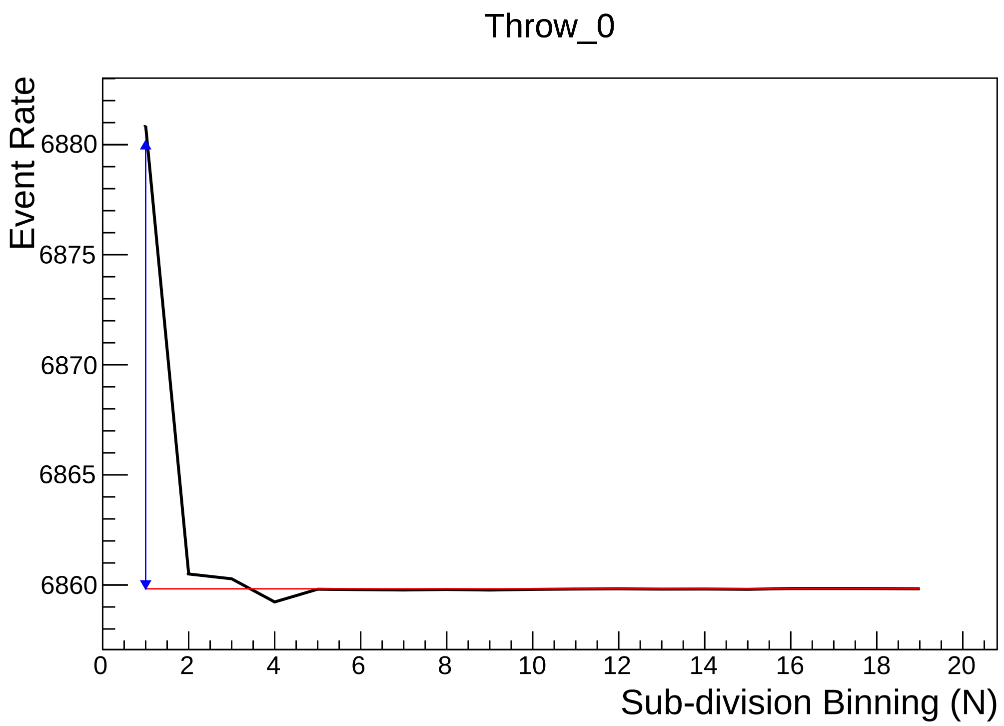

Figure 7.4: Event rate of the `SubGeV_elike_0dcy` sample, for a particular oscillation parameter throw, as a function of the number of sub-divisions, N, per coarse bin. The difference between the mean event rate (red), $\bar{\lambda}$, and the event rate at $N = 1$, $\lambda^{N=1}$ is defined as $\lambda^N - \bar{\lambda}$ and illustrated by the blue arrow.

The aim of the study is to find the lowest value of N such that this variance is below 0.001. This utilises the width of the distributions given in Figure 7.5.

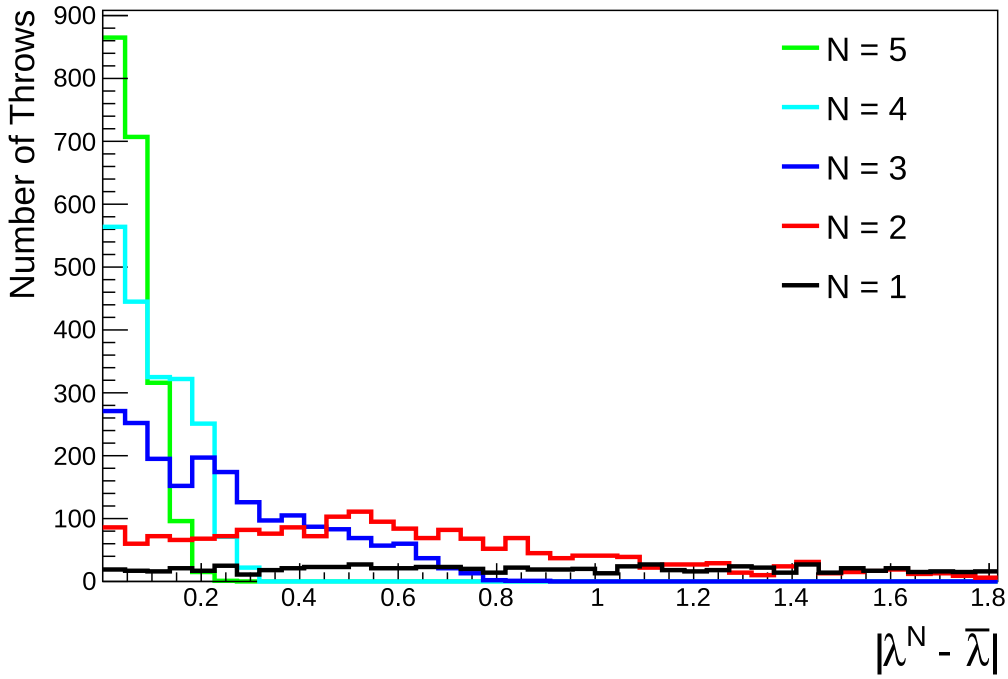

Figure 7.5: The distribution of $\lambda^N - \bar{\lambda}$ for various values of N. As expected, the distribution gets narrower for larger values of N.

This is the typical threshold used by T2K fitters to validate systematic implementation so has been set as the same criteria. The results of this study for each atmospheric sample used within this thesis are illustrated in Figure 7.6 for 2000 throws of the oscillation parameters. As can be seen, the variance is below the threshold at $N = 10$, and is driven primarily by the `SubGeV_mulike_1dcy` and `SubGeV_elike_0dcy` samples.

The second study to determine the value of N is as follows. The likelihood for each sample is computed against an Asimov data set created with Asimov A oscillation parameters (Table 2.2). Following Equation 7.3, the variance of the log-likelihood over all considered N is computed. The results are shown in Figure 7.7.

A choice of $N = 10$ sub-divisions per coarse bin has a variance in both event rate and log-likelihood residuals less than the required threshold of 0.001. The largest value of the likelihood variance is of order 10^{-7}, corresponding to an error on the log-likelihood of about 3×10^{-4} which is small enough to be

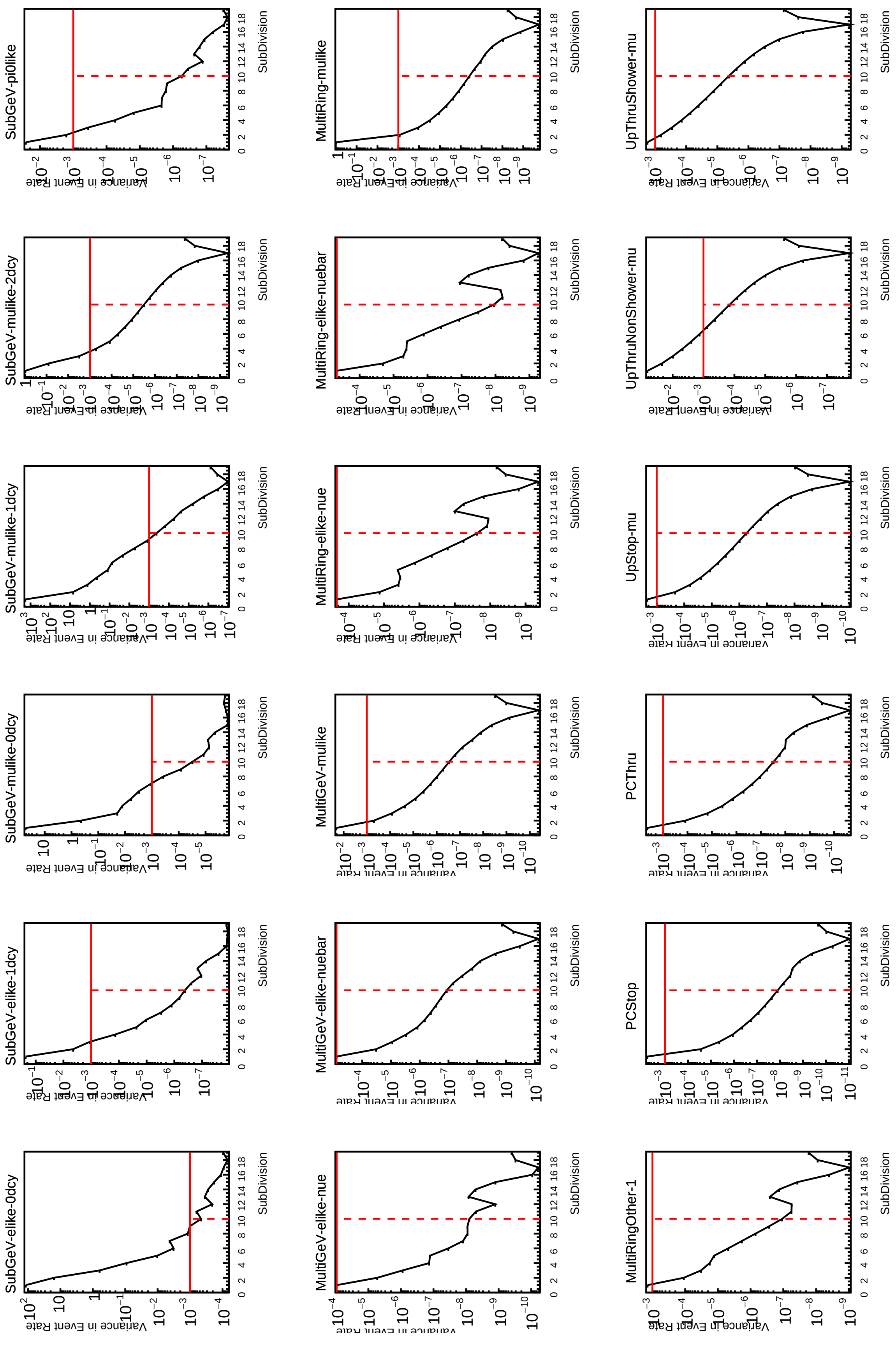

Figure 7.6: Variance of event rate for each atmospheric sample as a function of the number of sub-divisions per coarse bin. The solid red line indicates the 0.1% threshold and the dashed red line indicates the variance at a sub-division $N = 10$.

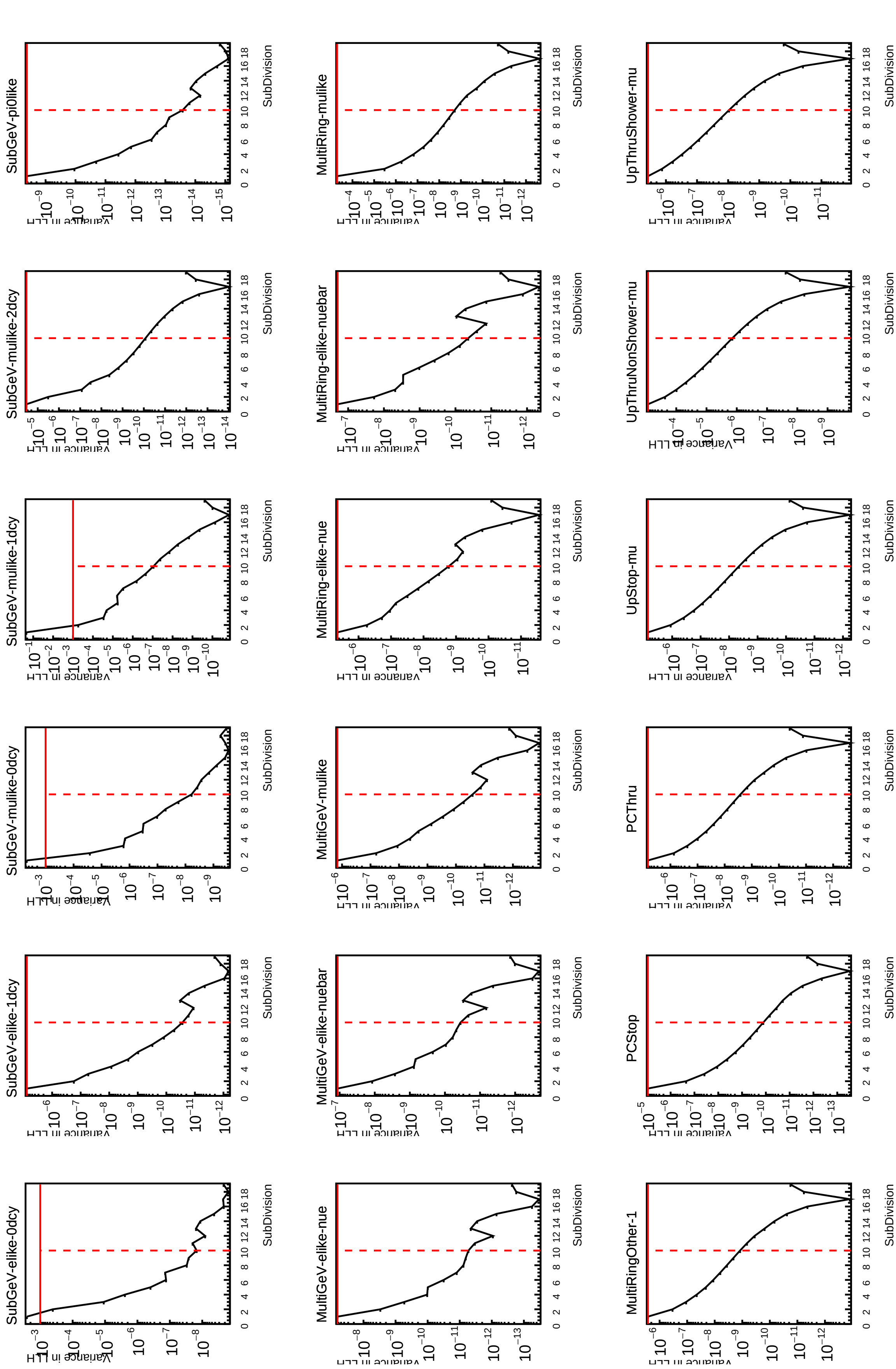

Figure 7.7: Variance of sample likelihood, when compared to 'Asimov data' set at Asimov A, for each atmospheric sample as a function of the number of sub-divisions per coarse bin. The solid red line indicates the 0.1% threshold and the dashed red line is a graphical indication of the variance at a sub-division $N = 10$.

negligible for the oscillation analysis.

Figure 7.8 illustrates the effect of the smearing using $N = 10$. The fast oscillations in the sub-GeV upgoing region have been replaced with a normalisation effect whilst the large matter resonance structure remains.

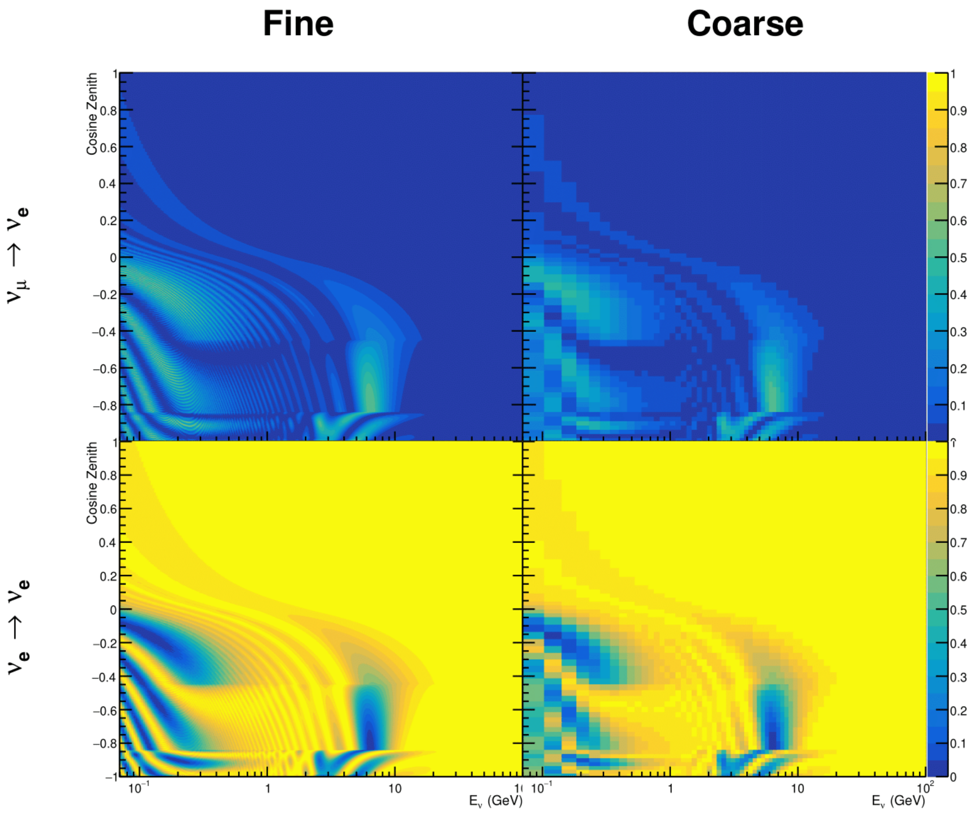

Figure 7.8: The oscillation probability, $P(\nu_\mu \rightarrow \nu_e)$ (top row) and $P(\nu_e \rightarrow \nu_e)$ (bottom row), given as a function of neutrino energy and zenith angle. The left column gives the “fine” binning used to calculate the oscillation probabilities and the right column illustrates the “coarse” binning used to reweight the Monte Carlo events. The fine binning choice is given with $N = 10$, which was determined to be below the threshold from Figure 7.6 and Figure 7.7.

7.2 Calculation Engine

As previously discussed in section 7.1, the calculation of oscillation probabilities is performed at run-time. Consequently, the time per calculation is crucial for fit performance. The initial fitting framework used for this analysis was developed with ProbGPU [213]. This is a GPU-only implementation of the prob3 engine [214]. It is primarily designed for neutrino propagation in a beam experiment (single layer of constant density) with the atmospheric propagation code not being used prior to the analysis in this thesis.

Another engine, CUDAProb3 [215], has been interfaced with the fitting framework used in this analysis. This interfacing was done by the author of this thesis. It has been specifically optimised for atmospheric neutrino oscillation calculation so does not contain the code to replace the beam oscillation calculation. The engine utilises object-orientated techniques as compared to the functional implementation of ProbGPU. This allows the energy and cosine zenith arrays to be kept on GPU memory, rather than having to load these arrays onto GPU memory for each calculation. Reducing the memory transfer between CPU and GPU significantly reduces the time required for calculation. This can be seen in Figure 7.9, where the GPU implementation of CUDAProb3 is approximately three times faster than the ProbGPU engine.

Another significant advantage of CUDAProb3 is that it contains a CPU multi-threaded implementation which is not possible with the ProbGPU or prob3 engines. This eliminates the requirement for GPU resources when submitting jobs to batch systems. As illustrated in Figure 7.9, the calculation speed depends on the number of available threads. Using 8 threads (which is typical of the batch systems being used) is approximately twice as slow as the ProbGPU engine implementation, but would allow the fitting framework to be run on many more resources. This fact is utilised for any SK-only fits but GPU resources are required for any fits which include beam samples due to the ProbGPU requirement. Based on the benefits shown by the implementation in this section, efforts are being placed into including linear propagation for beam neutrino propagation into the engine [216].

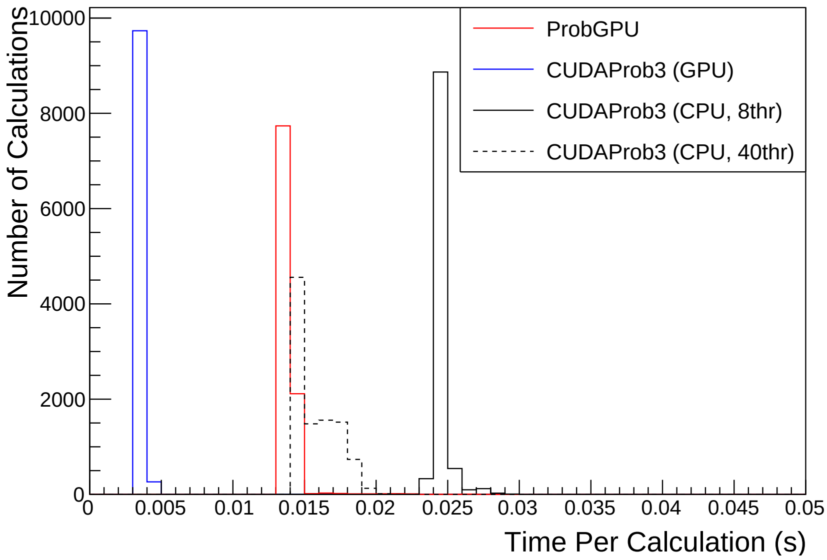

Figure 7.9: The calculation time taken to both calculate the oscillation probabilities and fill the "coarse" oscillograms, following the technique given in section 7.1, for the `CUDAProb3` and `ProbGPU` (Red) calculation engines. `CUDAProb3` has both a GPU (Blue) and CPU (Black) implementation, where the CPU implementation is multi-threaded. Therefore, 8-threads (solid) and 40-threads (dashed) configurations have been tested. `Prob3`, which is a CPU single-thread implementation has a mean step time of 1.142s.

7.3 Matter Density Profile

For an experiment observing neutrinos propagating through the Earth, a model of the Earth's density profile is required. The model used within this analysis is based on the Preliminary Reference Earth Model (PREM) [80], as illustrated in Figure 2.8. Table 2.3 documents the density and radii of the layers used within the constant density approximation used by the SK-only analysis [79]. The density measurements provided in the PREM model are provided in terms of mass density, whereas neutrino oscillations are sensitive to the electron number density. This value can be computed as the product of the chemical composition, or the Z/A value, and the mass density of each layer. Currently, the only way to measure the chemical composition value for layers close to the Earth's core is through neutrino oscillations. The chemical composition of the upper layers of the Earth's Mantle and the Transition zone is well known due to it being predominantly pyrolite which has a chemical composition value of 0.496 [217].

The chemical composition dial for the core layers is set to a value of 0.468, as calculated in [218]. As this value is less well known, it is assigned a Gaussian error with a standard deviation equivalent to the difference in chemical composition in core and mantle layers. Figure 7.10 illustrates the effect of moving from the $Z/A = 0.5$ method which is used in the official SK-only analysis to these more precise values.

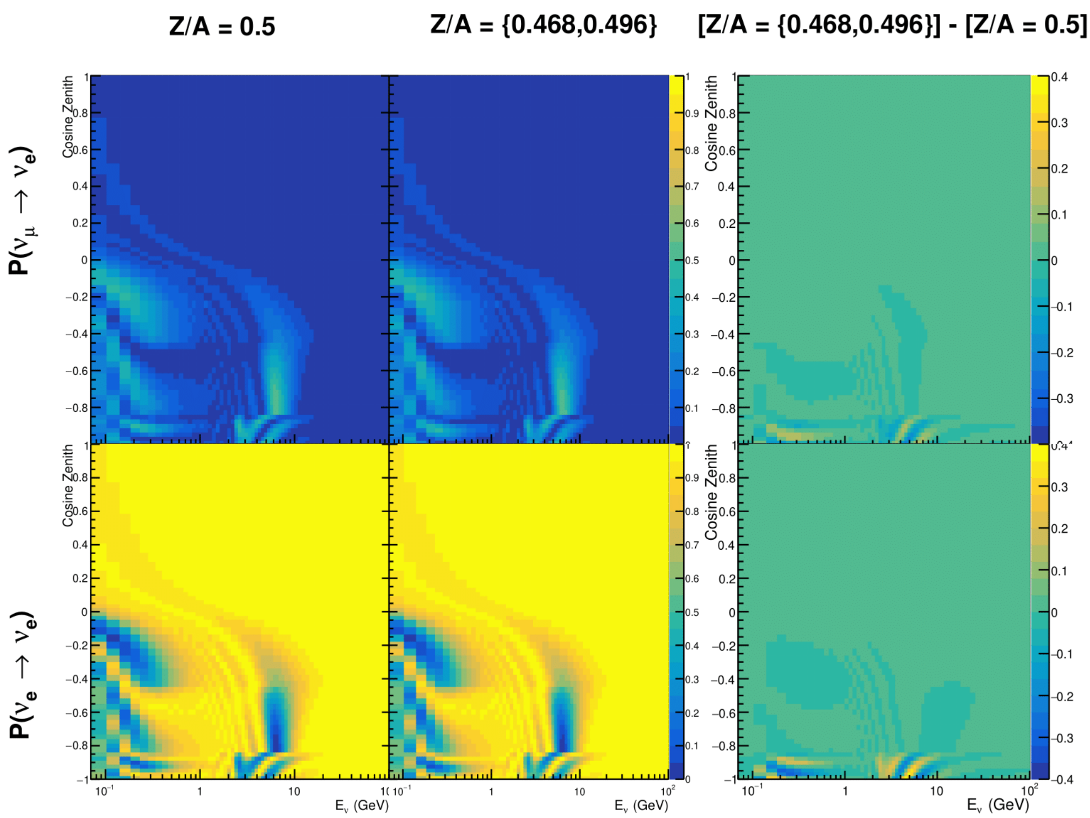

Figure 7.10: The oscillation probability, $P(\nu_\mu \rightarrow \nu_e)$ (top row) and $P(\nu_e \rightarrow \nu_e)$ (bottom row), given as a function of neutrino energy and zenith angle. The left column gives probabilities where the constant $Z/A = 0.5$ approximation which is used in the official SK-only analysis. The middle column gives the probabilities where $Z/A = [0.468, 0.498]$ values are used, as given in Table 2.3. The right column illustrates the difference in oscillation probability between the two different techniques.

The beam oscillation probability in this thesis uses a baseline of 295km, density 2.6g/cm^3, and chemical composition 0.5 as is done by the official T2K-only analysis [219].

For a neutrino with given E_ν, $\cos(\theta_Z)$, the oscillation probability calculation engine must be passed a list of the matter regions that the neutrino traversed, with the path length and fixed density in each region. However, a neutrino passing through the earth experiences a range of radii, and thus a range of densities, in each region. In the SK-only analysis, the earth density model used is piecewise-constant, thereby ignoring this effect. For this thesis, the density values for the calculation engine are found by averaging the earth density along the neutrino's path in each layer,

$$\langle \rho \rangle_i = \frac{1}{t_{i+1} - t_i} \int_{t_i}^{t_i+1} \rho(t) dt \tag{7.4}$$

where t_i are the intersection points between each layer and t is the path length of the trajectory across the layer. This leads to an improved approximation. For this averaging, the simplification of the PREM model developed in [220] is used. The layers of the prem model are combined into four to reduce calculation time, with a quadratic fit to each section. This fit was not performed by the author of the thesis and is documented in [212]. The coefficients of the quadratic fit to each layer are given in Table 7.1 with the final distribution illustrated in Figure 7.11. The quadratic approximation is clearly much closer to the PREM model as compared to the constant density approximation.

Layer	Outer Radius [km]	Density [g/cm^3]
Inner Core	1220	$13.09 - 8.84x^2$
Outer Core	3480	$12.31 + 1.09x - 10.02x^2$
Lower Mantle	5701	$6.78 - 1.56x - 1.25x^2$
Transition Zone	6371	$-50.42 + 123.33x - 69.95x^2$

Table 7.1: The quadratic polynomial fits to the PREM model for four assumed layers of the PREM model. The fit to calculate the coefficients is given in [212], where $x = R/R_{Earth}$.

The effect of using the quadratic density per $\cos(\theta_Z)$ model is highlighted in Figure 7.12. The slight discontinuity in the oscillation probability around $\cos(\theta_Z) \sim -0.45$ in the fixed density model, which is due to the transition to mantle layer boundary, has been reduced. This is expected as the difference in

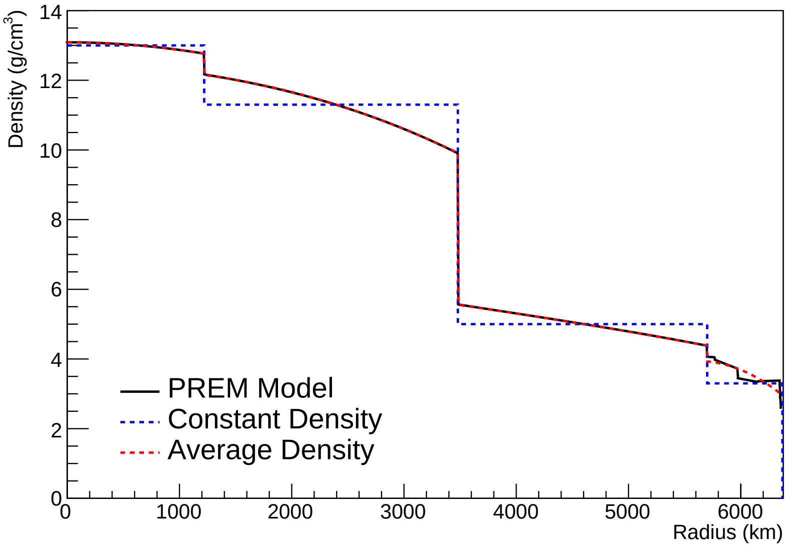

Figure 7.11: The density of the Earth given as a function of the radius, as given by the PREM model (Black), the constant density four-layer approximation (Blue), as used in the official SK-only analysis, and the quadratic approximation of the PREM model (Red).

the density across this boundary is significantly smaller in the quadratic density model as compared to the constant density model. Whilst the difference in density across the other layer transitions is reduced, there is still a significant difference. This means the discontinuities in the oscillation probabilities remain but are significantly reduced. However, as the quadratic density approximation matches the PREM model well in this region, these discontinuities are due to the Earth model rather than an artifact of the oscillation calculation.

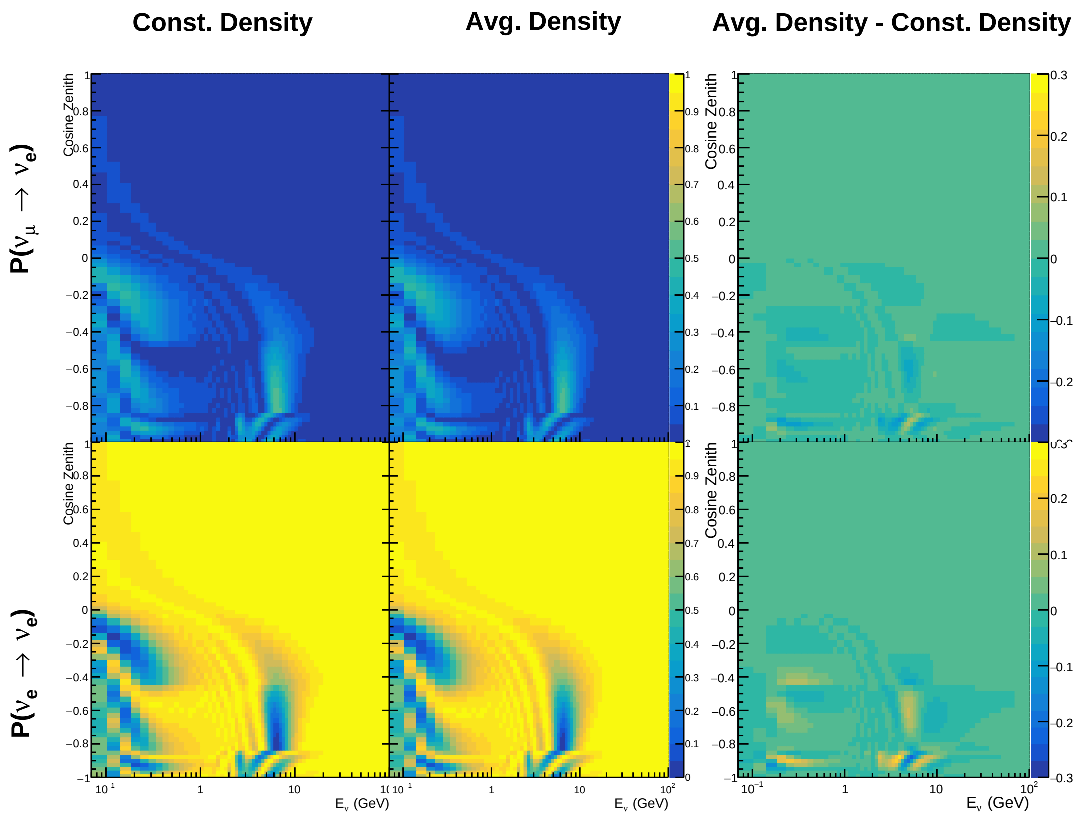

Figure 7.12: The oscillation probability, $P(\nu_\mu \rightarrow \nu_e)$ (top row) and $P(\nu_e \rightarrow \nu_e)$ (bottom row), given as a function of neutrino energy and zenith angle. The left column gives probabilities where the four-layer constant density approximation is used. The middle column gives the probabilities where the density is integrated over the trajectory, using the quadratic PREM approximation, for each $\cos(\theta_Z)$ is used. The right column illustrates the difference in oscillation probability between the two different techniques.

7.4 Production Height Averaging

As discussed in section 2.5, the height at which the cosmic ray flux interacts in the atmosphere is not known on an event-by-event basis. The production height can vary from the Earth's surface to $\sim$ 50km above that. The SK-only analysis methodology (described in section 7.1) for including the uncertainty on the production height is to include variations from the Honda model when pre-calculating the oscillation probabilities prior to the fit. This technique is not possible for this analysis which uses continuous oscillation parameters that can not be known prior to the fit. Consequently, an analytical averaging technique was developed in [212]. The author of this thesis was not responsible for the derivation of the technique but has performed the implementation and validation of the technique for this analysis alone.

Using the 20 production heights per Monte Carlo neutrino event, provided as 5% percentiles from the Honda flux model, a production height distribution $p_j(h|E_\nu, \cos\theta_Z)$ is built for each neutrino flavour $j = \nu_e, \bar{\nu}_e, \nu_\mu, \bar{\nu}_\mu$. In practice, a histogram is filled with 20 evenly spaced bins in production height h between 0 and 50km. The neutrino energy and cosine zenith binning of the histogram are the same as that provided in section 7.1. The average production height, $\bar{h} = \int dh \frac{1}{4} \sum_j p_j(h|E_\nu, \cos(\theta_Z))$, is calculated. This assumes a linear average over the four flavours of neutrino which are considered to be generated in cosmic ray showers. The production height binning of this histogram is then translated into $\delta t(h) = t(\bar{h}) - t(h)$, where $t(h)$ is the distance travelled along the trajectory.

For the i^{th} traversed layer, the transition amplitude, $D_i(t_{i+1}, t_i)$, is computed. The time-ordered product of these is then used as the overall transition amplitude via

$$A(t_{n+1}, t_0) = D_n(t_{n+1}, t_n)...D_1(t_2, t_1)D_0(t_1, t_0), \tag{7.5}$$

where,

$$\begin{aligned} D_n(t_{n+1}, t_n) &= \exp[-iH_n(t_{n+1} - t_n)] \\ &= \sum_{k=1}^{3} C_k \exp[ia_k(t_{n+1} - t_n)] \end{aligned} \tag{7.6}$$

is expressed as a diagonalised time-dependent solution to the Schrodinger equation. The 0^{th} layer is the propagation through the atmosphere and is the only term that depends on the production height. Using the substitution $t_0 = t(\bar{h}) - \delta t(h)$, it can be shown that

$$D_0(t_1, t_0) = D_0(t_1, \bar{h}) D_0(\delta t). \tag{7.7}$$

Thus Equation 7.5 becomes

$$\begin{aligned} A(t_{n+1}, t_0) &= D_n(t_{n+1}, t_n) ... D_1(t_2, t_1) D_0(t_1, \bar{h}) D(\delta t) \\ &= A(t_{n+1}, \bar{h}) \sum_{k=1}^{3} C_k \exp[ia_k \delta t], \\ &= \sum_{k=1}^{3} B_k \exp[ia_k \delta t]. \end{aligned} \tag{7.8}$$

The oscillation probability averaged over production height is then calculated as

$$\begin{aligned} \overline{P}(\nu_j \to \nu_i) &= \int d(\delta t) p_j(\delta t | E_\nu, \cos\theta_Z) P(\nu_j \to \nu_i) \\ &= \int d(\delta t) p_j(\delta t | E_\nu, \cos\theta_Z) A(t_{n+1}, t_0) A^*(t_{n+1}, t_0) \\ &= \sum_{km} (B_k)_{ij} (B_m)^*_{ij} \int d(\delta t) p_j(\delta t | E_\nu, \cos\theta_Z) \exp[i(a_k - a_m)\delta t] \end{aligned} \tag{7.9}$$

It is important to note that the exact value of $\bar{h}$ used does not matter as the values of δt would change to compensate for any modification to the value of $\bar{h}$.

In practice, implementation in CUDAProb3 [215] is relatively straightforward as the majority of these terms are already calculated in the standard oscillation calculation. Figure 7.13 illustrates the results of the production height averaging.

As expected, the main effect is observed in the low-energy downward-going and horizontal-going events. Upward-going events have to travel the radius of the Earth, $R_E = 6371$km, where the production height uncertainty is a small fraction of the total path length.

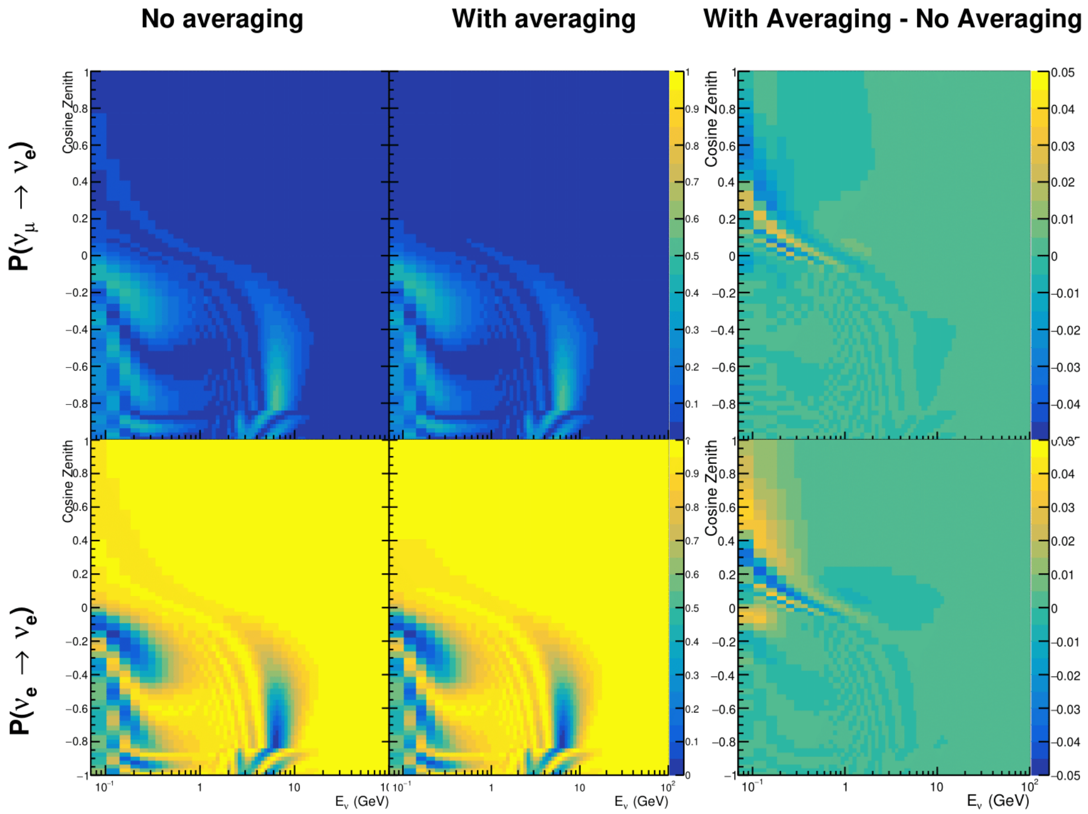

Figure 7.13: The oscillation probability, $P(\nu_\mu \to \nu_e)$ (top row) and $P(\nu_e \to \nu_e)$ (bottom row), given as a function of neutrino energy and zenith angle. The left column gives probabilities where a fixed production height of 25km is used. The middle column gives the probabilities where the production height is analytically averaged. The right column illustrates the difference in oscillation probability between the two different techniques.

8
Oscillation Analysis

Using the samples and systematics defined in chapter 6, this chapter documents a simultaneous beam and atmospheric oscillation analysis from the T2K and SK experiments. The `MaCh3` Bayesian MCMC framework introduced in chapter 4 is used for all studies performed within this thesis.

The `MaCh3` framework used throughout this thesis has been validated through many tests. The code which handles the beam far detector samples was developed by the author and validated by comparison to the 2020 T2K analysis [75]. The sample event rates and likelihood evaluations of beam samples generated by the framework used within this thesis were compared to those from the T2K analysis by the author of this thesis. Variations of the sample predictions were compared at $\pm 1\sigma$ and $\pm 3\sigma$ and good agreement was found in all cases. A similar study, led by Dr. C. Wret was used to validate the near detector portion of the code [205]. The implementation of the atmospheric samples within `MaCh3` was completed and cross-checked by the author of this thesis against the P-Theta framework (Introduced in section 3.2). Both fitters are provided with the same inputs and can therefore cross-validate each other. These validations compared the event rate and likelihood calculation. Documentation of all the above validations can be found in [205].

8.1 Monte Carlo Prediction

Using the three sets of dial values (generated, pre-BANFF, and post-BANFF tunes) defined in subsection 6.4.3, the predicted event rates for each sample are defined in Table 8.1. The oscillated (AsimovA defined in Table 2.2) and un-oscillated event rates are calculated for each tune.

	Total Predicted Events					
	Generated		Pre-fit		Post-fit	
Sample	Osc	UnOsc	Osc	UnOsc	Osc	UnOsc
`SubGeV-elike-0dcy`	7121.0	7102.6	6556.8	6540.0	7035.2	7015.7
`SubGeV-elike-1dcy`	704.8	725.5	693.8	712.8	565.7	586.0
`SubGeV-mulike-0dcy`	1176.5	1737.2	1078.6	1588.1	1182.7	1757.1
`SubGeV-mulike-1dcy`	5850.7	8978.1	5351.7	8205.1	5867.0	9009.9
`SubGeV-mulike-2dcy`	446.9	655.2	441.6	647.7	345.9	505.6
`SubGeV-pi0like`	1438.8	1445.4	1454.9	1461.1	1131.1	1136.2
`MultiGeV-elike-nue`	201.4	195.6	201.1	195.3	202.6	196.7
`MultiGeV-elike-nuebar`	1141.5	1118.3	1060.7	1039.5	1118.5	1095.7
`MultiGeV-mulike`	1036.7	1435.8	963.1	1334.1	1015.2	1405.9
`MultiRing-elike-nue`	1025.1	982.2	1026.8	984.3	1029.8	986.4
`MultiRing-elike-nuebar`	1014.8	984.5	991.0	962.0	1008.9	978.5
`MultiRing-mulike`	2510.0	3474.4	2475.6	3425.8	2514.6	3480.4
`MultiRingOther-1`	1204.5	1279.1	1205.8	1280.3	1207.4	1281.0
`PCStop`	349.2	459.2	338.4	444.7	346.8	456.1
`PCThru`	1692.8	2192.5	1661.5	2149.8	1689.2	2187.8
`UpStop-mu`	751.2	1295.0	739.7	1271.6	750.4	1293.0
`UpThruNonShower-mu`	2584.4	3031.6	2577.9	3019.4	2586.8	3034.0
`UpThruShower-mu`	473.0	488.6	473.2	488.7	473.8	489.4
`FHC1Rmu`	328.0	1409.2	301.1	1274.7	345.1	1568.0
`RHC1Rmu`	133.0	432.3	122.7	396.2	135.0	443.9
`FHC1Re`	84.6	19.2	77.4	18.2	93.7	19.7
`RHC1Re`	15.7	6.4	14.6	6.1	15.9	6.3
`FHC1Re1de`	10.5	3.2	10.3	3.1	8.8	2.9

Table 8.1: The Monte Carlo predicted event rate of each far detector sample used within this analysis. Three model parameter tunes are considered, as defined in subsection 6.4.3. Un-oscillated and oscillated predictions are given, where the oscillated predictions assume Asimov A oscillation parameters provided in Table 2.2.

Generally, the samples which target CCQE interaction modes observe a decrease in prediction when using the pre-fit dial values. This is in accordance with the Monte Carlo being produced assumed $M_A^{QE} = 1.21\text{GeV}$ [164] whilst the pre-fit dial value is set to $M_A^{QE} = 1.03$GeV as suggested by [203]. Furthermore, the predicted event rates of samples that target CCRES interaction modes are significantly reduced when considering the post-BANFF fit. This follows the observations in subsection 6.4.3. The strength of the accelerator neutrino experiment can be seen in the remarkable difference between the oscillated and unoscillated predictions in the `FHC1Rmu` and `RHC1Rmu` samples. There is a very clear decrease in the expected event rate between the oscillated and un-oscillated predictions which is not as obvious as in the atmospheric samples. This is due to the fact that the beam energy is tuned to the maximum disappearance probability which is not the case for the naturally generated atmospheric neutrinos.

8.1.1 Likelihood Scans

Using the definition of the likelihood presented in section 6.5, the response of each sample to a variation of a particular parameter can be studied. Figure 8.1 presents the variation of all the samples (beam and atmospheric) at the far detector to the oscillation parameters of interest: δ_{CP}, $\sin^2(\theta_{13})$, $\sin^2(\theta_{23})$, and Δm^2_{32}. These plots are colloquially called 'likelihood scan' (or 'log-likelihood scans'). The process of making these plots is as follows. An Asimov data set (following technique detailed in section 6.5) is built using the AsimovA oscillation parameters and pre-fit systematic tune. The Monte Carlo is then reweighted using the value of the oscillation parameter at each point on the x-axis of the scan. The likelihood is then calculated between the Asimov data and Monte Carlo prediction and plotted. This process identifies which samples drive the determination of the oscillation parameters in the joint fit.

Due to the caveat of fixed systematic parameters and the correlations between oscillation parameters being ignored when creating these likelihood scans, the value of $\chi^2 = 1$ (or $-2 \times \ln(\text{Likelihood}) = 1$) does not equate to the typical 1σ sensitivity. However, it does give an indication of which samples respond the strongest to a variation in a particular oscillation parameter. The point at which the likelihood tends to zero illustrates the value of the parameter used to build the Asimov data prediction.

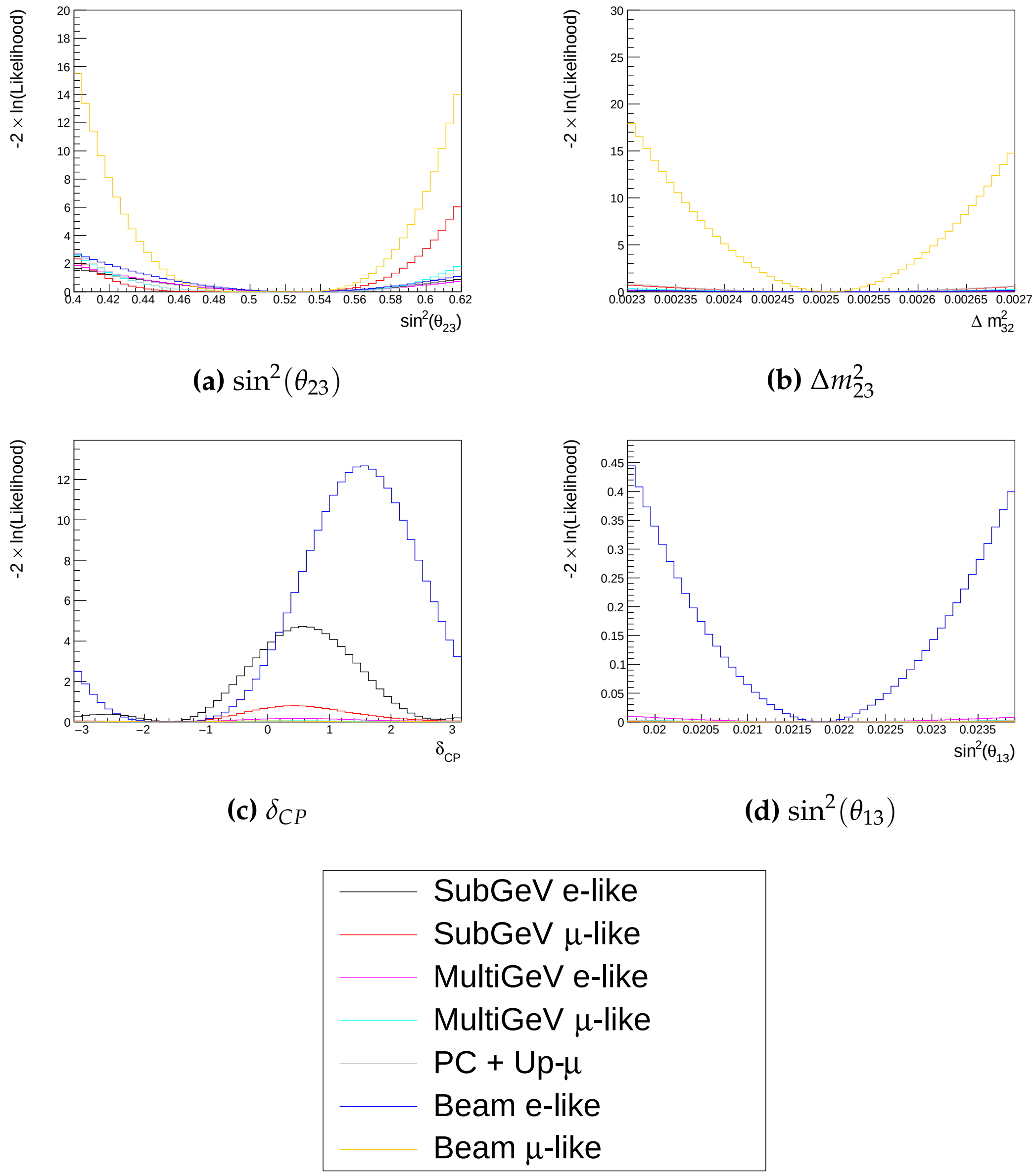

(a) $\sin^2(\theta_{23})$ **(b)** Δm^2_{23}

(c) δ_{CP} **(d)** $\sin^2(\theta_{13})$

Figure 8.1: The response of the likelihood, as defined in section 6.5, illustrating the response of the samples to a variation of an oscillation parameter.

The sensitivity to $\sin^2(\theta_{23})$ is mostly dominated by the beam muon-like samples. The response of an individual atmospheric sample is small but non-negligible such that the summed response over all atmospheric samples becomes comparable to that of the muon-like beam samples. Consequently, the sensitivity of the joint fit to $\sin^2(\theta_{23})$would be expected to be greater than the beam-only analysis. The only sample which respond to the $\sin^2(\theta_{13})$ oscillation parameter is the electron-like beam samples. Consequently, no increase in sensitivity beyond that of the T2K-only analysis would be expected from the joint fit. Regardless, the sensitivity of the beam sample is significantly weaker than the external reactor constraint so prior knowledge will dominate any measurement that is included within this thesis. The Δm^2_{21} and $\sin^2(\theta_{12})$ parameters are not considered as there is simply no sensitivity in any sample considered within this analysis. The response to Δm^2_{32} is completely dominated by the beam muon-like samples. This is because the beam neutrino energy can be specifically tuned to match the maximal disappearance probability. Despite this, improvements to the $|\Delta m^2_{32}|$ sensitivity may be expected due to additional mass hierarchy determination added by the atmospheric samples.

Two-dimensional scans of the appearance ($\sin^2(\theta_{13})$-δ_{CP}) and disappearance ($\sin^2(\theta_{23})$-Δm^2_{32}) parameters are illustrated in Figure 8.2 and Figure 8.3, respectively. The caveat of fixed systematic parameters and correlations between other oscillation parameters being neglected still apply.

The appearance log-likelihood scans show the distinct difference in how the beam and atmospheric samples respond. The beam samples have an approximately constant width of the 2σ and 3σ contours, throughout all ranges of δ_{CP}. The response of the atmospheric samples to $\sin^2(\theta_{13})$ is very strongly correlated to the value of δ_{CP} being evaluated, with the strongest constraints around $\delta_{CP} \sim 1$. Consequently, this difference allows some of the degeneracy in a beam-only fit to be broken. Comparing the beam-only and joint fit likelihood scans, the 2σ continuous contour in δ_{CP} for beam samples is broken when the atmospheric samples are added. This may result in a stronger sensitivity to δ_{CP}. Similarly, the width of the 3σ contours also becomes dependent upon the value of δ_{CP}. Whilst these are encouraging results for the joint fit, these are not sensitivity measurements as the systematic parameters are fixed and the correlation between oscillation parameters is neglected. An interesting point to note is that the atmospheric samples have little sensitivity to $\sin^2(\theta_{13})$ on their own, as evidenced in Figure 8.1, but can improve sensitivity to the parameter when combined within the simultaneous fit.

The response of the atmospheric samples in Figure 8.2 shows an interesting behaviour when considering the application of the reactor constraint. At higher values of $\sin^2(\theta_{13})$, two lobes appear around $\delta_{CP} \sim -\pi/2$ and $\delta_{CP} \sim 2.4$. If this distribution was projected onto the δ_{CP} axis, these lobes would mean the posterior distribution would have a significant dip between these values. However, the region of $\sin^2(\theta_{13})$ near the reactor constraint ($\sin^2(\theta_{13}) = (2.18 \pm 0.08) \times 10^{-2}$) is flatter across the range of δ_{CP}. Therefore, if we were to project only this region onto the δ_{CP} axis, the dip between the peaks would not be as significant. If this behaviour was to be seen in the results of a fit, these marginalisation effects would actually conspire to reduce the sensitivity to δ_{CP} if the reactor constraint was to be applied.

The disappearance log-likelihood scans in $\sin^2(\theta_{23})$-Δm^2_{32} space (Figure 8.3) show the expected behaviour when considering the one-dimensional scans already discussed. The uncertainty on the width of $|\Delta m^2_{32}|$ is mostly driven by the beam-only sensitivities. However, the width of this contour in the inverted mass region ($\Delta m^2_{32} < 0$) is significantly reduced due to the ability of the atmospheric samples to select the correct (normal) mass hierarchy. The width of the uncertainty in $\sin^2(\theta_{23})$ is also reduced compared to the beam-only sensitivities, with a further decrease in the inverted hierarchy region due to the better mass hierarchy determination.

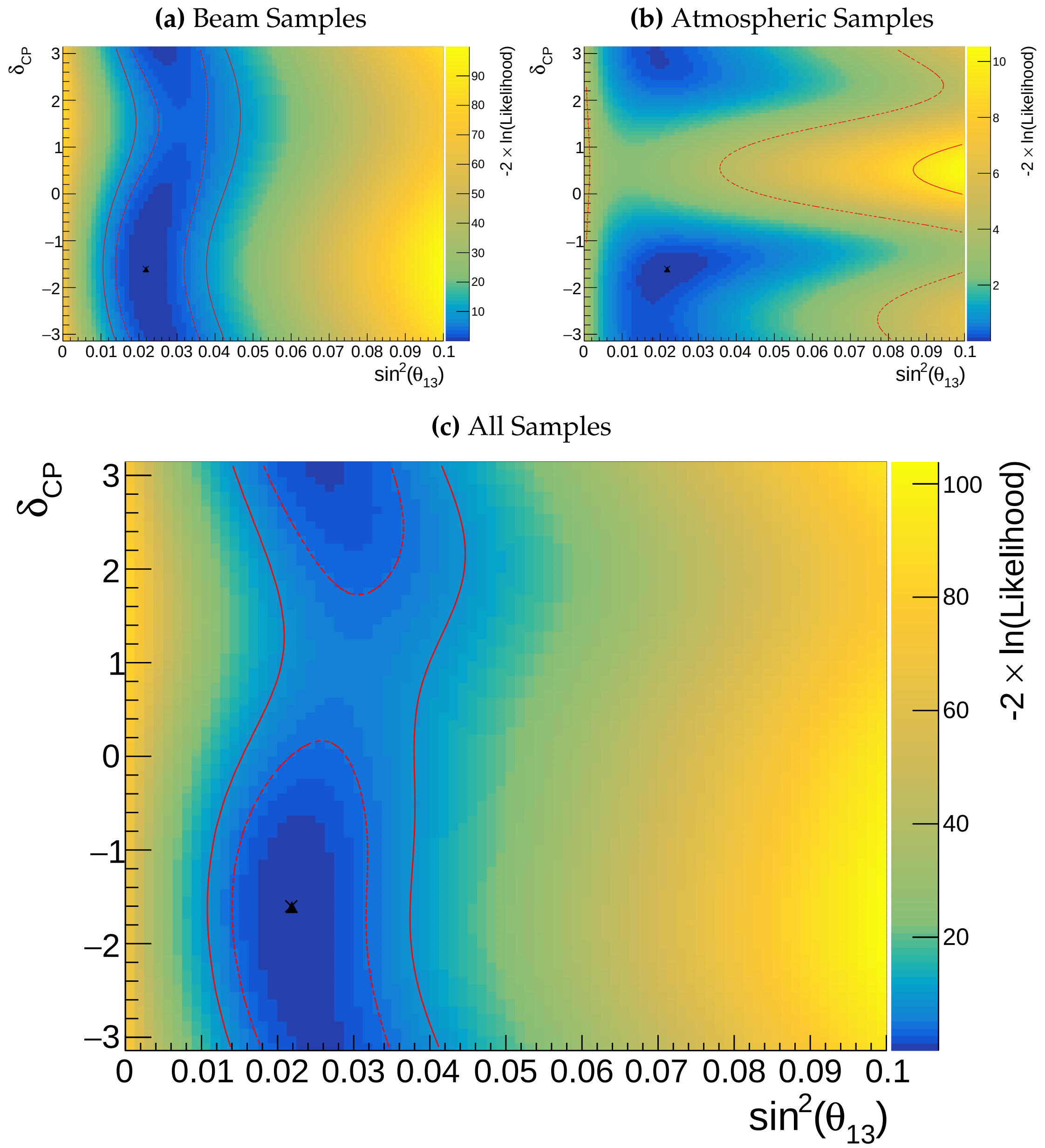

Figure 8.2: Two-dimensional log-likelihood scan of the appearance ($\sin^2(\theta_{13})$-δ_{CP}) parameters showing the response of the beam samples (top left), atmospheric samples (top right) and the summed response (bottom). The Asimov A oscillation parameters, defined in Table 2.2, are known to be the true point (Black Cross). The position of the smallest log-likelihood is highlighted with the triangle. Prior uncertainty terms of the oscillation parameters are neglected. The two(three) sigma contour levels are illustrated with the dashed(solid) red line.

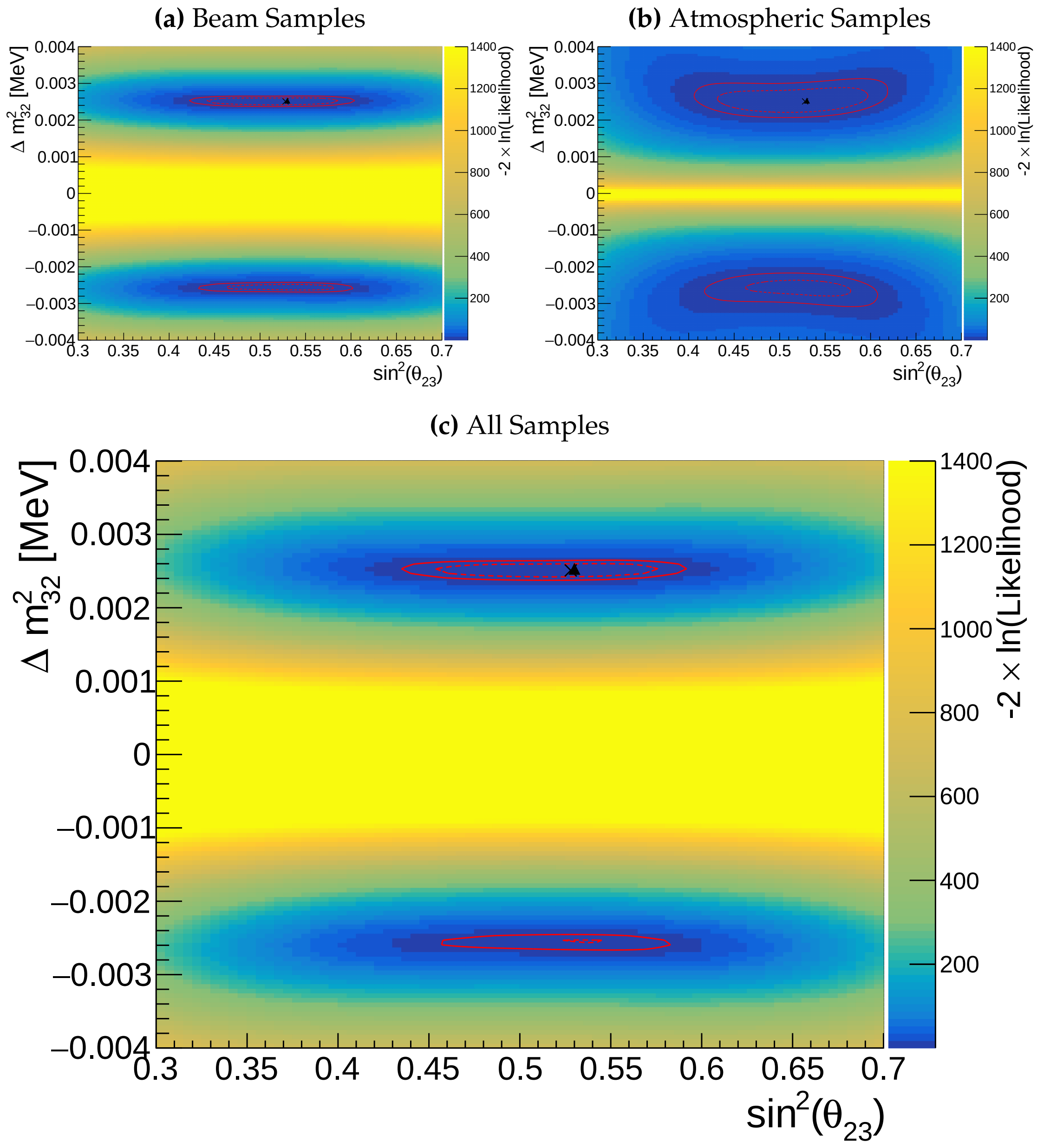

Figure 8.3: Two-dimensional log-likelihood scan of the disappearance ($\sin^2(\theta_{23})$-Δm^2_{32}) parameters showing the response of the beam samples (top left), atmospheric samples (top right) and the summed response (bottom). The Asimov A oscillation parameters, defined in Table 2.2, are known to be the true point (Black Cross). The position of the smallest log-likelihood is highlighted with the triangle. Prior uncertainty terms of the oscillation parameters are neglected. The two(three) sigma contour levels are illustrated with the dashed(solid) red line.

The likelihood scans illustrated thus far only consider the sensitivity of this analysis for a fixed set of true oscillation parameters, namely Asimov A defined in Table 2.2. Whilst computational infeasible to run many fits at different parameter sets, it is possible to calculate the likelihood response to different Asimov data sets. Figure 8.4 and Figure 8.5 illustrate how the sensitivity changes for differing true values of δ_{CP} and $\sin^2(\theta_{23})$, respectively. For both of these plots, the other oscillation parameters are fixed at their Asimov A values. Consequently, the caveat of fixed systematic parameters and correlations between other oscillation parameters being neglected still applies.

To explain how these plots are made, consider Figure 8.4. This plot is built by considering multiple one-dimensional log-likelihood scans, each creating an Asimov data with the value of δ_{CP} taken from the x-axis. The likelihood to a particular Asimov data set is calculated after reweighting the Monte Carlo prediction to each value of δ_{CP} on the y-axis.

Figure 8.4 illustrates the sensitivity to δ_{CP}. Notably, the 1σ intervals contain regions in the off-diagonal for which the beam and atmospheric samples have broken and discontinuous contours. This indicates that there are regions of δ_{CP} which are degenerate. For example, for the x-axis value of $\delta_{CP} = 0$, the beam samples sensitivity would include two discontinuous regions excluded from the 1σ interval: $\delta_{CP} \sim 0$ and $\delta_{CP} \sim \pi$. The offset in δ_{CP} between the beam and atmospheric samples allows the joint fit to have increased sensitivity in these regions. Consequently, the difference between the beam-only and joint beam-atmospheric fit should be studied using multiple Asimov data sets.

Despite the increased sensitivity at 1σ, the 2σ intervals from the joint fit are more similar to the two independent sensitivities and the off-diagonal degeneracies mostly remain. This indicates that the joint fit has the strength to aid parameter determination but can not entirely break the degeneracies in δ_{CP} at higher confidence levels.

Figure 8.5 illustrates a similar analysis as above, although the value of $\sin^2(\theta_{23})$ is varied and δ_{CP} is fixed to the Asimov A parameter value. Due to the beam parameters and baseline being tuned to specifically target this oscillation parameter, the average sensitivity of the beam samples is stronger than the atmospheric samples. However, the degeneracy around maximal mixing ($\sin^2(\theta_{23}) = 0.5$) is significantly more peaked in the beam samples compared to the atmospheric samples. This behaviour is strengthened when considering the 2σ intervals, to the point where two distinct discontinuous regions of the 2σ intervals exist around the Asimov point $\sin^2(\theta_{23}) \sim 0.41, 0.6$. Given the caveat of only considering likelihood scans, the joint analysis would mostly eliminate the discontinuous intervals in these regions. This means that the joint fit could feasible have an increased preference for the correct octant hypothesis.

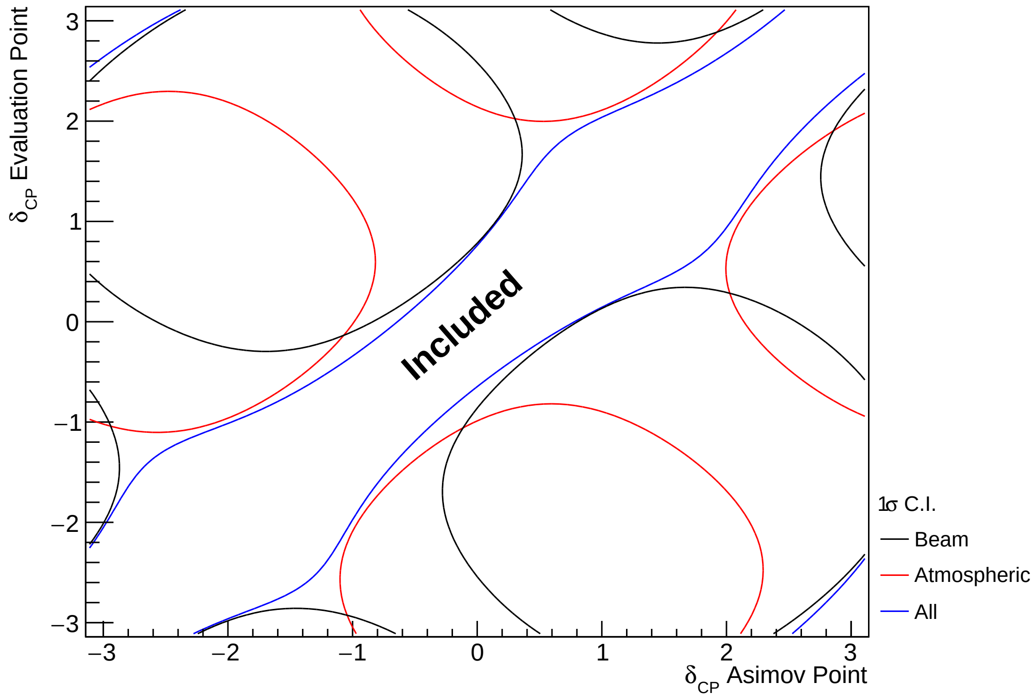

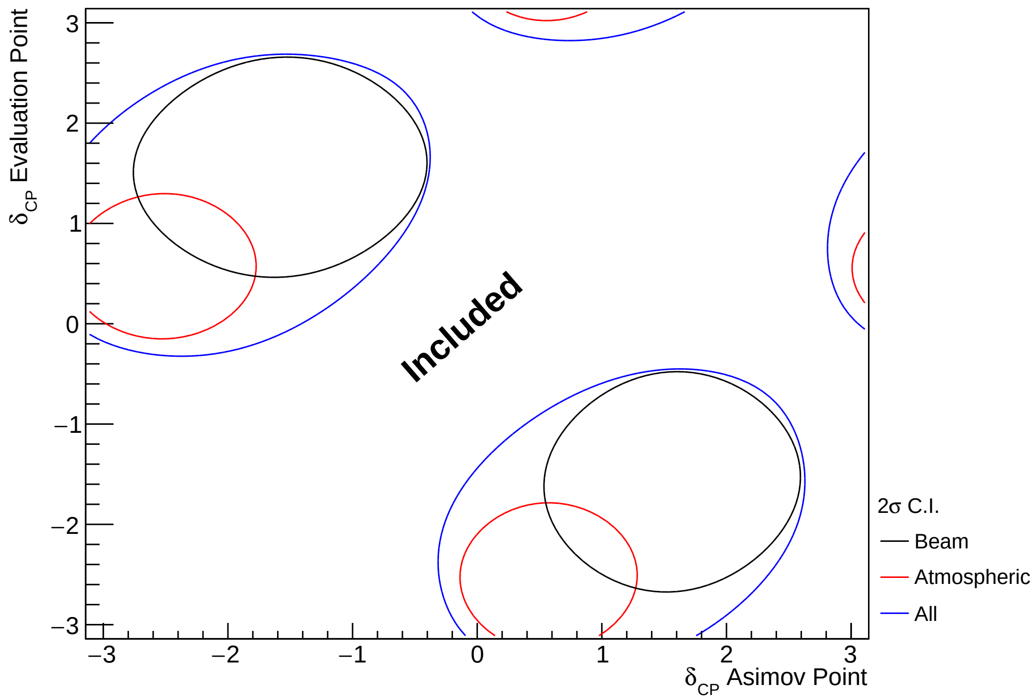

Figure 8.4: A series of one-dimensional likelihood scans over δ_{CP}, where an Asimov data set is built for each value of δ_{CP} on the x-axis and the likelihood is evaluated for each value of δ_{CP} on the y-axis. The diagonal represents the minimum log-likelihood and defines the region included within the 1σ (Top) and 2σ (Bottom) confidence intervals. The beam (black) and atmospheric (red) samples are individually plotted and the joint fit (blue) is the sum of the two.

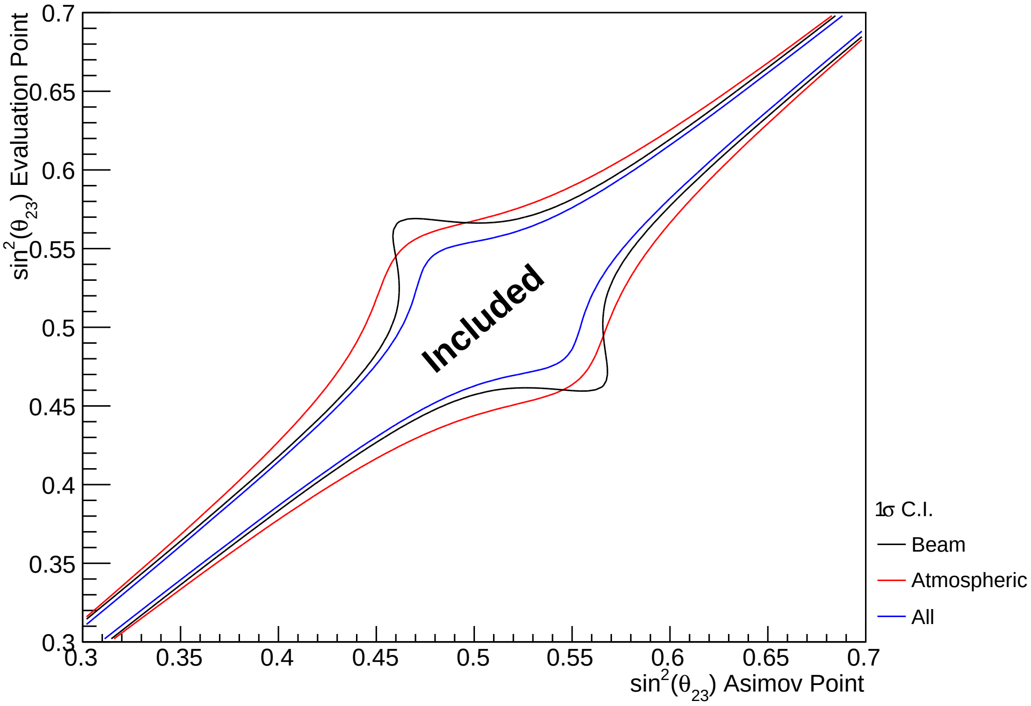

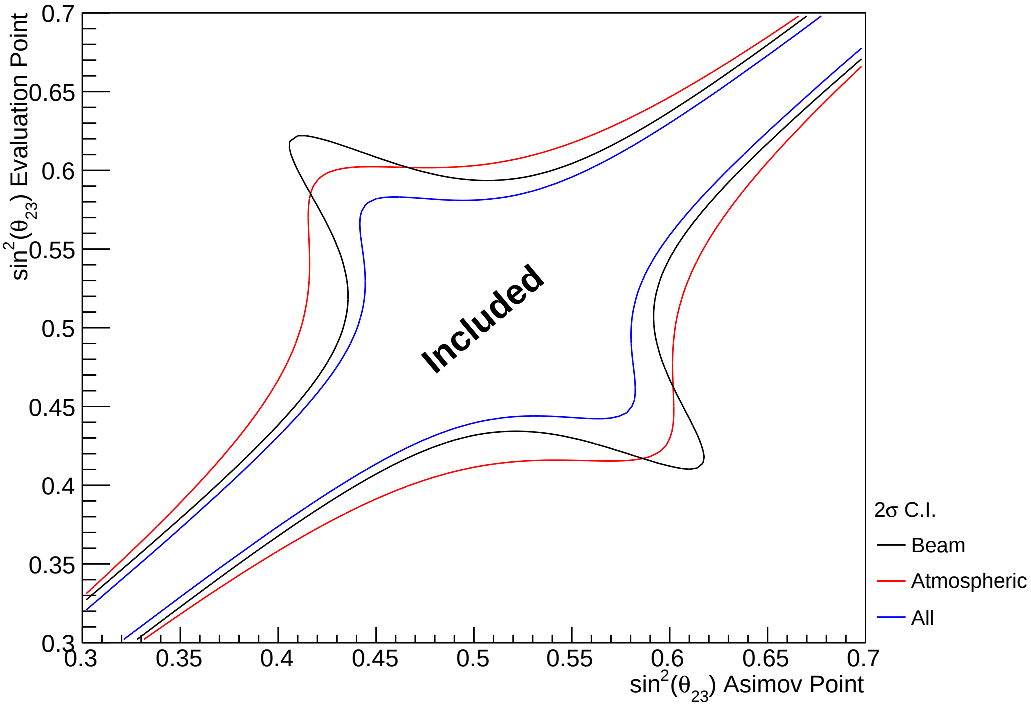

Figure 8.5: A series of one-dimensional likelihood scans over $\sin^2(\theta_{23})$, where an Asimov data set is built for each value of $\sin^2(\theta_{23})$ on the x-axis and the likelihood is evaluated for each value of $\sin^2(\theta_{23})$ on the y-axis. The diagonal represents the minimum log-likelihood and defines the region included within the 1σ (Top) and 2σ (Bottom) confidence intervals. The beam (black) and atmospheric (red) samples are individually plotted and the joint fit (blue) is the sum of the two.

Alongside oscillation parameters (Figure 8.1), the sensitivity to systematic parameters can also be studied for the joint fit. As some of these parameters are correlated between the beam and atmospheric events, the response of the atmospheric samples can modify the constraint. This means the systematics can have additional constraints than what they would from a beam-only analysis. Therefore, the response from the beam and the atmospheric samples to various systematic parameters has been compared in Figure 8.6. The Asimov data set has been created using the AsimovA oscillation parameter and the pre-fit systematic tune. For example, the systematic parameter controlling the effective axial mass coupling in CCQE interactions, M_A^{QE}, is clearly dominated by the ND constraint. An example where the response of the atmospheric sample is approximately similar to the near detector constraint is the `2p2h_CtoO` normalisation systematic. This systematic models the scaling of the 2p2h interaction cross-section on a carbon target to an oxygen target. There are also systematics which have no near detector constraint. For example, the systematic parameters which describe the normalisation of the NC1Gamma and NCOther interaction modes. The atmospheric samples are significantly more sensitive to these systematics than the beam samples due to their similar interaction contributions but relatively higher statistics (Table 8.1). As an example of how the atmospheric samples can help constrain systematic parameters used within the T2K-only analysis, these NC background events in beam electron-like samples will be considerably more constrained with the additional sensitivity of atmospheric samples. This would be expected to reduce the overall uncertainty of the beam electron-like event rates in the joint analysis compared to the beam-only studies. This could modify the sensitivity of the beam samples due to the more constrained background events.

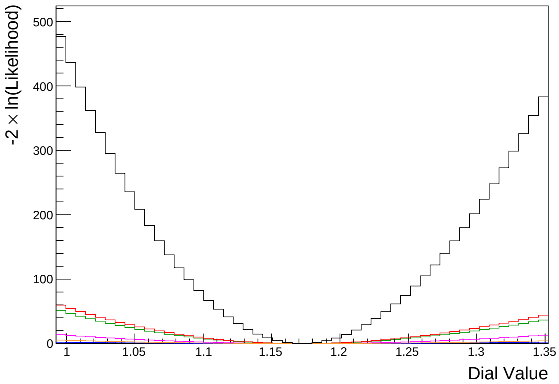

(a) M_A^{QE}

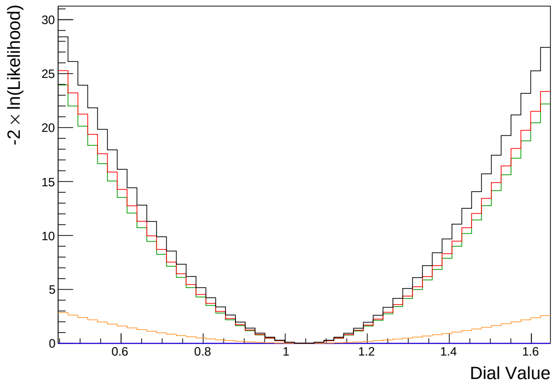

(b) `2p2h_Cto0` Norm.

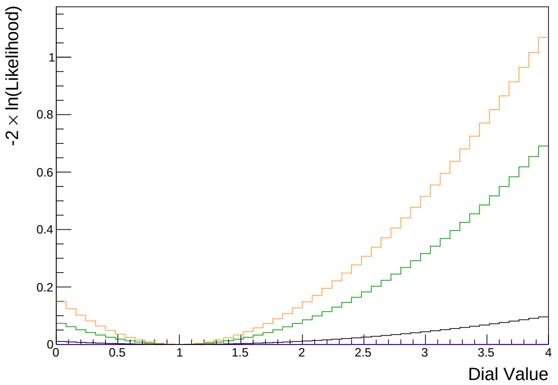

(c) NC1Gamma Norm.

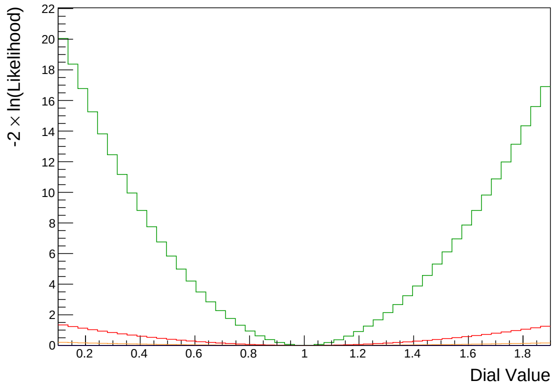

(d) NC Other Norm.

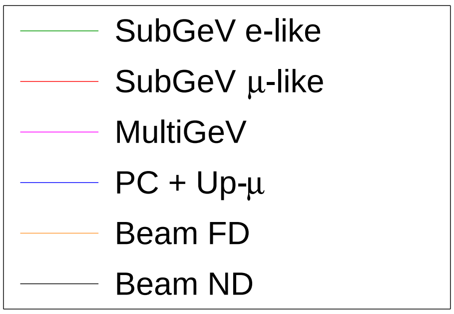

Figure 8.6: The response of the likelihood, as defined in section 8.2, illustrating the response of the samples to the various cross-section systematic parameters.

8.2 Sensitivities

The sensitivities of the joint T2K and SK oscillation analysis are presented in the form of Asimov fits. This technique builds as Asimov data set (following section 6.5) using the AsimovA oscillation parameters and post-BANFF systematic tune.

In practice, the Asimov fits presented within this analysis are modified from the above definition. An Asimov prediction of both beam and atmospheric far detector samples is fit whilst the true data is used for near detector samples. The Asimov predictions at the far detector are built using the BANFF tuning (as discussed in section 3.2). These modifications mean that the results are equivalent to performing a far detector Asimov fit using inputs from the BANFF data fit. Consequently, this allows the results to be cross-checked with the results from the P-Theta analysis. The comparison has been performed and is documented in [221]. No significant discrepancies were found between the fitters.

This section proceeds with the following studies. Firstly, the sensitivity of the atmospheric samples after the T2K cross-section has been applied to the low-energy events is detailed in subsection 8.2.1. This includes studying the choice of applying the 2020 PDG reactor constraint [76] to the atmospheric samples, which is documented in subsection 8.2.2. Additionally, the effect of applying the near-detector constraints onto the atmospheric samples is discussed in subsection 8.2.3. The main result is the sensitivity of the simultaneous beam and atmospheric fit. The sensitivities, both with and without the application of the reactor constraint, are presented in subsection 8.2.4 and subsection 8.2.5, respectively. To indicate the benefit of the joint analysis, the sensitivities are compared to the 2020 T2K sensitivities [75, 186] in subsection 8.2.6 and subsection 8.2.7. As shown in subsection 8.1.1, the response of the beam and atmospheric samples change depending upon the true set of oscillation parameters assumed. Therefore, subsection 8.2.8 documents the sensitivities at an alternative oscillation parameter set. It is important to note that these results have been published at the Neutrino 2022 conference on behalf of the T2K and SK collaborations [111].

8.2.1 Atmospheric-Only Sensitivity Without Reactor Constraint

This section presents the results of an Asimov fit using samples from the near detector and only atmospheric samples from the far detector. The results are presented as one-dimensional or two-dimensional histograms which have been marginalised over all other parameters using the technique outlined in subsection 4.3.1. Each histogram displays the posterior probability density and illustrates the credible intervals, calculated using the technique in subsection 4.3.2. For these fits in this subsection, a flat penalty term is used for $\sin^2(\theta_{13})$ such the reactor constraint is not applied. The Asimov data is generated assuming the AsimovA oscillation parameter set defined in Table 2.2 and the post-BANFF systematic parameter tune.

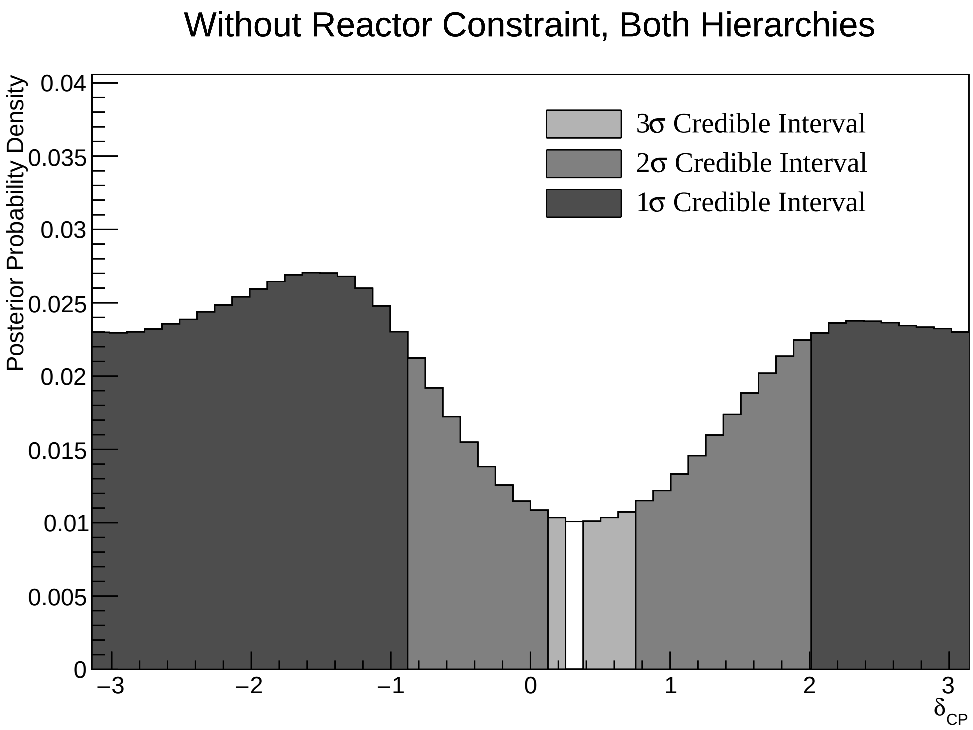

Figure 8.7: The one-dimensional posterior probability density distribution in δ_{CP}, marginalised over both hierarchies, from the SK atmospheric-only fit. The reactor constraint is not applied.

Figure 8.7 illustrates the posterior probability density for δ_{CP}, marginalised over both hierarchies. If instead, only steps in the normal hierarchy were considered, the shape of the contours would change. The fit favours the known oscillation parameter ($\delta_{CP} = -1.601$) although the posterior probability is very flat through the range of $-\pi < \delta_{CP} < -1$ and $2 < \delta_{CP} < \pi$. There is also a region around $\delta_{CP} \sim 0.4$ which is disfavoured at 2σ. This indicates that the SK samples can rule out some parts of the CP conserving parameter space reasonably well, near $\delta_{CP} \sim 0.4$, when the true value of $\delta_{CP} \sim \pi/2$.

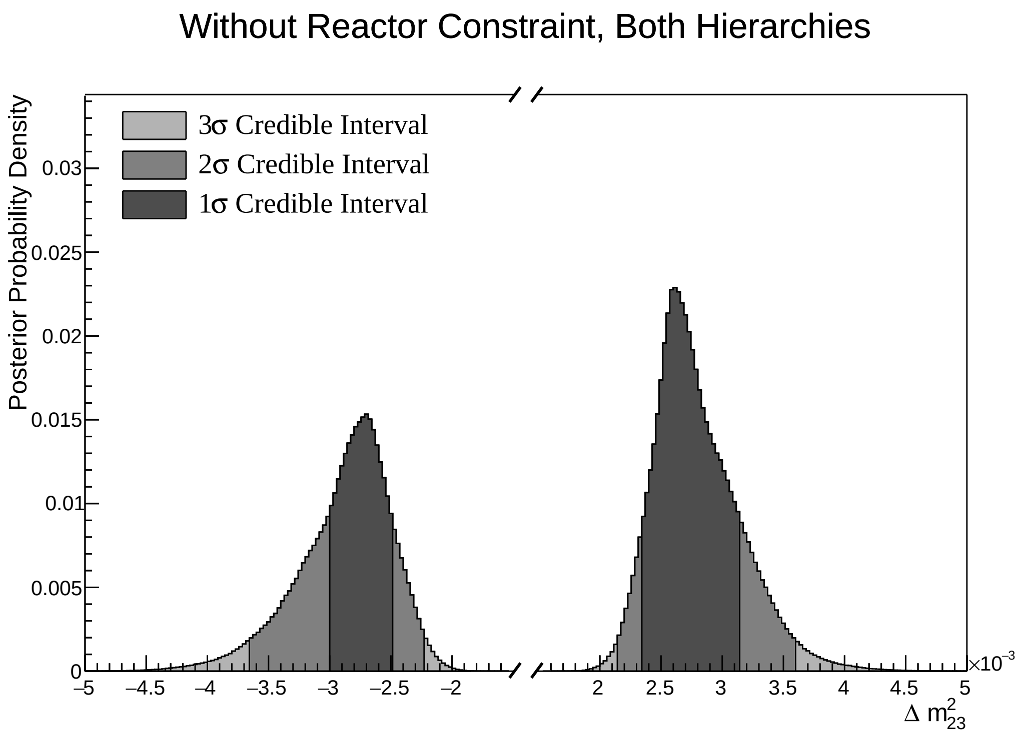

Figure 8.8: The one-dimensional posterior probability density distribution in Δm^2_{32}, marginalised over both hierarchies, from the SK atmospheric-only fit. The reactor constraint is not applied.

The posterior probability density in Δm^2_{32} is given in Figure 8.8. This distribution includes steps in both the normal hierarchy $\left(\text{NH}, \Delta m^2_{32} > 0\right)$ and the inverse hierarchy $\left(\text{IH}, \Delta m^2_{32} < 0\right)$. The highest posterior probability density is found within the NH, which agrees with the known oscillation parameter value. However, all of the credible intervals span both of the hierarchies hypotheses. If instead, only steps in the normal hierarchy were considered, the shape of the contours would change. The known oscillation parameter is $2.509 \times 10^{-3}\text{eV}^2$, which is contained within the 1σ credible interval.

	LO $\left(\sin^2\theta_{23} < 0.5\right)$	UO $\left(\sin^2\theta_{23} > 0.5\right)$	Sum
NH $\left(\Delta m^2_{32} > 0\right)$	0.17	0.40	0.58
IH $\left(\Delta m^2_{32} < 0\right)$	0.13	0.29	0.42
Sum	0.31	0.69	1.00

Table 8.2: The distribution of steps in an SK atmospheric-only fit, presented as the fraction of steps in the upper (UO) and lower (LO) octants and the normal (NH) and inverted (IH) hierarchies. The reactor constraint is not applied. The Bayes factors are calculated as $B(\mathrm{NH}/\mathrm{IH}) = 1.37$ and $B(\mathrm{UO}/\mathrm{LO}) = 2.24$.

Following the discussion in subsection 4.3.3, the Bayes factor for hierarchy preference can be calculated by determining the fraction of steps that fall into the NH and the IH regions, as an equal prior is placed on both hypotheses. A similar calculation can be performed by calculating the fraction of steps which fall in the lower octant $\left(\mathrm{LO},\ \sin^2\theta_{23} < 0.5\right)$ or upper octant $\left(\mathrm{UO},\ \sin^2\theta_{23} > 0.5\right)$. The fraction of steps, broken down by hierarchy and octant, are given in Table 8.2. The Bayes factor for preferred hierarchy model is $B(\mathrm{NH}/\mathrm{IH}) = 1.37$. Table 4.1 states this value of the Bayes factor indicates a weak preference for the normal hierarchy model. The Bayes factor for choice of octant is $B(\mathrm{UO}/\mathrm{LO}) = 2.24$. This is also classified as a weak preference for the UO. Both of these show that the fit is returning the correct choice of models (NH and UO) for the known Asimov A oscillation parameters defined in Table 2.2.

The 1σ credible intervals, broken down by hierarchy, and position in parameter space of the highest posterior probability density is given in Table 8.3. These are taken from the one-dimensional projections of the oscillation parameters, marginalised over all other parameters within the fit. For the known Asimov value of $\delta_{CP} = -1.601$, the 1σ credible interval rules out a region between $\delta_{CP} = -0.86$ and $\delta_{CP} = 1.96$, when marginalising over both hierarchies. The position of the highest posterior density is $\delta_{CP} = -1.57$ which is clearly compatible with the known oscillation parameter value.

The sensitivity of the atmospheric samples to $\sin^2(\theta_{13})$ is presented in Figure 8.9. The likelihood scans presented in Figure 8.1 suggest that the sensitivity

Parameter	Interval	HPD
δ_{CP}, (BH)	$[-\pi, -0.86], [1.96, \pi]$	-1.57
δ_{CP}, (NH)	$[-\pi, -0.86], [1.88, \pi]$	-1.57
δ_{CP}, (IH)	$[-\pi, -0.94], [1.96, \pi]$	-1.57
Δm^2_{32} (BH) $[\times 10^{-3}\text{eV}^2]$	$[-3.00, -2.50], [2.35, 3.15]$	2.65
Δm^2_{32} (NH) $[\times 10^{-3}\text{eV}^2]$	$[2.39, 3.04]$	2.64
Δm^2_{32} (IH) $[\times 10^{-3}\text{eV}^2]$	$[-3.15, -2.45]$	-2.70
$\sin^2(\theta_{23})$ (BH)	$[0.476, 0.59]$	0.542
$\sin^2(\theta_{23})$ (NH)	$[0.476, 0.59]$	0.554
$\sin^2(\theta_{23})$ (IH)	$[0.476, 0.59]$	0.542

Table 8.3: The position of the highest posterior probability density (HPD) and width of the 1σ credible interval for the SK atmospheric-only fit. The reactor constraint is not applied. The values are presented by which hierarchy hypothesis is assumed: marginalised over both hierarchies (BH), normal hierarchy only (NH), and inverted hierarchy only (IH).

to $\sin^2(\theta_{13})$ will be small. This behaviour is also seen in the fit results, where the width of the 1σ credible intervals span the region of $\sin^2(\theta_{13}) = [0.008, 0.08]$. This is more than an order of magnitude worse than the constraint from reactor experiments [76].

As previously discussed, the correlations between oscillation parameters are also important to understand how the atmospheric samples respond. Figure 8.10 illustrates the two dimensional $\sin^2(\theta_{13}) - \delta_{CP}$ sensitivity, marginalised over all other parameters. The displayed contours are calculated by marginalising over both hierarchies. The shape of the 1σ credible interval shows that the constraining power of the fit on δ_{CP} is dependent upon the value of $\sin^2(\theta_{13})$. Furthermore, they show a strong resemblance to the likelihood scans illustrated in Figure 8.2. Whilst the atmospheric samples do not strongly constrain the value of $\sin^2(\theta_{13})$, the value of $\sin^2(\theta_{13})$ does impact the atmospherics sensitivity to δ_{CP}. A value of $\sin^2(\theta_{13}) \sim 0.02$ would select a continuous contour over all values of δ_{CP}. This shows the effect of the marginalisation effect previously described.

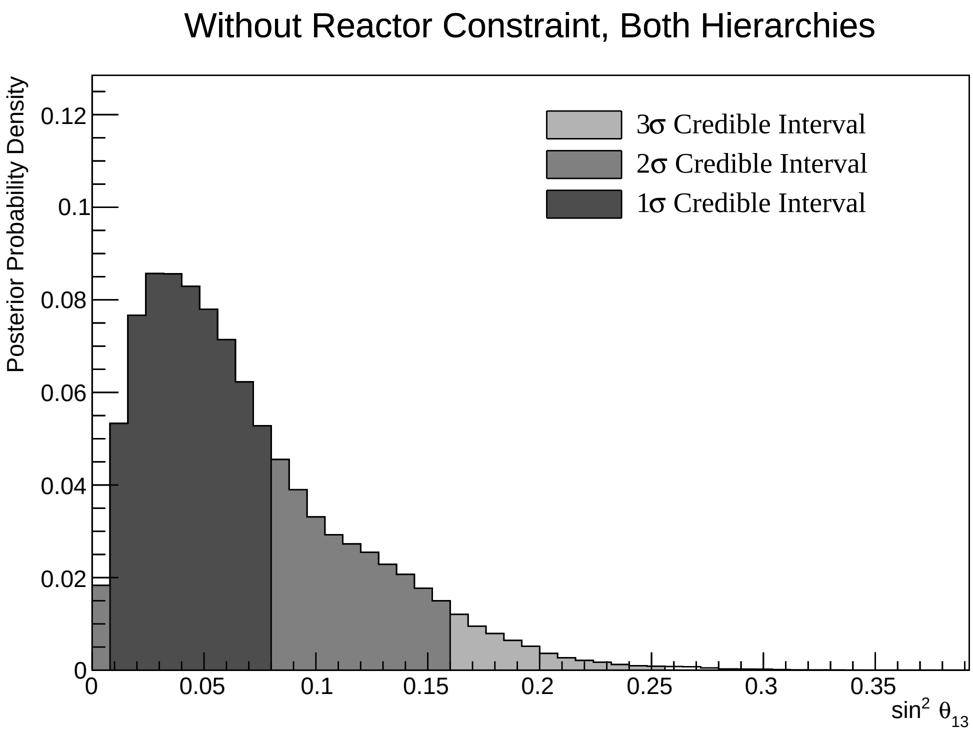

Figure 8.9: The one-dimensional posterior probability density distribution in $\sin^2(\theta_{13})$, marginalised over both hierarchies, from the SK atmospheric-only fit. The reactor constraint is not applied.

The $\sin^2(\theta_{23}) - \Delta m^2_{32}$ disappearance contours are illustrated in Figure 8.11. As expected, the area contained in the inverted hierarchy 1σ credible interval is slightly smaller than that in the normal hierarchy. This follows from the Bayes factor showing a weak preference for NH meaning that more of the steps will exist in the $\Delta m^2_{32} > 0$ region. The known oscillation parameters of $\sin^2(\theta_{23}) = 0.528$ and $\Delta m^2_{32} = 2.509 \times 10^{-3}\text{eV}^2$ are contained within the 1σ credible interval.

Figure 8.12 illustrates the two-dimensional projections for each permutation of oscillation parameters which this analysis is sensitive to: δ_{CP}, $\sin^2(\theta_{13})$, $\sin^2(\theta_{23})$, and Δm^2_{32}. The purpose of this plot is to illustrate the correlations between the oscillation parameters. The contours are calculated whilst marginalising over both hierarchies, however, only the NH is illustrated when plotting the Δm^2_{32} parameter. As expected the correlations play a significant role in these sensitivity measurements, especially the choice of the $\sin^2(\theta_{13})$ constraint. The application of reactor constraint would be expected to alter both the width and position of the

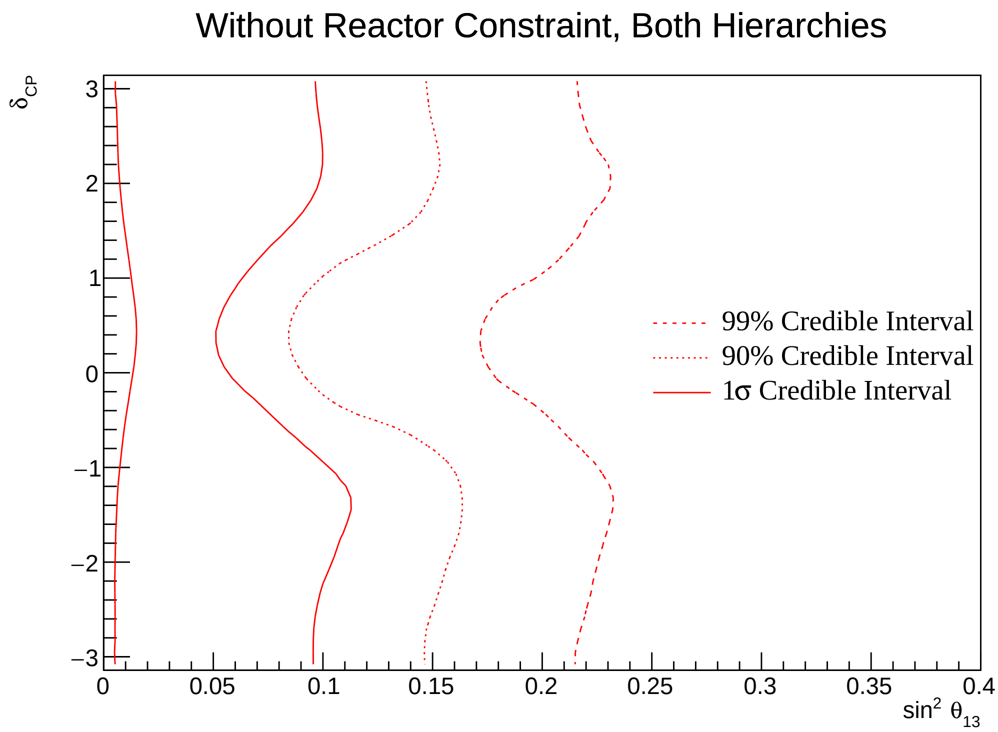

Figure 8.10: The two-dimensional posterior probability density distribution in $\delta_{CP} - \sin^2(\theta_{13})$, marginalised over both hierarchies, from the SK atmospheric-only fit. The reactor constraint is not applied.

Δm^2_{32}, δ_{CP}, and $\sin^2(\theta_{23})$ constraints. The majority of the octant model preference comes from the region of $\sin^2(\theta_{13}) \sim 0.03$ such that the application of the reactor constraint would not be expected to significantly change the octant preference. The reactor constraint would result in lower values of $|\Delta m^2_{32}|$. Interestingly, the distribution of steps in the δ_{CP}-$\sin^2(\theta_{13})$ plot is slightly flatter in the region of the reactor constraint. Both the posterior distribution from this fit and the distribution in Figure 8.2 show a region of low negative log-likelihood extending out towards higher values of $\sin^2(\theta_{13})$ in the $\delta_{CP} \sim -\pi/2$ and $\delta_{CP} \sim 2$ region. Consequently, the reactor constraint could feasibly reduce the sensitivity of the atmospheric samples to δ_{CP}, due to the previously discussed marginalisation effects.

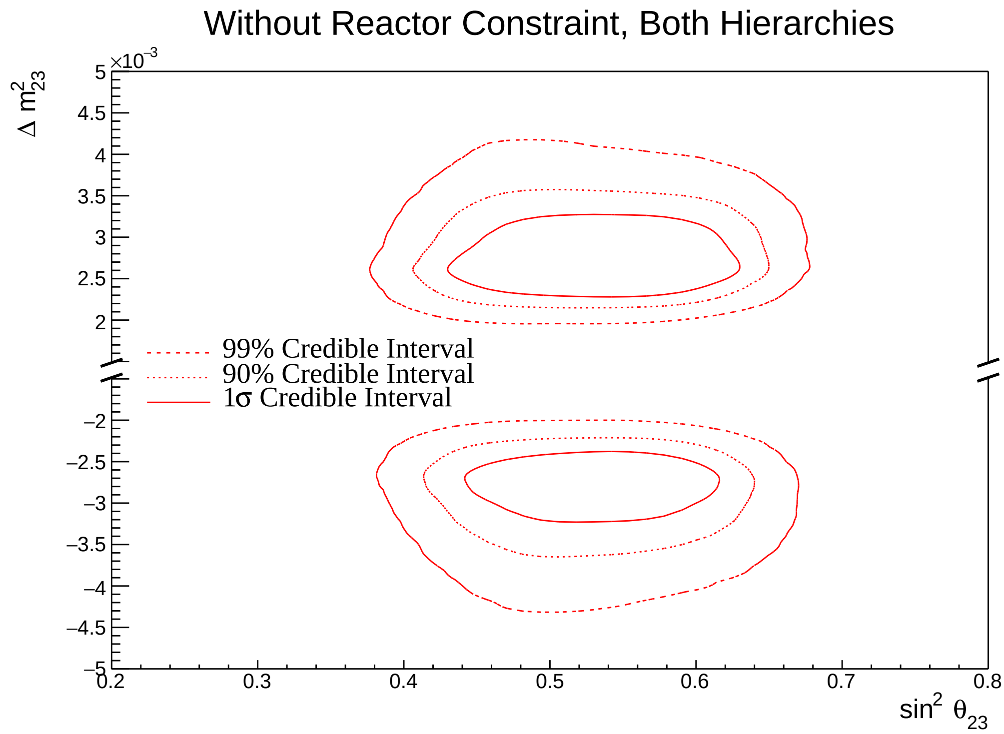

Figure 8.11: The two-dimensional posterior probability density distribution in $\Delta m^2_{32} - \sin^2(\theta_{23})$, marginalised over both hierarchies, from the SK atmospheric-only fit. The reactor constraint is not applied.

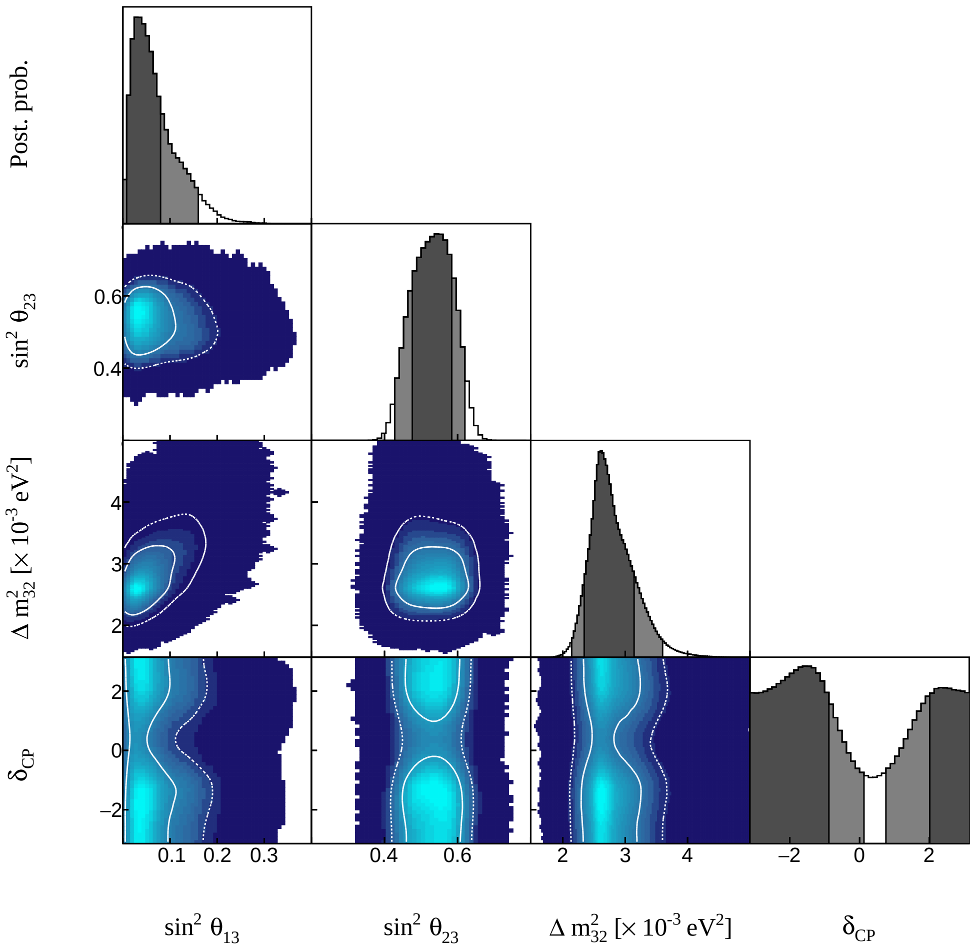

Figure 8.12: The posterior probability density distribution from the SK atmospheric-only fit. The reactor constraint is not applied. The distribution is given for each two-dimensional permutation of the oscillation parameters of interest. The one-dimensional distribution of each parameter is also given.

8.2.2 Atmospheric-Only Sensitivity With Reactor Constraint

The results in subsection 8.2.1 discuss the atmospheric sensitivity when the reactor constraint is not applied. The correlations illustrated in Figure 8.12 indicate that the marginalisation effects could contribute to differing sensitivities when the external reactor constraint is applied. Using the technique discussed in subsection 4.1.1, the posterior distribution of the fit in subsection 8.2.1 can be reweighted to include the reactor constraint of $\sin^2(\theta_{13}) = (2.18 \pm 0.08) \times 10^{-2}$ [76].

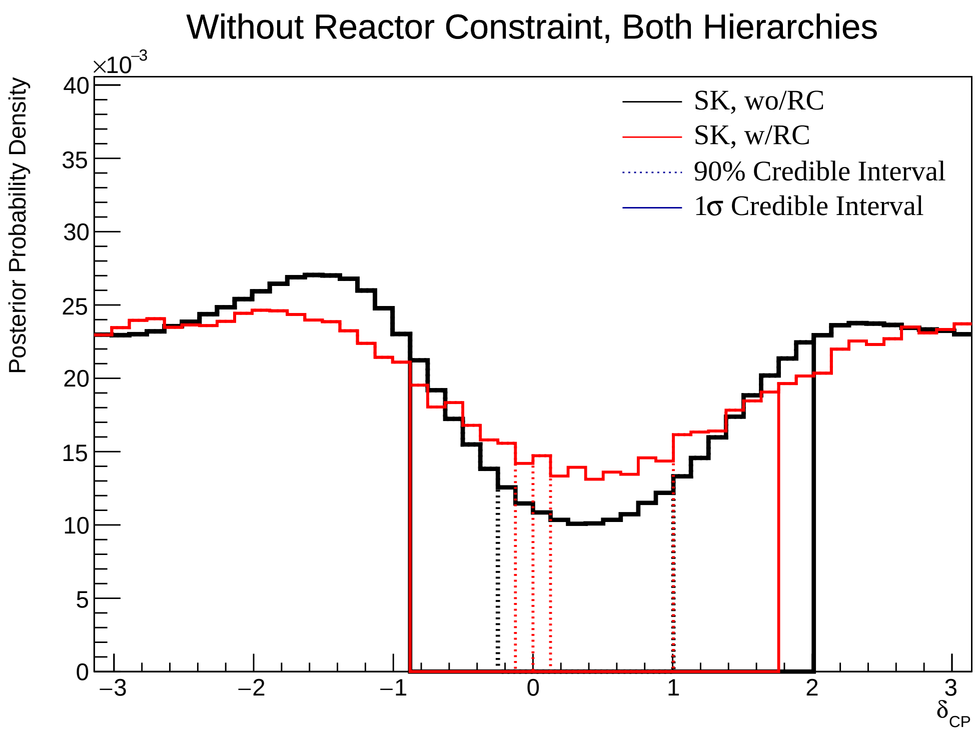

Figure 8.13: The one-dimensional posterior probability density distribution in δ_{CP} compared between the SK atmospheric-only fit (Black) and the SK atmospheric fit with the reactor constraint applied (Red). The distributions are marginalised over both hierarchies.

Figure 8.13 illustrates the sensitivity to δ_{CP} of the atmospheric fit with reactor constraint applied. The distribution is less peaked than the previous results. This is due to the expected marginalisation effect previously discussed. The width of the 1σ credible interval is increased when the reactor constraint is applied, indicating less sensitivity to δ_{CP} in the region of $\sin^2(\theta_{13})$ preferred by the reactor constraint.

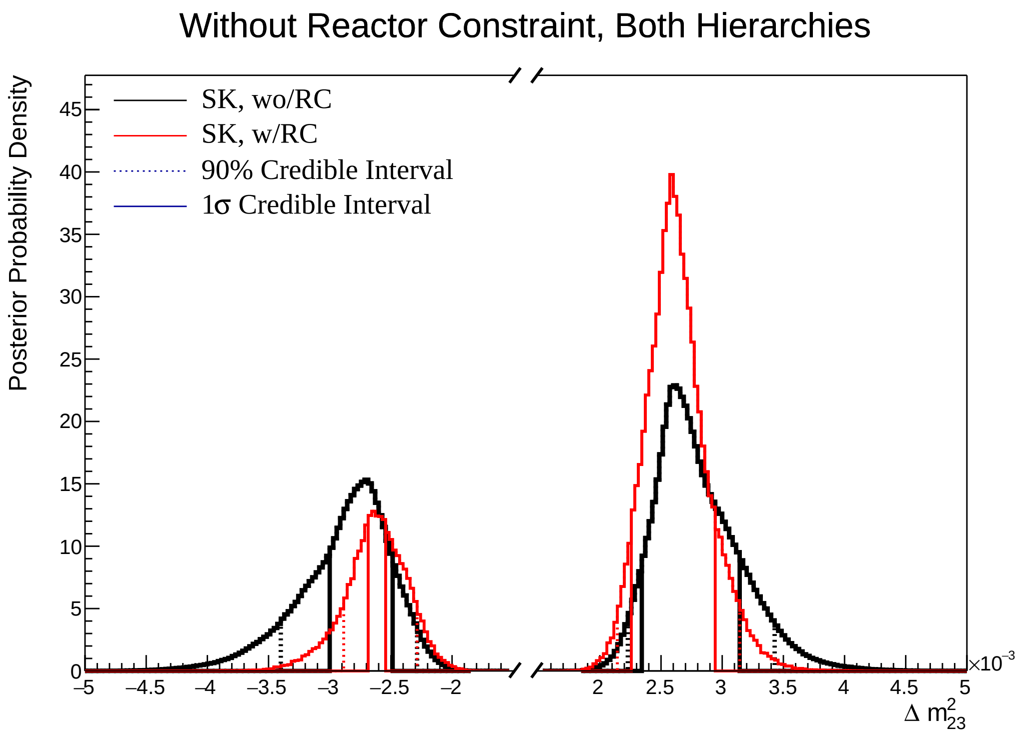

Figure 8.14: The one-dimensional posterior probability density distribution in Δm^2_{32} compared between the SK atmospheric-only fit (Black) and the SK atmospheric fit with the reactor constraint applied (Red). The distributions are marginalised over both hierarchies.

The reactor constraint increases the sensitivity of the atmospheric samples to Δm^2_{32} as illustrated in Figure 8.14. The 1σ credible interval in Δm^2_{32} is determined to be $[-2.70, -2.55] \times 10^{-3}\text{eV}^2$ and $[2.25, 2.95] \times 10^{-3}\text{eV}^2$. The width of the IH credible interval is reduced by $\sim$ 70% when the reactor constraint is applied. Due to the marginalisation effects observed in Figure 8.12, the favoured region of Δm^2_{32} moves closer to zero for both hierarchies. A clear explanation of this behaviour is illustrated in Figure 8.15 which illustrates the posterior distribution in the $\Delta m^2_{32} - \sin^2(\theta_{13})$ parameters, marginalised over both hierarchies. The correlation between Δm^2_{32} and $\sin^2(\theta_{13})$ is such that lower values of $\sin^2(\theta_{13})$ tend towards lower values of $|\Delta m^2_{32}|$. This moves the posterior distribution towards the known oscillation parameter $\Delta m^2_{32} = 2.509 \times 10^{-3}\text{eV}^2$.

Table 8.4 presents the fraction of steps in each hierarchy and octant model for the fit after the reactor constraint has been applied. The reactor constraint significantly increases the NH preference, increasing the Bayes factor from

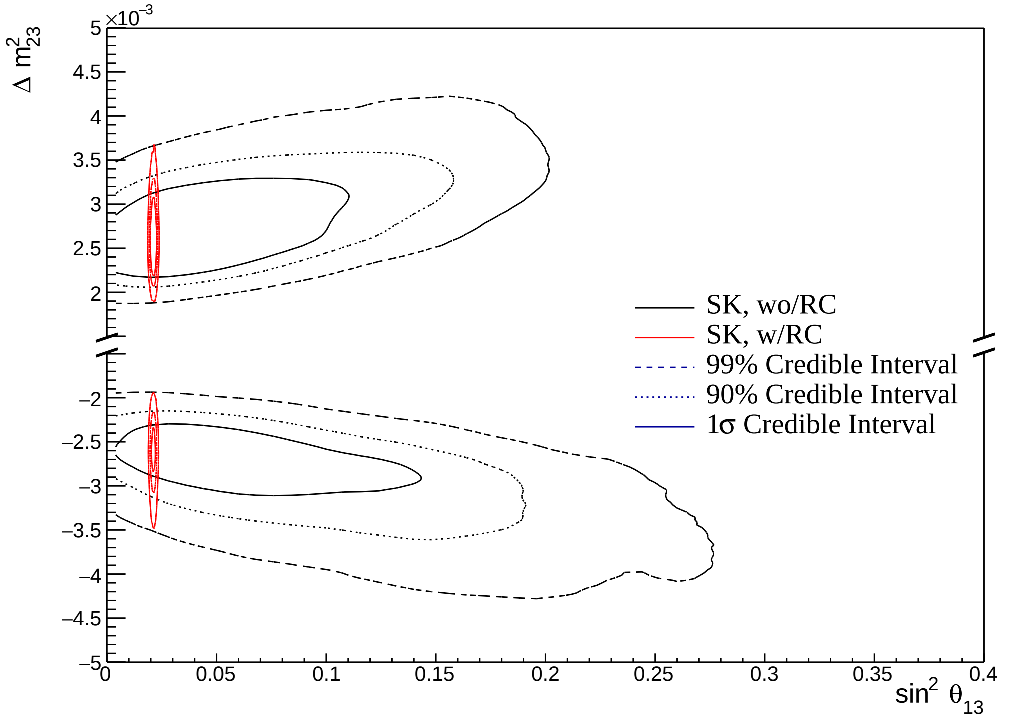

Figure 8.15: The two-dimensional posterior probability density distribution in $\Delta m^2_{32} - \sin^2(\theta_{13})$ compared between the SK atmospheric-only fit (Black) and the SK atmospheric fit with the reactor constraint (Red). The distributions are marginalised over both hierarchies.

	LO $(\sin^2\theta_{23} < 0.5)$	UO $(\sin^2\theta_{23} > 0.5)$	Sum
NH $(\Delta m^2_{32} > 0)$	0.21	0.53	0.74
IH $(\Delta m^2_{32} < 0)$	0.08	0.18	0.26
Sum	0.29	0.71	1.00

Table 8.4: The distribution of steps in an SK atmospheric with reactor constraint fit, presented as the fraction of steps in the upper (UO) and lower (LO) octants and the normal (NH) and inverted (IH) hierarchies. The Bayes factors are calculated as $B(\mathrm{NH/IH}) = 2.86$ and $B(\mathrm{UO/LO}) = 2.39$.

$B(\mathrm{NH/IH}) = 1.37$ to $B(\mathrm{NH/IH} = 2.86$ when the reactor constraint is applied. This is still defined as a weak preference for NH hypothesis according to Jeffrey's scale (see Table 4.1), however, it is a stronger preference than when the constraint is not applied. The preference for the correct octant model is slightly increased by the application of the reactor constraint which is consistent with expectation. However, the conclusion that would be made does not significantly change.

8.2.3 Application of Near Detector Constraints for Atmospheric Samples

The choice of applying the near detector constraints to the low-energy atmospheric samples was introduced in subsection 6.4.3. This subsection illustrates the effect of that choice on the sensitivities of the atmospheric samples to the oscillation parameters. This Asimov data was generated assuming the 'AsimovA' oscillation parameter set defined in Table 2.2 and the post-BANFF systematic parameter tune.

The change in sensitivity on δ_{CP} is given in Figure 8.16. The reactor constraint is not applied in either of the fits within this comparison. The shape of the posterior is similar although less peaked at the Asimov point ($\delta_{CP} = -1.601$) and more symmetric between the regions of $\delta_{CP} = -1.601$ and $\delta_{CP} \sim 2.5$. The width of the 1σ credible intervals are approximately the same (identical to within a bin width) and the same conclusion holds for the higher credible intervals. The change in sensitivity to other oscillation parameters has been studied and no significant discrepancies were found. As expected, the sensitivities are statistics dominated and the exact choice of systematic model and constraint does not significantly affect the physics conclusions one would make from this analysis.

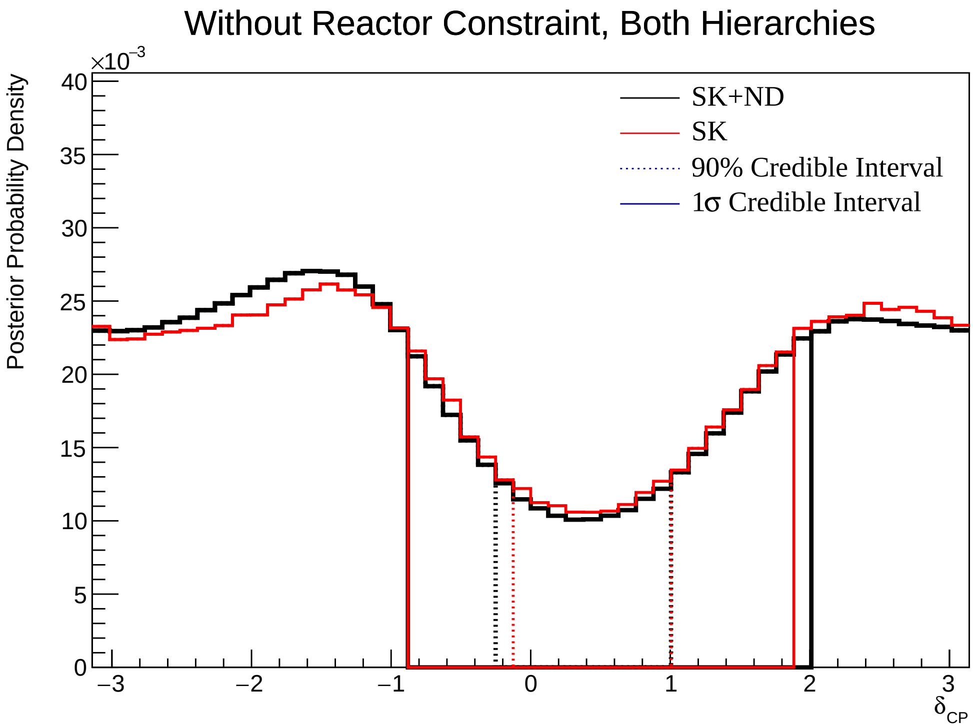

Figure 8.16: The one-dimensional posterior probability density distribution in δ_{CP} compared between the SK atmospheric-only fit where the near detector constraint is (Black) and is not (Red) applied. The distributions are marginalised over both hierarchies.

8.2.4 Atmospheric and Beam Sensitivity without Reactor Constraint

This section presents the sensitivities of the simultaneous beam and atmospheric analysis where the reactor constraint is not applied. Similar to the previous studies, the Asimov data is built assuming the post-BANFF cross-section tune and Asimov A oscillation parameters defined in Table 2.2. This fit uses all 18 near detector beam samples, 5 far detector beam samples, and 18 atmospheric samples. The sensitivity to δ_{CP}, marginalised over both hierarchies, is given in Figure 8.17.

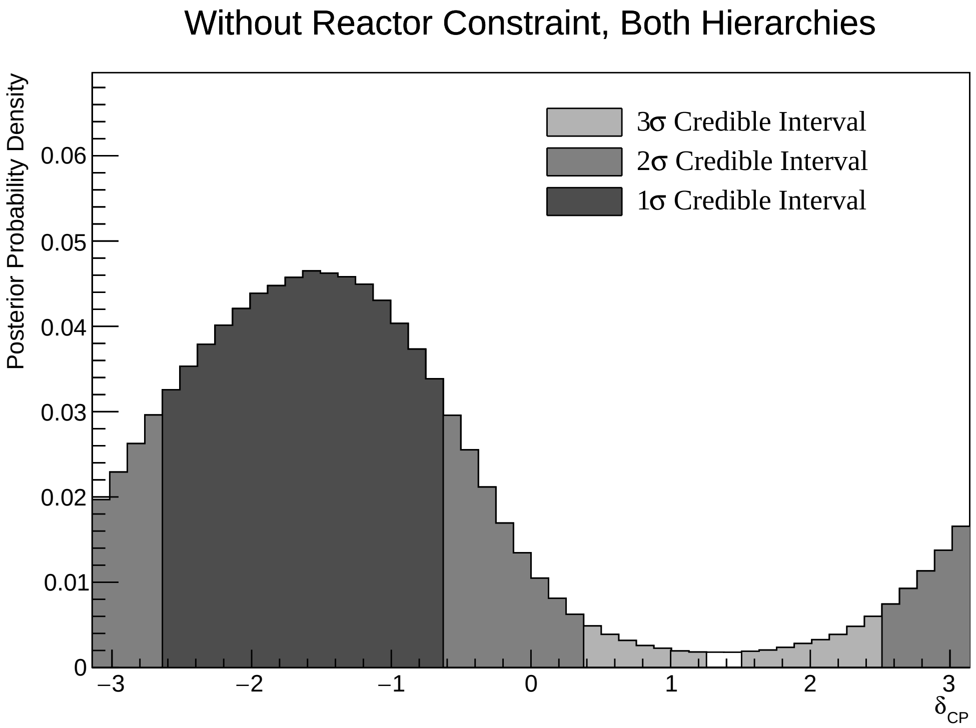

Figure 8.17: The one-dimensional posterior probability density distribution in δ_{CP}, marginalised over both hierarchies, from the joint beam and atmospheric fit. The reactor constraint is not applied.

The credible intervals and highest posterior distribution for each oscillation parameter is given in Table 8.5. The highest posterior probability density is $\delta_{CP} = -1.58$ and is compatible with the known Asimov A value of $\delta_{CP} = -1.601$. The CP-conserving values of $\delta_{CP} = 0, \pi, -\pi$ are disfavoured at 1σ credible interval. There is also a region around $\delta_{CP} = 1.4$ which is disfavoured at more than 3σ. Whilst these conclusions can only be made at this particular Asimov point, it does show that if the true value of δ_{CP} was CP-violating, this joint analysis would be able to disfavour CP conserving values at over 1σ without any external constraints. The highest posterior probability density does move further away from the Asimov point when only steps in the NH region are considered. This is due to the correlations between the value of δ_{CP} and the mass hierarchy, as will be later discussed.

Parameter	Interval	HPD
δ_{CP}, (BH)	$[-2.64, -0.63]$	-1.57
δ_{CP}, (NH)	$[-2.76, -0.63]$	-1.45
δ_{CP}, (IH)	$[-2.39, -0.88]$	-1.57
Δm^2_{32} (BH) $[\times 10^{-3}\text{eV}^2]$	$[2.46, 2.58]$	2.49
Δm^2_{32} (NH) $[\times 10^{-3}\text{eV}^2]$	$[2.48, 2.56]$	2.51
Δm^2_{32} (IH) $[\times 10^{-3}\text{eV}^2]$	$[-2.60, -2.52]$	-2.55
$\sin^2(\theta_{23})$ (BH)	$[0.48, 0.55]$	0.509
$\sin^2(\theta_{23})$ (NH)	$[0.48, 0.55]$	0.509
$\sin^2(\theta_{23})$ (IH)	$[0.48, 0.55]$	0.521

Table 8.5: The position of the highest posterior probability density (HPD) and width of the 1σ credible interval for the joint beam and atmospheric fit. The reactor constraint is not applied. The values are presented by which hierarchy hypothesis is assumed: marginalised over both hierarchies (BH), normal hierarchy only (NH), and inverted hierarchy only (IH).

The sensitivity to Δm^2_{32} is illustrated in Figure 8.18, marginalised over both hierarchies. Notably, the 1σ credible interval is entirely contained within the normal hierarchy region, as illustrated in Table 8.5. This is illustrates reasonable sensitivity to the mass hierarchy model. This is also reflected in the 1σ credible intervals being approximately the same when they are made considering both hierarchies and when considering only the NH. The known oscillaton parameter is $\Delta m^2_{32} = 2.509 \times 10^{-3}\text{eV}^2$. The normal hierarchy distribution favours this value with the highest posterior probability density of $\Delta m^2_{32} = 2.51 \times 10^{-3}\text{eV}^2$.

The fraction of steps in each of the mass hierarchy regions and octants of $\sin^2(\theta_{23})$ is given in Table 8.6. The Bayes factors are determined to be $B(\text{NH}/\text{IH}) =$

3.67 and $B(\mathrm{UO/LO}) = 1.74$. Jeffrey's scale (presented in Table 4.1) states that this value of the hierarchy Bayes factor illustrates substantial evidence for the normal hierarchy hypothesis. This corresponds to the correct hypothesis given the known oscillation parameters. It is a stronger statement than the atmospheric-only analysis can provide. It is important to note that this is a substantial preference that requires no external constraints required. The Bayes factor for octant determination represents a weak preference for the upper octant but does select the correct octant model.

	LO $\left(\sin^2\theta_{23} < 0.5\right)$	UO $\left(\sin^2\theta_{23} > 0.5\right)$	Sum
NH $\left(\Delta m^2_{32} > 0\right)$	0.29	0.50	0.79
IH $\left(\Delta m^2_{32} < 0\right)$	0.08	0.13	0.21
Sum	0.37	0.63	1.00

Table 8.6: The distribution of steps in a joint beam and atmospheric fit, presented as the fraction of steps in the upper (UO) and lower (LO) octants and the normal (NH) and inverted (IH) hierarchies. The reactor constraint is not applied. The Bayes factors are calculated as $B(\mathrm{NH/IH}) = 3.67$ and $B(\mathrm{UO/LO}) = 1.74$.

The sensitivity to $\sin^2(\theta_{23})$ is presented in Figure 8.19. There is a clear preference for the upper octant but the peak of the distribution is relatively flat. It peaks at $\sin^2(\theta_{23}) = 0.509$ which is in the region of the known value of $\sin^2(\theta_{23}) = 0.528$. The difference in the highest posterior distribution and the width of the credible interval is relatively unchanged when considering different hierarchy models showing no strong correlation between $\sin^2(\theta_{23})$ and $|\Delta m^2_{32}|$.

The sensitivity presented as a function of the appearance parameters ($\sin^2(\theta_{13}) - \delta_{CP}$) is given in Figure 8.20. As expected, the contours follow that given in Figure 8.2, where the 2σ credible intervals have a closed contour excluding the region around $\delta_{CP} \sim 1.2$. The width of the 3σ credible interval is also clearly dependent upon the value of δ_{CP}. Close to the Asimov point, $\delta_{CP} = -1.601$, the width of the 3σ credible interval approximately spans $\sin^2(\theta_{13}) = [0.013, 0.04]$. This is reduced to a region of $\sin^2(\theta_{13}) = [0.023, 0.042]$ at the most disfavoured value of δ_{CP}. This follows the behaviour shown in the likelihood scans. The 1σ

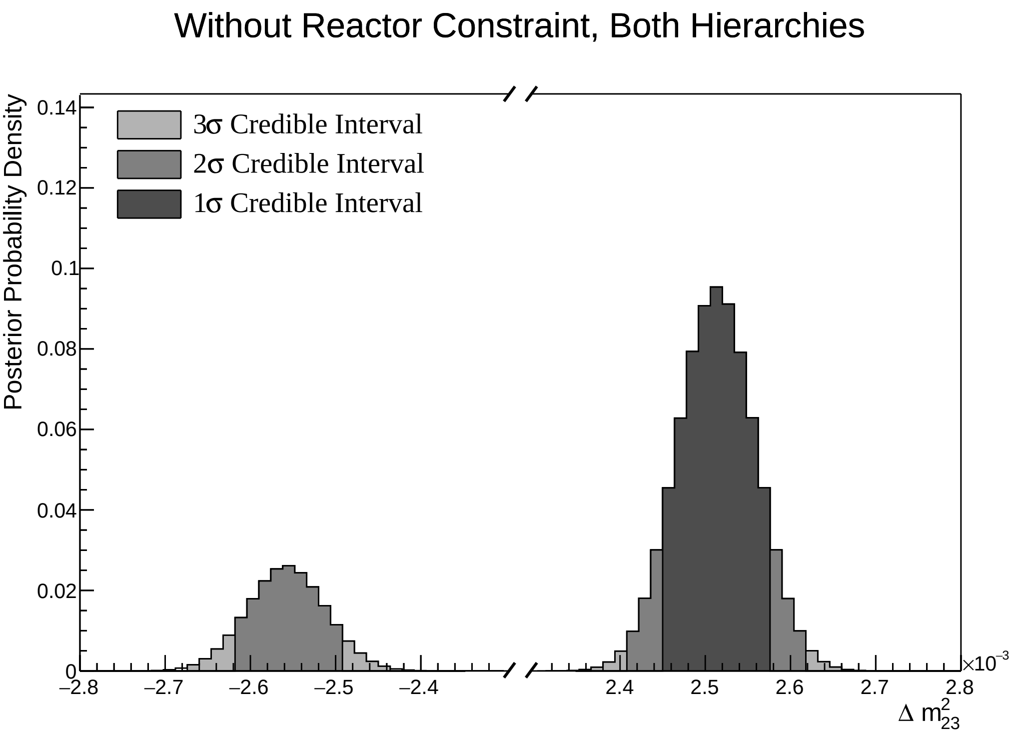

Figure 8.18: The one-dimensional posterior probability density distribution in Δm^2_{32}, marginalised over both hierarchies, from the joint beam and atmospheric fit. The reactor constraint is not applied.

credible interval is consistent with both the known oscillation parameter and the reactor constraint ($\sin^2(\theta_{13}) = (2.18 \pm 0.08) \times 10^{-2}$). Application of the reactor constraint would be expected to decrease the width of the 1σ credible intervals of δ_{CP} due to the triangular shape of the posterior probability.

The sensitivity in terms of the 'disappearance' parameters marginalised over both hierarchies is given in Figure 8.21. The area contained within the IH credible intervals is significantly smaller than those in the NH region. This is reflected in the IH credible intervals being tighter in the $\sin^2(\theta_{23})$ dimension. No significant correlation is observed between the value of $\sin^2(\theta_{23})$ and $|\Delta m^2_{32}|$.

The two-dimensional posterior distribution for each permutation of the oscillation parameters of interest is given in Figure 8.22. The most notable observation is that the $\sin^2(\theta_{13})$ and $\sin^2(\theta_{23})$ are anti-correlated. If the value of $\sin^2(\theta_{13})$ was known to be closer to the known oscillation parameter value, the preferred value of $\sin^2(\theta_{23})$ would increase furthering the preference for the UO. That

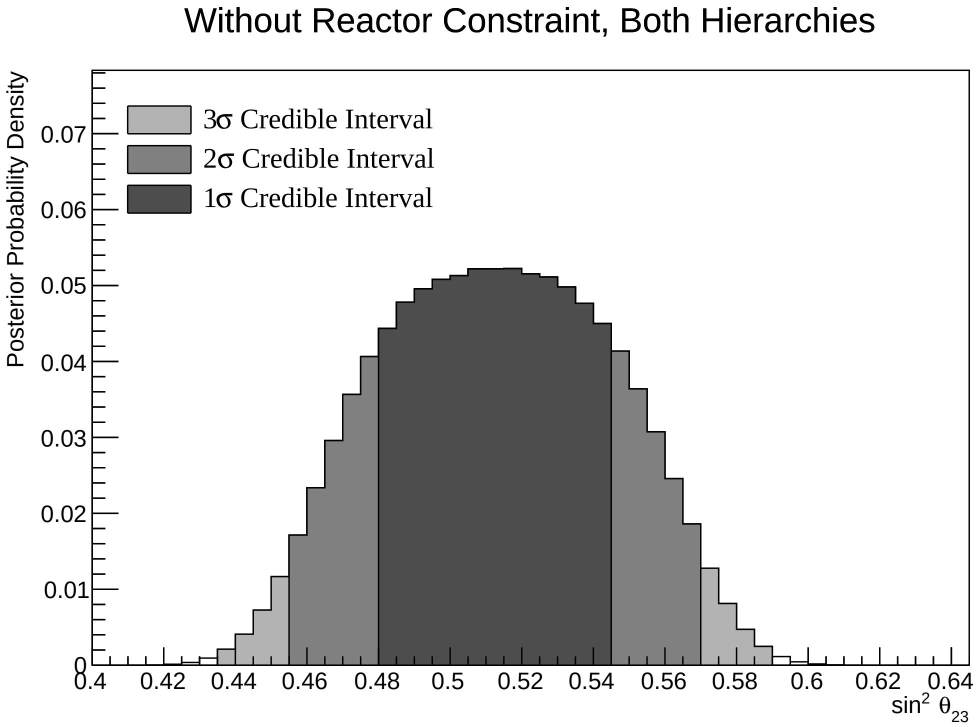

Figure 8.19: The one-dimensional posterior probability density distribution in $\sin^2(\theta_{23})$, marginalised over both hierarchies, from the joint beam-atmospheric fit. The reactor constraint is not applied.

would move the highest posterior probability closer in line with the Asimov value. This also means that the preference for the UO would be increased if the reactor constraint was to be applied.

Furthermore, the δ_{CP} and $|\Delta m^2_{32}|$ oscillation parameters are anti-correlated, such that higher values of $|\Delta m^2_{32}|$ prefer lower values of δ_{CP}. Whilst this is an interesting result on its own, the width of the Δm^2_{32} contours also depend on $\sin^2(\theta_{13})$. This introduces another correlation effect that could modify the sensitivity to δ_{CP} once the reactor constraint is applied.

The correlation between $\sin^2(\theta_{13})$ and Δm^2_{32} can be seen in Figure 8.23. A much larger fraction of the posterior distribution is contained in the NH for lower values of $\sin^2(\theta_{13})$. Consequently, the application of the reactor constraint would be expected to significantly increase the preference for NH.

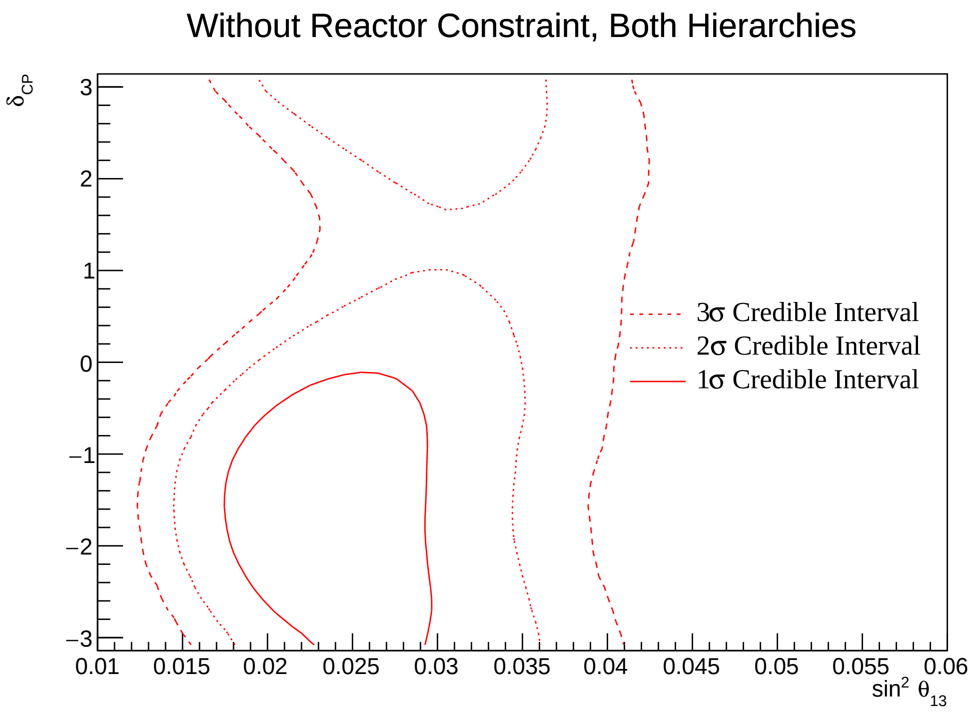

Figure 8.20: The two-dimensional posterior probability density distribution in δ_{CP} – $\sin^2(\theta_{13})$, marginalised over both hierarchies, from the joint beam and atmospheric fit. The reactor constraint is not applied.

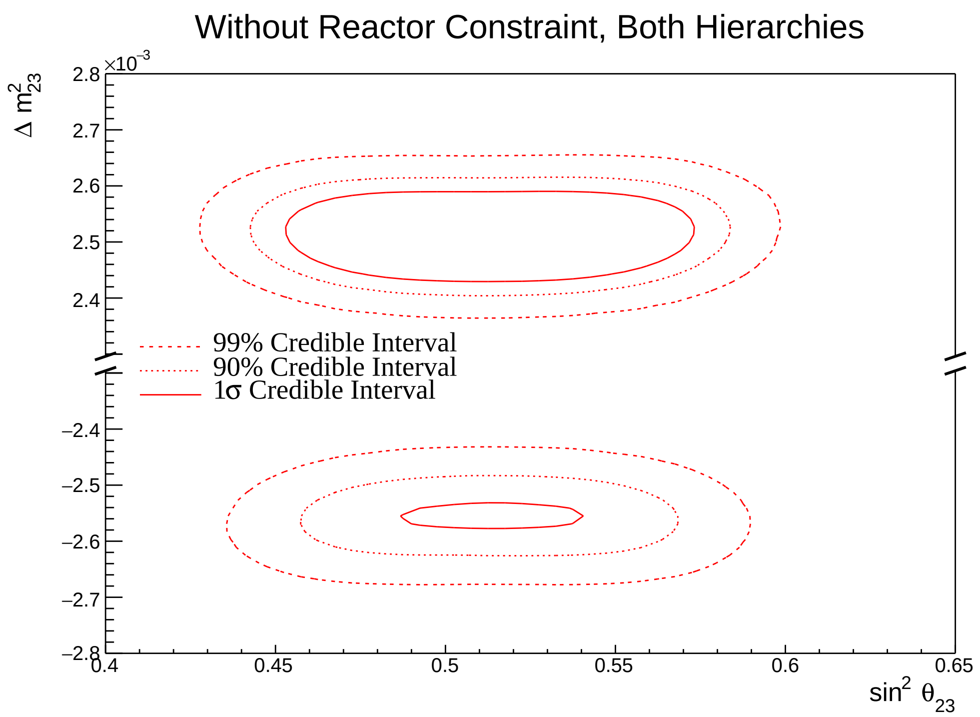

Figure 8.21: The two-dimensional posterior probability density distribution in Δm^2_{32} – $\sin^2(\theta_{23})$, marginalised over both hierarchies, from the joint beam and atmospheric fit. The reactor constraint is not applied.

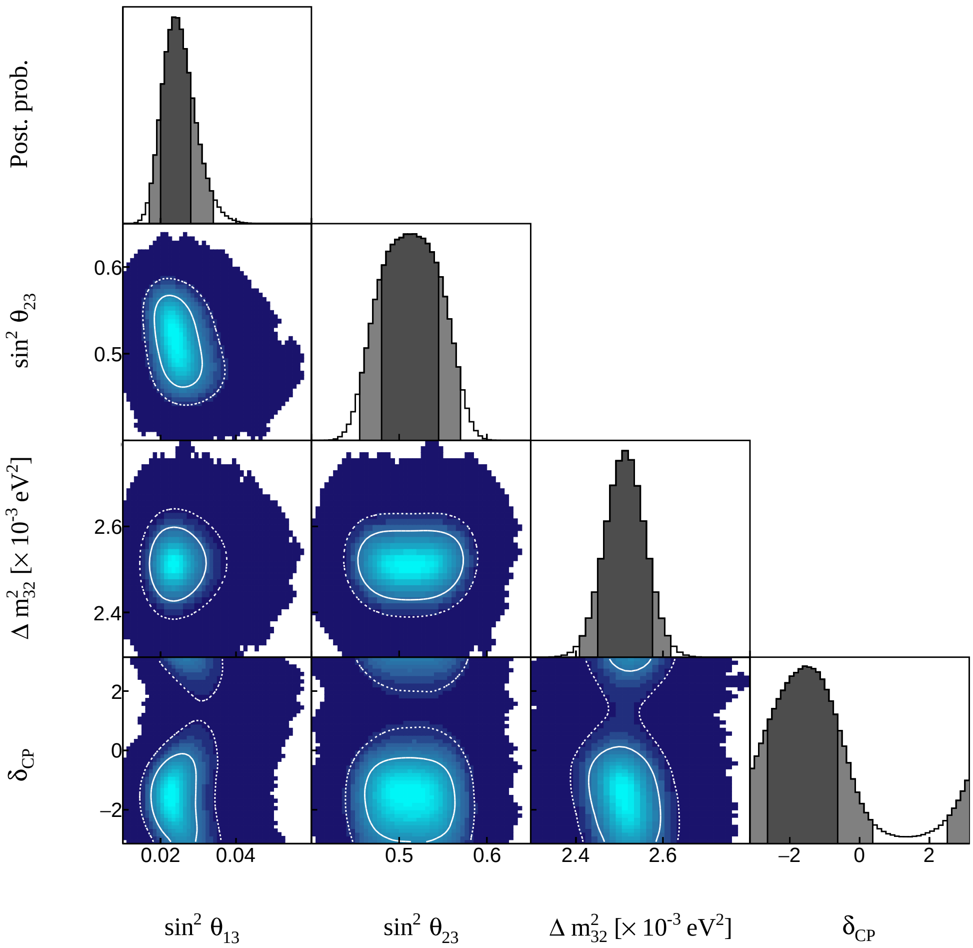

Figure 8.22: The posterior probability density distribution from the joint beam and atmospheric fit. The reactor constraint is not applied. The distribution is given for each two-dimensional permutation of the oscillation parameters of interest. The one-dimensional distribution of each parameter is also given.

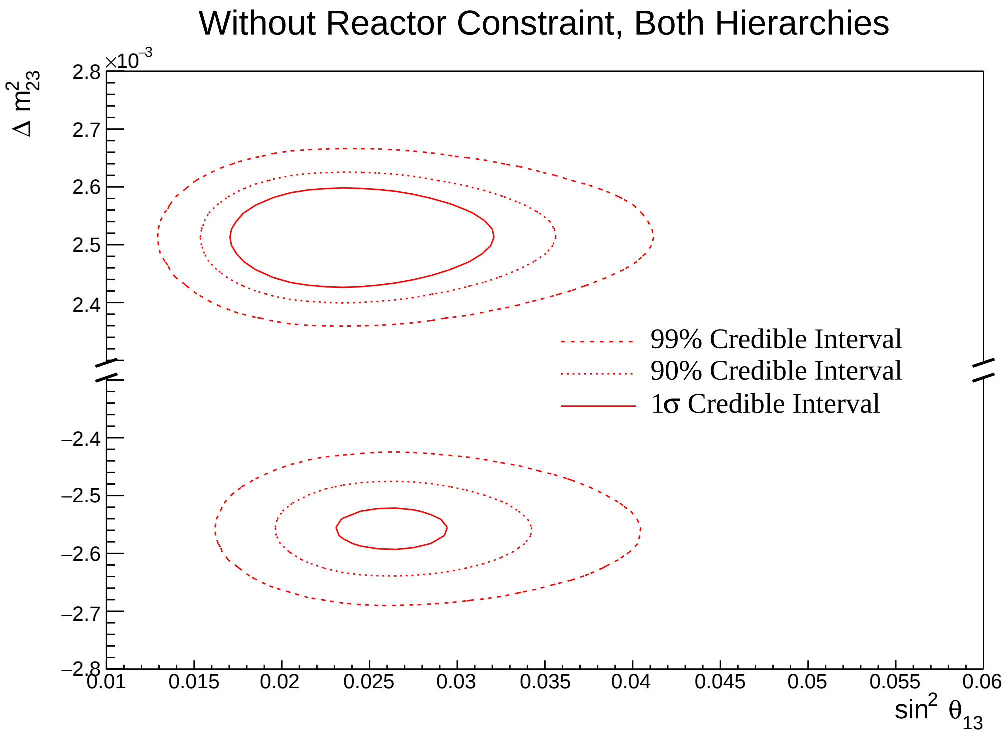

Figure 8.23: The two-dimensional posterior probability density distribution in $\Delta m^2_{32} - \sin^2(\theta_{13})$, marginalised over both hierarchies, from the joint beam and atmospheric fit. The reactor constraint is not applied.

8.2.5 Atmospheric and Beam Sensitivity with Reactor Constraint

This section presents the sensitivities of the joint beam and atmospheric fit when the reactor constraint is applied to $\sin^2(\theta_{13})$. As with the previous studies, the Asimov data is made using the AsimovA oscillation parameter set defined in Table 2.2 and the post-BANFF systematic parameter tune.

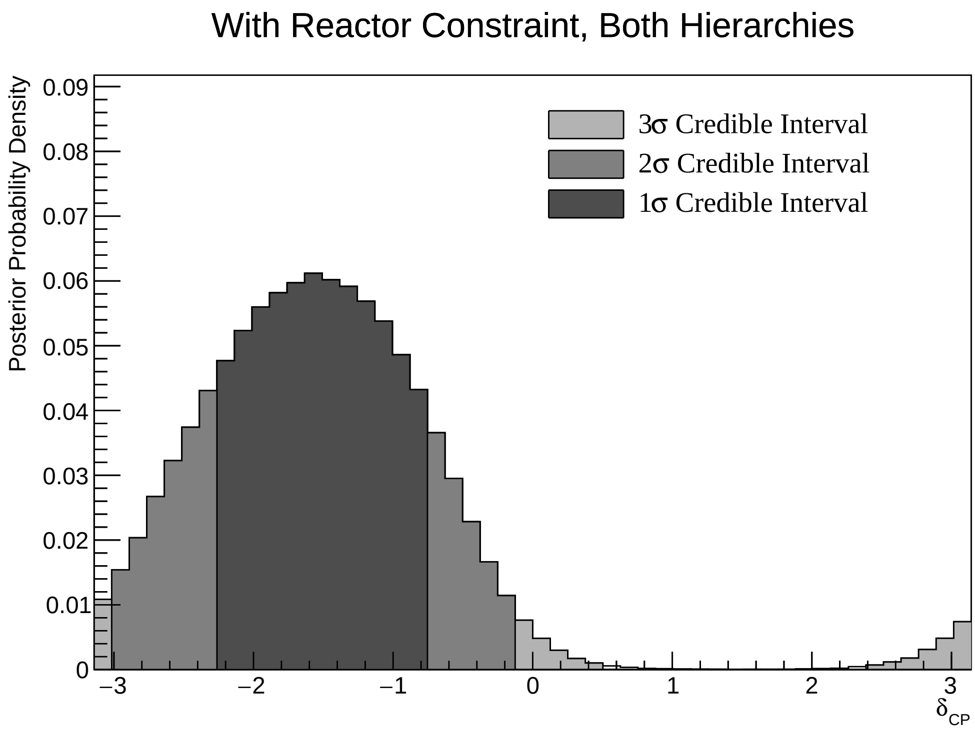

Figure 8.24: The one-dimensional posterior probability density distribution in δ_{CP}, marginalised over both hierarchies, from the joint beam and atmospheric fit where the reactor constraint is applied.

Figure 8.24 illustrates the sensitivity to δ_{CP}, marginalised over both hierarchies. The CP-conserving values of $\delta_{CP} = -\pi, 0, \pi$ are disfavoured at 2σ. Furthermore, the 3σ credible interval excludes the region of $\delta_{CP} = [0.50, 2.39]$. Thus clearly disfavouring the region of $\delta_{CP} = \pi/2$ at more than 3σ for this particular set of known oscillation parameters. The width of the 1σ credible intervals and the position of the highest posterior probability density is given in Table 8.7. The highest posterior probability density in δ_{CP} is calculated as $\delta_{CP} = -1.57$ showing no significant biases in the determination of the known oscillation parameters. The posterior distribution is more peaked around the known oscillation parameter value of $\delta_{CP} = -1.601$, as compared to the sensitivities when the reactor constraint is not applied (subsection 8.2.4). This follows from the correlations shown in Figure 8.20, where a lower value of $\sin^2(\theta_{13})$ results in tighter constraints on δ_{CP}.

The effect of applying the reactor constraint for δ_{CP} in the joint beam-atmospheric fit is presented in Figure 8.25. The posterior distribution from the two fits are marginalised over both hierarchies. Clearly, the reactor constraint improves the ability of the fit to select the known oscillation parameter as the shape of the distribution is much more peaked. This is also evidenced by the tightening of the 1σ and 90% credible intervals. Additionally, the disfavoured region of $1 < \delta_{CP} < 2$ is wider when the reactor constraint is applied.

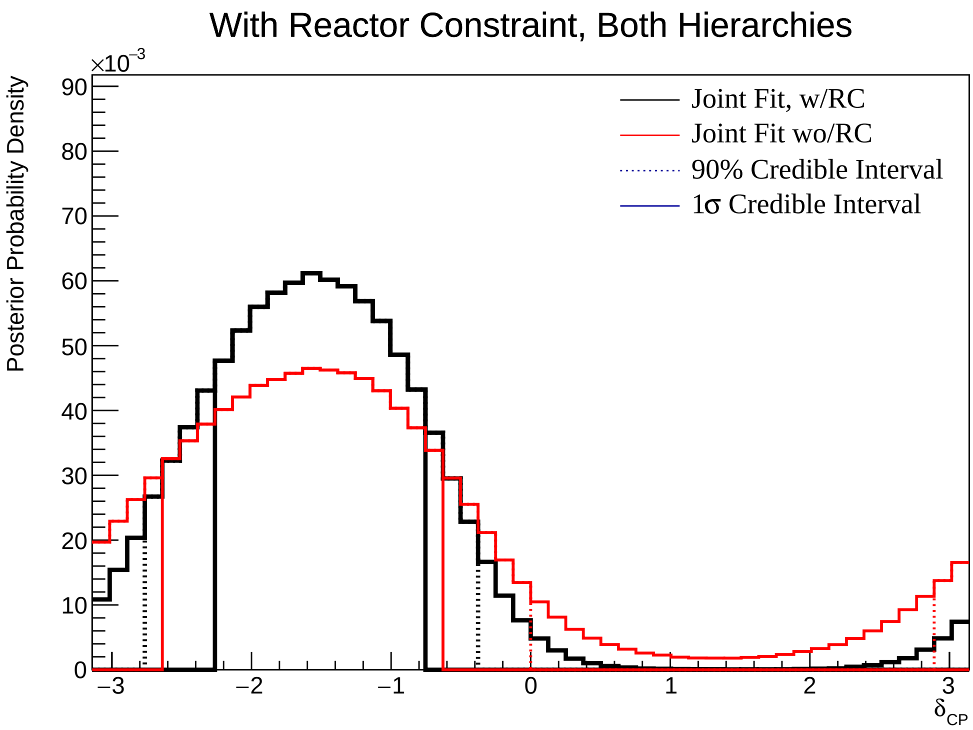

Figure 8.25: The one-dimensional posterior probability density distribution in δ_{CP} compared between the joint beam-atmospheric fit (Red) and the joint beam and atmospheric fit with the reactor constraint (Black). The distributions are marginalised over both hierarchies.

The sensitivity to $\sin^2(\theta_{23})$, marginalised over both hierarchies, is given in Figure 8.26. The highest posterior probability density is located at $\sin^2(\theta_{23}) = 0.527$

Parameter	Interval	HPD
δ_{CP}, (BH)	$[-2.26, -0.75]$	-1.57
δ_{CP}, (NH)	$[-2.26, -0.75]$	-1.57
δ_{CP}, (IH)	$[-2.13, -1.00]$	-1.57
Δm^2_{32} (BH) $[\times 10^{-3}\text{eV}^2]$	$[2.46, 2.52]$	2.49
Δm^2_{32} (NH) $[\times 10^{-3}\text{eV}^2]$	$[2.48, 2.56]$	2.51
Δm^2_{32} (IH) $[\times 10^{-3}\text{eV}^2]$	$[-2.60, -2.52]$	-2.55
$\sin^2(\theta_{23})$ (BH)	$[0.49, 0.55]$	0.527
$\sin^2(\theta_{23})$ (NH)	$[0.49, 0.55]$	0.527
$\sin^2(\theta_{23})$ (IH)	$[0.50, 0.56]$	0.539

Table 8.7: The position of the highest posterior probability density (HPD) and width of the 1σ credible interval for the joint beam and atmospheric fit where the reactor constraint is applied. The values are presented by which hierarchy hypothesis is assumed: marginalised over both hierarchies (BH), normal hierarchy only (NH), and inverted hierarchy only (IH).

which agrees with the known value of $\sin^2(\theta_{23}) = 0.528$. The distribution clearly favours the UO with almost the entirety of the 1σ credible interval contained in the region. Figure 8.27 highlights the sensitivity of the joint fit both with and without the reactor constraint. The fit where the reactor constraint is applied selects the known value much better ($\sin^2(\theta_{23}) = 0.528$). Furthermore, the reactor constraint increases the UO preference which is evidenced by the distribution moving further away from the octant boundary. This indicates that there are marginalisation effects between the two mixing parameters. The follows from the correlation illustrated between $\sin^2(\theta_{23}) - \sin^2(\theta_{13})$ in Figure 8.22. The posterior distribution of the fit with reactor constraint is more peaked compared to the flatter distribution when the reactor constraint is not applied.

The fraction of steps contained within the two hierarchy and two octant models is given in Table 8.8. The reactor constraint significantly reduces the fraction of steps that are contained within the IH-LO region from 0.08 to 0.02, whilst significantly increasing the fraction of steps within the NH-UO region from 0.53 to 0.64. The application of the reactor constraint increases the Bayes factor

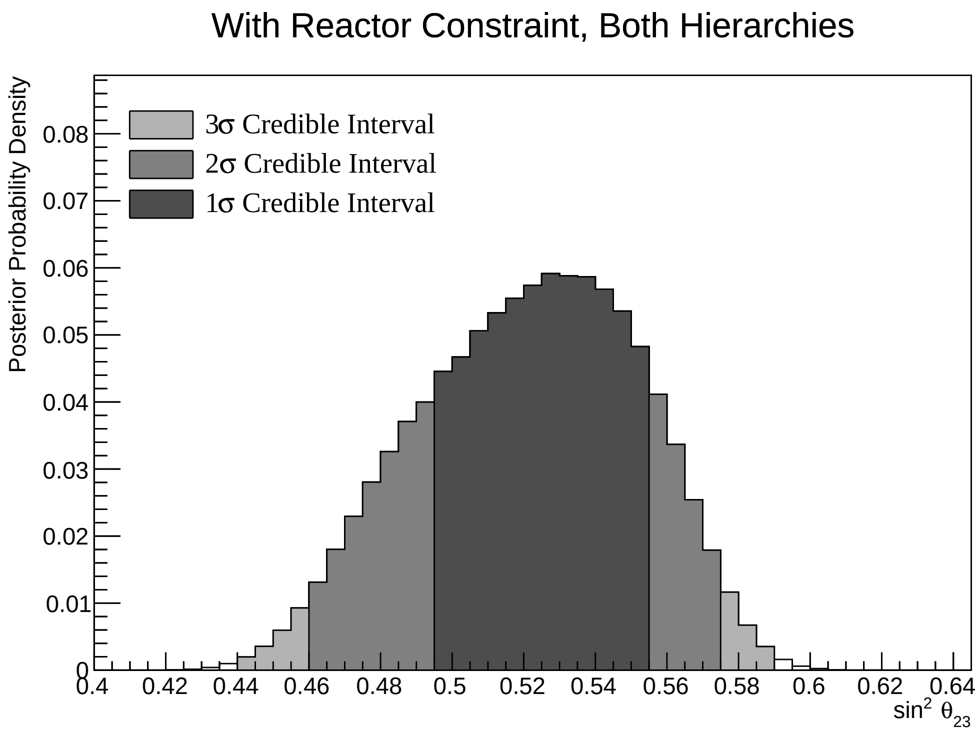

Figure 8.26: The one-dimensional posterior probability density distribution in $\sin^2(\theta_{23})$, marginalised over both hierarchies, from the joint beam and atmospheric fit where the reactor constraint is applied.

from B(NH/IH) = 3.67 to $B(\mathrm{NH/IH}) = 7.29$. There is a very clear preference for the NH, with the Jeffreys scale stating a substantial preference for both fits (see subsection 4.3.3). The Bayes factor for UO preference is calculated as $B(\mathrm{UO/LO}) = 2.86$. Whilst still a weak preference, this is certainly a stronger statement than the sensitivity when the reactor constraint is not applied.

	LO $\left(\sin^2\theta_{23} < 0.5\right)$	UO $\left(\sin^2\theta_{23} > 0.5\right)$	Sum
NH $\left(\Delta m^2_{32} > 0\right)$	0.24	0.64	0.88
IH $\left(\Delta m^2_{32} < 0\right)$	0.02	0.10	0.12
Sum	0.26	0.74	1.00

Table 8.8: The distribution of steps in a joint beam and atmospheric with the reactor constraint fit applied, presented as the fraction of steps in the upper (UO) and lower (LO) octants and the normal (NH) and inverted (IH) hierarchies. The Bayes factors are calculated as $B(\mathrm{NH/IH}) = 7.29$ and $B(\mathrm{UO/LO}) = 2.86$.

The sensitivity to Δm^2_{32}, with the reactor constraint applied, is presented in

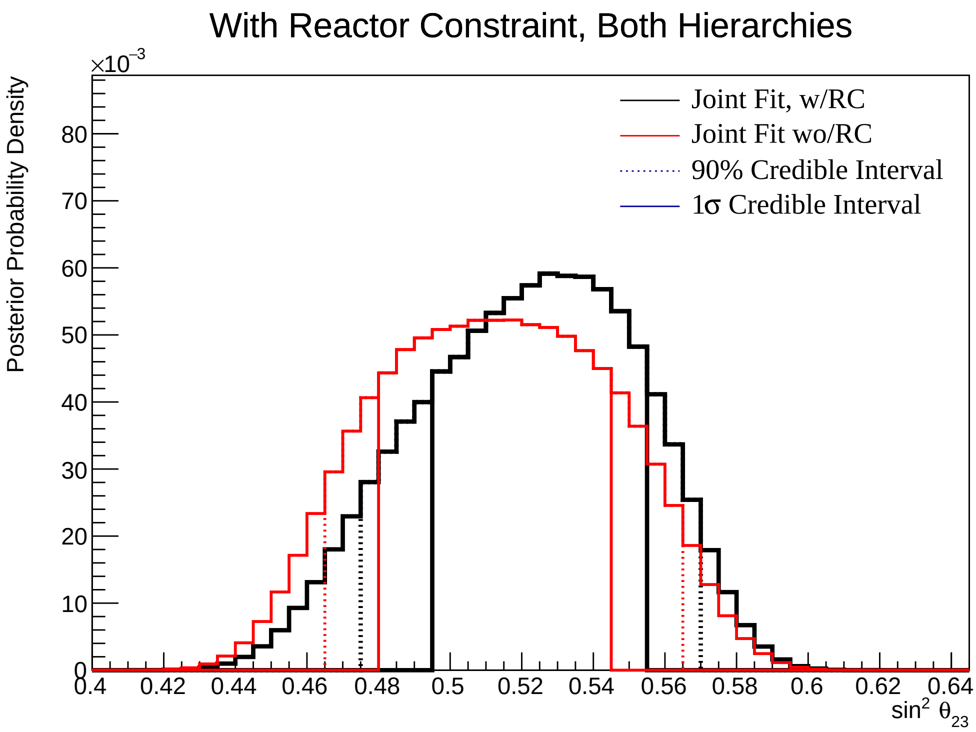

Figure 8.27: The one-dimensional posterior probability density distribution in $\sin^2(\theta_{23})$ compared between the joint beam-atmospheric fit (Red) and the joint beam and atmospheric fit with the reactor constraint (Black). The distributions are marginalised over both hierarchies.

Figure 8.28. The posterior distribution is marginalised over both hierarchies. As expected, the 1σ credible interval is entirely contained within the NH region. The position of the highest posterior probability density is given as 2.49×10^{-3}eV^2, illustrating no significant bias between the fit results and the known oscillation parameters. The application of the reactor constraint does move significantly the position of the credible intervals but does reduce their width.

The sensitivity to the appearance parameters ($\sin^2(\theta_{13}) - \delta_{CP}$) is given in Figure 8.29. The distribution is mostly uncorrelated between the two parameters and is centered at the known oscillation parameters. The 1σ credible interval excludes $\delta_{CP} = 0$ and $\delta_{CP} = (-)\pi$. Furthermore, the 3σ credible intervals exclude the region of $\delta_{CP} = \pi/2$.

The sensitivity to the disappearance parameters ($\sin^2(\theta_{23}) - \Delta m^2_{32}$) is illustrated in Figure 8.30. As expected from the one-dimensional distribution, the 1σ credible interval is entirely contained within the NH region. Both the NH and

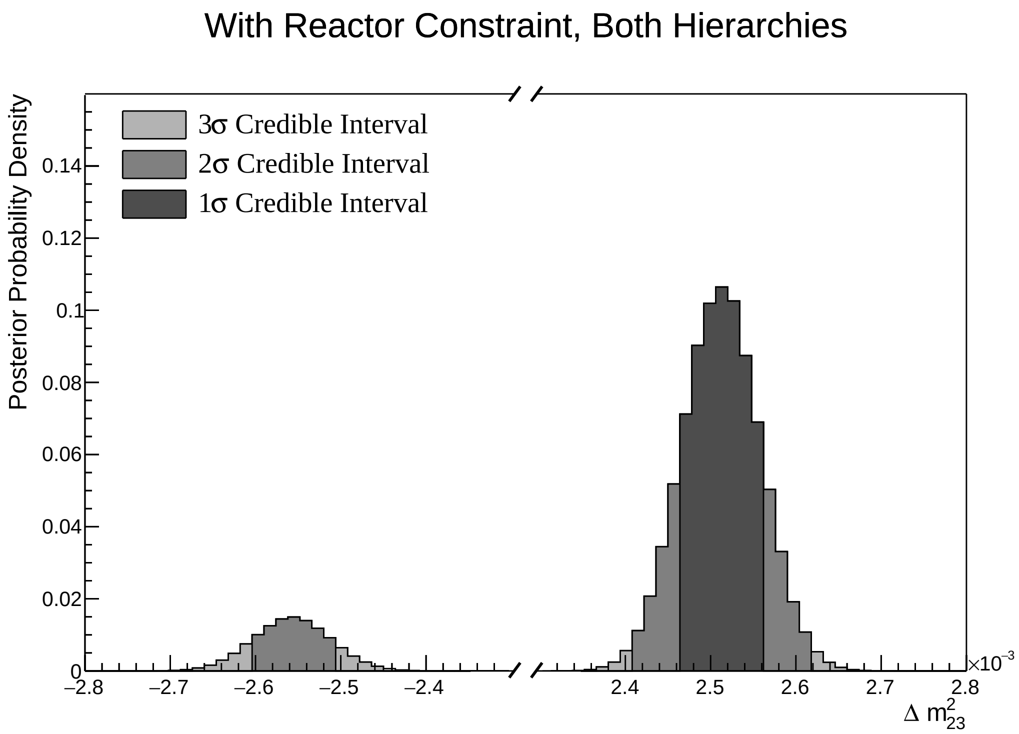

Figure 8.28: The one-dimensional posterior probability density distribution in Δm^2_{32}, marginalised over both hierarchies, from the joint beam and atmospheric fit where the reactor constraint is applied.

IH regions favour the UO, with a visually similar preference in both hierarchies. The width of the Δm^2_{32} 1σ credible interval does not significantly depend upon the value or octant of $\sin^2(\theta_{23})$. This shows that there are no strong correlations between these two parameters.

Figure 8.31 illustrates the posterior distribution for each permutation of two oscillation parameters of interest. The application of the reactor constraint significantly reduces the correlations previously seen in Figure 8.22. There is still a small correlation between δ_{CP} and Δm^2_{32}. The application of the reactor constraint has not significantly affected this correlation. The width of the 1σ credible interval in Δm^2_{32} is wider for a value of $\delta_{CP} = 0$ as compared to a value of $\delta_{CP} = \pi$. Similarly, the width of the 1σ credible interval in δ_{CP} is smaller for lower values of $\sin^2(\theta_{23})$.

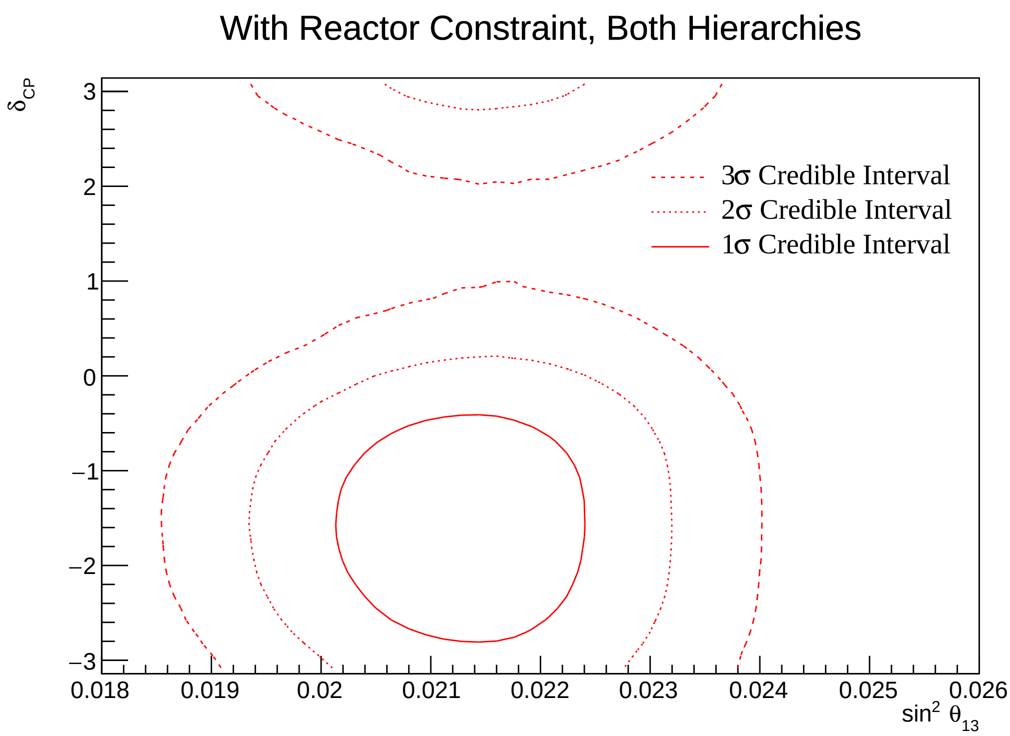

Figure 8.29: The two-dimensional posterior probability density distribution in $\delta_{CP} - \sin^2(\theta_{13})$, marginalised over both hierarchies, from the joint beam and atmospheric fit where the reactor constraint is applied.

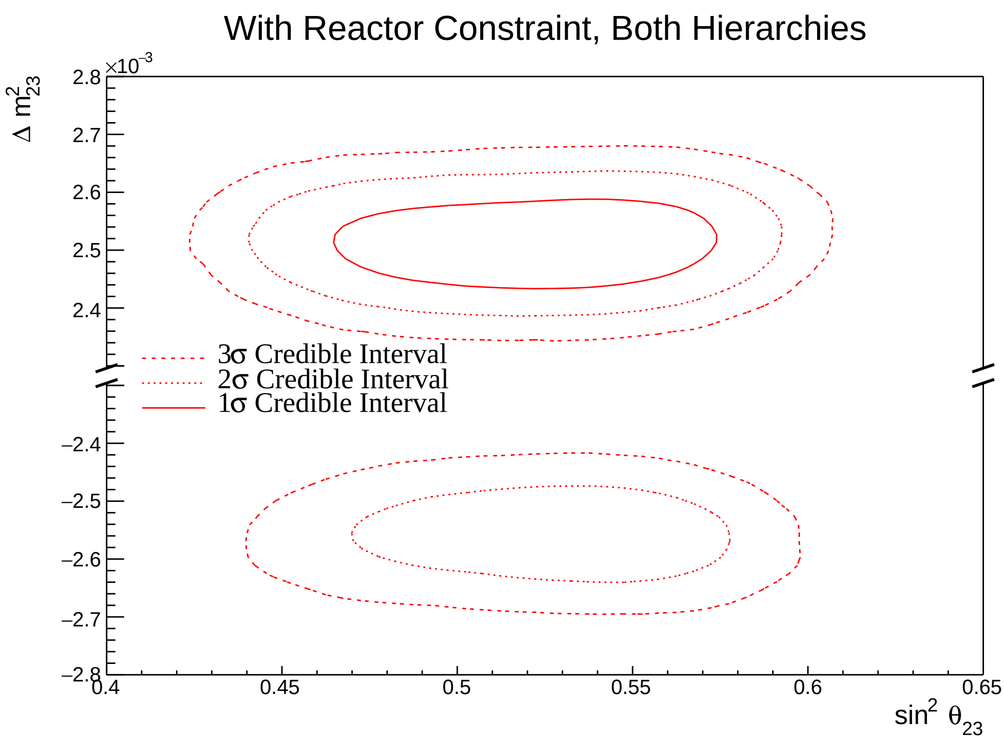

Figure 8.30: The two-dimensional posterior probability density distribution in $\Delta m^2_{32} - \sin^2(\theta_{23})$, marginalised over both hierarchies, from the joint beam and atmospheric fit where the reactor constraint is applied.

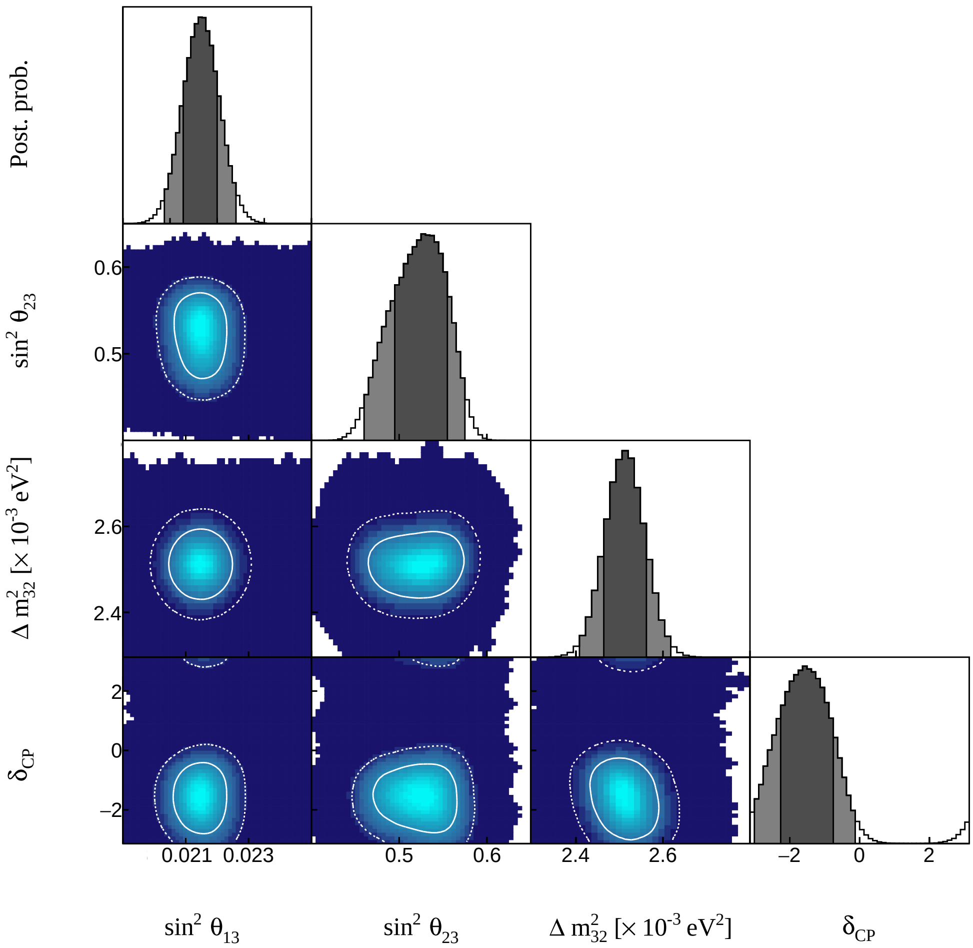

Figure 8.31: The posterior probability density distribution from the joint beam and atmospheric fit where the reactor constraint is applied. The distribution is given for each two-dimensional permutation of the oscillation parameters of interest. The one-dimensional distribution of each parameter is also given.

8.2.6 Comparison to Latest T2K Sensitivities without Reactor Constraint

The benefits of the joint beam and atmospheric analysis can be determined by comparing the sensitivities to the beam-only analysis. This section presents those comparisons for sensitivities built using the Asimov A oscillation parameters defined in Table 2.2 and the post-BANFF systematic tune. The reactor constraint is not applied within either of the fits used in these comparisons.

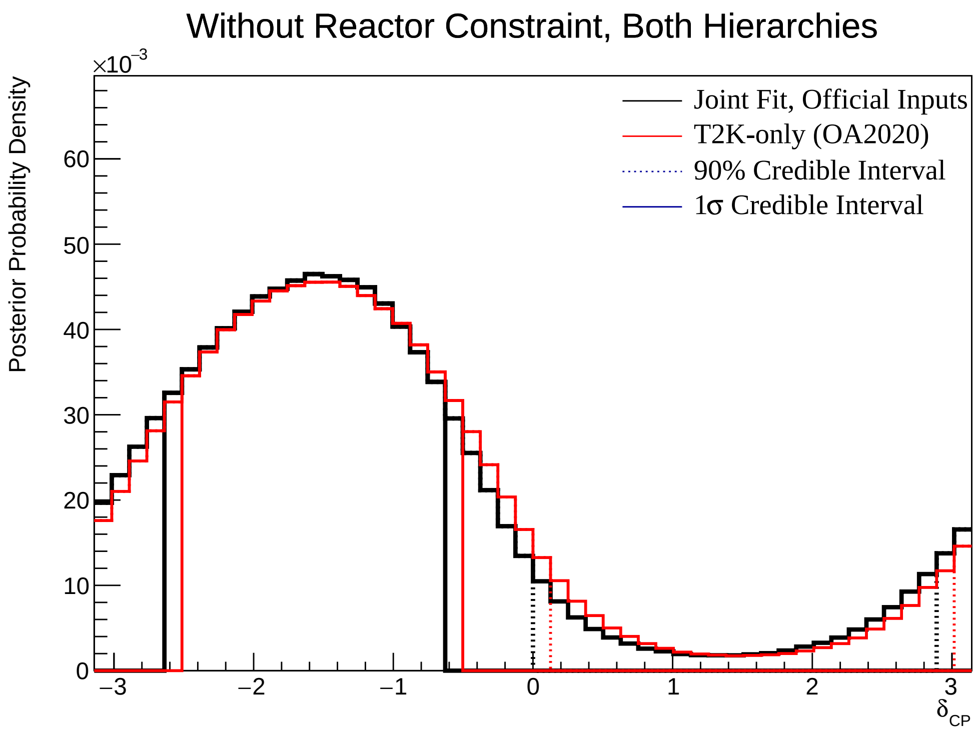

Figure 8.32: The one-dimensional posterior probability density distribution in δ_{CP} compared between the joint beam-atmospheric fit (Black) and the latest T2K sensitivities (Red) [186]. The reactor constraint is not applied in either fit. The distributions are marginalised over both hierarchies.

The sensitivity, marginalised over both hierarchies, to δ_{CP} from the joint beam-atmospheric and beam-only fits is presented in Figure 8.32. As expected from the likelihood scans (Figure 8.4), the sensitivity to δ_{CP} is not significantly increased. This is because the known oscillation parameter value ($\delta_{CP} = -1.601$) lies at the position where the beam samples dominate the sensitivity compared to the SK samples.

The sensitivity to Δm^2_{32} of the joint beam-atmospheric fit is illustrated in Figure 8.33, where the posterior distribution has been marginalised over both hierarchies. The 1σ credible interval of the joint beam and atmospheric fit is entirely contained within the NH region. This shows the significant increase in the ability of the fit to determine the correct mass hierarchy, as compared to the beam-only analysis. This is further evidenced by the fact that the 90% credible intervals from the joint fit are also tighter in the IH region as compared to the beam-only analysis. The Bayes factor for mass hierarchy determination for the beam-only and joint beam and atmospheric are $B(\mathrm{NH/IH}) = 1.91$ and $B(\mathrm{NH/IH}) = 3.67$, respectively. According to Jeffrey's scale (Table 4.1), the beam-only analysis represents a weak preference for the NH hypothesis whereas the joint fit returns a substantial preference for the NH hypothesis. To summarise, the joint beam-atmospheric fit has a substantial preference for the correct hierarchy without the requirement of external constraints.

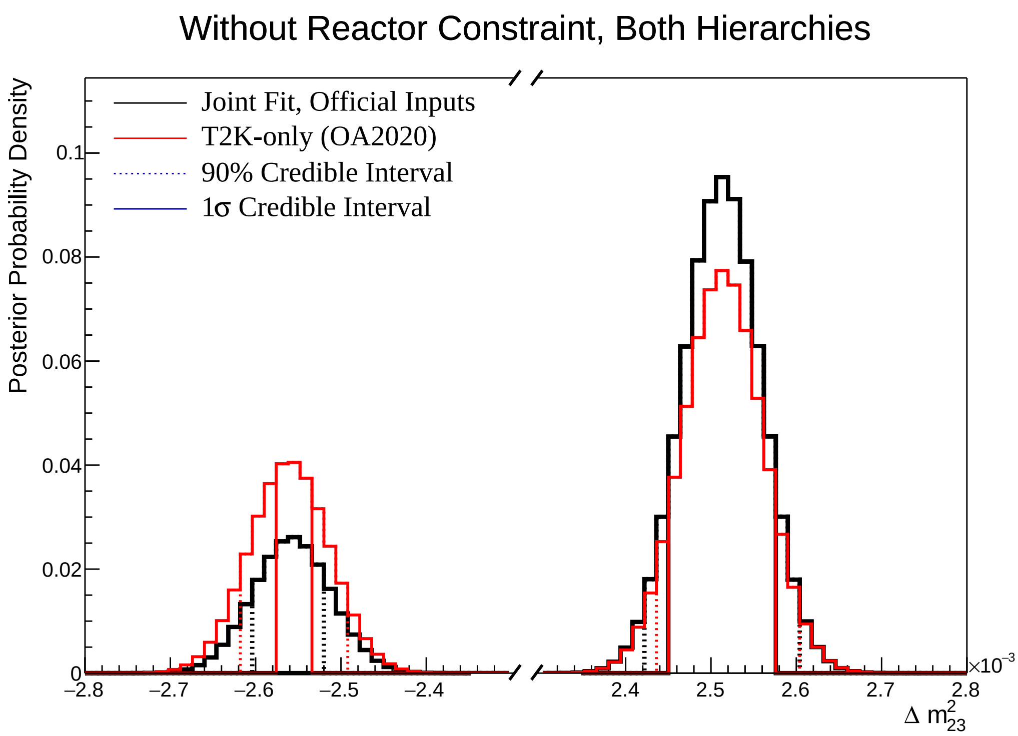

Figure 8.33: The one-dimensional posterior probability density distribution in Δm^2_{32} compared between the joint beam-atmospheric fit (Black) and the latest T2K sensitivities (Red) [186]. The reactor constraint is not applied in either fit. The distributions are marginalised over both hierarchies.

The sensitivity to $\sin^2(\theta_{23})$, marginalised over both hierarchies, for both the beam-only and joint beam and atmospheric analysis are presented in Figure 8.34. The peak of the posterior distribution from the joint analysis is more aligned with the known value of $\sin^2(\theta_{23}) = 0.528$ as compared to the beam-only analysis. This indicates that the marginalisation effects from other oscillation parameters ($\sin^2(\theta_{13}) - \sin^2(\theta_{23})$ presented in Figure 8.22) are less prevalent in the projection of this parameter. The Bayes factors for the beam-only and joint beam-atmospheric fit are $B(\mathrm{UO}/\mathrm{LO}) = 1.56$ and $B(\mathrm{UO}/\mathrm{LO}) = 1.74$, respectively. Therefore, the joint beam-atmospheric fit does prefer the UO more strongly than the beam-only analysis, albeit slightly.

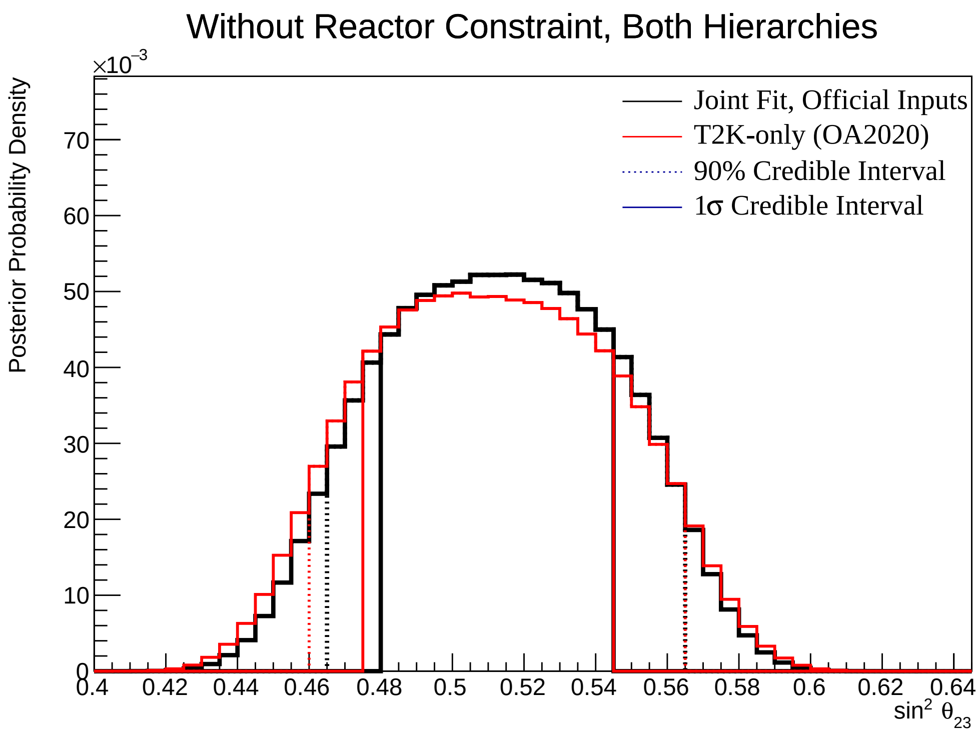

Figure 8.34: The one-dimensional posterior probability density distribution in $\sin^2(\theta_{23})$ compared between the joint beam-atmospheric fit (Black) and the latest T2K sensitivities (Red) [186]. The reactor constraint is not applied in either fit. The distributions are marginalised over both hierarchies.

Whilst the beam-only and joint beam-atmospheric fits have similar sensitivity to δ_{CP} and $\sin^2(\theta_{23})$ when projected in one-dimension, the benefit of the joint analysis becomes more obvious when the sensitivities are presented in two-dimensions. The sensitivity of the two fits to the appearance parameters ($\delta_{CP} - \sin^2(\theta_{13})$) are illustrated in Figure 8.35.

The width of the 99% joint fit credible interval in $\sin^2(\theta_{13})$ is squeezed in the region of $\delta_{CP} \sim 0$ compared to the beam-only analysis. This is the same behaviour that is seen in the appearance likelihood scans presented in Figure 8.2. The 1σ and 90% also exhibit slightly tighter constraints on δ_{CP}. This is most prevalent in the region of $\delta_{CP} \sim 0$ and $sin^2(\theta_{13}) \sim 0.03$. Whilst the atmospheric samples do not have significant sensitivity to $\sin^2(\theta_{13})$ (as shown in Figure 8.1), they aid in breaking the degeneracy between the oscillation parameters allowing for tighter constraints.

The sensitivity to the disappearance parameters $\sin^2(\theta_{23}) - \Delta m^2_{32}$, marginalised over both hierarchies, is presented in Figure 8.36 for both the beam-only and joint beam-atmospheric fits. Whilst the one-dimensional sensitivity comparisons considered so far show the improvements of the joint fit, the two-dimensional projection really shows the benefit of adding the atmospheric samples to the beam samples. The area contained within the IH credible intervals is drastically reduced in the joint fit. This follows from the better determination of the mass hierarchy seen in the Bayes factor comparisons. The 1σ joint fit credible interval in the IH region more strongly favours the UO as compared to the beam-only fit. Even in the NH region, the width of the credible intervals in $\sin^2(\theta_{23})$ decrease, albeit to a smaller extent.

The change in sensitivity to $\delta_{CP} - \Delta m^2_{32}$ is illustrated in Figure 8.37. As expected, the contours presented within the IH region are much smaller in the joint fit due to the increased sensitivity to mass hierarchy determination. This culminates in a region around $\delta_{CP} \sim \pi/2$ which is excluded at 3σ. This behaviour is not present within the beam-only analysis. Consistent with the previous observations, the area contained within the IH credible intervals is significantly reduced in comparison to the beam-only analysis.

The sensitivity to Δm^2_{32} and $\sin^2(\theta_{23})$, as a function of $\sin^2(\theta_{13})$, is presented in Figure 8.38 and Figure 8.39, respectively. These sensitivities are marginalised

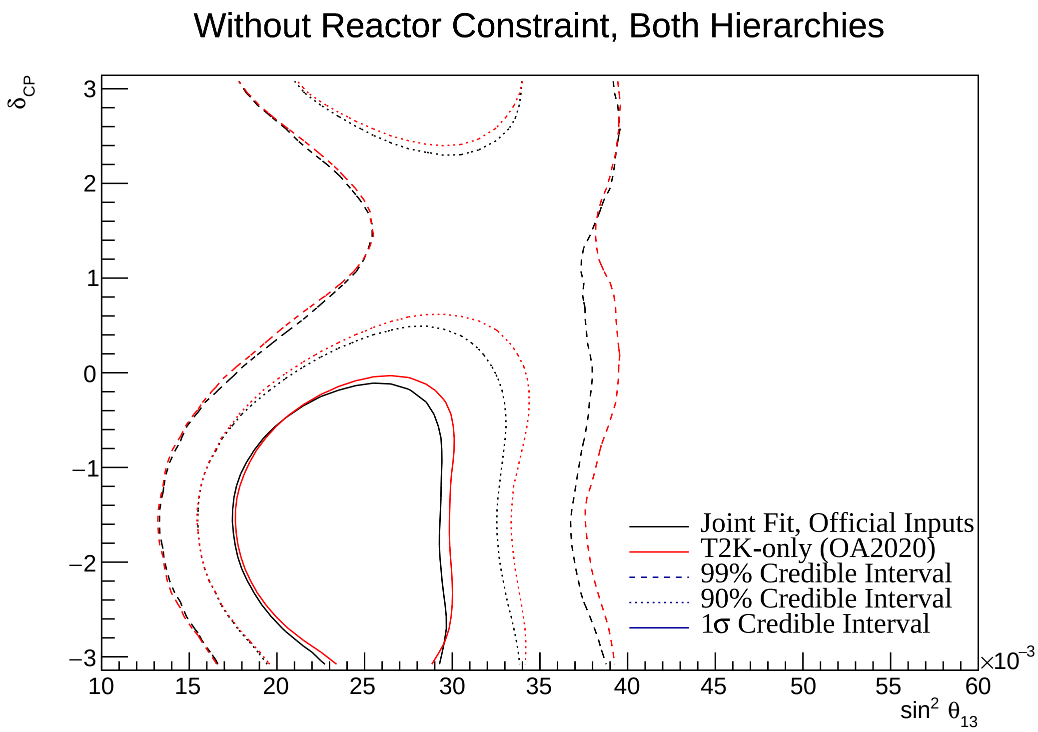

Figure 8.35: The two-dimensional posterior probability density distribution in $\delta_{CP} - \sin^2(\theta_{13})$ compared between the joint beam-atmospheric fit (Black) and the latest T2K sensitivities (Red) [186]. The reactor constraint is not applied in either fit. The distributions are marginalised over both hierarchies.

over both hierarchies. As expected from the previous observations, the Δm^2_{32} contours within IH region of the joint fit are much smaller than the beam-only analysis. Notably, the joint fit IH 1σ credible intervals exclude the region around the reactor constraint. This is not a bias from the fit as the known value for Δm^2_{32} is in the NH region. This does suggest that the application of the reactor constraint would further increase the preference for NH in the joint fit as compared to its effect on the beam-only analysis.

The beam-only and joint beam-atmospheric fits have a slightly different contour shape between the $\sin^2(\theta_{13})$ and $\sin^2(\theta_{23})$ parameters, as illustrated by Figure 8.39. The joint analysis disfavours the wrong octant hypothesis more strongly in the region of high $\sin^2(\theta_{13})$. This suggests that the application of the reactor constraint will favour the UO more strongly in the joint analysis compared to the beam-only analysis.

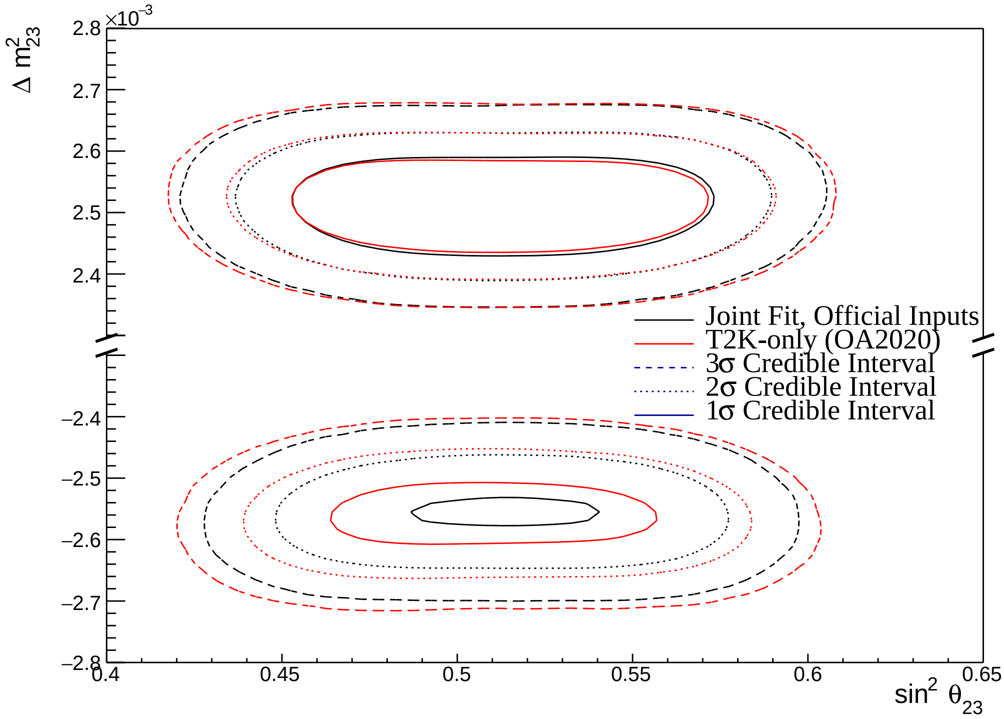

Figure 8.36: The two-dimensional posterior probability density distribution in $\Delta m^2_{32} - \sin^2(\theta_{23})$ compared between the joint beam-atmospheric fit (Black) and the latest T2K sensitivities (Red) [186]. The reactor constraint is not applied in either fit. The distributions are marginalised over both hierarchies.

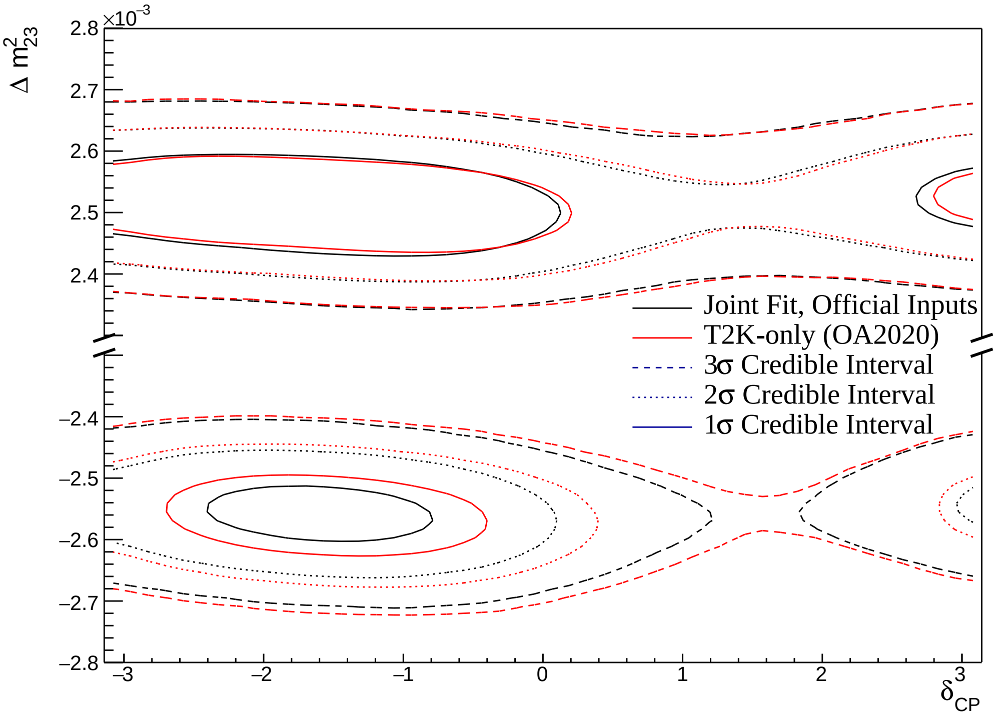

Figure 8.37: The two-dimensional posterior probability density distribution in $\Delta m^2_{32} - \Delta_{CP}$ compared between the joint beam-atmospheric fit (Black) and the latest T2K sensitivities (Red) [186]. The reactor constraint is not applied in either fit. The distributions are marginalised over both hierarchies.

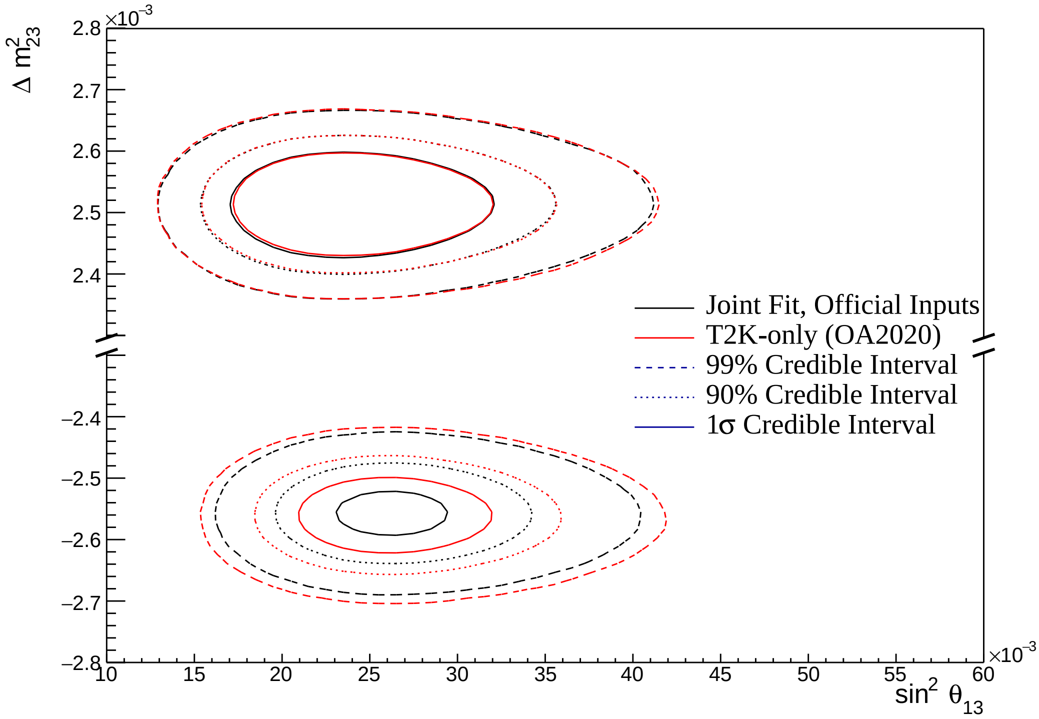

Figure 8.38: The two-dimensional posterior probability density distribution in $\Delta m^2_{32} - \sin^2(\theta_{23})$ compared between the joint beam-atmospheric fit (Black) and the latest T2K sensitivities (Red) [186]. The reactor constraint is not applied in either fit. The distributions are marginalised over both hierarchies.

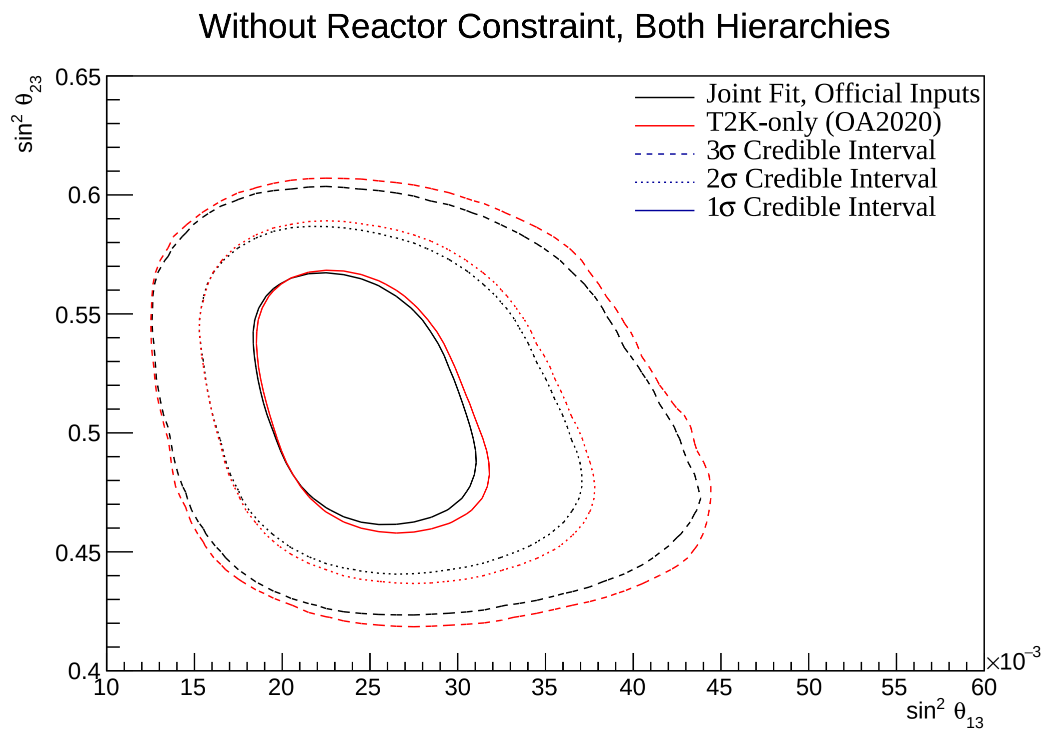

Figure 8.39: The two-dimensional posterior probability density distribution in $\sin^2(\theta_{23}) - \sin^2(\theta_{13})$ compared between the joint beam-atmospheric fit (Black) and the latest T2K sensitivities (Red) [186]. The reactor constraint is not applied in either fit. The distributions are marginalised over both hierarchies.

8.2.7 Comparison to Latest T2K Sensitivities with Reactor Constraint

The comparison between the beam-only and joint beam-atmospheric fits are compared in subsection 8.2.6. Those comparisons were made with the reactor constraint not applied to either of the fits. This section illustrates the comparison when the reactor constraint is applied. As shown in Figure 8.38, the application of the reactor constraint is expected to significantly increase the joint fit's preference for the NH hypothesis, as compared to the beam-only analysis. Figure 8.40 illustrates the sensitivities of the two fits to the disappearance parameters ($\sin^2(\theta_{23}) - \Delta m^2_{32}$) marginalised over both hierarchies and with the reactor constraint applied. This plot clearly illustrates the benefit of the joint beam and atmospheric analysis. The 1σ credible interval in the IH region is entirely removed in the joint analysis, illustrating the improved NH preference.

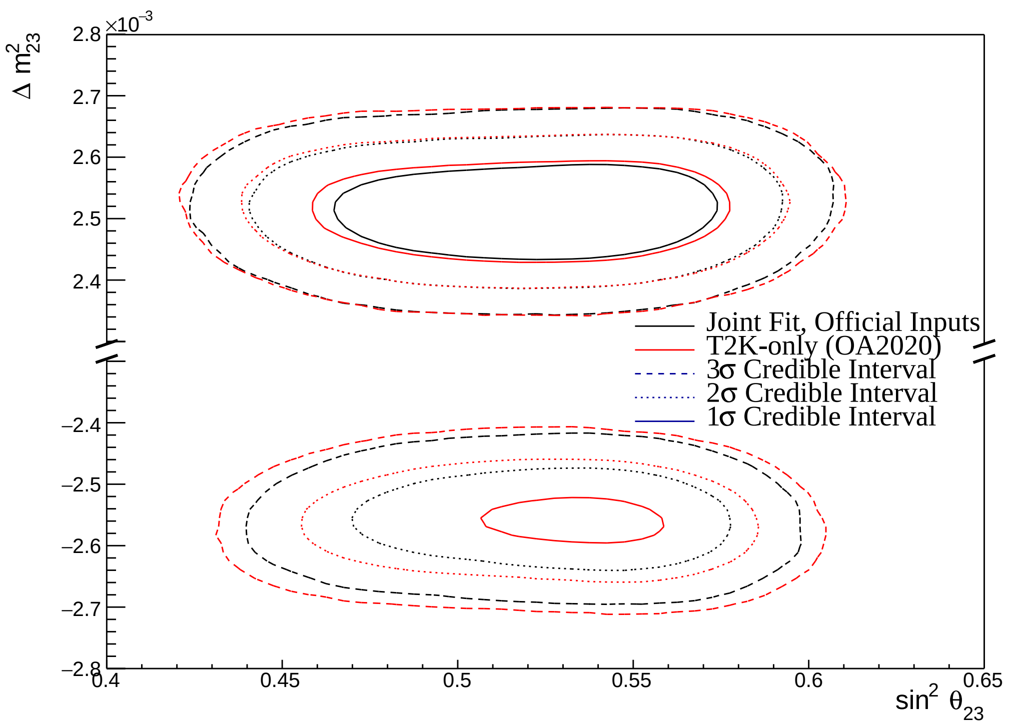

Figure 8.40: The two-dimensional posterior probability density distribution in $\Delta m^2_{32} - \sin^2(\theta_{23})$ compared between the joint beam-atmospheric fit (Black) and the latest T2K sensitivities (Red) [186]. The reactor constraint is applied in both fits. The distributions are marginalised over both hierarchies.

The credible intervals of the joint fit are also tighter in the $\sin^2(\theta_{23})$ dimension than the beam-only analysis in both mass hierarchy regions. This shows that beyond the ability of the joint fit to prefer the NH more strongly than the beam-only analysis, the precision to which it can measure $\sin^2(\theta_{23})$ is also improved. The Bayes factor for NH preference is calculated as $B(\mathrm{NH}/\mathrm{IH}) = 7.29$ and $B(\mathrm{NH}/\mathrm{IH}) = 3.41$ for the joint beam-atmospheric and beam-only analysis, respectively. Whilst both present a significant preference for the NH hypothesis (Table 4.1), the joint fit's preference is much stronger. A similar conclusion can be made regarding the Bayes factors for UO preference which are $B(\mathrm{UO}/\mathrm{LO}) = 2.86$ and $B(\mathrm{UO}/\mathrm{LO}) = 2.67$ for the joint beam-atmospheric and beam-only analysis, respectively. Both of these represent a mild preference for the UO but there is a stronger preference observed in the joint analysis.

The sensitivity of the beam-only and joint beam-atmospheric analyses, to the appearance parameters ($\delta_{CP} - \sin^2(\theta_{13})$), are compared in Figure 8.41. These results are marginalised over both hierarchies and include the reactor constraint on $\sin^2(\theta_{13})$. For this particular set of known oscillation parameters (AsimovA defined in Table 2.2), the beam-only analysis dominates the sensitivity. The joint fit does slightly increase the sensitivity to δ_{CP} but it does not change any conclusions that would be made.

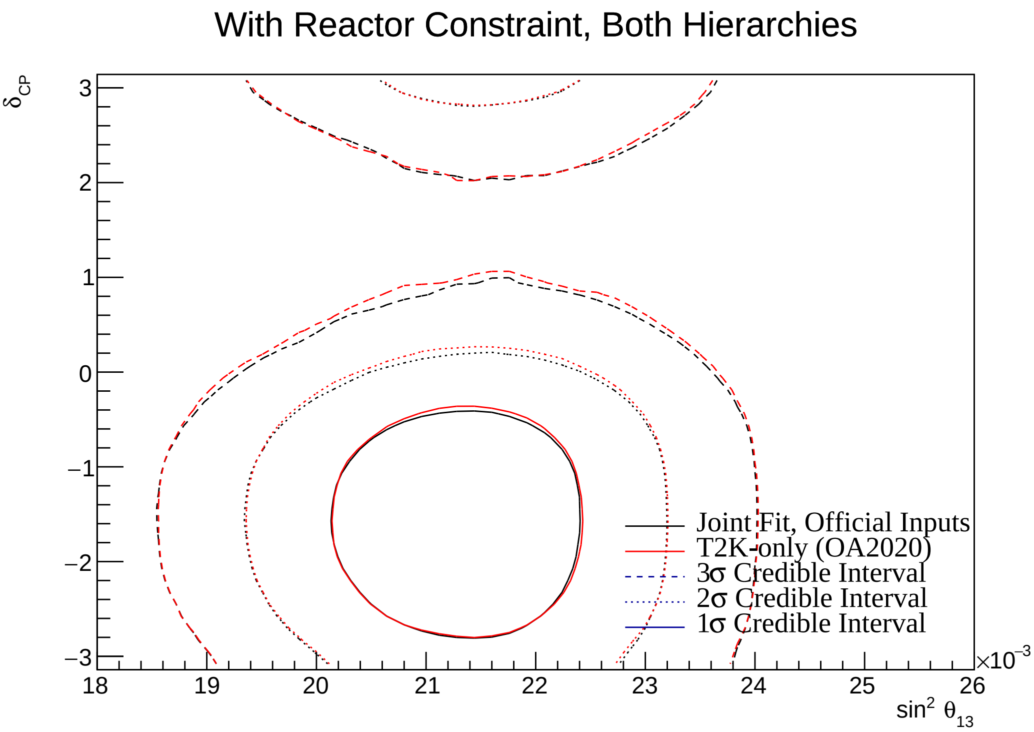

Figure 8.41: The two-dimensional posterior probability density distribution in $\delta_{CP} - \sin^2(\theta_{13})$ compared between the joint beam-atmospheric fit (Black) and the latest T2K sensitivities (Red) [186]. The reactor constraint is applied in both fits. The distributions are marginalised over both hierarchies.

8.2.8 Effect of Asimov Parameter Set

Figure 8.4 and Figure 8.5 show that the choice of the parameter set at which the Asimov data is made can affect the conclusion. 'AsimovA' oscillation parameters are defined at a region of δ_{CP} which is dominated by the T2K experiment. This explains why the addition of the atmospheric samples does not significantly increase the sensitivity to δ_{CP}, as illustrated in subsection 8.2.6 and subsection 8.2.7. This section presents the sensitivities when 'AsimovB' oscillation parameters, as defined in Table 2.2, are assumed (alongside the post-BANFF tune) when building the Asimov data.

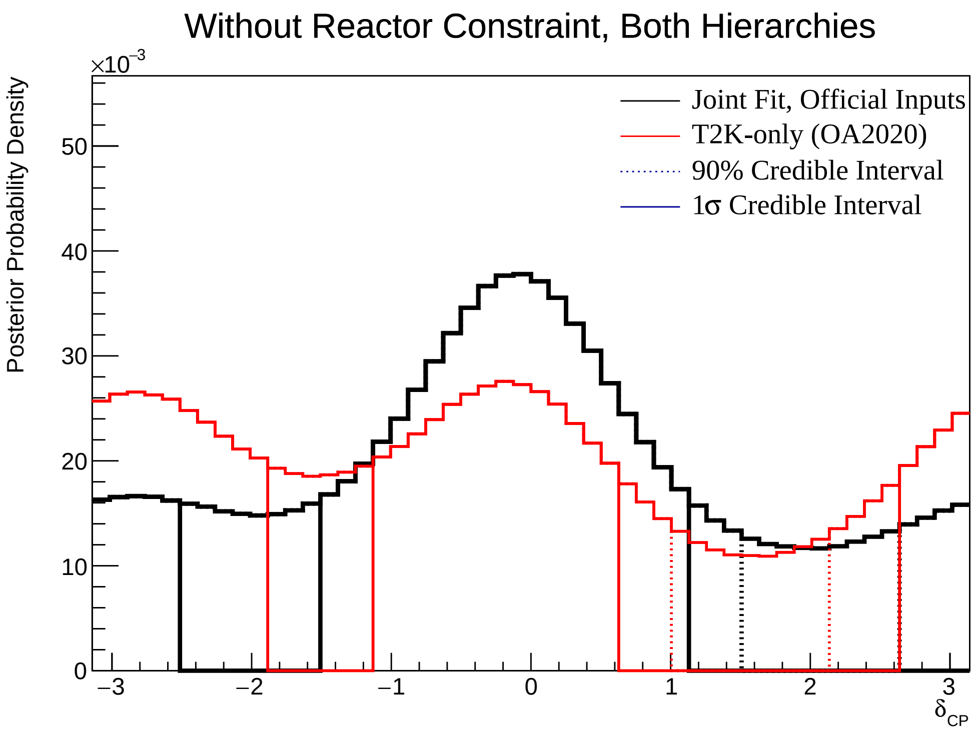

Figure 8.42: The one-dimensional posterior probability density distribution in δ_{CP} compared between the joint beam-atmospheric fit (Black) and the latest T2K sensitivities (Red) [186]. The reactor constraint is not applied in either fit. The distributions are marginalised over both hierarchies.

The sensitivity to δ_{CP} for the joint beam and atmospheric fit is presented in Figure 8.42. The results are compared to those from the beam-only analysis in [186]. The reactor constraint is not applied in either of the fits. The known oscillation parameter value is $\delta_{CP} = 0$. The shape of the posterior distribution from the joint analysis is more peaked at $\delta_{CP} = 0$ as compared to the beam-only analysis which has approximately the same posterior probability density at $\delta_{CP} = 0$ and $\delta_{CP} = \pi$. This shows the ability of the joint analysis to better determine the correct phase of δ_{CP} if the true value was CP-conserving. The 1σ credible intervals and the position of the highest posterior probability density are given in Table 8.9.

Parameter	Interval	HPD
δ_{CP}, (BH)	$[-\pi, -2.51], [-1.51, 1.31]$	-0.06
δ_{CP}, (NH)	$[-1.13, 1.63]$	0.06
δ_{CP}, (IH)	$[-3.02, -1.88], [-1.76, 0.13]$	-0.44
Δm^2_{32} (BH) $[\times 10^{-3}\text{eV}^2]$	$[-2.60, -2.49], [2.46, 2.59]$	2.51
Δm^2_{32} (NH) $[\times 10^{-3}\text{eV}^2]$	$[2.47, 2.56]$	2.52
Δm^2_{32} (IH) $[\times 10^{-3}\text{eV}^2]$	$[-2.61, -2.52]$	-2.57
$\sin^2(\theta_{23})$ (BH)	$[0.43, 0.48], [0.55, 0.59]$	0.45
$\sin^2(\theta_{23})$ (NH)	$[0.43, 0.49], [0.55, 0.58]$	0.45
$\sin^2(\theta_{23})$ (IH)	$[0.44, 0.48], [0.54, 0.59]$	0.57

Table 8.9: The position of the highest posterior probability density (HPD) and width of the 1σ credible interval for the SK atmospheric-only fit. The reactor constraint is not applied. The values are presented by which hierarchy hypothesis is assumed: marginalised over both hierarchies (BH), normal hierarchy only (NH) and inverted hierarchy only (IH).

Naively, if just the 1σ credible interval were considered without observing the shape of the distribution, it would appear that the joint analysis would have a worse sensitivity to δ_{CP} due to the larger interval around δ_{CP}. The 1σ credible interval for the beam-only analysis is given as the range $\delta_{CP} = [-\pi, -1.88], [-1.13, 0.63]$ and $[2.64, \pi]$ which contains 56% of all values of δ_{CP}. The joint beam and atmospheric analysis contains 52% of all δ_{CP} values within the 1σ credible interval. Therefore, if the area within the 1σ credible interval were to be compared between the two fits, the joint analysis would be shown to have better precision.

This contradiction stems from the methodology in which the credible interval is calculated. The technique used in this analysis (documented in subsection 4.3.2) fills the credible interval by selecting bins in order of magnitude until 68% of the posterior density is contained. If instead, the credible interval was calculated by expanding around the highest posterior probability, the benefits of the joint fit would be more obvious. In the case where the shape of the posterior was Gaussian, these two techniques would be equivalent.

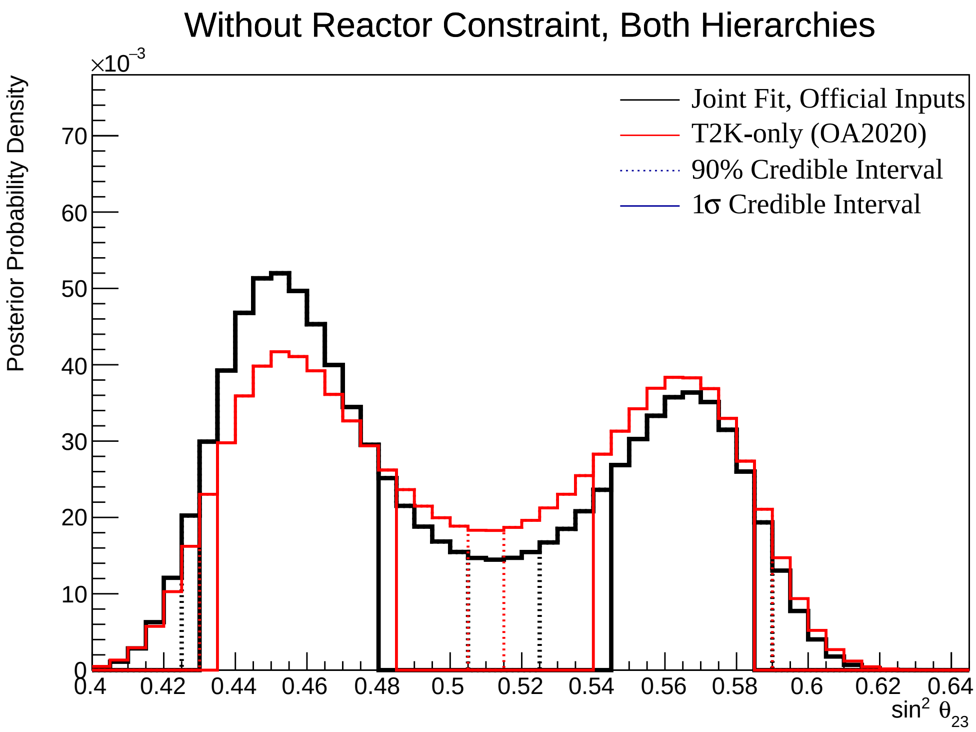

Figure 8.43: The one-dimensional posterior probability density distribution in $\sin^2(\theta_{23})$ compared between the joint beam-atmospheric fit (Black) and the latest T2K sensitivities (Red) [186]. The reactor constraint is not applied in either fit. The distributions are marginalised over both hierarchies.

The sensitivity of the joint beam and atmospheric fit to $\sin^2(\theta_{23})$ is presented in Figure 8.43. The sensitivity is compared to that of the beam-only analysis in [186]. The reactor constraint is not applied in either of the fits being compared. The Asimov parameter value is $\sin^2(\theta_{23}) = 0.45$ and the sensitivities are marginalised over both hierarchies. Clearly, the joint beam and atmospheric fit has a much larger probability density in the region surrounding the known oscillation parameters. This shows the better octant determination of the joint analysis compared to the beam-only fit. The ratio of the posterior density at the peak of the lower octant to the peak of the upper octant from the joint fit is 1.43 compared to 1.09 from the beam-only analysis. This shows further support for the joint analysis in correctly selecting the lower octant, which is the correct hypothesis given the known oscillation parameters.

	LO $\left(\sin^2\theta_{23} < 0.5\right)$	UO $\left(\sin^2\theta_{23} > 0.5\right)$	Sum
NH $\left(\Delta m^2_{32} > 0\right)$	0.35	0.24	0.59
IH $\left(\Delta m^2_{32} < 0\right)$	0.19	0.22	0.41
Sum	0.54	0.46	1.00

Table 8.10: The distribution of steps in a joint beam and atmospheric fit, presented as the fraction of steps in the upper (UO) and lower (LO) octants and the normal (NH) and inverted (IH) hierarchies. The reactor constraint is not applied. The Bayes factors are calculated as $B(\mathrm{NH}/\mathrm{IH}) = 1.43$ and $B(\mathrm{LO}/\mathrm{UO}) = 1.19$.

The distribution of steps, split by hierarchy and octant hypothesis, is presented in Table 8.10. The Bayes factor for hierarchy and octant determination are $B(\mathrm{NH}/\mathrm{IH}) = 1.43$ and $B(\mathrm{LO}/\mathrm{UO}) = 1.19$, respectively. The octant Bayes factor is now presented as LO/UO as the known oscillation parameter is contained within the lower octant. These values compare to $B(\mathrm{NH}/\mathrm{IH}) = 1.08$ and $B(\mathrm{LO}/\mathrm{UO}) = 0.91$ from the beam-only analysis. This shows additional evidence of the joint analysis's preference for selecting the correct octant and hierarchy hypothesis. Comparisons to the AsimovA Bayes factors presented in Table 8.6 show how the preference for the correct octant and hierarchy depend on the true value of δ_{CP} and $\sin^2(\theta_{23})$.

The sensitivity of the beam-only and joint beam-atmospheric analysis to Δm^2_{32} is given in Figure 8.44. Both of the results are marginalised over both hierarchies and the reactor constraint is not applied in either analysis. The joint analysis has a stronger preference for the correct hierarchy (NH) which is shown by the higher Bayes factor ($B(\mathrm{NH}/\mathrm{IH}) = 1.43$) compared to the beam-only analysis ($B(\mathrm{NH}/\mathrm{IH}) = 1.08$).

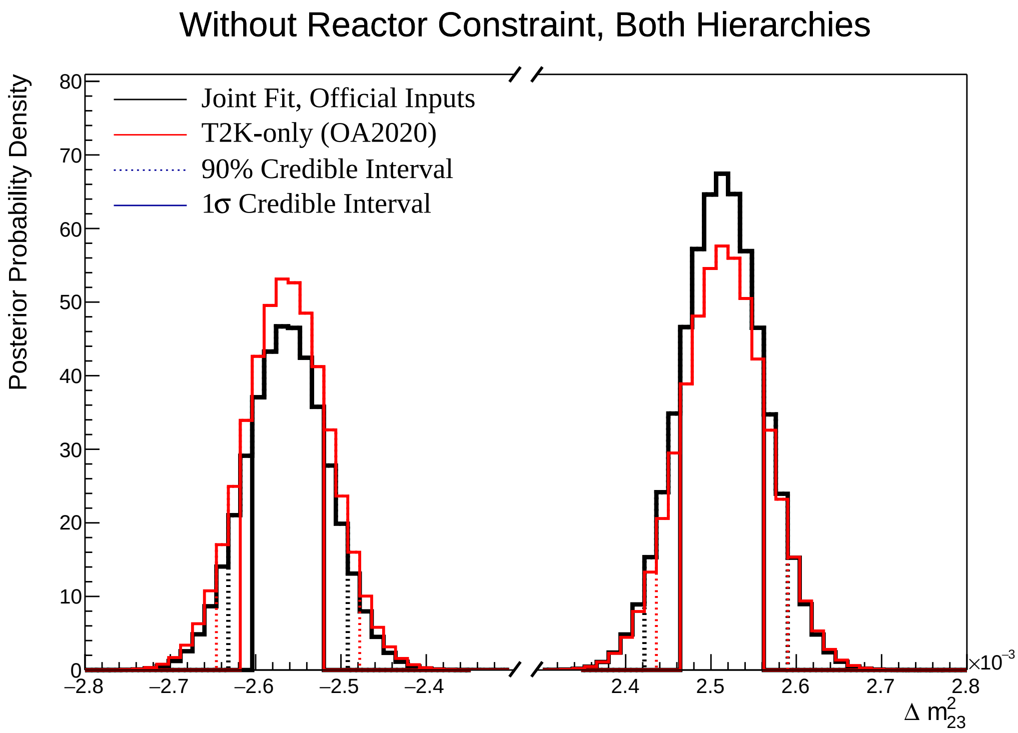

Figure 8.44: The one-dimensional posterior probability density distribution in Δm^2_{32} compared between the joint beam-atmospheric fit (Black) and the latest T2K sensitivities (Red) [186]. The reactor constraint is not applied in either fit. The distributions are marginalised over both hierarchies.

9
Conclusions and Outlook

Appendices

A

Atmospheric Sample Spectra

This appendix documents theinteraction mode breakdown of all the atmospheric samples used within the analysis. The generated tune of the model parameters and the Asimov A oscillation parameter set (defined in Table 2.2) are assumed. The livetime of SK-IV is taken to be 3244.4 days.

A.1 Binning

The lepton momentum and cosine zenith binning edges for the atmospheric samples used within this analysis are defined in Table A.1.

A.2 Fully Contained Sub-GeV Samples

The interaction mode breakdown of the fully contained Sub-GeV samples are shown in Figure A.1 and Figure A.2, for the samples with enriched CC0π and CC1$\pi^{\pm}$ respectively.

The CC0π sample are dominated by CCQE events ($\sim$ 70%) with smaller contributions of 2p2h ($\sim$ 12%) and CC1π ($\sim$ 10%) components. The energy peaks around 300 MeV, which is slightly below that of the T2K samples but still has significant contribution upto 1 GeV which overlaps the T2K sample energy range.

Sample	$\cos(\theta_Z)$ Bins	Momentum Bin Edges ($\log_{10}(P)$ MeV)
`SubGeV-elike-0dcy`	10	2.0, 2.4, 2.6, 2.8, 3.0, 3.2
`SubGeV-elike-1dcy`	1	2.0, 2.4, 2.6, 2.8, 3.0, 3.2
`SubGeV-mulike-0dcy`	10	2.0, 2.4, 2.6, 2.8, 3.0, 3.2
`SubGeV-mulike-1dcy`	10	2.0, 2.4, 2.6, 2.8, 3.0, 3.2
`SubGeV-mulike-2dcy`	1	2.0, 2.4, 2.6, 2.8, 3.0, 3.2
`SubGeV-pi0like`	1	2.0, 2.2, 2.4, 2.6, 2.8, 3.2
`MultiGeV-elike-nue`	10	3.0, 3.4, 3.7, 4.0, 5.0
`MultiGeV-elike-nuebar`	10	3.0, 3.4, 3.7, 4.0, 5.0
`MultiGeV-mulike`	10	3.0, 3.4, 5.0
`MultiRing-elike-nue`	10	3.0, 3.4, 3.7, 5.0
`MultiRing-elike-nuebar`	10	3.0, 3.4, 3.7, 5.0
`MultiRing-mulike`	10	2.0, 3.124, 3.4, 3.7, 5.0
`MultiRing-Other1`	10	3.0, 3.4, 3.7, 4.0, 5.0
`PC-Stop`	10	2.0, 3.4, 5.0
`PC-Through`	10	2.0, 3.124, 3.4, 3.7, 5.0
`Upmu-Stop`	10	3.2, 3.4, 3.7, 8.0
`Upmu-Through-Showering`	10	2.0, 8.0
`Upmu-Through-NonShowering`	10	2.0, 8.0

Table A.1: The reconstructed cosine zenith and lepton momentum binning assigned to the atmospheric samples. The "$\cos(\theta_Z)$ Bins" column illustrates the number of bins uniformly distributed over the $-1.0 \leq \cos(\theta_Z) \leq 1.0$ region for fully and partially contained samples and $-1.0 \leq \cos(\theta_Z) \leq 0.0$ region for up-μ samples.

The one-ring CC1π samples, where the pion is tagged via its decay electron, are dominated by CC1π events ($\sim$ 75%) with a small contribution of CC$M\pi$ ($\sim$ 10%). The two-ring pion sample is mostly dominated by the NC1π^0 via resonances, and has several equally-sized contributions from CCQE, NC1$\pi^\pm$ via resonances, and NC coherent pion production, where the π^0 likely comes from nucleon and $\pi^\pm$ final state interactions in the nucleus.

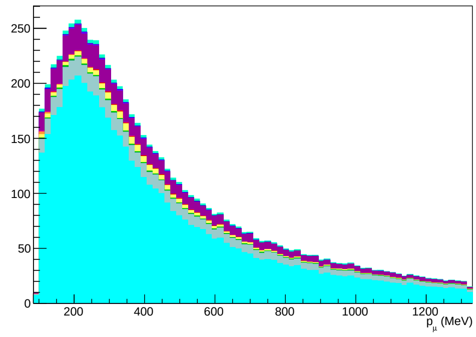

(a) FC Sub-GeV 1R e-like 0 de

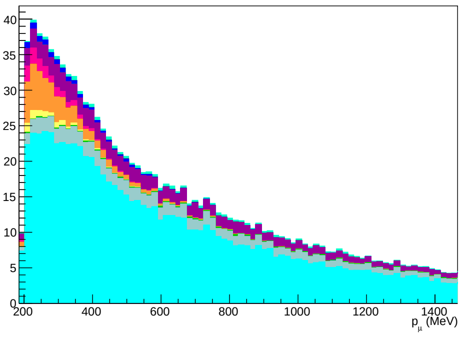

(b) FC Sub-GeV 1R μ-like 0 de

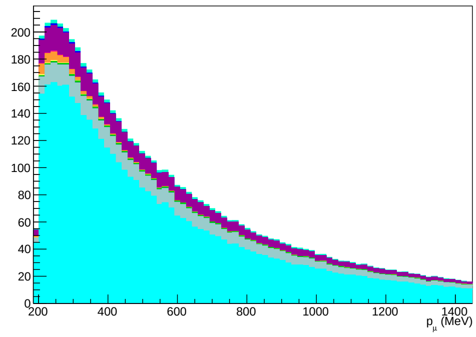

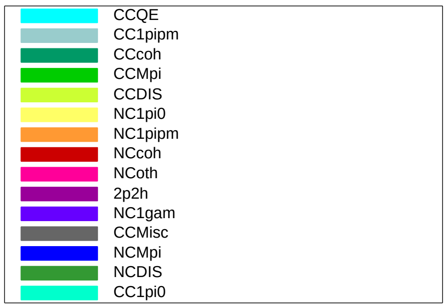

(c) FC Sub-GeV 1R μ-like 1 de

Figure A.1: Breakdown by interaction mode of the FC Sub-GeV atmospheric samples targeting CC0π events.

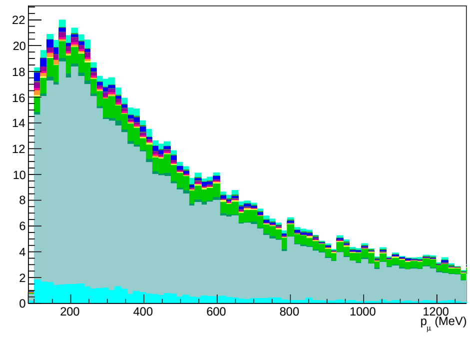

(a) FC Sub-GeV 1R e-like 1 de

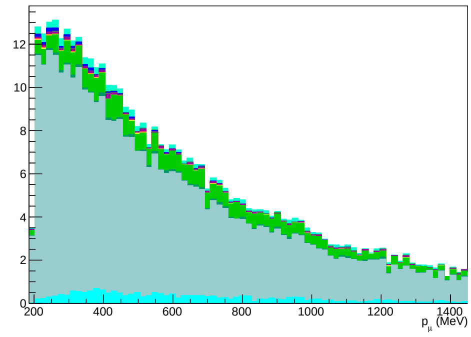

(b) FC Sub-GeV 1R μ-like 2 de

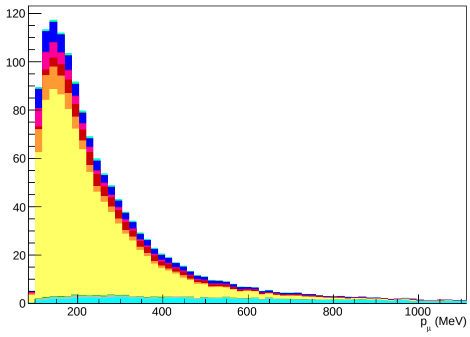

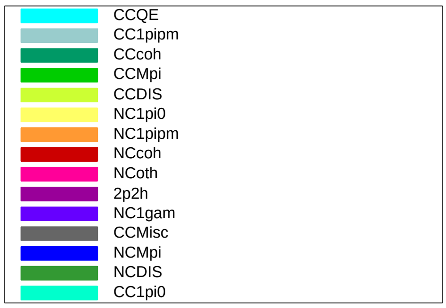

(c) FC Sub-GeV 2R π^0-like

Figure A.2: Breakdown by interaction mode of the FC Sub-GeV atmospheric samples targeting single pion events.

A.3 Fully Contained Multi-GeV Samples

The interaction mode breakdown of fully contained multi-GeV samples is highlighted in Figure A.3. Due to the event selection applied in SK which targets π^+ and π^- separation, the ν_e sample mainly consists of events with pions (single pion production or multi-pion/DIS interactions). The pion separation is explained in Section section 6.1. This reasoning also explains the significant CCQE contribution of the $\bar{\nu}_e$ sample. The muon-like sample is dominated by CCQE interactions with $\sim 10-15\%$ 2p2h and CC1π contribution of events.

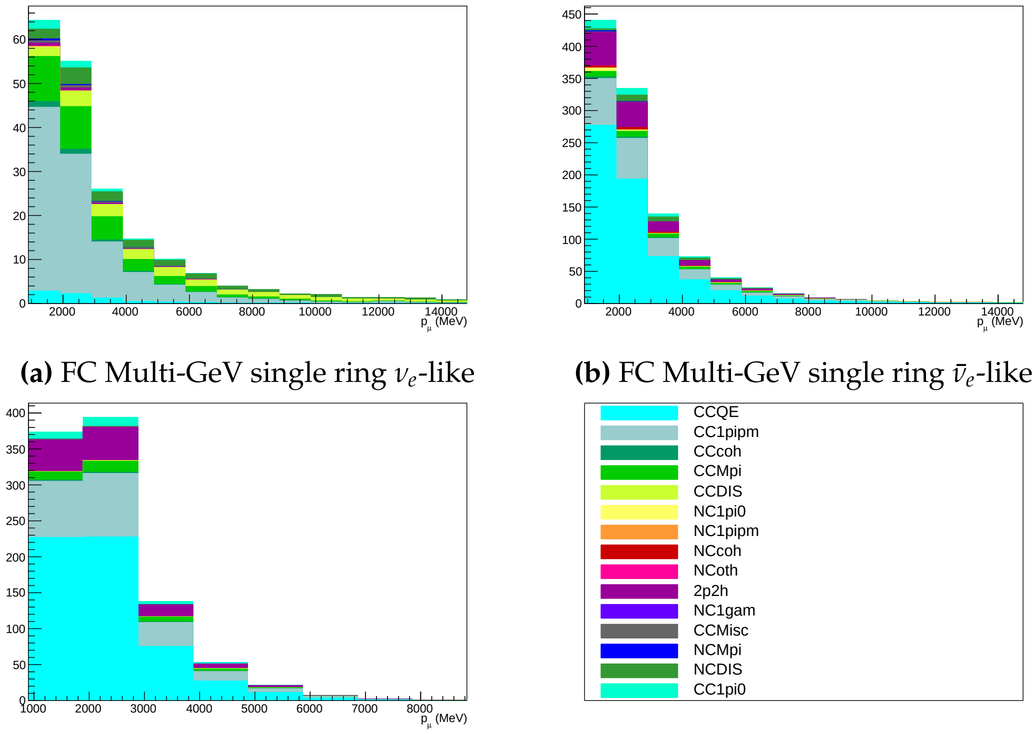

(a) FC Multi-GeV single ring ν_e-like

(b) FC Multi-GeV single ring $\bar{\nu}_e$-like

(c) FC Multi-GeV single ring μ-like

Figure A.3: Breakdown by interaction mode of the FC Multi-GeV single ring atmospheric samples.

A.4 Fully Contained Multi-Ring Samples

The interaction mode breakdown of fully contained multi-ring events is shown in Figure A.4. These samples see more interaction modes contributing in general, and there is a much larger contribution from multi-pion and DIS interaction modes, compared to the other samples.

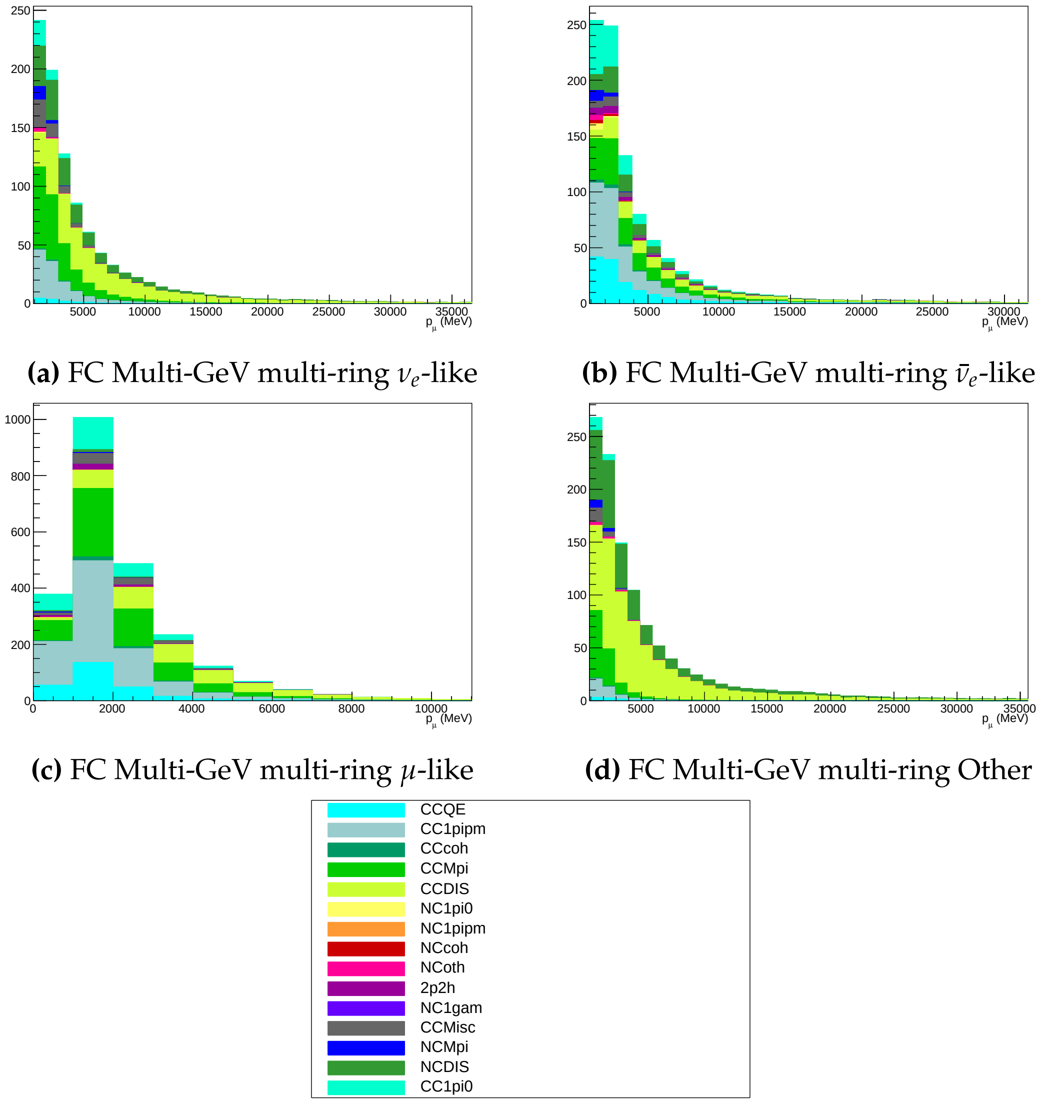

(a) FC Multi-GeV multi-ring ν_e-like **(b)** FC Multi-GeV multi-ring $\bar{\nu}_e$-like

(c) FC Multi-GeV multi-ring μ-like **(d)** FC Multi-GeV multi-ring Other

Figure A.4: Breakdown by interaction mode of the FC Multi-GeV multi-ring atmospheric samples.

A.5 Partially Contained Samples

The breakdown for partially contained samples is highlighted in Figure A.5. As with the multi-ring samples, there is no dominating interaction mode. The neutrino energies of events in this sample extend into the tens of GeV and become dominated by DIS interaction modes in the high energy limit.

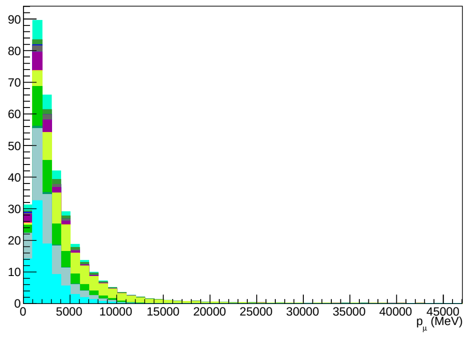

(a) PC stopping events

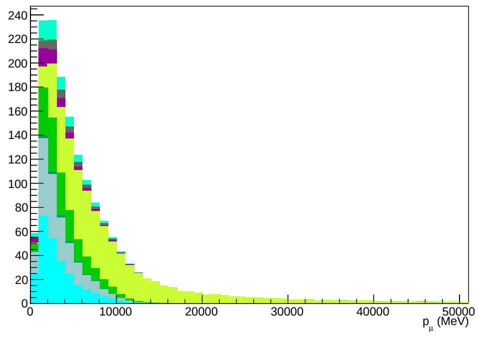

(b) PC through-going events.

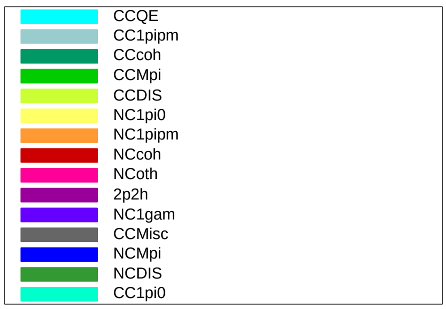

Figure A.5: Breakdown by interaction mode of the PC atmospheric samples.

A.6 Upward-Going Muon Samples

The breakdown for upward-going muons is illustrated in Figure A.6. These samples are significantly dominated by DIS interactions with energies extending up into the hundreds of GeV.

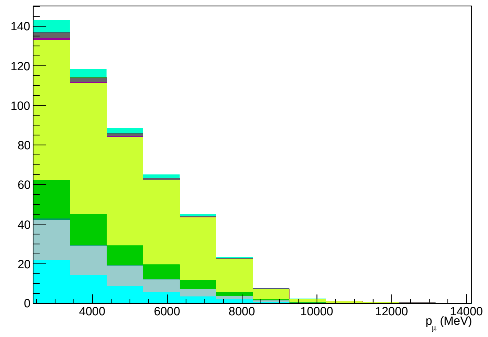

(a) Up-μ stopping events

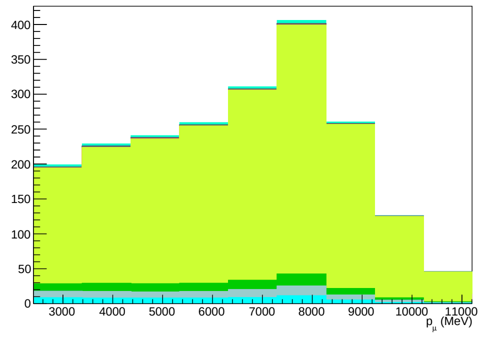

(b) Up-μ through going non showering events

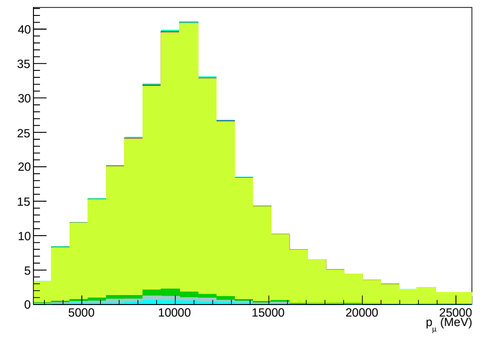

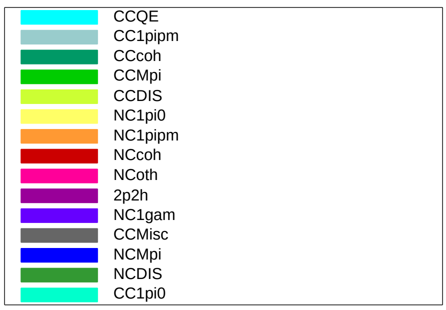

(c) Up-μ through going showering events

Figure A.6: Breakdown by interaction mode of the atmospheric upward going muon samples.

Bibliography

[1] J Chadwick. "Intensitätsverteilung im magnetischen Spectrum der β-Strahlen von radium B + C". In: *Verhandl. Dtsc. Phys. Ges.* 16 (1914), p. 383. URL: `http://cds.cern.ch/record/262756`.

[2] C D Ellis and W A Wooster. "The average energy of disintegration of radium E". en. In: *Proc. R. Soc. Lond. A Math. Phys. Sci.* 117.776 (Dec. 1927), pp. 109–123.

[3] W. Pauli. "Dear radioactive ladies and gentlemen". In: *Phys. Today* 31N9 (1978), p. 27.

[4] E. Fermi. "An attempt of a theory of beta radiation. 1." In: *Z. Phys.* 88 (1934), pp. 161–177.

[5] F. Reines and C. L. Cowan. "Detection of the Free Neutrino". In: *Phys. Rev.* 92 (3 1953), pp. 830–831. URL: `https://link.aps.org/doi/10.1103/PhysRev.92.830`.

[6] C. L. Cowan et al. "Detection of the Free Neutrino: a Confirmation". In: *Science* 124.3212 (1956), pp. 103–104. eprint: `http://science.sciencemag.org/content/124/3212/103.full.pdf`. URL: `http://science.sciencemag.org/content/124/3212/103`.

[7] G. Danby et al. "Observation of High-Energy Neutrino Reactions and the Existence of Two Kinds of Neutrinos". In: *Phys. Rev. Lett.* 9 (1 1962), pp. 36–44. URL: `https://link.aps.org/doi/10.1103/PhysRevLett.9.36`.

[8] K. Kodama et al. "Observation of tau neutrino interactions". In: *Physics Letters B* 504.3 (2001), pp. 218 –224. URL: `http://www.sciencedirect.com/science/article/pii/S0370269301003070`.

[9] A. Aguilar-Arevalo et al. "Evidence for neutrino oscillations from the observation of anti-neutrino(electron) appearance in a anti-neutrino(muon) beam". In: *Phys. Rev.* D64 (2001), p. 112007. arXiv: `hep-ex/0104049 [hep-ex]`.

[10] A. A. Aguilar-Arevalo et al. "Improved Search for $\overline{\nu}_\mu \to \overline{\nu}_e$ Oscillations in the MiniBooNE Experiment". In: *Phys. Rev. Lett.* 110 (16 2013), p. 161801. URL: `https://link.aps.org/doi/10.1103/PhysRevLett.110.161801`.

[11] Planck Collaboration et al. "Planck 2018 results. VI. Cosmological parameters". In: *aap* 641 (Sept. 2020).

[12] J. A. Bagger et al. "Precision electroweak measurements on the Z resonance". In: *Physics Reports* 427.5 (2006), pp. 257 –454. URL: `http://www.sciencedirect.com/science/article/pii/S0370157305005119`.

[13] B. Pontecorvo. "Neutrino Experiments and the Problem of Conservation of Leptonic Charge". In: *Sov. Phys. JETP* 26 (1968). [Zh. Eksp. Teor. Fiz.53,1717(1967)], pp. 984–988.

[14] B. Pontecorvo. "Inverse beta processes and nonconservation of lepton charge". In: *Sov. Phys. JETP* 7 (1958). [Zh. Eksp. Teor. Fiz.34,247(1957)], pp. 172–173.

[15] Makoto Kobayashi and Toshihide Maskawa. "CP-Violation in the Renormalizable Theory of Weak Interaction". In: *Progress of Theoretical Physics* 49.2 (1973), pp. 652–657. URL: `http://dx.doi.org/10.1143/PTP.49.652`.

[16] Nicola Cabibbo. "Unitary Symmetry and Leptonic Decays". In: *Phys. Rev. Lett.* 10 (12 1963), pp. 531–533. URL: `https://link.aps.org/doi/10.1103/PhysRevLett.10.531`.

[17] A Maio and. "Search for Majorana neutrinos with the SNO+ detector at SNOLAB". In: *Journal of Physics: Conference Series* 587 (2015), p. 012030. URL: `https://doi.org/10.1088/1742-6596/587/1/012030`.

[18] A Yu Smirnov. "The MSW effect and solar neutrinos". In: (2003).

[19] S.P. Mikheyev and A.Y. Smirnov. "Resonance enhancement of oscillations in matter and solar neutrino spectroscopy". In: *Soviet Journal of Nuclear Physics* 42 (6 1985), pp. 913–917.

[20] L. Wolfenstein. "Neutrino oscillations in matter". In: *Phys. Rev. D* 17 (9 1978), pp. 2369–2374. URL: `https://link.aps.org/doi/10.1103/PhysRevD.17.2369`.

[21] Vernon D. Barger et al. "Matter Effects on Three-Neutrino Oscillations". In: *Phys. Rev. D* 22 (1980), p. 2718.

[22] Y. Ashie et al. "Evidence for an Oscillatory Signature in Atmospheric Neutrino Oscillations". In: *Phys. Rev. Lett.* 93 (10 2004), p. 101801. URL: `https://link.aps.org/doi/10.1103/PhysRevLett.93.101801`.

[23] Q. R. Ahmad et al. "Direct Evidence for Neutrino Flavor Transformation from Neutral-Current Interactions in the Sudbury Neutrino Observatory". In: *Phys. Rev. Lett.* 89 (1 2002), p. 011301. URL: `https://link.aps.org/doi/10.1103/PhysRevLett.89.011301`.

[24] *2015 Nobel prize in Physics as listed by Nobelprize.org*. `https://www.nobelprize.org/nobel_prizes/physics/laureates/2015/`. Accessed: 22-06-2022.

[25] J. A. Formaggio and G. P. Zeller. "From eV to EeV: Neutrino Cross Sections Across Energy Scales". In: *Rev. Mod. Phys.* 84 (2012), pp. 1307–1341. arXiv: `1305.7513 [hep-ex]`.

[26] A Oralbaev, M Skorokhvatov, and O Titov. "The inverse beta decay: a study of cross section". In: *Journal of Physics: Conference Series* 675.1 (2016), p. 012003. URL: `https://doi.org/10.1088/1742-6596/675/1/012003`.

[27] A Bellerive. "Review of solar neutrino experiments". en. In: *Int. J. Mod. Phys. A* 19.08 (Mar. 2004), pp. 1167–1179.

[28] Raymond Davis, Don S. Harmer, and Kenneth C. Hoffman. "Search for Neutrinos from the Sun". In: *Phys. Rev. Lett.* 20 (21 1968), pp. 1205–1209. URL: `https://link.aps.org/doi/10.1103/PhysRevLett.20.1205`.

[29] Núria Vinyoles et al. "A new generation of standard solar models". In: *Astrophys. J.* 835.2 (Jan. 2017), p. 202.

[30] V Gribov and B Pontecorvo. "Neutrino astronomy and lepton charge". en. In: *Phys. Lett. B* 28.7 (Jan. 1969), pp. 493–496.

[31] K. S. Hirata et al. "Observation of ^{8}B solar neutrinos in the Kamiokande-II detector". In: *Phys. Rev. Lett.* 63 (1 1989), pp. 16–19. URL: `https://link.aps.org/doi/10.1103/PhysRevLett.63.16`.

[32] W Hampel et al. "GALLEX solar neutrino observations: results for GALLEX IV". en. In: *Phys. Lett. B* 447.1-2 (Feb. 1999), pp. 127–133.

[33] J. N. Abdurashitov et al. "Measurement of the solar neutrino capture rate with gallium metal". In: *Phys. Rev. C* 60 (5 1999), p. 055801. URL: `https://link.aps.org/doi/10.1103/PhysRevC.60.055801`.

[34] Q R Ahmad et al. "Direct evidence for neutrino flavor transformation from neutral-current interactions in the Sudbury neutrino observatory". en. In: *Phys. Rev. Lett.* 89.1 (June 2002).

[35] Borexino Collaboration. "Comprehensive measurement of pp-chain solar neutrinos". en. In: *Nature* 562.7728 (Oct. 2018), pp. 505–510.

[36] B Aharmim et al. "A search for neutrinos from the SolarhepReaction and the diffuse supernova neutrino background with the Sudbury neutrino observatory". en. In: *Astrophys. J.* 653.2 (Dec. 2006), pp. 1545–1551.

[37] M Agostini et al. "Experimental evidence of neutrinos produced in the CNO fusion cycle in the Sun". In: (2020).

[38] G Danby et al. "Observation of high-energy neutrino reactions and the existence of two kinds of neutrinos". In: *Phys. Rev. Lett.* 9.1 (July 1962), pp. 36–44.

[39] K. Abe et al. "T2K neutrino flux prediction". In: *Physical Review D* 87.1 (2013). URL: `https://doi.org/10.1103%2Fphysrevd.87.012001`.

[40] D. G. Michael et al. "Observation of Muon Neutrino Disappearance with the MINOS Detectors in the NuMI Neutrino Beam". In: *Phys. Rev. Lett.* 97 (19 2006), p. 191801. URL: `https://link.aps.org/doi/10.1103/PhysRevLett.97.191801`.

[41] G. Danby et al. "Observation of High-Energy Neutrino Reactions and the Existence of Two Kinds of Neutrinos". In: *Phys. Rev. Lett.* 9 (1 1962), pp. 36–44. URL: `https://link.aps.org/doi/10.1103/PhysRevLett.9.36`.

[42] M. A. Acero et al. "First measurement of neutrino oscillation parameters using neutrinos and antineutrinos by NOvA". In: *Phys. Rev. Lett.* 123 (15 2019), p. 151803. URL: `https://link.aps.org/doi/10.1103/PhysRevLett.123.151803`.

[43] K. Abe et al. "The T2K experiment". In: *Nuclear Instruments and Methods in Physics Research Section A: Accelerators, Spectrometers, Detectors and Associated Equipment* 659.1 (2011), pp. 106 –135. eprint: `http://www.sciencedirect.com/science/article/pii/S0168900211011910`.

[44] B Abi et al. "Long-baseline neutrino oscillation physics potential of the DUNE experiment". en. In: *Eur. Phys. J. C Part. Fields* 80.10 (Oct. 2020).

[45] Hyper-Kamiokande Proto-Collaboration et al. "Physics potential of a long-baseline neutrino oscillation experiment using a J-PARC neutrino beam and Hyper-Kamiokande". In: *Prog. Theor. Exp. Phys.* 2015.5 (May 2015), pp. 53C02–0.

[46] Carlos Blanco, Dan Hooper, and Pedro Machado. "Constraining sterile neutrino interpretations of the LSND and MiniBooNE anomalies with coherent neutrino scattering experiments". In: *Physical Review D* 101.7 (2020). URL: `https://doi.org/10.1103%2Fphysrevd.101.075051`.

[47] MicroBooNE Collaboration et al. *Search for an Excess of Electron Neutrino Interactions in MicroBooNE Using Multiple Final State Topologies*. 2021. URL: `https://arxiv.org/abs/2110.14054`.

[48] B. Armbruster et al. "Upper limits for neutrino oscillations $\overline{\nu}_\mu \to \overline{\nu}_e$ from muon decay at rest". In: *Phys. Rev. D* 65 (11 2002), p. 112001. URL: `https://link.aps.org/doi/10.1103/PhysRevD.65.112001`.

[49] T K Gaisser and M Honda. "Flux of Atmospheric Neutrinos". In: (2002).

[50] G. D. Barr et al. "Three-dimensional calculation of atmospheric neutrinos". In: *Physical Review D* 70.2 (2004). URL: `https://doi.org/10.1103/physrevd.70.023006`.

[51] M. Honda et al. "Calculation of atmospheric neutrino flux using the interaction model calibrated with atmospheric muon data". In: *Physical Review D* 75.4 (2007). URL: `https://doi.org/10.1103/physrevd.75.043006`.

[52] M. Honda et al. "New calculation of the atmospheric neutrino flux in a three-dimensional scheme". In: *Phys. Rev. D* 70 (4 2004), p. 043008. URL: `https://link.aps.org/doi/10.1103/PhysRevD.70.043008`.

[53] M. Honda et al. "Improvement of low energy atmospheric neutrino flux calculation using the JAM nuclear interaction model". In: *Phys. Rev. D* 83 (12 2011), p. 123001. URL: `https://link.aps.org/doi/10.1103/PhysRevD.83.123001`.

[54] A. Fasso et al. "FLUKA: status and prospects for hadronic applications". In: (2001).

[55] Y. Ashie et al. "Measurement of atmospheric neutrino oscillation parameters by Super-Kamiokande I". In: *Physical Review D* 71.11 (2005). URL: `https://doi.org/10.1103/physrevd.71.112005`.

[56] F Reines et al. "Evidence for high-energy cosmic-ray neutrino interactions". In: *Phys. Rev. Lett.* 15.9 (Aug. 1965), pp. 429–433.

[57] D. Casper et al. "Measurement of atmospheric neutrino composition with the IMB-3 detector". In: *Phys. Rev. Lett.* 66 (20 1991), pp. 2561–2564. URL: `https://link.aps.org/doi/10.1103/PhysRevLett.66.2561`.

[58] K S Hirata et al. "Observation of a small atmospheric ν_μ/ν_e ratio in Kamiokande". en. In: *Phys. Lett. B* 280.1-2 (Apr. 1992), pp. 146–152.

[59] Z. Li et al. "Measurement of the tau neutrino cross section in atmospheric neutrino oscillations with Super-Kamiokande". In: *Physical Review D* 98.5 (2018). URL: `https://doi.org/10.1103/physrevd.98.052006`.

[60] Kamiokande Collaboration et al. "Atmospheric neutrino oscillation analysis with external constraints in Super-Kamiokande I-IV". In: (2017).

[61] T2K Collaboration. "Constraint on the matter-antimatter symmetry-violating phase in neutrino oscillations". en. In: *Nature* 580.7803 (Apr. 2020), pp. 339–344.

[62] M A Acero et al. "First measurement of neutrino oscillation parameters using neutrinos and antineutrinos by NOvA". en. In: *Phys. Rev. Lett.* 123.15 (Oct. 2019), p. 151803.

[63] M G Aartsen et al. "Measurement of atmospheric neutrino oscillations at 6–56 GeV with IceCube DeepCore". In: *Phys. Rev. Lett.* 120.7 (Feb. 2018).

[64] P Adamson et al. "Combined analysis of$\nu\mu$Disappearance and$\nu\mu\rightarrow\nu e$Appearance in MINOS using accelerator and atmospheric neutrinos". In: *Phys. Rev. Lett.* 112.19 (May 2014).

[65] M. Sajjad Athar et al. "Status and perspectives of neutrino physics". In: *Progress in Particle and Nuclear Physics* 124 (2022), p. 103947. URL: `https://doi.org/10.1016/Fj.ppnp.2022.103947`.

[66] Soo-Bong Kim, Thierry Lasserre, and Yifang Wang. "Reactor Neutrinos". In: *Adv. High Energy Phys.* 2013 (2013), pp. 1–34.

[67] Mohammad Sajjad Athar et al. "Status and perspectives of neutrino physics". In: *Prog. Part. Nucl. Phys.* 124 (2022), p. 103947. arXiv: `2111.07586 [hep-ph]`.

[68] K Abe et al. "First gadolinium loading to Super-Kamiokande". en. In: *Nucl. Instrum. Methods Phys. Res. A* 1027.166248 (Mar. 2022), p. 166248.

[69] F. P. An et al. "Observation of Electron-Antineutrino Disappearance at Daya Bay". In: *Phys. Rev. Lett.* 108 (17 2012), p. 171803. URL: `https://link.aps.org/doi/10.1103/PhysRevLett.108.171803`.

[70] J. K. Ahn et al. "Observation of Reactor Electron Antineutrinos Disappearance in the RENO Experiment". In: *Phys. Rev. Lett.* 108 (19 2012), p. 191802. URL: `https://link.aps.org/doi/10.1103/PhysRevLett.108.191802`.

[71] Y. Abe et al. "Indication of Reactor $\overline{\nu}_e$ Disappearance in the Double Chooz Experiment". In: *Phys. Rev. Lett.* 108 (13 2012), p. 131801. URL: `https://link.aps.org/doi/10.1103/PhysRevLett.108.131801`.

[72] JUNO Collaboration et al. *TAO Conceptual Design Report: A Precision Measurement of the Reactor Antineutrino Spectrum with Sub-percent Energy Resolution*. 2020. arXiv: `2005.08745 [physics.ins-det]`.

[73] M P Decowski. "KamLAND's precision neutrino oscillation measurements". en. In: *Nucl. Phys. B.* 908 (July 2016), pp. 52–61.

[74] A. Gando et al. "Constraints on θ_{13} from a three-flavor oscillation analysis of reactor antineutrinos at KamLAND". In: *Phys. Rev. D* 83 (5 2011), p. 052002. URL: `https://link.aps.org/doi/10.1103/PhysRevD.83.052002`.

[75] Patrick Dunne. *Latest Neutrino oscillation results from T2K*. 2020.

[76] Particle Data Group et al. "Review of particle physics". en. In: *Prog. Theor. Exp. Phys.* 2020.8 (Aug. 2020).

[77] R. L. Workman and Others. "Review of Particle Physics". In: *PTEP* 2022 (2022), p. 083C01.

[78] K. Abe et al. "Precise Measurement of the Neutrino Mixing Parameter θ_{23} from Muon Neutrino Disappearance in an Off-Axis Beam". In: *Phys. Rev. Lett.* 112 (18 2014), p. 181801. URL: `https://link.aps.org/doi/10.1103/PhysRevLett.112.181801`.

[79] Roger Wendell. "Three Flavor Oscillation Analysis of Atmospheric Neutrinos in Super-Kamiokande". PhD thesis. University of North Carolina, 2008.

[80] Adam M Dziewonski and Don L Anderson. "Preliminary reference Earth model". en. In: *Phys. Earth Planet. Inter.* 25.4 (June 1981), pp. 297–356.

[81] Y Fukuda et al. "Evidence for oscillation of atmospheric neutrinos". In: *Phys. Rev. Lett.* 81.8 (Aug. 1998), pp. 1562–1567.

[82] K. Abe et al. "Calibration of the Super-Kamiokande detector". In: *Nuclear Instruments and Methods in Physics Research Section A: Accelerators, Spectrometers, Detectors and Associated Equipment* 737 (2014), pp. 253–272. URL: `https://doi.org/10.1016/j.nima.2013.11.081`.

[83] Linyan Wan. "Atmospheric Neutrino_Super-K". In: (2022). URL: `https://zenodo.org/record/6694761`.

[84] Miao Jiang. "Study of the neutrino mass hierarchy with the atmospheric neutrino data collected in Super-Kamiokande IV". PhD thesis. Kyoto University, 2019.

[85] S Fukuda et al. "The super-kamiokande detector". en. In: *Nucl. Instrum. Methods Phys. Res. A* 501.2-3 (Apr. 2003), pp. 418–462.

[86] S. Fukuda et al. "The Super-Kamiokande detector". In: *Nuclear Instruments and Methods in Physics Research Section A: Accelerators, Spectrometers, Detectors and Associated Equipment* 501.2 (2003), pp. 418 –462. eprint: `http://www.sciencedirect.com/science/article/pii/S016890020300425X`.

[87] Y Itow et al. "The JHF-Kamioka neutrino project". In: (2001).

[88] M Jiang et al. "Atmospheric neutrino oscillation analysis with improved event reconstruction in Super-Kamiokande IV". en. In: *Prog. Theor. Exp. Phys.* 2019.5 (May 2019).

[89] H. Kume et al. "20 inch diameter photomultiplier". In: *Nuclear Instruments and Methods in Physics Research* 205.3 (1983), pp. 443–449. URL: `https://www.sciencedirect.com/science/article/pii/0167508783900078`.

[90] A. Suzuki et al. "Improvement of 20 in. diameter photomultiplier tubes". In: *Nuclear Instruments and Methods in Physics Research Section A: Accelerators, Spectrometers, Detectors and Associated Equipment* 329.1-2 (May 1993), pp. 299–313. URL: `https://doi.org/10.1016/0168-9002(93)90949-i`.

[91] Y Nakano et al. "Measurement of the radon concentration in purified water in the Super-Kamiokande IV detector". en. In: *Nucl. Instrum. Methods Phys. Res. A* 977.164297 (Oct. 2020), p. 164297.

[92] Hamamatsu. *Hamamatsu Photonics Photomultiplier Tubes Handbook*. URL: `https://www.hamamatsu.com/content/dam/hamamatsu-photonics/sites/documents/99\_SALES\_LIBRARY/etd/PMT\_handbook\_v4E.pdf`.

[93] K Abe et al. "First gadolinium loading to Super-Kamiokande". en. In: *Nucl. Instrum. Methods Phys. Res. A* 1027.166248 (Mar. 2022), p. 166248.

[94] John F. Beacom and Mark R. Vagins. "Antineutrino Spectroscopy with Large Water Čerenkov Detectors". In: *Phys. Rev. Lett.* 93 (17 2004), p. 171101. URL: `https://link.aps.org/doi/10.1103/PhysRevLett.93.171101`.

[95] Ll Marti et al. "Evaluation of gadolinium's action on water Cherenkov detector systems with EGADS". en. In: *Nucl. Instrum. Methods Phys. Res. A* 959.163549 (Apr. 2020), p. 163549.

[96] Ll Marti et al. "Evaluation of gadolinium's action on water Cherenkov detector systems with EGADS". In: (2019).

[97] Mark Vagins. *Solar/DSNB Neutrino_SK-Gd*. 2022.

[98] John Focht. PhD thesis. Masschusetts Institute of Technology, 2004.

[99] T. Tanimori et al. "Design and performance of semi-custom analog IC including two TACs and two current integrators for 'Super-Kamiokande'". In: *IEEE Transactions on Nuclear Science* 36.1 (1989), pp. 497–501.

[100] J. Hosaka et al. "Solar neutrino measurements in Super-Kamiokande-I". In: *Phys. Rev. D* 73 (11 2006), p. 112001. URL: `https://link.aps.org/doi/10.1103/PhysRevD.73.112001`.

[101] H Nishino et al. "High-speed charge-to-time converter ASIC for the Super-Kamiokande detector". en. In: *Nucl. Instrum. Methods Phys. Res. A* 610.3 (Nov. 2009), pp. 710–717.

[102] S. Yamada et al. "Commissioning of the New Electronics and Online System for the Super-Kamiokande Experiment". In: *IEEE Transactions on Nuclear Science* 57.2 (2010), pp. 428–432.

[103] Satoru Yamada et al. "New online system without hardware trigger for the Super-Kamiokande experiment". In: *2007 IEEE Nuclear Science Symposium Conference Record*. Honolulu, HI, USA: IEEE, Oct. 2007.

[104] Giada Carminati. "The new wide-band solar neutrino trigger for super-kamiokande". In: *Phys. Procedia* 61 (2015), pp. 666–672.

[105] P A Čerenkov. "Visible radiation produced by electrons moving in a medium with velocities exceeding that of light". In: *Phys. Rev.* 52.4 (Aug. 1937), pp. 378–379.

[106] I Frank and Ig Tamm. "Coherent visible radiation of fast electrons passing through matter". In: *Selected Papers*. Berlin, Heidelberg: Springer Berlin Heidelberg, 1991, pp. 29–35.

[107] The T2K Collaboration. "Letter of Intent: Neutrino Oscillation Experiment at JHF". In: *KEK Proposal* (2001). eprint: `http://neutrino.kek.jp/jhfnu/loi/loi.v2.030528.pdf`.

[108] Y Itow et al. "The JHF-Kamioka neutrino project". In: (June 2001). arXiv: `hep-ex/0106019 [hep-ex]`.

[109] The K2K Collaboration and S H Ahn. "Detection of Accelerator-Produced Neutrinos at a Distance of 250 km". In: (Feb. 2001). arXiv: `hep-ex/0103001 [hep-ex]`.

[110] The T2K Collaboration. "Tokai-to-Kamioka (T2K) Long Baseline Neutrino Oscillation Experiment Proposal". In: *KEK Proposal* (2006). eprint: `{{http://j-parc.jp/researcher/Hadron/en/pac\_0606/pdf/p11-Nishikawa.pdf}}`.

[111] Christophe Bronner. *Accelerator Neutrino I_Recent results from T2K*. 2022.

[112] K. Abe et al. "Observation of Electron Neutrino Appearance in a Muon Neutrino Beam". In: *Phys. Rev. Lett.* 112 (6 2014), p. 061802. eprint: `https://link.aps.org/doi/10.1103/PhysRevLett.112.061802`.

[113] T. Fukuda et al. "Proposal for precise measurement of neutrinop-water cross-section in NINJA physics run". Proposal for J-PARC and KEK. 2017.

[114] T. Ovsiannikova et al. "New experiment WAGASCI to measure cross sections of neutrino interactions in water and hydrocarbon using J-PARC beam". In: *Physics of Particles and Nuclei* 48.6 (2017), pp. 1014–1017. eprint: `https://doi.org/10.1134/S1063779617060478`.

[115] M. Antonova et al. "Baby MIND: a magnetized segmented neutrino detector for the WAGASCI experiment". In: *Journal of Instrumentation* 12.07 (2017), p. C07028. eprint: `http://stacks.iop.org/1748-0221/12/i=07/a=C07028`.

[116] K. Abe et al. "First measurement of the charged current $\overline{\nu}_\mu$ double differential cross section on a water target without pions in the final state". In: *Phys. Rev. D* 102 (1 2020), p. 012007. URL: `https://link.aps.org/doi/10.1103/PhysRevD.102.012007`.

[117] K Abe et al. "Measurements of $\bar{\nu}_\mu$ and $\bar{\nu}_\mu + \nu_\mu$ charged-current cross-sections without detected pions or protons on water and hydrocarbon at a mean anti-neutrino energy of 0.86 GeV". In: *Progress of Theoretical and Experimental Physics* 2021.4 (Mar. 2021). URL: `https://doi.org/10.1093/ptep/ptab014`.

[118] K. Matsuoka et al. "Design and performance of the muon monitor for the T2K neutrino oscillation experiment". In: *Nuclear Instruments and Methods in Physics Research Section A: Accelerators, Spectrometers, Detectors and Associated Equipment* 624.3 (2010), pp. 591 –600. eprint: `http://www.sciencedirect.com/science/article/pii/S016890021002098X`.

[119] K Abe et al. "Improved constraints on neutrino mixing from the T2K experiment with 3.13×1021 protons on target". en. In: *Phys. Rev. D.* 103.11 (June 2021).

[120] Tomislav Vladisavljevic. *Predicting the T2K neutrino flux and measuring oscillation parameters*. 1st ed. Springer theses. Cham, Switzerland: Springer Nature, Sept. 2020.

[121] D Beavis, A Carroll, and I Chiang. "Long baseline neutrino oscillation experiment at the AGS. Physics design report". In: (Apr. 1995).

[122] P.-A. Amaudruz et al. "The T2K fine-grained detectors". In: *Nuclear Instruments and Methods in Physics Research Section A: Accelerators, Spectrometers, Detectors and Associated Equipment* 696 (Dec. 2012), pp. 1–31. URL: `https://doi.org/10.1016/j.nima.2012.08.020`.

[123] N. Abgrall et al. "Time projection chambers for the T2K near detectors". In: *Nuclear Instruments and Methods in Physics Research Section A: Accelerators, Spectrometers, Detectors and Associated Equipment* 637.1 (May 2011), pp. 25–46. URL: `https://doi.org/10.1016/j.nima.2011.02.036`.

[124] S. Assylbekov et al. "The T2K ND280 off-axis pi–zero detector". In: *Nuclear Instruments and Methods in Physics Research Section A: Accelerators, Spectrometers, Detectors and Associated Equipment* 686 (Sept. 2012), pp. 48–63. URL: `https://doi.org/10.1016/j.nima.2012.05.028`.

[125] D Allan et al. "The electromagnetic calorimeter for the T2K near detector ND280". In: *Journal of Instrumentation* 8.10 (2013), P10019–P10019. URL: `https://doi.org/10.1088%2F1748-0221%2F8%2F10%2Fp10019`.

[126] *UA1 magnet sets off for a second new life*. 2022. URL: `https://cerncourier.com/a/ua1-magnet-sets-off-for-a-second-new-life/`.

[127] F. Vannucci. "The NOMAD Experiment at CERN". In: *Advances in High Energy Physics* 2014 (2014), pp. 1–20. URL: `https://doi.org/10.1155/2014/129694`.

[128] S. Aoki et al. "The T2K Side Muon Range Detector (SMRD)". In: *Nuclear Instruments and Methods in Physics Research Section A: Accelerators, Spectrometers, Detectors and Associated Equipment* 698 (Jan. 2013), pp. 135–146. URL: `https://doi.org/10.1016/j.nima.2012.10.001`.

[129] K. Suzuki et al. "Measurement of the muon beam direction and muon flux for the T2K neutrino experiment". In: *Progress of Theoretical and Experimental Physics* 2015.5 (2015), pp. 53C01–0. URL: `https://doi.org/10.1093%2Fptep%2Fptv054`.

[130] S. Brooks et al. *Handbook of Markov Chain Monte Carlo*. CRC Press, 2011.

[131] W. R. Gilks, S. Richardson, and D. J. Spiegelhalter. *Markov Chain Monte Carlo in Practice*. Chapman & Hall/CRC Interdisciplinary Statistics, 1995.

[132] Clarence Wret. "Minimising systematic uncertainties in the T2K experiment using near-detector and external data". PhD thesis. Imperial College London, 2018.

[133] Kirsty Elizabeth Duffy. "Measurement of the Neutrino Oscillation Parameters $\sin^2\theta_{23}$, Δm^2_{32}, $\sin^2\theta_{13}$, and δ_{CP} in Neutrino and Antineutrino Oscillation at T2K". PhD thesis. Oriel College, University of Oxford, 2016.

[134] C. Bojechko and A. Kabooth. "Muon neutrino disappearance simultaneous fit of ND280 and SK with Run 1+2+3 data using Markov Chain Monte Carlo Analysis". In: *T2K Technical Note* 140 (2013).

[135] Thomas Bayes Rev. "An essay toward solving a problem in the doctrine of chances". In: *Phil. Trans. Roy. Soc. Lond.* 53 (1764), pp. 370–418.

[136] Artur Sztuc. "Standard and Non-Standard Neutrino-Antineutrino Oscillation Analyses and Event Reconstruction Studies using Markov Chain Monte Carlo Methods at T2K". PhD thesis. Imperial College London, 2021.

[137] N. Metropolis et al. "Equation of State Calculations by Fast Computing Machines". In: *Journal of Chemical Physics* 21.6 (1970).

[138] W. K. Hastings. "Monte Carlo Sampling Methods Using Markov Chains and Their Applications". In: *Biometrika* 57.1 (1970).

[139] Joanna Dunkley et al. "Fast and reliable Markov chain Monte Carlo technique for cosmological parameter estimation". en. In: *Mon. Not. R. Astron. Soc.* 356.3 (Jan. 2005), pp. 925–936.

[140] Harold Jeffreys. *The Theory of Probability*. Oxford Classic Texts in the Physical Sciences. 1939.

[141] Robert E Kass and Adrian E Raftery. "Bayes factors". en. In: *J. Am. Stat. Assoc.* 90.430 (June 1995), pp. 773–795.

[142] T.T. Böhlen et al. “The FLUKA Code: Developments and Challenges for High Energy and Medical Applications”. In: *Nuclear Data Sheets* 120 (2014), pp. 211 –214. eprint: `http://www.sciencedirect.com/science/article/pii/S0090375214005018`.

[143] René Brun et al. *GEANT: Detector Description and Simulation Tool; Oct 1994*. CERN Program Library. Long Writeup W5013. Geneva: CERN, 1993. eprint: `http://cds.cern.ch/record/1082634`.

[144] K. Abe et al. “T2K neutrino flux prediction”. In: *Phys. Rev. D* 87 (1 2013), p. 012001. URL: `https://link.aps.org/doi/10.1103/PhysRevD.87.012001`.

[145] C. Zeitnitz and T.A. Gabriel. “The GEANT-CALOR interface and benchmark calculations of ZEUS test calorimeters”. In: *Nuclear Instruments and Methods in Physics Research Section A: Accelerators, Spectrometers, Detectors and Associated Equipment* 349.1 (1994), pp. 106 –111. eprint: `http://www.sciencedirect.com/science/article/pii/0168900294906130`.

[146] A. Fiorentini et al. “Flux Prediction and Uncertainty Updates with NA61 2009 Thin Target Data and Negative Focussing Mode Predictions”. In: *T2K Technical Note* 217 (2017).

[147] N. Abgrall et al. “Measurements of cross sections and charged pion spectra in proton-carbon interactions at 31 GeV/<mml:math xmlns:mml="http://www.w3.org/1998/Math/MathML" display="inline"><mml:mi>c</mml:mi></mml:math>”. In: *Physical Review C* 84.3 (2011). URL: `https://doi.org/10.1103%2Fphysrevc.84.034604`.

[148] N. Abgrall et al. “Measurement of production properties of positively charged kaons in proton-carbon interactions at 31 GeV/<mml:math xmlns:mml="http://www.w3.org/1998/Math/MathML" display="inline"><mml:mi>c</mml:mi></mml:math>”. In: *Physical Review C* 85.3 (2012). URL: `https://doi.org/10.1103%2Fphysrevc.85.035210`.

[149] N. Abgrall et al. “Pion emission from the T2K replica target: Method, results and application”. In: *Nuclear Instruments and Methods in Physics Research Section A: Accelerators, Spectrometers, Detectors and Associated Equipment* 701 (2013), pp. 99 –114. eprint: `http://www.sciencedirect.com/science/article/pii/S016890021201234X`.

[150] M. Apollonio et al. “Forward production of charged pions with incident protons on nuclear targets at the CERN Proton Synchrotron”. In: *Phys. Rev. C* 80 (3 2009), p. 035208. eprint: `https://link.aps.org/doi/10.1103/PhysRevC.80.035208`.

[151] B. Blau et al. “The superconducting magnet of AMS-02”. In: *Nuclear Physics B - Proceedings Supplements* 113.1-3 (Dec. 2002), pp. 125–132. URL: `https://doi.org/10.1016/s0920-5632(02)01831-5`.

[152] S. Haino et al. “Measurements of primary and atmospheric cosmic-ray spectra with the BESS-TeV spectrometer”. In: *Physics Letters B* 594.1-2 (July 2004), pp. 35–46. URL: `https://doi.org/10.1016/j.physletb.2004.05.019`.

[153] NASA. *U.S. Standard Atmosphere, 1976*. 1976.

[154] S. Roesler, R. Engel, and J. Ranft. “The Monte Carlo Event Generator DPMJET-III”. In: *Advanced Monte Carlo for Radiation Physics, Particle Transport Simulation and Applications*. Springer Berlin Heidelberg, 2001, pp. 1033–1038. URL: `https://doi.org/10.1007/978-3-642-18211-2\_166`.

[155] Koji Niita et al. “PHITS—a particle and heavy ion transport code system”. In: *Radiation Measurements* 41.9-10 (Oct. 2006), pp. 1080–1090. URL: `https://doi.org/10.1016/j.radmeas.2006.07.013`.

[156] T Sanuki et al. “Measurements of atmospheric muon spectra at mountain altitude”. In: *Physics Letters B* 541.3-4 (2002), pp. 234–242. URL: `https://doi.org/10.1016%2Fs0370-2693%2802%2902265-7`.

[157] P. Achard et al. “Measurement of the atmospheric muon spectrum from 20 to 3000 GeV”. In: *Physics Letters B* 598.1-2 (2004), pp. 15–32. URL: `https://doi.org/10.1016%2Fj.physletb.2004.08.003`.

[158] Kazufumi Sato. *Atmospheric Neutrino_Reviews on neutrino fluxes (low E atm nu)*. 2022.

[159] Yoshinari Hayato and Luke Pickering. “The NEUT neutrino interaction simulation program library”. In: *The European Physical Journal Special Topics* 230.24 (Oct. 2021), pp. 4469–4481. URL: `https://doi.org/10.1140/epjs/s11734-021-00287-7`.

[160] Yoshinari Hayato. “A Neutrino Interaction Simulation Program Library NEUT”. In: *Acta Physica Polonica B* 40.9 (2009).

[161] C.H. Llewellyn Smith. “Neutrino reactions at accelerator energies”. In: *Physics Reports* 3.5 (1972), pp. 261 –379. eprint: `http://www.sciencedirect.com/science/article/pii/0370157372900105`.

[162] Omar Benhar, Adelchi Fabrocini, and Stefano Fantoni. “The nucleon spectral function in infinite nuclear matter”. In: *Nuclear Physics A* 497 (June 1989), pp. 423–430. URL: `https://doi.org/10.1016/0375-9474(89)90484-3`.

[163] R. Bradford et al. “A New Parameterization of the Nucleon Elastic Form Factors”. In: *Nuclear Physics B - Proceedings Supplements* 159 (2006). Proceedings of the 4th International Workshop on Neutrino-Nucleus Interactions in the Few-GeV Region, pp. 127 –132. eprint: `http://www.sciencedirect.com/science/article/pii/S0920563206005184`.

[164] A. A. Aguilar-Arevalo et al. “First measurement of the muon neutrino charged current quasielastic double differential cross section”. In: *Physical Review D* 81.9 (2010). URL: `https://doi.org/10.1103%2Fphysrevd.81.092005`.

[165] R. Gran et al. “Neutrino-nucleus quasi-elastic and 2p2h interactions up to 10 GeV”. In: *Phys. Rev. D* 88 (11 2013), p. 113007. eprint: `https://link.aps.org/doi/10.1103/PhysRevD.88.113007`.

[166] Ch. Berger and L. M. Sehgal. “Lepton mass effects in single pion production by neutrinos”. In: *Phys. Rev. D* 76 (11 2007), p. 113004. URL: `https://link.aps.org/doi/10.1103/PhysRevD.76.113004`.

[167] Ch. Berger and L. M. Sehgal. “Partially conserved axial vector current and coherent pion production by low energy neutrinos”. In: *Phys. Rev. D* 79 (5 2009), p. 053003. eprint: `https://link.aps.org/doi/10.1103/PhysRevD.79.053003`.

[168] Torbjörn Sjöstrand. "High-energy-physics event generation with PYTHIA 5.7 and JETSET 7.4". In: *Computer Physics Communications* 82.1 (Aug. 1994), pp. 74–89. URL: `https://doi.org/10.1016/0010-4655(94)90132-5`.

[169] Christophe Bronner and Mark Hartz. "Tuning of the Charged Hadrons Multiplicities for Deep Inelastic Interactions in NEUT". In: *Proceedings of the 10th International Workshop on Neutrino-Nucleus Interactions in Few-GeV Region (NuInt15)*. Journal of the Physical Society of Japan, Dec. 2016. URL: `https://doi.org/10.7566/jpscp.12.010041`.

[170] M. Glück, E. Reya, and A. Vogt. "Dynamical parton distributions revisited". In: *The European Physical Journal C* 5.3 (1998), pp. 461–470. URL: `https://doi.org/10.1007%2Fs100529800978`.

[171] Arie Bodek and Un-ki Yang. *Axial and Vector Structure Functions for Electron- and Neutrino- Nucleon Scattering Cross Sections at all Q^2 using Effective Leading order Parton Distribution Functions*. 2010. URL: `https://arxiv.org/abs/1011.6592`.

[172] Arie Bodek and Un-Ki Yang. "Update to the Bodek-Yang Unified Model for Electron- and Neutrino- Nucleon Scattering Cross Sections". In: (2010). URL: `https://arxiv.org/abs/1012.0261`.

[173] Sowjanya Gollapinni. "Neutrino Cross section Future". In: (2016). URL: `https://arxiv.org/abs/1602.05299`.

[174] E. S. Pinzon Guerra et al. "Using world $\pi^{\pm}$-nucleus scattering data to constrain an intranuclear cascade model". In: *Phys. Rev. D* 99 (5 2019), p. 052007. URL: `https://link.aps.org/doi/10.1103/PhysRevD.99.052007`.

[175] S. Agostinelli et al. "GEANT4: A Simulation toolkit". In: *Nucl. Instrum. Meth.* A506 (2003), pp. 250–303.

[176] R. Brun et al. "GEANT3". In: (Sept. 1987).

[177] et al. A. Himmel. "Super-Kamiokande events and data quality studies for T2K Runs 5 and 6". In: *T2K Technical Note* 219 (2015).

[178] et al. S. Berkman. "fiTQun: A New Reconstruction Algorithm for Super-K". In: *T2K Technical Note* 146 (2013).

[179] R.B. Patterson et al. "The extended-track event reconstruction for MiniBooNE". In: *Nuclear Instruments and Methods in Physics Research Section A: Accelerators, Spectrometers, Detectors and Associated Equipment* 608.1 (2009), pp. 206–224. URL: `https://doi.org/10.1016\%2Fj.nima.2009.06.064`.

[180] M. Shiozawa. "Reconstruction algorithms in the Super-Kamiokande large water Cherenkov detector". In: *Nuclear Instruments and Methods in Physics Research Section A: Accelerators, Spectrometers, Detectors and Associated Equipment* 433.1-2 (Aug. 1999), pp. 240–246. URL: `https://doi.org/10.1016/s0168-9002(99)00359-9`.

[181] K. Abe et al. “Search for <mml:math xmlns:mml="http://www.w3.org/1998/Math/MathML" display="inline"><mml:mi>C</mml:mi><mml:mi>P</mml:mi></mml:math> Violation in Neutrino and Antineutrino Oscillations by the T2K Experiment with <mml:math xmlns:mml="http://www.w3.org/1998/Math/MathML" display="inline"><mml:mn>2.2</mml:mn><mml:mo>×</mml:mo><mml:msup><mml:mn Protons on Target”. In: *Physical Review Letters* 121.17 (Oct. 2018). URL: `https://doi.org/10.1103/physrevlett.121.171802`.

[182] K. Abe et al. “Measurements of neutrino oscillation in appearance and disappearance channels by the T2K experiment with<mml:math xmlns:mml="http://www.w3.org/1998/Math/MathML" display="inline"><mml:mn>6.6</mml:mn><mml:mo>×</mml:mo><mml:mn>1</mml:mn on target”. In: *Physical Review D* 91.7 (Apr. 2015). URL: `https://doi.org/10.1103/physrevd.91.072010`.

[183] F and James. “MINUIT: Function Minimization and Error Analysis Reference Manual”. In: (1998). CERN Program Library Long Writeups. URL: `https://cds.cern.ch/record/2296388`.

[184] Xiaoyue Li and Michael Wilking. “FiTQun Event Selection Optimization”. In: *T2K Technical Note* 319 (2017).

[185] Shimpei Tobayama. “An Analysis of the Oscillation of Atmospheric Neutrinos”. PhD thesis. British Columbia U., 2016.

[186] et al. D. Barrow. “Super-Kamiokande Data Quality, MC, and Systematics in Run 10”. In: *T2K Technical Note* 399 (2020).

[187] A. Maghrabi, A. Aldosari, and M. Almutairi. “Correlation analyses between solar activity parameters and cosmic ray muons between 2002 and 2012 at high cutoff rigidity”. In: *Advances in Space Research* 68.7 (Oct. 2021), pp. 2941–2952. URL: `https://doi.org/10.1016/j.asr.2021.05.016`.

[188] K. Abe et al. “Atmospheric neutrino oscillation analysis with external constraints in Super-Kamiokande I-IV”. In: *Phys. Rev. D* 97 (7 2018), p. 072001. eprint: `https://link.aps.org/doi/10.1103/PhysRevD.97.072001`.

[189] J. Beringer et al. “Review of Particle Physics”. In: *Phys. Rev. D* 86 (1 2012), p. 010001. URL: `https://link.aps.org/doi/10.1103/PhysRevD.86.010001`.

[190] S. Nakayama K. Iyogi and Y. Obayashi. “T2K data acquisition and FC event selection at Super-Kamiokande”. In: *T2K Technical Note* 027 (2011).

[191] LeeKaPik. “Study of the neutrino mass hierarchy with the atmospheric neutrino data observed in Super-Kamiokande”. PhD thesis. Tokyo University, 2012.

[192] R. Wendell et al. “Atmospheric neutrino oscillation analysis with subleading effects in Super-Kamiokande I, II, and III”. In: *Phys. Rev. D* 81 (9 2010), p. 092004. URL: `https://link.aps.org/doi/10.1103/PhysRevD.81.092004`.

[193] J. Hosaka et al. “Three flavor neutrino oscillation analysis of atmospheric neutrinos in Super-Kamiokande”. In: *Phys. Rev. D* 74 (3 2006), p. 032002. URL: `https://link.aps.org/doi/10.1103/PhysRevD.74.032002`.

[194] Laura Munteanu et al. "Constraining the Flux and Cross Section Models with Data from ND280 using FGD1 and FGD2 for the 2020 Oscillation Analysis". In: *T2K Technical Note* 395 (2020).

[195] P. Bartet et al. "ν_μ CC event selections in the ND280 tracker using Run 2+3+4 data". In: *T2K Technical Note* 212 (2015).

[196] Will Parker. "Constraining Systematic Uncertainties at T2K using Near Detector Data". PhD thesis. Royal Holloway University of London, 2020.

[197] V. Berardi et al. "$\bar{\nu}_\mu$ event selection in the ND280 tracker using Run 5c and Run 6 anti-neutrino beam data". In: *T2K Technical Note* 246 (2015).

[198] James Missert. "TN-318: Fit to Super-K Atmospheric Neutrino Data for Optimization of the fiTQun Fiducial Volume Cuts and Estimation of Detector Uncertainties". In: *T2K Technical Note* 318 (2017).

[199] et al. J. Chakrani. "NIWG model and uncertainties for 2021 oscillation analysis". In: *T2K Technical Note* 414 (2022).

[200] Morgan Wascko. "T2K Status, Results, and Plans". Neutrino 2018. 2018.

[201] et al. Tomislav Vladisavljevic. "Flux Prediction and Uncertainty with NA61/SHINE 2009 Replica-Target Data (TN354 version 3.3)". In: *T2K Technical Note* 354 (2020).

[202] G Ambrosini et al. "K/π production ratios from 450 GeV/c protons on beryllium". en. In: *Phys. Lett. B* 420.1-2 (Feb. 1998), pp. 225–232.

[203] et al. Edward Atkin. "NIWG model and uncertainties for 2019-2020 oscillation analysis". In: *T2K Technical Note* 344 (2019).

[204] et al. D. Barrow. "Flux and interaction models for the initial T2K-SK atmospheric joint fit studies". In: *T2K Technical Note* 422 (2022).

[205] et al. D. Barrow. "SK atmospheric T2K beam joint fit technical note, MaCh3 details". In: *T2K Technical Note* 426 (2022).

[206] A. A. Aguilar-Arevalo et al. "Measurement of ν_μ and $\overline{\nu}_\mu$ induced neutral current single π^0 production cross sections on mineral oil at $E_\nu \sim \mathcal{O}$ (1 GeV)". In: *Phys. Rev. D* 81 (1 2010), p. 013005. eprint: `https://link.aps.org/doi/10.1103/PhysRevD.81.013005`.

[207] Patrick de Perio and James Imber. "Super-K Systematic Uncertainties for RUN1-4 Joint ν_e and ν_μ Analyses". In: *T2K Technical Note* 186 (2014).

[208] Patrick de Perio and James Imber. "Update of SK ν_e systematic error for 2012a oscillation analysis". In: *T2K Technical Note* 107 (2012).

[209] Cris Vilela Daniel Barrow. *T2K-SK Detector Matrix Uncertainties - MaCh3 Integration*. `https://git.t2k.org/t2k-sk/t2ksk-detcovmat/-/tree/feature/MaCh3Integration`. Accessed: 22-06-2022.

[210] Roger Barlow and Christine Beeston. "Fitting using finite Monte Carlo samples". en. In: *Comput. Phys. Commun.* 77.2 (Oct. 1993), pp. 219–228.

[211] J S Conway. *Incorporating nuisance parameters in likelihoods for multisource spectra*. 2011.

[212] et al. D. Barrow. “Oscillation probability calculation for the T2K+SK atmospheric joint fit”. In: *T2K Technical Note* 425 (2022).

[213] R G Calland, A C Kaboth, and D Payne. “Accelerated event-by-event neutrino oscillation reweighting with matter effects on a GPU”. In: 9.04 (Apr. 2014), P04016–P04016. URL: `https://doi.org/10.1088/1748-0221/9/04/p04016`.

[214] R. Wendell. http://www.phy.duke.edu/ raw22/public/Prob3++/.

[215] Felix Kallenborn et al. “Massively parallel computation of atmospheric neutrino oscillations on CUDA-enabled accelerators”. In: *Computer Physics Communications* 234 (2019), pp. 235–244. URL: `https://www.sciencedirect.com/science/article/pii/S0010465518302790`.

[216] Liban Warsame. *MaCh3 Analysis Progress*. URL: `https://indico.fnal.gov/event/50217/contributions/241232/attachments/155318/202209/MaCh3ProgressforDUNELBL\underscoreMay17%20%282%29.pdf`.

[217] Simon Bourret, João A B Coelho, and Véronique Van Elewyck and. “Neutrino oscillation tomography of the Earth with KM3NeT-ORCA”. In: *Journal of Physics: Conference Series* 888 (2017), p. 012114. URL: `https://doi.org/10.1088%2F1742-6596%2F888%2F1%2F012114`.

[218] C. Rott, A. Taketa, and D. Bose. “Spectrometry of the Earth using Neutrino Oscillations”. In: *Scientific Reports* 5.1 (Oct. 2015). URL: `https://doi.org/10.1038/srep15225`.

[219] Kaoru Hagiwara, Naotoshi Okamura, and Ken ichi Senda. “The earth matter effects in neutrino oscillation experiments from Tokai to Kamioka and Korea”. In: *Journal of High Energy Physics* 2011.9 (Sept. 2011). URL: `https://doi.org/10.1007/jhep09(2011)082`.

[220] Dave Typinski. *Earth Gravity*. `http://www.typnet.net/Essays/EarthGravGraphics/EarthGrav.pdf`. Accessed: 24-06-2022.

[221] D. Barrow. *T2K Beam + SK Atmospheric Joint Fit*. 2022.